

# The Anatomy of the Wing

## OUTLINE

<b>9.1 Introduction</b>	301	<b>9.3.4 Dihedral or Anhedral, <math>\Gamma</math></b>	318
9.1.1 <i>The Content of this Chapter</i>	301	9.3.5 <i>Wing Twist – Washout and Washin, <math>\phi</math></i>	319
9.1.2 <i>Definition of Reference Area</i>	302	Geometric Washout	319
9.1.3 <i>The Process of Wing Sizing</i>	302	Aerodynamic Washout	319
The Establishment of Basic Datum	302	A Combined Geometric and Aerodynamic Washout	323
<b>9.2 The Trapezoidal Wing Planform</b>	303	Panknin and Culver Wing Twist Formulas	324
9.2.1 <i>Definitions</i>	303	9.3.6 <i>Wing Angle-of-incidence, <math>i_W</math></i>	325
Aspect Ratio for HT and VT	305	Step 1: Determine the Optimum AOA for the Fuselage	326
Aspect Ratio for Multi-wing Configurations	305	Step 2: Determine the Representative AOA at Cruise	326
Derivation of Equations (9-6), (9-8), and (9-10)	305	Step 3: Determine the Recommended Wing Angle-of-incidence	326
9.2.2 <i>Poor Man's Determination of the MGC</i>	306	Step 4: Determine the Recommended HT Angle-of-incidence	327
9.2.3 <i>Planform Dimensions in Terms of S, <math>\lambda</math>, and AR</i>	307	Derivation of Equation (9-43)	327
Derivation of Equation (9-20)	307	Derivation of Equation (9-45)	327
Derivation of Equation (9-21)	308	Decalage Angle for a Monoplane	328
9.2.4 <i>Approximation of an Airfoil Cross-sectional Area</i>	308	9.3.7 <i>Wing Layout Properties of Selected Aircraft</i>	329
Derivation of Equations (9-22) and (9-23)	308		
<b>9.3 The Geometric Layout of the Wing</b>	309	<b>9.4 Planform Selection</b>	329
9.3.1 <i>Wing Aspect Ratio, AR</i>	309	9.4.1 <i>The Optimum Lift Distribution</i>	329
Illustrating the Difference Between Low and High AR Wings	310	9.4.2 <i>Methods to Present Spanwise Lift Distribution</i>	331
Determining AR Based on a Desired Range	312	9.4.3 <i>Constant-chord ("Hershey-bar") Planform</i>	332
Derivation of Equation (9-26)	312	Pros	333
Determining AR Based on Desired Endurance	313	Cons	333
Derivation of Equation (9-28)	313	9.4.4 <i>Elliptic Planforms</i>	333
Estimating AR Based on Minimum Drag	314	Pros	334
Estimating AR for Sailplane Class Aircraft	315	Cons	334
9.3.2 <i>Wing Taper Ratio, TR or <math>\lambda</math></i>	315	9.4.5 <i>Straight Tapered Planforms</i>	334
9.3.3 <i>Leading Edge and Quarter-chord Sweep Angles, <math>\Lambda_{LE}</math> and <math>\Lambda_{C/4}</math></i>	317	Pros	334
Impact of Sweep Angle on the Critical Mach Number	317	Cons	334
Impact of Sweep Angle on the $C_{L_{max}}$	318	Straight Leading or Trailing Edges	335
Impact of Sweep Angle on Structural Loads	318	Pros	335
Impact of Sweep Angle on Stall Characteristics	318	Cons	335
		The Compound Tapered Planform	335
		9.4.6 <i>Swept Planforms</i>	336
		The Aft-swept Planform	336
		Pros	336

Cons	336	<b>Step 3:</b> Determine the AOA at which Local $C_l$ Intersects $C_{l\max}$	355
The Forward-swept Planform	337	<b>Step 4:</b> Compute $C_{l\max}$	355
Variable Swept Planform	338	<b>9.5.12 Step-by-step: <math>C_{l\max}</math> Estimation per USAF DATCOM Method 2</b>	356
<b>9.4.7 Cranked Planforms</b>	338	Step 1: Determine the Taper Ratio	
Semi-tapered Planform	339	Correction Factor	357
Crescent Planform	339	Step 2: Determine if Wing Qualifies as "High AR"	357
Schuemann Planform	339	Step 3: Determine the Leading Edge Parameter	357
<b>9.4.8 Delta Planforms</b>	340	Step 4: Determine the Max Lift Ratio	357
The Delta Planform Shape	340	Step 5: Determine the Mach Number Correction Factor	357
The Double-delta Planform Shape	341	Step 6: Calculate the $C_{l\max}$	358
<b>9.4.9 Some Exotic Planform Shapes</b>	341	Step 7: Determine Zero Lift Angle and Lift Curve Slope	358
Disc- or Circular-shaped Planform	341	Step 8: Determine a Correction for the Stall Angle-of-attack	358
Other Configurations	342	Step 9: Determine the Wing Stall Angle-of-attack	359
<b>9.5 Lift and Moment Characteristics of a 3D Wing</b>	342	<b>9.5.13 <math>C_{l\max}</math> for Selected Aircraft</b>	360
<b>9.5.1 Properties of the Three-dimensional Lift Curve</b>	342	<b>9.5.14 Estimation of Oswald's Span Efficiency</b>	363
Lift Curve Slope, $C_{L\alpha}$	343	Basic Definition	363
Maximum and Minimum Lift Coefficients, $C_{L\max}$ and $C_{L\min}$	343	Method 1: Empirical Estimation for Straight Wings	363
$C_L$ at Zero AOA, $C_{L0}$	343	Method 2: Empirical Estimation for Swept Wings	363
Angle-of-attack at Zero Lift, $\alpha_{ZL}$	343	Method 3: Douglas Method	364
Linear Range	343	Method 4: Lifting Line Theory	364
Angle-of-attack where Lift Curve Becomes Non-linear, $\alpha_{NL}$	343	Method 5: USAF DATCOM Method for Swept Wings – Step-by-step	364
Angle-of-attack for Maximum Lift Coefficient, $\alpha_{stall}$	343	Step 1: Calculate the Lift Curve Slope	365
Design Lift Coefficient, $C_{LC}$	343	Step 2: Calculate the Leading Edge Suction Parameter	365
Angle-of-attack for Design Lift Coefficient, $\alpha_C$	343	Step 3: Calculate Special Parameter 1	365
Derivation of Equation (9-49)	343	Step 4: Calculate Special Parameter 2	365
<b>9.5.2 The Lift Coefficient</b>	344	Step 5: Read or Calculate the Leading Edge Suction Parameter	365
The Relationship between Airspeed, Lift Coefficient, and Angle-of-attack	344	<b>9.6 Wing Stall Characteristics</b>	366
Wide-range Lift Curve	344	<b>9.6.1 Growth of Flow Separation on an Aircraft</b>	367
<b>9.5.3 Determination of Lift Curve Slope, <math>C_{L\alpha}</math>, for a 3D Lifting Surface</b>	345	<b>9.6.2 General Stall Progression on Selected Wing Planform Shapes</b>	369
Derivation of Equation (9-53)	346	<b>9.6.3 Deviation from Generic Stall Patterns</b>	369
Derivation of Equation (9-54)	347	<b>9.6.4 Tailoring the Stall Progression</b>	369
<b>9.5.4 The Lift Curve Slope of a Complete Aircraft</b>	347	Design Guidelines	369
Derivation of Equations (9-59) and (9-60)	347	Tailoring Stall Characteristics of Wings with Multiple Airfoils	371
<b>9.5.5 Step-by-step: Transforming the Lift Curve from 2D to 3D</b>	348	Other Issues Associated with Wings with Multiple Airfoils	373
<b>9.5.6 The Law of Effectiveness</b>	349	<b>9.6.5 Cause of Spanwise Flow for a Swept-back Wing Planform</b>	374
<b>9.5.7 Flexible Wings</b>	349	<b>9.6.6 Pitch-up Stall Boundary for a Swept-back Wing Planform</b>	375
<b>9.5.8 Ground Effect</b>	350		
<b>9.5.9 Impact of <math>C_{l\max}</math> and Wing Loading on Stalling Speed</b>	353		
<b>9.5.10 Step-by-step: Rapid <math>C_{l\max}</math> Estimation</b>	353		
<b>9.5.11 Step-by-step: <math>C_{l\max}</math> Estimation per USAF DATCOM Method 1</b>	355		
<b>Step 1:</b> Determine the Two-dimensional Maximum Lift Coefficient	355		
<b>Step 2:</b> Plot the Distribution of Section Lift Coefficients	355		

Derivation of Equations (9-94) and (9-95)	377	Change in Induced Angle-of-attack	387
9.6.7 Influence of Manufacturing Tolerances on Stall Characteristics	378	Derivation of Equations (9-124) through (9-128)	387
<b>9.7 Numerical Analysis of the Wing</b>	<b>379</b>	Derivation of Equation (9-130)	388
9.7.1 Prandtl's Lifting Line Theory	379	9.7.4 Accounting for a Fuselage in Prandtl's Lifting Line Method	390
The Vortex Filament and the Biot-Savart Law	380	9.7.5 Computer code: Prandtl's Lifting Line Method	393
Helmholz's Vortex Theorems	381		
Lifting Line Formulation	381		
9.7.2 Prandtl's Lifting Line Method – Special Case: The Elliptical Wing	384	<b>Exercises</b>	<b>396</b>
Derivation of Equations (9-113) through (9-119)	384	<b>Variables</b>	<b>397</b>
9.7.3 Prandtl's Lifting Line Method – Special Case: Arbitrary Wings	386	<b>References</b>	<b>398</b>

## 9.1 INTRODUCTION

Now that the characteristics of airfoils have been discussed, it is time to evaluate their use in lifting surfaces. A lifting surface can be defined as a three-dimensional body whose primary purpose is to generate aerodynamic loads; primarily lift. A wing is a lifting surface capable of structurally reacting the load it generates, up to certain airspeeds of course.

The geometry of lifting surfaces is usually defined in terms of two two-dimensional shapes; the *airfoil* and *planform*. The former has already been treated in Chapter 8, *The anatomy of the airfoil*. However, the combination of the two is the topic of this section. The history of aviation shows that a great many combinations of airfoils and planform shapes have been used, some with great success, others less so. It is the responsibility of the design team, usually the aerodynamics group, to select airfoils and a planform shape that not only fulfill the aerodynamic and performance goals, but also that allow the requirements of other design groups to be met. A part of this responsibility calls for the geometry of the wing and stabilizing surfaces, and their relative spatial location, to be defined so the combination yields an aircraft that is both safe and easy to handle. At the same time, the wing must feature enough internal volume to accommodate systems, landing gear, fuel, and so on. The aero group must also recognize that any systems required to enhance lift will increase the cost of manufacturing and maintenance, not to mention increase risk when flight-tested. The goal should always be to select the simplest system that does the job.

We have seen in Chapter 5, *Aircraft structural layout*, how the wing and stabilizing surfaces are typically constructed. A spar-rib-stringers-skin is always used for aluminum structures and spar-rib-stiffened-skin

construction for composite structures. A planform shape that deviates from the shapes shown in Section 9.4, *Planform selection*, can present serious structural challenges. If a challenging planform is chosen, it would be wise to lay out the structure early in the process and work out possible manufacturing problems and not just aerodynamic ones. Such problems may range from limited fuel volume, space claims for retractable landing gear, the high-lift system and primary control system, curved spars, to unexpected aeroelastic issues.

In short, this section assumes the wing area and vertical position of the wing (low, mid, high, parasol) have already been determined and what remains is:

- (1) determine the planform shape (general geometry, taper ratio, and leading edge sweep)
- (2) determine wing twist (washout)
- (3) determine the lift and pitching moment characteristics ( $C_{L\alpha}$ ,  $C_{L\max}$ ,  $C_{L\min}$ ,  $\alpha_{stall}$ ,  $C_M$ , Oswald's span efficiency, and others).

Note that weight and drag characteristics of the wing are treated in Chapter 6, *Aircraft weight analysis*, and Chapter 15, *Aircraft drag analysis*, respectively.

### 9.1.1 The Content of this Chapter

- Section 9.2 presents a handy formulation to calculate various properties of trapezoidal surfaces, which is the most common planform shape for lifting surfaces such as wings, and horizontal and vertical tails.
- Section 9.3 presents various concepts, topics, and methods for laying out the wing planform. These include aspect ratio, taper ratio, washout, and wing incidence angle.
- Section 9.4 is intended to help with the selection of a suitable planform shape. It introduces a number of

different geometries and presents information about their pros and cons, in addition to giving ideas of the distribution of section lift coefficients.

- **Section 9.5** presents a number of methods to evaluate the lift and pitching moment characteristics of the wing (methods to evaluate drag are presented in Chapter 15, *Aircraft drag analysis*).
- **Section 9.6** presents a number of issues that have to do with wing stall characteristics and how to improve them.
- **Section 9.7** presents Prandtl's Lifting Line Theory, which is a numerical method used to estimate the aerodynamic properties of the wing. A computer function, written in Visual Basic for Applications, intended for use with Microsoft Excel is also presented.

### 9.1.2 Definition of Reference Area

One of the most important concepts in aircraft design (as well as in the entire discipline of aerodynamics) is the *reference area*. Characteristics such as lift, drag, and moment coefficients all require this area to be specified, as does performance; stability and control; and load analyses, just to name a few. The shaded areas in Figure 9-1 show how aircraft designers typically define the reference area. However, this is not to say it couldn't be defined in some other way; in fact, the shaded regions may not be at all what the manufacturers did for these particular aircraft, just what would be a plausible approach.

Since the definition of this area takes place in the early stages of the airplane's design, it is almost always defined in a simple manner. As a consequence, when the geometry gets modified at a later time (for instance, a wingtip is

reshaped) the reference area is not changed (as this would be likely to require a large number of documents to be revised, even certification documents), but the change will be manifested through a change in maximum lift coefficient, modified drag polar and similar definitions. An added wingtip shape, strakes, or leading edge extensions are typically omitted because they are often afterthoughts or added as a consequence of a wind tunnel or a flight test program (stall and spin recovery) or added features (wingtip tanks for greater range or modifications to the initial wing/fuselage fairing).

### 9.1.3 The Process of Wing Sizing

The concept of *Wing Sizing* refers to the process required to determine the size, shape, and three-dimensional positioning of the wing surfaces. This procedure is listed in Table 9-1.

#### ***The Establishment of Basic Datum***

The positioning of the wing is the determination of where, with respect to some reference point in space, the wing shall be located. During the design of the aircraft it is usually decided that the reference datum for the airplane may be a point on the fuselage or the wing or a point in space (typically ahead of the nose of the aircraft as discussed in Section 6.6.11, *Center of gravity envelope*).

Among those are evaluation of dynamic stability and compliance with the design checklist of Section 23.3, *GA aircraft design checklist*. Typically, this will consider the following:

- Stability derivatives such as  $C_{m\alpha}$ ,  $C_{m\delta_e}$ ,  $C_{mq}$ ,  $C_{y\beta}$ ,  $C_{n\beta}$ ,  $C_{n\delta_r}$ ,  $C_{nr}$ , and others.

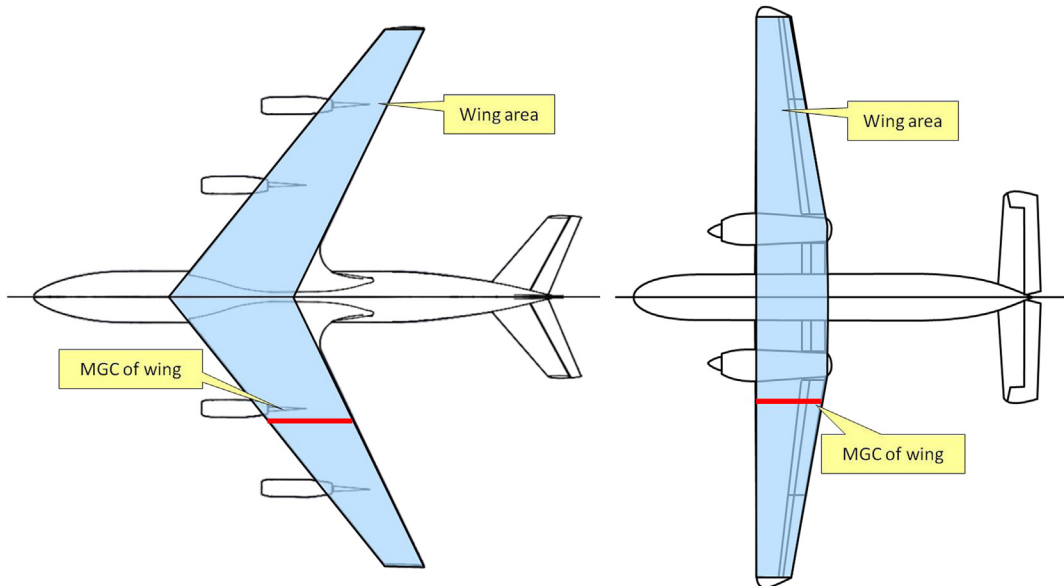


FIGURE 9-1 Reference area for the Boeing 707 and De Havilland of Canada DHC-7 Caribou (drawing is not to scale).

**TABLE 9-1** Initial Sizing and Layout Algorithm for the Wing of a GA Aircraft

Step	Task	Section
1	It is assumed that the required wing area has already been determined using the constraint analysis method of Section 3.2, <i>Constraint analysis</i> . Verify the predicted stalling speed is within regulatory margins (e.g. 45 KCAS if LSA, 61 KCAS is 14 CFR Part 23, etc.) before proceeding.	3.2
2	Select the wing planform geometry (see Section 9.4, <i>Planform selection</i> ). This may or may not be the final shape.	9.4
3	As a starting point, select a candidate aspect ratio and taper ratio. For AR consider the use of Equations (9-26) or (9-28). In the absence of specific target values, initial values can be selected by considering the class of aircraft being designed. For instance, refer to Tables 4-2 regarding the specific class of airplanes and then Tables 9-3 and 9-4 for additional help. These are initial values that are likely to change, but are a reasonable starting point.	4.2 9.3.1 9.3.2
4	Select candidate airfoils for the root and tip. Do not assign a wing washout at this time.	8
5	Evaluate the need for wing sweep. Is this a high-subsonic aircraft? Is there a possible problem with CG location that calls for a wing sweep to solve?	9.3.3
6	Once the airplane takes shape, a more sophisticated reshaping is required, in accordance with the design algorithm of Section 1.3.1, <i>Conceptual design algorithm for a GA aircraft</i> . This reshaping takes into account performance, stability and control, structural, and systems considerations.	1.3.2

- Impact on the non-linear behavior of the above stability derivatives.
- Structures (structural weight, aeroelasticity, etc.).
- Control authority in extreme flight conditions.
- Control system complexity.
- Operation (e.g. tail length may interfere with T-O rotation, require excessive control surface deflection, and subject the structure to high stresses, etc.).
- Stall tailoring; i.e. the design of the wing for benign stall characteristics.

Methods to treat planform shapes that are either cranked or described with piecewise continuous mathematical functions are given in Appendix D: *Geometry of lifting surfaces*.

### 9.2.1 Definitions

Figure 9-2 shows the general definitions for the geometry of the trapezoidal planform and indicates important details of such sections. A *leading edge* is the part of a lifting surface that faces the direction of intended movement. The *trailing edge* is opposite to that side. The *root* is the inboard side of the planform and, as can be seen in the figure, is where the two trapezoids join. This would typically be the centerline of the aircraft or the plane of symmetry. Although the term root sometimes refers to where the wing intersects the fuselage, that definition is not used in this text because the geometry of the fuselage may be changing and thus defining a wing chord there would lead to some undesirable issues. The *tip* is the side opposite of the root – it is the outboard side. The distance between the left and right tip is called the *span*, denoted by the variable  $b$ . The transverse dimension is called *chord*. Thus we talk about a *root-chord* or *tip-chord* as the length of the corresponding sides, denoted by the variables  $C_r$  and  $C_t$ , respectively. We also call the ratio of the tip-chord to the root-chord the *taper ratio*, denoted by  $\lambda$ . Another important ratio is the *aspect ratio*,  $AR$ , which indicates the slenderness of the wing. Both are expressed mathematically below.

The *quarter-chord line* is drawn from a point one-fourth of the distance from the leading edge of the root-chord to a point one-fourth of the distance from the leading edge of the tip chord. It is important because

## 9.2 THE TRAPEZOIDAL WING PLANFORM

The trapezoidal planform represents the simplest geometric shape selected for aircraft lifting surfaces. Although basic, it is important enough to warrant a specific discussion. One of the primary advantages of this geometry is the simple mathematics that can be used to describe it. Absence of curvature or leading and trailing edge discontinuities results in a simple mathematical representation, in turn, offering convenience when sizing the airplane and extremely helpful when performing trade studies or during optimization.

This class of planform shapes includes a range of geometric shapes ranging from elementary forms, such as the constant-chord planform ("Hershey-bar") to tapered planform shapes that may be swept forward or aft. It is important to know well the geometric relationships between span, aspect ratio, taper ratio, and chord. These will come in handy in a multitude of analyses, ranging from weight estimation to multi-disciplinary optimization.

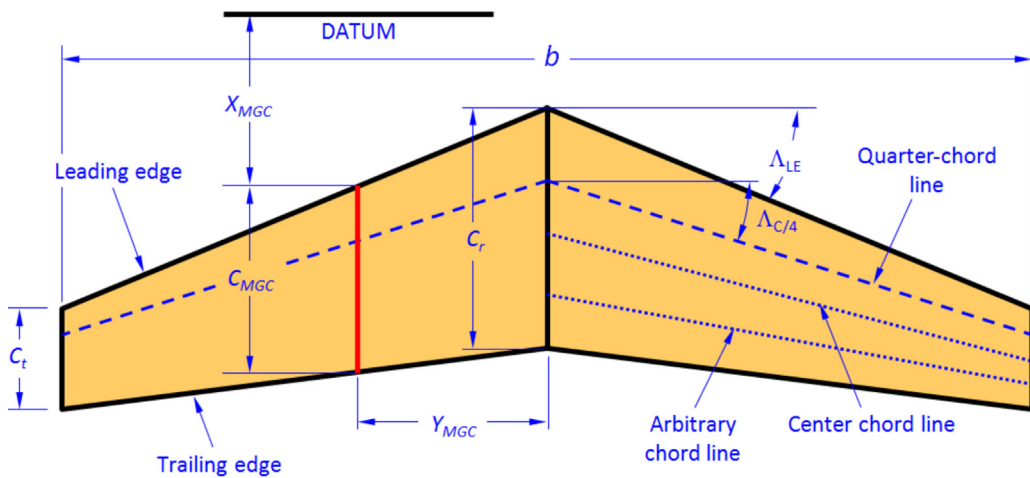


FIGURE 9-2 Fundamental definitions of a trapezoidal wing planform.

two-dimensional aerodynamic data frequently uses the quarter-chord point as a reference when presenting pitching moment data. Scientific literature, for instance the USAF DATCOM, regularly uses the quarter-chord as a reference point for its graphs and computational techniques. Additionally, this is often the location of the main spar in lifting surfaces and it is very convenient to the structural analysts to not have to perform moment transformation during the design of the structure.

The *center chord line* is obtained in a similar fashion to the quarter-chord line and is sometimes used as a reference in scientific literature, although not as frequently. Other important parameters are the sweep angles of the leading edge and quarter-chord line, denoted by  $\Delta_{LE}$  and  $\Delta_{C/4}$ , respectively.

The *mean geometric chord* (MGC) of the planform is often (and erroneously) referred to as the *mean aerodynamic chord* (MAC), which is the chord at the location on the planform at which the center of pressure is presumed to act. The problem is that this location is dependent on three-dimensional influences, such as that of the airfoils, twist, sweep and other factors, not to mention angle-of-attack, in particular when flow separation begins. Authors who refer to the MGC as the MAC typically acknowledge the shortcoming, present the geometric formulation presented here to calculate it, before continuing to call it the MAC. In this text, we will break from this convention and simply call it by its appropriate title – the MGC. The importance of the MGC is that it can be considered a reference location on a wing, to which the location of the center of gravity is referenced and even for a quick preliminary estimation of wing bending moments inside it. Therefore, it is important to also estimate what its spanwise station,  $y_{MGC}$ , is.

Considering Figure 9-2, we will now derive mathematical expressions for the aforementioned important properties of the wing:

Wing area:

$$S = b \left( \frac{C_r + C_t}{2} \right) \quad (9-1)$$

Aspect ratio – general:

$$AR = \frac{b^2}{S} \quad (9-2)$$

Aspect ratio – constant-chord:

$$AR = \frac{b}{C_{avg}} \quad (9-3)$$

Taper ratio:

$$\lambda = \frac{C_t}{C_r} \quad (9-4)$$

Average chord:

$$C_{avg} = \frac{C_r + C_t}{2} = \frac{C_r}{2}(1 + \lambda) \quad (9-5)$$

Mean geometric chord:

$$C_{MGC} = \left( \frac{2}{3} \right) C_r \left( \frac{1 + \lambda + \lambda^2}{1 + \lambda} \right) \quad (9-6)$$

Mean aerodynamic chord:

$$C_{MAC} \approx C_{MGC} \quad (9-7)$$

$Y$ -location of  $MGC_{LE}$ :

$$y_{MGC} = \left( \frac{b}{6} \right) \left( \frac{1 + 2\lambda}{1 + \lambda} \right) \quad (9-8)$$

$X$ -location of  $MGC_{LE}$ :

$$x_{MGC} = y_{MGC} \tan \Delta_{LE} \quad (9-9)$$

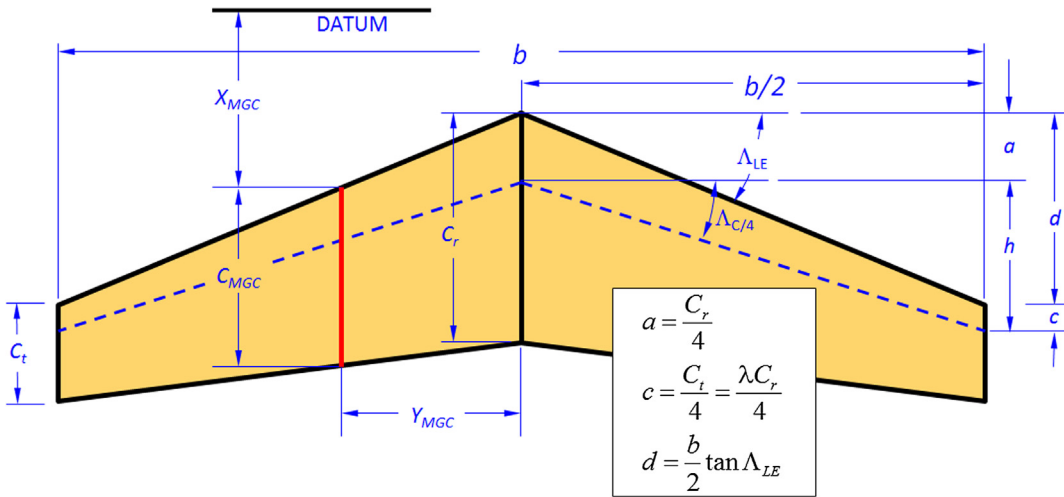


FIGURE 9-3 Deriving the quarter-chord angle.

Angle of quarter-chord line:

$$\tan \Lambda_{C/4} = \tan \Lambda_{LE} + \frac{C_r}{2b}(\lambda - 1) \quad (9-10)$$

Angle of an arbitrary chord line:

$$\tan \Lambda_n = \tan \Lambda_m - \frac{4}{AR} \left[ (n - m) \frac{1 - \lambda}{1 + \lambda} \right] \quad (9-11)$$

Equation (9-11) is obtained from USAF DATCOM [1], where  $m$  and  $n$  are chordwise fractions of the chord line (0.25 for quarter-chord, 0.5 for the center chord line, etc.) and  $m$  is the fraction for a known angle, and  $n$  for the unknown angle (see Example 9-1 for example of use).

### Aspect Ratio for HT and VT

The aspect ratio for a horizontal tail (HT) is calculated exactly as it is for the wing. The aspect ratio for a vertical tail (VT) is calculated using the following expression:

Aspect ratio for a VT:

$$AR_{VT} = \frac{b_{VT}^2}{S_{VT}} \quad (9-12)$$

where

$b_{VT}$  = height of the VT from its base to tip, in ft or m  
 $S_{VT}$  = area of the VT, in  $\text{ft}^2$  or  $\text{m}^2$

The aspect ratio for a twin tail is calculated by applying Equation (9-12) to one tail only, where  $S_{VT}$  refers to one half the total area of the VT.

### Aspect Ratio for Multi-wing Configurations

The aspect ratio for multi-wing aircraft, such as biplanes and triplanes, is given below:

Aspect ratio for a biplane:

$$AR_{biplane} = \frac{2b_{\text{larger wing}}^2}{S} \quad (9-13)$$

Aspect ratio for a triplane:

$$AR_{triplane} = \frac{3b_{\text{largest wing}}^2}{S} \quad (9-14)$$

### Derivation of Equations (9-6), (9-8), and (9-10)

**Equation (9-6):** see Section D.5.3, *Derivation of MGC*.

**Equation (9-8):** see Section D.5.2, *Spanwise location of the MGC*.

**Equation (9-10):** refer to the Figure 9-3 to define the dimensions  $a$ ,  $b/2$ ,  $c$ ,  $d$ , and  $h$ .

$$\left. \begin{aligned} a &= \frac{C_r}{4} \\ d &= \frac{b}{2} \tan \Lambda_{LE} \\ c &= \frac{C_t}{4} = \frac{\lambda C_r}{4} \end{aligned} \right\} \Rightarrow h = d + c - a = \frac{b}{2} \tan \Lambda_{LE} + \frac{\lambda C_r}{4} - \frac{C_r}{4}$$

$$\begin{aligned} h &= \frac{1}{2} \left[ b \tan \Lambda_{LE} + \frac{\lambda C_r}{2} - \frac{C_r}{2} \right] = \frac{1}{2} \left[ b \tan \Lambda_{LE} + \frac{C_r}{2} (\lambda - 1) \right] \\ \tan \Lambda_{C/4} &= \frac{h}{b/2} = \frac{\left[ b \tan \Lambda_{LE} + \frac{C_r}{2} (\lambda - 1) \right]}{b} \\ &= \tan \Lambda_{LE} + \frac{C_r}{2b} (\lambda - 1) \end{aligned}$$

QED

### EXAMPLE 9-1: TRAPEZOIDAL WING PLANFORM

Determine the primary characteristics of the wing shown in Figure 9-4. Also calculate the angle of the center chord line using Equation (9-11).

#### Solution

Wing area:

$$S = b \left( \frac{C_r + C_t}{2} \right) = (10) \left( \frac{2+1}{2} \right) = 15 \text{ ft}^2$$

Aspect ratio – general:

$$AR = \frac{b^2}{S} = \frac{10^2}{15} = 6\frac{2}{3} \approx 6.667$$

Taper ratio:

$$\lambda = C_t/C_r = 0.5$$

Mean geometric chord:

$$C_{MGC} = \left( \frac{2}{3} \right) C_r \left( \frac{1+\lambda+\lambda^2}{1+\lambda} \right) = \left( \frac{2}{3} \right) (2) \left( \frac{1+0.5+0.5^2}{1+0.5} \right) \\ = 1\frac{5}{9} \text{ ft} \approx 1.556 \text{ ft}$$

Mean aerodynamic chord:

$$C_{MAC} \approx C_{MGC}$$

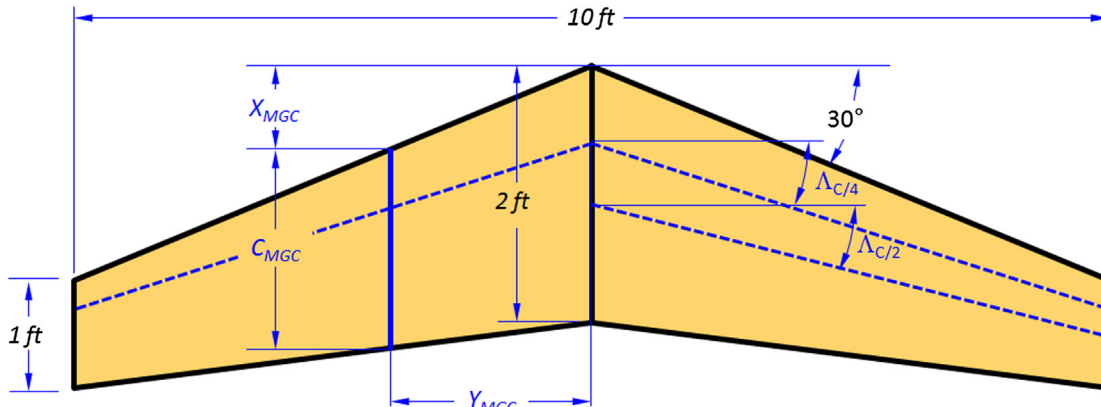


FIGURE 9-4 The wing geometry.

Y-location of  $MGC_{LE}$ :

$$y_{MGC} = \left( \frac{b}{6} \right) \left( \frac{1+2\lambda}{1+\lambda} \right) = \left( \frac{10}{6} \right) \left( \frac{1+2 \times 0.5}{1+0.5} \right) \\ = 2\frac{2}{3} \text{ ft} \approx 2.222 \text{ ft}$$

X-location of  $MGC_{LE}$ :

$$x_{MGC} = y_{MGC} \tan \Lambda_{LE} = (2\frac{2}{3}) \tan(30^\circ) \approx 1.283 \text{ ft}$$

Angle of quarter-chord line:

$$\tan \Lambda_{C/4} = \tan \Lambda_{LE} + \frac{C_r}{2b} (\lambda - 1) = \tan(30) \\ + \frac{2}{2(10)} (0.5 - 1) \approx 0.5274 \Rightarrow \Lambda_{C/4} \approx 27.8^\circ$$

Angle of the center chord line using the quarter-chord line ( $m = 0.25$ ,  $n = 0.50$ ) is obtained from Equation (9-11):

$$\tan \Lambda_n = \tan \Lambda_m - \frac{4}{AR} \left[ (n-m) \frac{1-\lambda}{1+\lambda} \right]$$

Inserting the given values, we get:

$$\tan \Lambda_{0.50C} = \tan \Lambda_{0.25C} - \frac{4}{6.667} \left[ (0.50 - 0.25) \frac{1-0.5}{1+0.5} \right] \\ = 0.4772 \Rightarrow \Lambda_{0.50C} = 25.5^\circ$$

#### 9.2.2 Poor Man's Determination of the MGC

In the absence of computational tools the designer can determine the location of the MGC using the graphical scheme in Figure 9-5. It is important to remember

that such graphical tools are the relics of a bygone era and at best are what the slide-rule is to the modern calculator — results from a digital calculator should always take precedence.

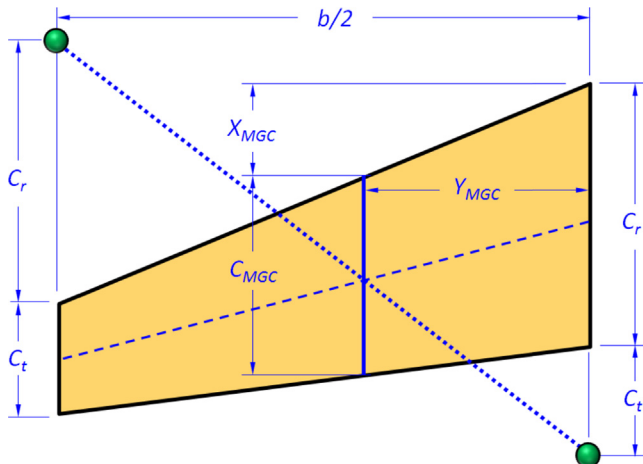


FIGURE 9-5 Graphical scheme to determine the MGC for a simple trapezoidal planform.

### 9.2.3 Planform Dimensions in Terms of $S$ , $\lambda$ , and $AR$

During the design phase, the basic dimensions of the wing (span and chord at root and tip) are sometimes defined by wing area, taper ratio, and aspect ratio as governing variables. This is convenient because these parameters can tell the designer a lot about the likely aerodynamic properties of the wing. With the wing parameters defined in this fashion use the following formulation to determine the required wingspan, root chord, and tip chord of a simple tapered planform like the one in Figure 9-6. These are based on Equations (9-2), (9-3), and (9-10):

From

$$AR = \frac{b^2}{S} \Rightarrow b = \sqrt{AR \cdot S} \quad (9-15)$$

From

$$AR = \frac{b}{C_{avg}} \Rightarrow C_{avg} = \left( \frac{C_r + C_t}{2} \right) = \frac{b}{AR} \quad (9-16)$$

Average chord:

$$C_{avg} = \frac{C_r + C_t}{2} = \frac{C_r}{2}(1 + \lambda) = \frac{S}{b} \quad (9-17)$$

From

$$2C_{avg} = \frac{2b}{AR} = C_r(1 + \lambda) \Rightarrow C_r = \frac{2b}{(1 + \lambda)AR} \quad (9-18)$$

From

$$2C_{avg} = \frac{2S}{b} = C_r(1 + \lambda) \Rightarrow C_r = \frac{2S}{(1 + \lambda)b} \quad (9-19)$$

Mean geometric chord:

$$C_{MGC} = \left( \frac{4b}{3AR} \right) \left( \frac{1 + \lambda + \lambda^2}{1 + 2\lambda + \lambda^2} \right) \quad (9-20)$$

Chord for a straight tapered wing:

$$c(y) = C_r \left( 1 + \frac{2(\lambda - 1)}{b} y \right) \quad (9-21)$$

#### Derivation of Equation (9-20)

Using Equation (9-18), we can calculate the root chord,  $C_r$ , using any set of values for the wingspan,  $b$ , and aspect ratio,  $AR$ :

$$C_r = \frac{2b}{(1 + \lambda)AR}$$

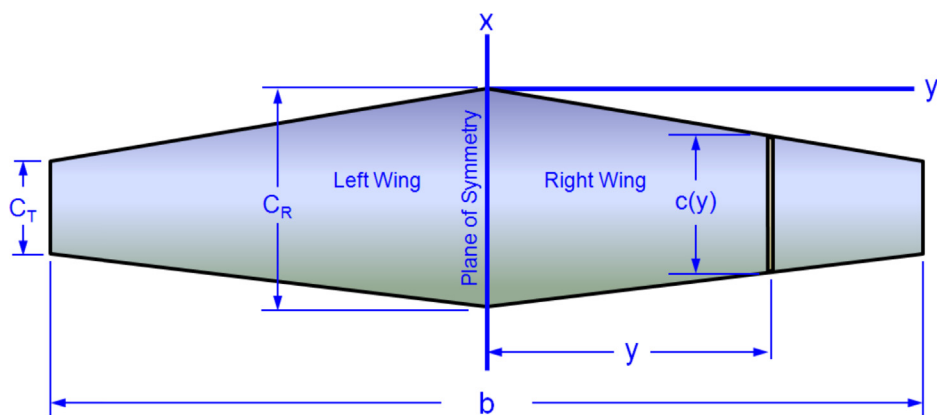


FIGURE 9-6 A simple tapered planform.

We then insert this into Equation (9-6) and manipulate as follows:

$$\begin{aligned} C_{MGC} &= \left(\frac{2}{3}\right)C_r\left(\frac{1+\lambda+\lambda^2}{1+\lambda}\right) \\ &= \left(\frac{2}{3}\right)\left(\frac{2b}{(1+\lambda)AR}\right)\left(\frac{1+\lambda+\lambda^2}{1+\lambda}\right) \\ &= \left(\frac{4b}{3AR}\right)\left(\frac{1+\lambda+\lambda^2}{1+2\lambda+\lambda^2}\right) \end{aligned}$$

QED

### Derivation of Equation (9-21)

Parametric formulation of the chord  $c$  as a function of spanwise station  $y$  for a straight tapered wing whose taper ratio is  $\lambda$ , root chord  $C_r$  and span is  $b$  is obtained by inserting the geometric parameters as follows (where the parameter  $t$  is  $2y/b$  and ranges from 0 to 1):

$$\begin{aligned} c(y) &= C_r(1-t) + \lambda C_r t = C_r\left(1 - \frac{2y}{b}\right) + \lambda C_r \frac{2y}{b} \\ &= C_r\left[1 - \frac{2y}{b} + \lambda \frac{2y}{b}\right] = C_r\left(1 + \frac{2(\lambda-1)}{b}y\right) \end{aligned}$$

QED

### EXAMPLE 9-2: TRAPEZOIDAL WING PLANFORM

A wing is to be designed such that  $S = 140 \text{ ft}^2$ ,  $\lambda = 0.5$ , and  $AR = 10$ . Determine the wingspan, root chord, and tip chord required for the wing. Also determine the chord at  $y = 10 \text{ ft}$ .

#### Solution

Wingspan:

$$AR = \frac{b^2}{S} \Rightarrow b = \sqrt{AR \cdot S} = \sqrt{(10) \cdot (140)} = 37.42 \text{ ft}$$

Wing root chord:

$$C_r = \frac{2S}{b(1+\lambda)} = \frac{2(140)}{(37.42)(1+0.5)} = 4.99 \text{ ft}$$

Wing tip chord:

$$C_t = \lambda C_r = 0.5(4.99) = 2.49 \text{ ft}$$

Chord at  $y = 10 \text{ ft}$ :

$$\begin{aligned} c(10) &= C_r\left(1 + \frac{2(\lambda-1)}{b}y\right) \\ &= (4.99)\left(1 + \frac{2(0.5-1)}{37.42}(10)\right) = 3.66 \text{ ft} \end{aligned}$$

#### 9.2.4 Approximation of an Airfoil Cross-sectional Area

Often, the cross-sectional area (internal area) of an airfoil must be evaluated as it yields useful clues about the internal volume of a wing available for fuel storage. In the absence of precise airfoil data the following approximation is used to estimate the internal area of geometry resembling that of an airfoil:

Total area:

$$A_{airfoil} = \frac{(k+3)C \cdot t}{6} \quad (9-22)$$

where

$C$  = airfoil chord, in ft or m

$k$  = location of the airfoil's maximum thickness as a fraction of  $C$

$t$  = airfoil thickness, in ft or m

Sometimes it is more convenient to present the thickness using the thickness-to-chord ratio, denoted by  $(t/c)$ .

This way, the thickness is expressed using the product  $(t/c) \cdot C$ . Thus, Equation (9-22) is written as follows:

Total area:

$$A_{airfoil} = \frac{(k+3)}{6} \left(\frac{t}{c}\right) C^2 \quad (9-23)$$

### Derivation of Equations (9-22) and (9-23)

Consider Figure 9-7, which shows an airfoil of chord  $C$  approximated by a parabolic D-cell and a triangular section. It is assumed the two sections join at the chord station of maximum thickness,  $t$ , whose location is given by  $k \cdot C$ , where  $k$  is the location of the airfoil's maximum thickness as a fraction of  $C$ . The cross-sectional areas of the two sections and the total area are given by the following expressions:

Parabolic section:

$$A_1 = \frac{2}{3}k \cdot C \cdot t \quad (\text{i})$$

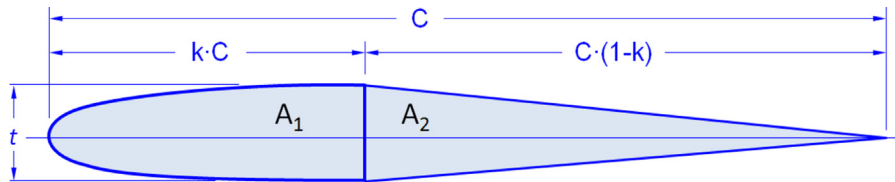


FIGURE 9-7 An approximation of an airfoil using elementary geometry.

Triangular section:

$$A_2 = \frac{1}{2}C \cdot (1 - k)t \quad (\text{ii})$$

Therefore, the internal area of the airfoil can be approximated by adding the two as shown below:

$$A_{\text{airfoil}} = A_1 + A_2 = \frac{2k \cdot C \cdot t}{3} + \frac{C \cdot (1 - k)t}{2} = \frac{(k + 3)C \cdot t}{6}$$

Then, multiply by  $C/C (=1)$  to get Equation (9-23).

QED

lift-induced drag ( $C_{Dl}$ ) and the slope of the lift curve ( $C_{L\alpha}$ ). As such, it also directly influences both performance and stability and control. Table 9-3 shows typical values of the AR for several classes of aircraft.

Figure 9-8 shows two planform shapes of equal planform area, but different AR. The stubby configuration ( $AR = 4$ ) has a shallower  $C_{L\alpha}$  and lower  $C_{L\max}$ , but higher stall  $AOA$  ( $\alpha_{\text{stall}}$ ) than the slender one ( $AR = 16$ ). The stubby planform has less roll damping than the high AR and, for that reason, is better suited for airplanes that require roll responsiveness, such as aerobatic aircraft. Additionally, it generates higher lift-induced drag ( $C_{Dl}$ ) than the slender one. A high

## 9.3 THE GEOMETRIC LAYOUT OF THE WING

Once the wing area and wingspan have been determined, it is possible to begin to establish the remaining geometric properties. The geometric layout of the wing refers to properties such as the aspect ratio, taper ratio, wing sweep, dihedral, and so on. These constitute the geometric layout of the wing. The layout has profound influence on the entire design process, affecting a large number of other areas in the development. These are not just aerodynamics, performance, and stability and control, but also structures and systems layout, just to name a few. The layout process assesses the topics listed below. The corresponding sections are listed as well.

The layout constitutes the geometric parameters presented in Table 9-2.

Of these, the AR, TR, and the LE sweep give the designer fundamental control over the aerodynamic characteristics of the wing. This is not to say the others are not important too, but rather that they can be considered more as dials to “fine-tune” the wing design. The determination of the AR, TR, and sweep may be the consequence of a complicated optimization; however, this is not always the case.

### 9.3.1 Wing Aspect Ratio, AR

The wing aspect ratio (AR) is a fundamental property that simultaneously affects the magnitude of the

TABLE 9-2 Typical Values of AR for Various Classes of Aircraft

Geometric property	Section
Planform shape	9.4
Aspect ratio (AR)	9.3.1
Taper ratio (TR or $\lambda$ )	9.3.2
Leading edge (LE) or quarter chord (C/4) sweep angle	9.3.3
Dihedral angle	9.3.4
Washout	9.3.5
Angle-of-incidence	9.3.6
Positioning of the wing on the fuselage	4.2.1
Partitioning of the wing into a roll control region (ailers), high lift region (flaps, slats), and lift suppression region (spoilers)	10

TABLE 9-3 Typical Values of AR for Various Classes of Aircraft

Type of Vehicle or Vehicle Component	AR Range
Missiles	0.5–1
Military fighters	2.5–4.0
GA aircraft	6–11
Aerobatic airplanes	5–6
Twin-engine commuters	10–14
Commercial jetliners	7–10
Sailplanes	10–51

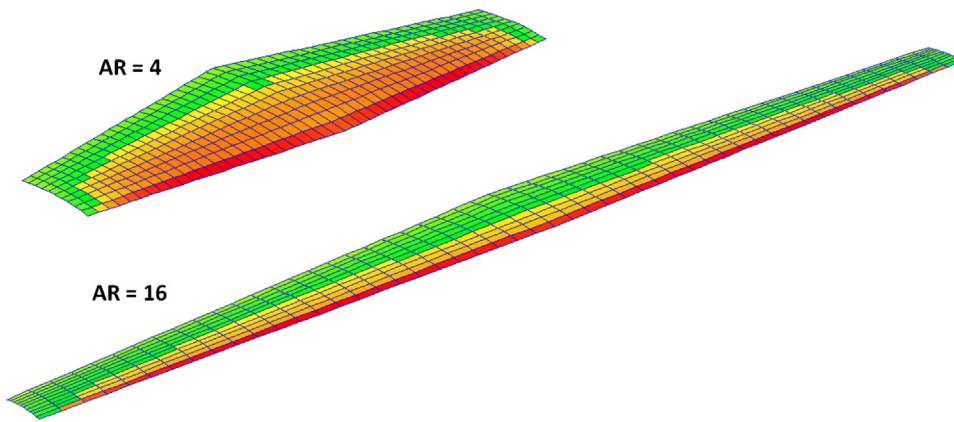


FIGURE 9-8 Two planform shapes of equal areas, but different aspect ratios.

AR wing is required for sailplanes and airplanes that are required to have long-range or endurance. They have high roll damping and will be structurally heavier because of larger bending moments.

Table 9-4 gives a general rule-of-thumb about the impact the AR has on selected aerodynamic properties.

The aspect ratio is defined as follows for monoplane and biplane configurations:

Monoplane:

$$AR = b^2/S \quad (9-24)$$

Biplane:

$$AR = 2b^2/S \quad (9-25)$$

where

$b$  = wingspan

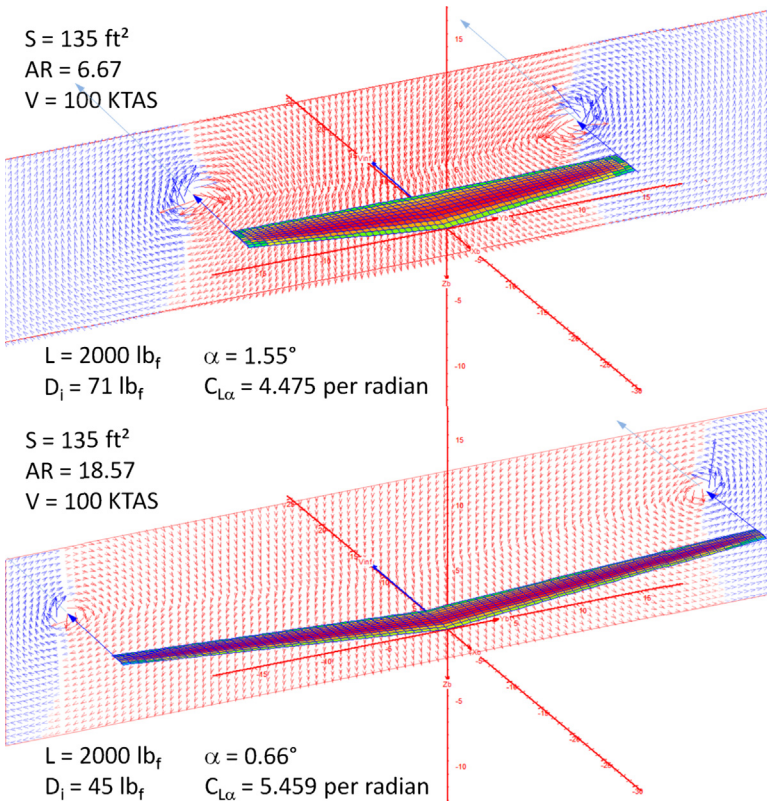
$S$  = wing area

### Illustrating the Difference Between Low and High AR Wings

The difference between a low and high AR is illustrated in Figure 9-9, which shows two wings of equal wing areas and taper ratios. The upper wing has a relatively low AR (6.67) while the lower one has a relatively large one (18.57). The airspeed in both cases is 100 KTAS and both are positioned at an AOA such they generate 2000 lb<sub>f</sub> of lift. The figure shows that the low AR wing requires an AOA of 1.55° but the high AR one 0.66°. In accordance with Section 15.3.4, *The lift-induced drag coefficient*:  $C_{Dl}$ , the higher AOA means the low AR wing generates higher induced drag. The greater flow field disruption is even visible by the larger wingtip vortex generated by the low AR wing in Figure 9-9. Here, a lift-induced drag value of 71 lb<sub>f</sub> was estimated for the low AR wing and 45 lb<sub>f</sub> for the high AR one. Additionally, the lift curve slope,  $C_{L\alpha}$ , for the low AR wing

TABLE 9-4 Typical Impact of Aspect Ratio on Aerodynamic Properties of the Wing

Aspect Ratio, AR	Pros	Cons
1.0	High stall angle-of-attack. High flutter speed. Low roll damping. Low structural weight. Great gust penetration capability (because of the shallow $C_{L\alpha}$ ).	Inefficient because of high induced drag. Shallow $C_{L\alpha}$ requires large changes in AOA with airspeed. Low $C_{L\max}$ (high stalling speed). Low $LD_{\max}$ .
5–7	Good roll response. Relatively high flutter speed. Limited adverse yaw. Reasonable gust penetration.	Inefficient to marginally efficient for long-range design. Relatively high induced drag.
7–12	Good balance between low induced drag and roll response. Good glide characteristics for powered aircraft.	Some adverse yaw may be noticed toward the higher extreme of AR. Resonable to marginal gust penetration capability (steep $C_{L\alpha}$ ).
20+	Low induced drag. Great glide characteristics. Steep $C_{L\alpha}$ (large change in lift with small changes in $\alpha$ ). High maximum lift coefficient.	High structural weight. Low flutter speed. High roll damping. High adverse yaw. Steep $C_{L\alpha}$ results in higher gust loads.



(4.475 per radian) is less than that of the high  $AR$  wing (5.459 per radian). Therefore, the low  $AR$  wing will stall at a higher  $AOA$  and airspeed than the high  $AR$  wing. However, it is far more responsive as its roll damping coefficient,  $C_{lp}$ , is lower.

The difference between the two configurations is further illustrated in Figure 9-10. The graphs were

**FIGURE 9-9** The difference between a low  $AR$  (top) and high  $AR$  (bottom) is illustrated. Both wings are of equal area and each generates 2000  $\text{lb}_f$  of lift at 100 KTAS. The flow solution is shown in a plane positioned aft of the wing trailing edge.

generated for three wings using the potential flow theory. The wings all have a constant  $TR$  (0.5), but varying  $AR$ . The left graph shows the spanwise distribution of section lift coefficients at an  $AOA$  of  $10^\circ$ . The tip loading that results from the  $TR$  (and will be discussed next) is evident. It can be seen that the high  $AR$  of 16 generates the highest  $C_l$  at the give  $AOA$ , as is to be expected since its  $C_{l\alpha}$  is the

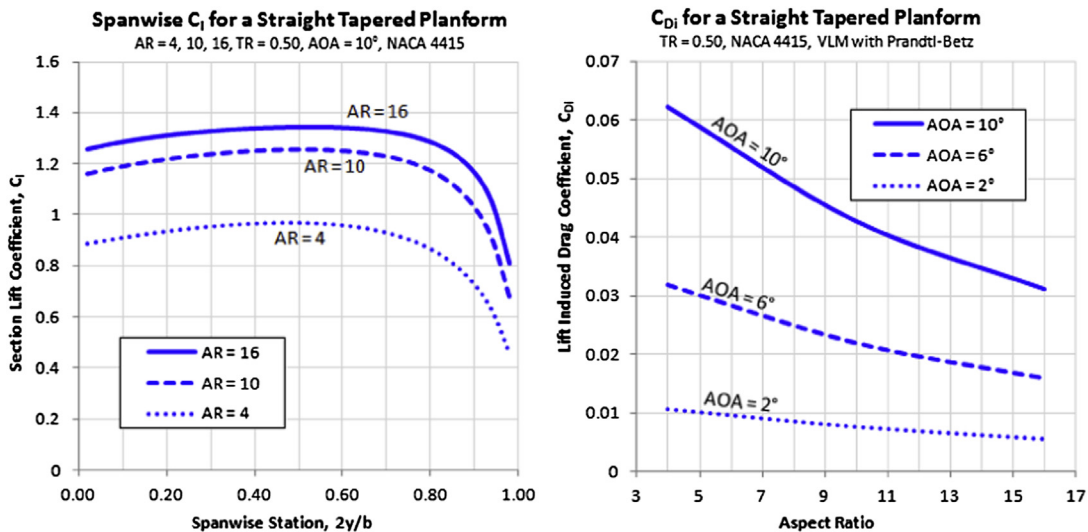


**FIGURE 9-10** The left graph shows the spanwise distribution of section lift coefficients for three different  $AR$ s, while the right graph shows the effect of  $AR$  on the lift induced drag coefficient.

highest. Other than the magnitude of the section lift coefficients, it is also evident that the *AR* does not have major changes on the general shape of the distribution; in other words, the *AR* has great effects on the magnitude of section lift coefficients at a given *AOA*, and relatively small influence on the shape of the distribution.

The left graph in Figure 9-10 shows how the *AR* affects the lift induced drag. This is illustrated for three *AOAs*; 2°, 6°, and 10°. The graph shows substantial reduction in lift-induced drag is to be had with larger *AR*.

### Determining AR Based on a Desired Range

It is possible to evaluate and recommend *AR* for some special design cases. One such is the determination of *AR* based on a desired range, *R*, at some desired cruising airspeed, *V<sub>C</sub>*. If the aircraft being designed belongs to a class of aircraft for which *C<sub>Dmin</sub>* can be estimated with reasonable accuracy and the expected initial and final cruise weights are known, denoted by *W<sub>ini</sub>* and *W<sub>fin</sub>*, respectively, then the average cruise lift coefficient can be used with Equation (20-12) to extract the effective aspect ratio, *AR<sub>e</sub>*, for the vehicle using the following expression:

$$AR_e = \frac{C_{LC}^2}{\pi} \frac{1}{\left( \frac{V_C C_{LC}}{R c_t} \ln \left( \frac{W_{ini}}{W_{fin}} \right) - C_{Dmin} \right)} \quad (9-26)$$

where

*C<sub>LC</sub>* = average cruise lift coefficient, corresponding to the average of *W<sub>ini</sub>* and *W<sub>fin</sub>*.

*R* = range in ft

*V<sub>C</sub>* = average cruising speed in ft/s

*c<sub>t</sub>* = thrust specific fuel consumption in 1/s

The denominator in Equation (9-26) results in a singularity when  $C_{Dmin} = \frac{V_C C_{LC}}{R c_t} \ln \left( \frac{W_{ini}}{W_{fin}} \right)$ . In fact, it returns negative values if the airspeed is lower than obtained by the following expression:

$$V_C > \frac{R \cdot c_t \cdot C_{Dmin}}{C_{LC} \ln \left( \frac{W_{ini}}{W_{fin}} \right)} \quad (9-27)$$

For this reason, Equation (9-26) should only be applied to airspeeds that are greater than the value obtained by the above expression. It should be used to guide the selection of the *AR* rather than obtain it directly, for instance by plotting isobars.

Note that *AR<sub>e</sub>* is the product of the *AR* and Oswald's span efficiency, *AR·e*. Once this product has been determined, it is the responsibility of the designer to devise a proper combination of *AR* and planform geometry to achieve this value. Also note that if the airplane features a swept back planform that the *AR* limits of Equation (9-94) must be considered as well.

Although the low *AR* surface is less efficient than the high *AR*, it is much better suited as a control surface for tail-aft configurations (i.e. as a horizontal and vertical tail). This results from the higher stall *AOA*, which is a consequence of the low *AR*. Delayed stall introduces a certain level of safety to the operation of tail-aft airplanes because it will require them to reach very high *AOA* or *AOY* before the stabilizing moments begin to drop. This is the reason why the horizontal and vertical tail surfaces on airplanes typically feature low aspect ratios.

### Derivation of Equation (9-26)

Assuming the simplified drag model, Equation (20-12) can be solved for the drag coefficient as follows:

$$\begin{aligned} R = \frac{V}{c_t} \frac{C_L}{C_D} \ln \left( \frac{W_{ini}}{W_{fin}} \right) &\Leftrightarrow C_D = C_{Dmin} + \frac{C_L^2}{\pi \cdot AR_e} \\ &= \frac{V}{R} \frac{C_L}{c_t} \ln \left( \frac{W_{ini}}{W_{fin}} \right) \end{aligned}$$

This can then be solved for the effective *AR* as follows:

$$AR_e = \frac{C_L^2}{\pi} \frac{1}{\left( \frac{V}{R} \frac{C_L}{c_t} \ln \left( \frac{W_{ini}}{W_{fin}} \right) - C_{Dmin} \right)}$$

Note that this is a generic case and the subscript *C* is used to denote some desired cruise conditions.

QED

### EXAMPLE 9-3

The Cirrus SR22 pilot operating handbook (POH) reveals that the airplane has an 899 nm range at 65% power at 10,000 ft. The POH states the cruising speed at this condition is 174 KTAS and fuel consumption is

15.4 gal/hr. This implies an  $SFC = 15.4 \text{ gal/hr} \times (6 \text{ lb}_f/\text{gal}) / (0.65 \times 310 \text{ BHP}) = 0.4586 \text{ lb}_f/\text{hr/BHP}$ . Evaluate the reliability of Equation (9-26) by considering the hypothetical design of a SR22 class aircraft, which "happens" to share a

### EXAMPLE 9-3 (cont'd)

number of parameters. This hypothetical airplane is designed for a range of 900 nm precisely at the same condition. Estimate the effective  $AR$  for this airplane using Equation (9-26) and compare to that of the SR22. Assume the weight at the beginning of cruise is 3379 lb<sub>f</sub> and 2910 lb<sub>f</sub> at end of cruise. Assume the wing area is 145 ft<sup>2</sup> and  $C_{D\min} = 0.02541$  (as calculated per Example 15-18).

#### Solution

Average weight during cruise:

$$W_{avg} = \frac{W_{ini} + W_{fin}}{2} = \frac{3379 + 2910}{2} = 3145 \text{ lb}_f$$

Density at 10,000 ft:

$$\begin{aligned}\rho &= 0.002378(1 - 0.0000068756 \times 10,000)^{4.2561} \\ &= 0.001756 \text{ slugs/ft}^3\end{aligned}$$

The airspeed in ft/s is  $174 \times 1.688 = 293.7$  ft/s, so the lift coefficient at cruise is:

$$C_{LC} = \frac{2W_{avg}}{\rho V_C^2 S} = \frac{2 \times 3145}{(0.001756)(293.7)^2(145)} = 0.2864$$

The thrust specific fuel consumption is found using Equation (20-9):

$$c_t = \frac{c_{bhp} V}{1,980,000 \eta_p} = \frac{0.4586 \times 293.7}{1,980,000(0.85)} = 8.0 \times 10^{-5} \text{ 1/s}$$

The desired range of 900 nm amounts to 5,468,400 ft, yielding the following effective AR:

$$\begin{aligned}AR_e &= AR \cdot e = \frac{C_{LC}^2}{\pi} \frac{1}{\left(\frac{V_C C_{LC}}{R c_t} \ln\left(\frac{W_{ini}}{W_{fin}}\right) - C_{D\min}\right)} \\ &= \frac{(0.2864)^2}{\pi} \frac{1}{\left(\frac{(293.7)}{5,468,400} \frac{(0.2864)}{8.0 \times 10^{-5}} \ln\left(\frac{3379}{2910}\right) - 0.2541\right)} \\ &= 7.86\end{aligned}$$

Note that the actual AR of the SR22 is 10. The answer therefore implies its Oswald efficiency is 0.786. This compares favorably to Equation (9-89) as follows:

$$e = 1.78(1 - 0.045 \times 10^{0.68}) - 0.64 = 0.7566$$

#### Determining AR Based on Desired Endurance

The  $AR$  can also be determined based on a desired endurance,  $E$ , at some desired cruising airspeed,  $V_C$ , similar to what was done for range and using the same basic variables. This time the method uses Equation (20-22) to extract the effective aspect ratio,  $AR_e$ , for the vehicle using the following expression:

$$AR_e = \frac{C_{LC}^2}{\pi} \frac{1}{\left(\frac{1}{E} \frac{C_{LC}}{c_t} \ln\left(\frac{W_{ini}}{W_{fin}}\right) - C_{D\min}\right)} \quad (9-28)$$

where  $E$  = endurance in seconds.

Like Equation (9-26), the denominator in Equation (9-28) has similar limitations and should be used with cruise lift coefficients greater than those obtained with the following expression:

$$C_{LC} > \frac{E \cdot c_t \cdot C_{D\min}}{\ln(W_{ini}/W_{fin})} \quad (9-29)$$

#### Derivation of Equation (9-28)

Assuming the simplified drag model, Equation (20-22) can be solved for the drag coefficient as follows:

$$\begin{aligned}E &= \frac{1}{c_t C_D} \ln\left(\frac{W_{ini}}{W_{fin}}\right) \Leftrightarrow C_D = C_{D\min} + \frac{C_L^2}{\pi \cdot AR_e} \\ &= \frac{1}{E c_t} \ln\left(\frac{W_{ini}}{W_{fin}}\right)\end{aligned}$$

This can then be solved for the effective  $AR$  as follows:

$$AR_e = \frac{C_L^2}{\pi} \frac{1}{\left(\frac{1}{E} \frac{C_L}{c_t} \ln\left(\frac{W_{ini}}{W_{fin}}\right) - C_{D\min}\right)}$$

Note that this is a generic case and the subscript C is used to denote some desired cruise conditions.

QED

### EXAMPLE 9-4

Use Equation (9-28) to estimate the effective AR for the SR22 class aircraft of Example 9-3, using the same parameters, if it is designed to cruise 900 nm at 174 KTAS.

#### Solution

Using Equation (9-28), the desired range of 900 nm at 174 KTAS amounts to 5.172 hrs, yielding the following effective AR:

$$AR_e = \frac{(0.2864)^2}{\pi} \frac{1}{\left( \frac{1}{(5.172 \times 3600)} \frac{(0.2864)}{8.0 \times 10^{-5}} \ln\left(\frac{3379}{2910}\right) - 0.2541 \right)} \\ = 7.87$$

effectively the same result as in the previous example.

Figure 9-11 shows the effect aspect ratio has on a wing's lift curve and drag polar. It compares the properties of some airfoil (for which  $AR_1$  is considered  $\infty$ ) to the same airfoil being used in a three-dimensional wing (whose  $AR_2$  is much, much smaller). It can be seen that as the AR reduces, so does the lift curve slope (denoted by  $C_{l\alpha}$  for the airfoil and  $C_{L\alpha}$  for the wing) and maximum lift coefficient (denoted by  $C_{l\max}$  for the airfoil and  $C_{L\max}$  for the wing). If the airfoil generates a specific lift coefficient at  $\alpha_1$ , it must be placed at a higher AOA,  $\alpha_2$ , once used on a three-dimensional wing. The cost of this is an increase in drag, which changes from  $C_d$  for the airfoil to  $C_D$  for the wing, as is shown in Figure 9-11. The difference between the two is the three-dimensional lift induced drag coefficient and the rise in the airfoil drag due to growth in the flow separation region.

#### Estimating AR Based on Minimum Drag

The AR can also be set based on the minimum drag of the airplane. This approach requires the design lift

coefficient to be determined (e.g. see Equation [9-49]). Then, assuming constant wing area, a relatively sophisticated estimation of the total drag coefficient of the airplane is accomplished. The estimation takes into account changes in the wing geometry as a function of AR (wing chords change since  $S$  is constant) and evaluates skin friction assuming either a fully turbulent or a mixed boundary layer. Then, using the appropriate form and interference factors, the minimum drag coefficient is estimated (see Chapter 15, *Aircraft drag analysis*). The lift-induced drag coefficient is also calculated, using an appropriate model of the Oswald's span efficiency. Adding the two coefficients comprises the total drag coefficient,  $C_D$ . This can then be plotted versus the AR, in a carpet plot, similar to that of Figure 9-12. The carpet plot is usually prepared using a range of lift coefficients. Such a plot reveals the location of the optimum AR. The upper and lower bounds in the figure are simply the optimum  $AR \pm 2$ , but the designer can widen or narrow this range depending on the project. Figure 9-12

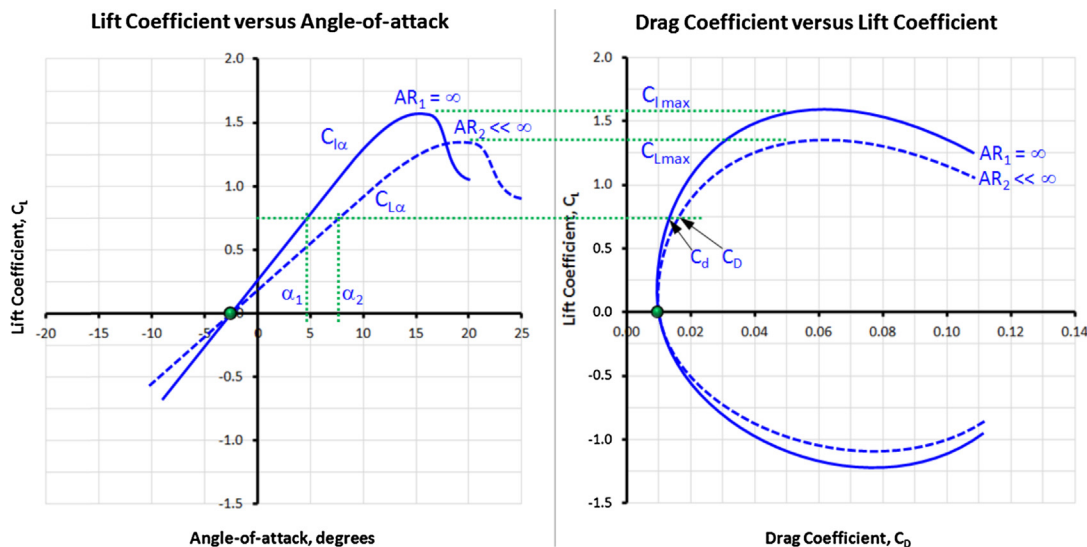


FIGURE 9-11 The effect of aspect ratio on a 3D lift curve and drag polar.

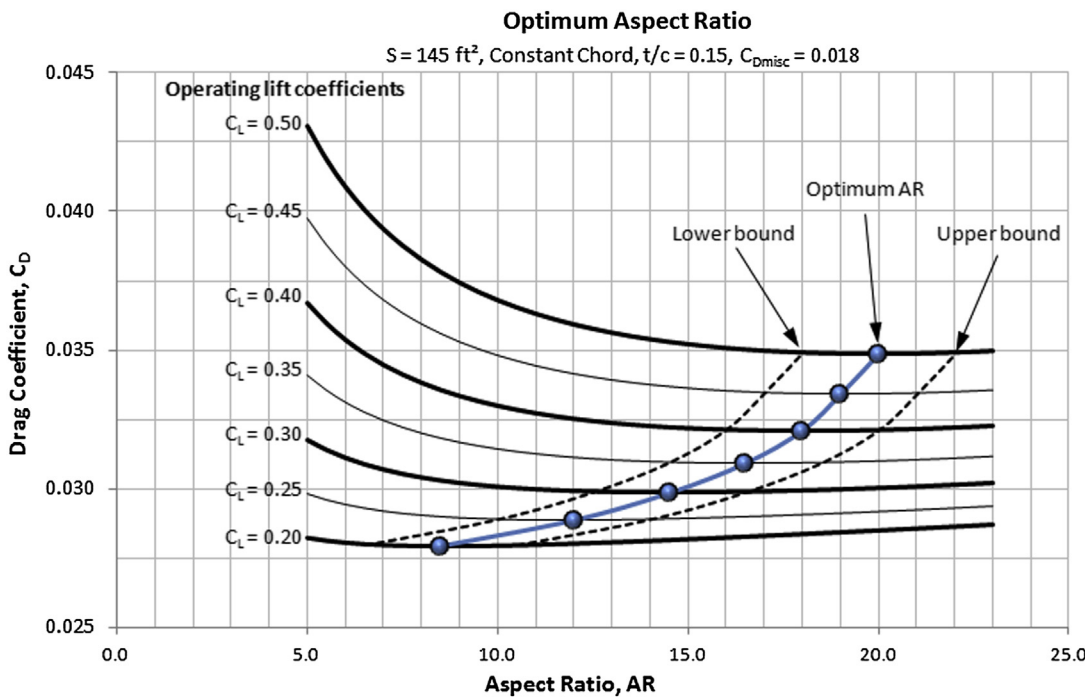


FIGURE 9-12 The effect of aspect ratio on the drag coefficient of a hypothetical aircraft.

shows that for the hypothetical aircraft being presented, practically any *AR* between the two limits will yield the lowest value of the total drag coefficient. This gives the designer room to accommodate other concerns such as structural weight.

#### **Estimating AR for Sailplane Class Aircraft**

A plausible *AR* for powered and unpowered sailplanes can be established using the historical data in Figure 9-13. The data points represent contemporary manufacturers' information collected from Ref. [2]. The maximum lift-to-drag ratios ( $LD_{\max}$ ) presented includes the drag of the fuselage and stabilizing surfaces and demonstrates the sophistication of the modern sailplane. The graph shows trends for both regular and powered sailplanes and presents accompanying least-squares curves. Note that these estimates do not replace analyses of the kind presented by Ref. [3], but rather supply initial estimates based on historical sailplanes.

Also plotted are theoretical predictions of the  $LD_{\max}$  using the *simplified drag model* (see Chapter 15, *Aircraft drag analysis*) and  $C_{D\min}$  of 0.01 (typical of many sailplanes). This model is often the first choice of the novice airplane designer, but it is inaccurate for sailplanes designed for extensive NLF as it does not model the drag bucket associated with such aircraft. These curves are merely presented here to demonstrate why the simplified drag model is a poor predictor.

The theoretical  $LD_{\max}$  was calculated using Equation (19-18), where the Oswald's span efficiency was

calculated per Equations (9-91) and (9-89) and. The curves shown assume a minimum drag coefficient of 0.01, which is a typical value for clean sailplanes. The graph shows clearly the limitation of the simplified drag model.

The following empirical formulation can be used to estimate the *AR* for the conceptual design of unpowered and powered sailplanes (as long as  $AR < 36$ ):

Sailplanes:

$$AR \approx 44.482 - \sqrt{1672.2 - 28.41LD_{\max}} \quad (9-30)$$

Powered sailplanes:

$$AR \approx \frac{LD_{\max} + 0.443}{1.7405} \quad (9-31)$$

Naturally, the calculated *AR* will not guarantee that a desired  $LD_{\max}$  will be achieved. Rather it indicates that, historically, sailplanes with that *AR* have achieved the said  $LD_{\max}$ . Achieving it will require the utmost attention to anything on the airplane that generates drag.

#### **9.3.2 Wing Taper Ratio, TR or $\lambda$**

The *taper ratio* is the second of the three most important geometric properties of a wing. It has a profound impact on how lift is distributed along the wingspan. For instance, consider Figure 9-14, which shows how it changes the spanwise distribution of section lift

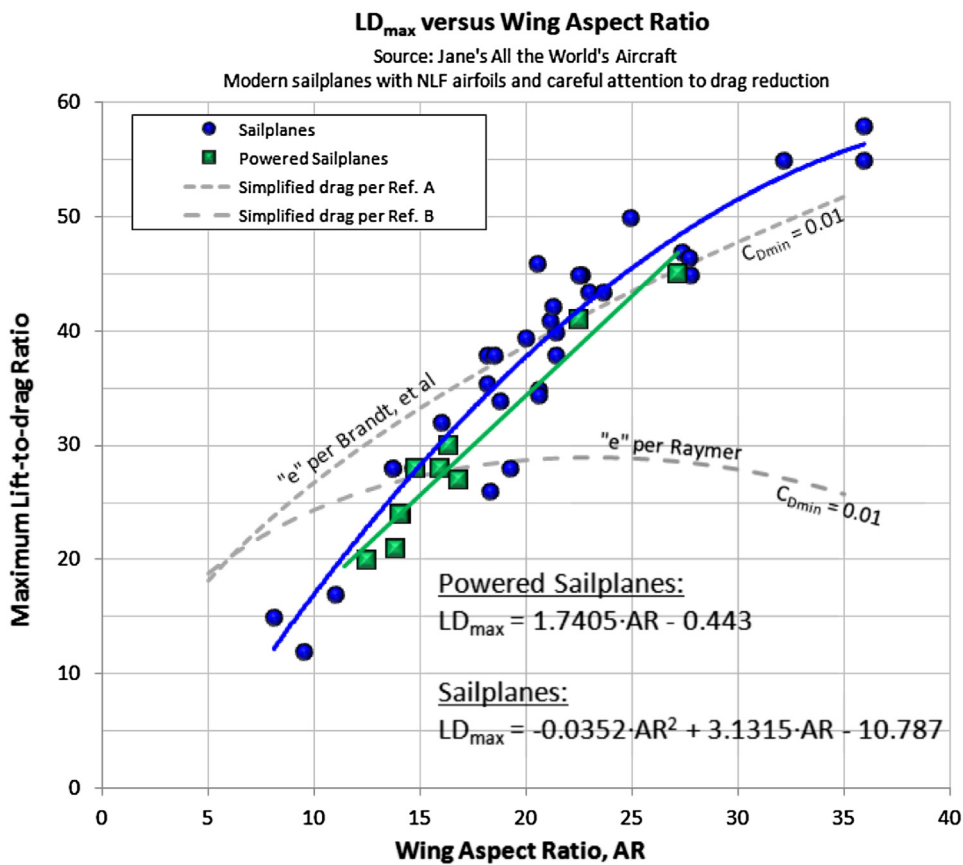


FIGURE 9-13 Maximum lift-to-drag ratio for modern sailplanes and powered sailplanes as a function of  $AR$ . Ref. A is Ref. [4] and Ref. B is Ref. [5].

coefficients (left graph) and lift force per unit length (right graph). It shows clearly how a highly tapered wing becomes “tip-loaded,” whereas a constant-chord wing is “root-loaded,” terms that refers to the distribution of section lift coefficients. This is of great importance when

tailoring stall characteristics and controlling the effectiveness of the wing. The right graph shows how the actual lift force of the highly tapered wing moves inboard. This reduces the bending moments and can help reduce the structural weight of the wing.

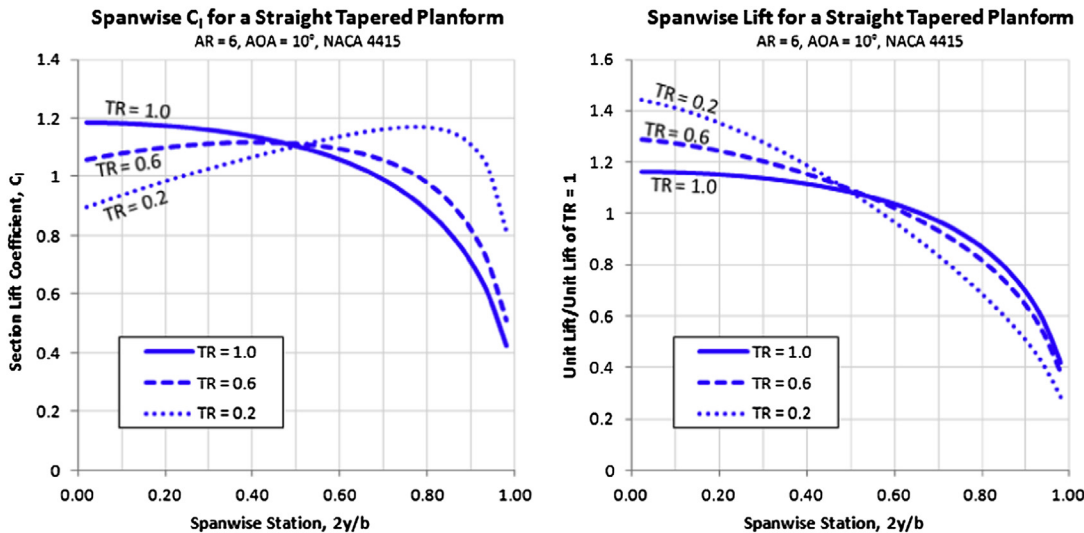


FIGURE 9-14 The effect of taper ratio on the spanwise distribution of section lift coefficients (left); and lift force (right).

**TABLE 9-5** Typical Impact of Taper Ratio on Aerodynamic Properties of the Wing

Taper Ratio, $\lambda$	Pros	Cons
0.3	Induced drag is close to that of an elliptical wing planform, but is much simpler to manufacture.	Poor stall characteristics. Tip-loaded planform requires a large washout to delay tip stall.
0.5	Good balance between low induced drag and good stall characteristics.	Stall begins mid-span and spreads to tip and root. Usually requires moderate washout.
1.0	Good stall progression. Washout generally not required. Simple to manufacture.	High induced drag.

Too much tip-loading of a wing can have serious consequences for its stall characteristics. It is evident from the shape of the spanwise  $C_l$  that the wing whose  $TR = 0.2$  will stall near the wingtip, as it peaks there. This would make the wing very susceptible to roll instability at stall, which could have dire consequences if ignored. The constant-chord wing, on the other hand, has its  $C_l$  peak inboard, near the root, which retains roll stability and results in benign stall characteristics. Such characteristics are very desirable for trainers and, frankly, should be one of the primary goals of any passenger-carrying aircraft.

Additionally, the left graph of Figure 9-14 shows that a  $TR$  in the neighborhood of 0.5–0.6 is a good compromise between efficiency and stall behavior, even though some wing twist (to be discussed later) will be required to ensure stall progression that protects roll stability at stall. The right graph of Figure 9-14 shows that even though the outboard airfoils of the highly tapered wing are working hard to generate lift, the actual force is less than that of the constant-chord wing because the chord is so much shorter. This is very beneficial from a structural standpoint as it brings the center of force inboard and reduces the wing bending moments, although torsional rigidity on the outboard wing suffers. Table 9-5 gives a general rule-of-thumb about the impact the  $TR$  has on selected aerodynamic properties.

### 9.3.3 Leading Edge and Quarter-chord Sweep Angles, $\Lambda_{LE}$ and $\Lambda_{C/4}$

The purpose of sweeping the wing forward or aft is primarily twofold: (1) to fix a CG problem and (2) to delay the onset of shockwaves. The latter is the reason for using swept wings for high-speed aircraft (high subsonic and supersonic). However,

the former is surprisingly common as well. Strictly speaking, sweep should be avoided unless necessary. It not only makes the wing less efficient aerodynamically, it is also detrimental to stall characteristics if swept back. Additionally, for slow-flying GA aircraft, it implies the spar has discontinuous breaks in it that make it less efficient structurally.

Of course, this is not to say that sweep is all bad. It is very helpful for the design of high-speed aircraft, where it enables the use of thicker airfoils, which lightens the airframe and makes up for some of the lost efficiency. For low-speed airplanes, it is a tool that allows a project to be salvaged if it is discovered that the CG is farther forward or aft than anticipated. This is the reason behind the aft-swept wings featured on the venerable Douglas DC-3 Dakota (C-47) [6]. The same holds for forward-swept configurations. The military scouting and trainer airplane SAAB MFI-15 Safari was designed with an improved field-of-view in mind, which is why it features a shoulder-mounted wing with the main spar behind the two occupants. The wing is swept forward to solve the CG issue that results from the engine and the two occupants sitting in front of the main spar.

#### **Impact of Sweep Angle on the Critical Mach Number**

The greatest benefit of wing sweep is a reduction in the strength of and delay in the onset of shock formation. The shock formation will not only cause a sharp increase in drag; it also changes the chordwise pressure distribution on the airfoil, causing the center of lift to move from approximately the airfoil's quarter-chord to mid-chord. The consequence of this is called "Mach-tuck," a severe increase in nose-down pitching moment. The change in drag due to this effect is detailed in Section 15.4.2, *The effect of Mach number*. Also, Figure 15-28 shows how the leading edge sweep increases the critical Mach number,  $M_{crit}$ , and delays the onset of the peak of the compressibility drag coefficient. This is helpful as it allows thicker and more structurally efficient airfoils to be used in the wing.

Consider the swept wing in Figure 9-15 and the deconstruction of the far-field airspeed into two components: one parallel to and the other perpendicular to the leading edge. In its simplest form the wing sweep theory contends that it is the airspeed component normal to the leading edge that dictates when shockwaves begin to form. This allows the following correction to the critical Mach number to be made (see Section 8.3.7, *The critical Mach number,  $M_{crit}$* ).

$$M_{crit} = \frac{(M_{crit})_{\Lambda_{LE}=0}}{\cos \Lambda_{LE}} \quad (9-32)$$

In practice, only half of this reduction is experienced.

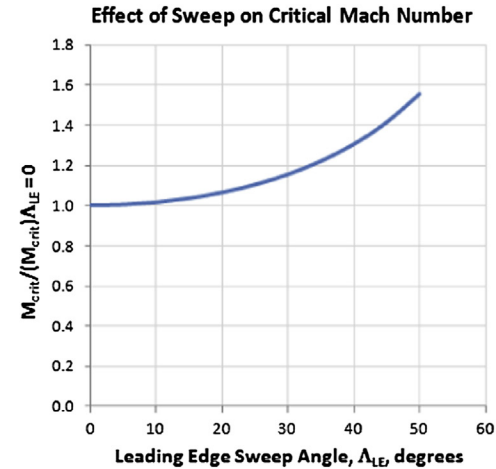
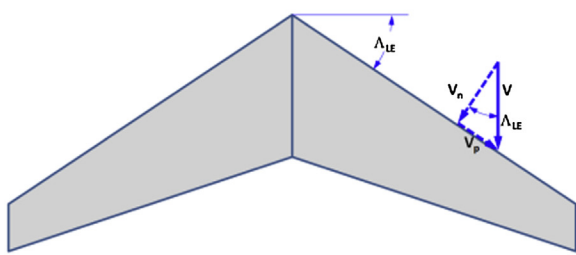


FIGURE 9-15 The deconstruction of the far-field into normal (n) and parallel (p) speed components (left). The effect of sweeping the leading edge is shown to increase the critical Mach number (right).

### Impact of Sweep Angle on the $C_{Lmax}$

The maximum lift coefficient is reduced with an increase in wing sweep angle. This is detailed in Section 9.5.10, *Step-by-step: Rapid  $C_{Lmax}$  estimation*.

### Impact of Sweep Angle on Structural Loads

The sweep has very important effect on structural loads. As discussed in Chapter 8, *The anatomy of the airfoil*, cambered airfoils inherently generate a pitching moment about their quarter chords whose tendency is to rotate the airfoil LE down. All flapped airfoils, cambered or not, generate extra pitching moment (torsion), which is added to the baseline moment. The total moment, regardless of composition, is reacted as shear flow in the wing structure. If the wing is swept aft, an additional and usually much larger pitching moment is generated because of the center of lift being moved a large distance aft. Consequently, the swept wing structure will be heavier than a straight wing designed for the same flight condition. Similarly, a forward-swept wing may also introduce a large LE up torsion, if the sweep angle is large enough, although this is reduced by an amount corresponding to the innate torsion of the airfoils of the wing.

### Impact of Sweep Angle on Stall Characteristics

Sweep angle has very detrimental effects on the stall characteristics for reasons detailed in Sections 9.6.5, *Cause of spanwise flow for a swept-back wing planform* and 9.6.6, *Pitch-up stall boundary for a swept-back wing planform*.

#### 9.3.4 Dihedral or Anhedral, $\Gamma$

The *dihedral* (or *anhedral*) is the angle the wing makes with respect to the ground plane or the  $x$ - $y$  plane (as it is

normally called) when viewing the airplane from the front (or back). A dihedral refers to the wingtip being higher (with respect to the ground) than the wing root. The opposite holds true for anhedral. The dihedral affects the lift of the configurations in two ways: due to the tilting of the lift force and how the dihedral changes the *AOA* of the wing. Consider a wing that has dihedral angle  $\Gamma$  subjected to an *AOA* given by  $\alpha$ . The geometry of the configuration reveals that the *AOA* seen by the airfoil, and denoted by  $\alpha_N$ , is reduced by the factor  $\cos \Gamma$  (for instance, if  $\Gamma = 0^\circ$ , then  $\alpha_N = \alpha$  and if  $\Gamma = 90^\circ$ , then  $\alpha_N = 0^\circ$ , no matter the magnitude of  $\alpha$ ). Therefore, we can write:

Impact on *AOA*:

$$\alpha_N = \alpha \cdot \cos \Gamma \quad (9-33)$$

Similarly, the lift generated in the plane of symmetry is the product of the lift normal to the wing surface, denoted by  $L_N$ , reduced by the same factor,  $\cos \Gamma$ .

Tilting of lift force:

$$L = L_N \cdot \cos \Gamma \quad (9-34)$$

Since  $L_N$  can be written as  $L_N = qSC_{LN} = qSC_{L\alpha}\alpha_N = qSC_{L\alpha}\alpha \cos \Gamma$ , the lift in the plane of symmetry can be presented as follows:

Lift of a wing with dihedral:

$$L = qSC_{L\alpha}\alpha \cos^2 \Gamma \quad (9-35)$$

where

$C_{L\alpha}$  = lift curve slope of the wing assuming  $\Gamma = 0^\circ$

$q$  = dynamic pressure

$S$  = reference wing area

This result has been experimentally confirmed, for instance see Ref. [7]. It allows wing lift to be determined

in terms of variables that refer to a wing with no dihedral. Furthermore, see discussion of V-tails in Section 11.3.4, *V-tail or butterfly tail*. Typical wings feature a dihedral of  $4^\circ$ – $7^\circ$ . The term  $\cos^2 \Gamma$  amounts to 0.995 to 0.985 and, therefore, is usually ignored in the estimation of stability derivatives.

Dihedral plays an essential role in the generation of *dihedral effect*. It is discussed further in Section 4.2.3, *Wing dihedral*. Values for several classes of aircraft are given in Table 9-6.

### 9.3.5 Wing Twist – Washout and Washin, $\phi$

Many aircraft feature wings that are twisted so the tip airfoil is at a different angle of incidence with respect to the fuselage than the root airfoil. This is called *wing washout* if the incidence of the tip is less than that of the root, and *washin* if it is larger. Washin is rarely used, but is mostly used to describe the aeroelastic effects high *AOA* has on forward-swept wings, where aerodynamic loads tend to twist the wing so the *AOA* at the tip is increased even further. This article, however, deals with the intentional twisting of the wing, where its purpose is generally twofold:

- To prevent the wingtip region from stalling before the wing root.** If the wingtip stalls before the root, there is an increased risk the aircraft will roll abruptly and uncontrollably at stall, a condition that may lead to incipient stall. Roll tendency at stall contributes significantly to fatal accidents<sup>1</sup> as it will often take place at low altitudes when an airplane banks to establish final approach before landing. An aircraft with such a roll-off tendency may stall if the pilot banks steeply and it may, ultimately, result in a crash as lack of altitude will prevent successful recovery. In the real world, manufacturing tolerances inevitably lead to airplanes not being perfectly symmetrical. This promotes one side of the airplane to stall before the other one, generating a rolling moment at stall. A wing twist can be used to build a “buffer” so the wingtips remain un-stalled when the rest of the wing stalls, greatly improving roll stability.
- To modify the spanwise lift distribution to help achieve minimum drag at mission condition.** The wing is most efficient when the section lift coefficients are constant along the span, as it is for an elliptical wing planform. Twisting the wing will allow the spanwise distribution of section lift coefficients to be modified for a tip-loaded wing,

bringing the general distribution closer to that of an elliptical wing. A byproduct of this is a reduction in wing bending moments as the center of lift is brought closer to the plane of symmetry.

#### Geometric Washout

Geometric washout usually refers to the difference in angles of incidence of the root and tip airfoils (see Figure 9-16). It is denoted by  $\phi_G$ . Generally the wing twist ranges from  $0^\circ$  to  $-4^\circ$ , where the negative sign indicates that the leading edge of the tip is lower than that of the root. Thus, if we say the “washout is  $3^\circ$ ” we mean that  $\phi_G = -3^\circ$  and the LE of the tip is lower than that of the root. If we say the “washin is  $3^\circ$ ” we mean that  $\phi_G = +3^\circ$  and the LE of the tip is higher than that of the root. For instance, the inserted image of the root and tip airfoils in Figure 9-16 displays a washout. However, sometimes twist is highly complicated along the wingspan as in the case of the McDonnell-Douglas AV-8B, whose twist varies in a segmented fashion to a maximum of  $-8^\circ$  at the tip [8].

Note that if the twist is linear, the relative angle of twist at any spanwise station can be determined using the following expression:

$$\phi(y) = \frac{2y}{b} \phi_G \quad (9-36)$$

The expression assumes the reference angle is  $0$  when  $y = 0$  (the plane of symmetry) and becomes  $\phi_G$  at the wingtip (where  $y = b/2$ ).

#### Aerodynamic Washout

Aerodynamic washout is another way of designing roll stability at stall into the wing. In this case, two different airfoils are selected for the root and tip that are specifically based on one of two parameters: (1) their individual zero-lift *AOA* or (2) their two-dimensional stall *AOA* or maximum section lift coefficient. The former is favored when analyzing wings using methods such as the lifting line theory. Typically the idea is to provide roll stability at high *AOA* by ensuring the tip airfoil remains un-stalled before the inboard airfoil.

The primary reason for selecting an aerodynamic washout is that it allows the main wing spar caps to be straight, something that is important for the construction of composite aircraft. A spar cap in a composite aircraft mostly consists of unidirectional fibers, whose strength is very sensitive to fiber alignment. Once two airfoils have been selected, the aerodynamic washout is defined as follows (see Figure 9-17):

<sup>1</sup>For instance, see the “Nall Report,” an annual publication that evaluates aircraft accidents.

TABLE 9-6 Various Wing Layout Properties for Selected Aircraft (Based on Ref. [9])

Aircraft	Aspect Ratio AR	Taper Ratio $\lambda$	Dihedral $\Gamma$	Washout $\phi_G$	Incidence (Root) $i_{\text{root}}$	Leading Edge Sweep $\Lambda_{\text{LE}}$
<b>COMMERCIAL JETLINERS</b>						
Airbus A300-600	7.7	-	-	-	-	28° (0.250C)
Airbus A310	8.8	0.260	11.13° (IB) 4.05° (OB)	-	5.05°	28° (0.250C)
Airbus A320-200	9.4	-	5.2°	-		25° (0.250C)
Boeing 707	7.056	0.275	7°	-	2°	35° (0.250C)
Boeing 727	7.2	0.304	3°	-	2°	32° (0.250C)
Boeing 737-100, -200	8.83	0.340	6°	-	1°	25° (0.250C)
Boeing 747-100, -200	6.96	0.245	7°	-	2°	37.5° (0.250C)
Boeing 757	7.77	0.211	5°	-	3.2°	25° (0.250C)
Boeing 767	7.9	0.267	6°	-	4.25°	31.5° (0.250C)
Fokker F28 Fellowship	8.4	0.239	2.5°	-	-	17.4° (0.250C)
McDonnell-Douglas DC-9/MD87	9.62	0.156	3°	-	1.25°	24.5° (0.250C)
McDonnell-Douglas DC-10-30/40	7.5	0.252	5.24° (IB) 3.03° (OB)	-	-	35° (0.250C)
<b>MILITARY JET AIRCRAFT</b>						
Aermacchi MB-339	6.1	-	-	-	-	11.3°
Aero L-39 Albatros	4.4	-	2.5°	-	2°	6.43°
BAC 167 Strikemaster	5.84	0.545	6°	3°	3°	-
Cessna A-37 Dragonfly	6.2	0.682	3°	2.63°	3.63°	0° (0.225C)
DBD Alpha Jet	4.8	-	-6°	-	-	28° (0.250C)
Hawker Siddeley Harrier	3.175	0.354	-12°	-8°	1.75°	34° (0.250C)
Microjet 200B	9.3	-	5.03°	-	3°	0° (0.300C)
<b>TURBOPROPS, COMMUTER AND MILITARY</b>						
ATR 42	11.08	0.549	2.5°	-	2°	3.1° (0.250C)
ATR 72	12.0	0.549	2.5°	-	2°	2.8° (0.250C)
De Havilland DHC-6 Twin Otter	10.1	1	-	-	-	-
De Havilland DHC-7 Dash 7	10.1	0.441	4.5°	-	3°	3.2° (0.250C)
De Havilland DHC-8 Dash 8	12.4	-	2.5°	-	3°	3.03° (0.250C)
Dornier Do 28 Skyservant	8.3	1	1.5°	-	4°	0°
Fokker F27 Friendship	12.0	0.404	2.5°	2°	3°	0° (0.250C)
IAI-101, 201 Arava	10	1	1.5°	-	0.45°	0°
LET L-410	10.79	-	1.75°	2.5°	2°	0° (0.250C)
Lockheed C-130 Hercules	10.09	0.852	2.5°	3°	3°	0° (0.250C)
Mitsubishi MU-2	7.71	-	0°	3°	2°	0.35° (0.250C)
SAAB 340	11.0	0.375	7°	-	2°	3.6° (0.250C)
Shorts SD3-30	12.3	1	3°	-	-	0°
Shorts Skyvan Series 3M	11	1	2.03°	-	2.5°	0°

**TABLE 9-6** Various Wing Layout Properties for Selected Aircraft (Based on Ref. [9])—cont'd

Aircraft	Aspect Ratio AR	Taper Ratio $\lambda$	Dihedral $\Gamma$	Washout $\phi_G$	Incidence (Root) $i_{\text{root}}$	Leading Edge Sweep $\Lambda_{\text{LE}}$
<b>GA SINGLE-ENGINE, PISTON AND TURBOPROP</b>						
Beechcraft Sierra/Sundowner	7.5	1	6.5°	2°	3°	0°
Beechcraft T-34C Mentor	6.22	0.412	7°	3°	4°	0° (0.250C)
Beechcraft V35 Bonanza	6.2	0.5	6°	3°	4°	0° (0.250C)
Cessna 150/152	6.7	0.687	1°	1°	1°	-
Cessna 172 Skyhawk	7.52	0.687	2.73°	3°	1.5°	-
Cessna 177 Cardinal	7.31	0.726	1.5°	3°	3.5°	0°
Cessna 182 Skylane	7.37	0.669	1.73°	3.62°	0.78°	0°
Cessna 208 Caravan	9.61	0.616	3°	3.22°	2.62°	-
Cessna 210 Centurion	7.66	0.726	1.5°	3°	1.5°	-
Cirrus SR20/22	10	0.5	4.5°	0°	0.25°	0° (0.250C)
Pilatus PC-6 Turbo-Porter	8.4	1	1°	-	2°	0°
Piper PA-28 Cherokee Arrow II	6.11	1	7°	-	2°	0°
Piper PA-28 Cherokee Warrior	7.24	0.669	7°	3°	2°	-
Piper PA-46 Malibu	10.57	-	4°	-	-	-
SIAI-Marchetti SF260	6.3	0.49	6.33°	2.75°	2.75°	0° (0.250C)
Valmet L-70 Miltainer	6.62	-	-	-	-	-
Valmet L-90 Redigo	7.25	0.6	6°	3°	3°	-
Zlin 142	6.4	1	6°	-	-	-4.33°
<b>GA TWIN-ENGINE</b>						
Beechcraft B58 Baron	7.16	0.42	6°	4°	4°	-
Beechcraft B60 Duke	7.243	0.32	6°	4°	4°	-
Beechcraft B99 Airliner	7.51	0.5	7°	4.8°	4.8°	-
Britten-Norman BN-2A (standard)	7.4	1	0°	-	2°	0°
Cessna 310	7.3	0.674	5°	3°	2.5°	-
Cessna 337 Skymaster	7.18	0.667	3°	2°	4.5°	-
Partenavia P.68 Victor	7.7	1	1°	-	1.5°	0°
Piaggio P.180 Avanti	11.8	0.352	2°	-	0°	0° (0.150C)
Piper PA-31 Cheyenne	7.22	-	5°	2.5°	1.5°	0° (0.300C)
Piper PA-31-310 Navajo	7.22	-	-	1.0° (aero) 2.5° (geo)	-	-
<b>BUSINESS JETS</b>						
Cessna M550 Citation II	7.8	-	4°	3°	2.5°	-
Cessna M650 Citation III	8.94	-	3°	-	-	25° (0.250C)
Dassault Falcon 20	6.4	-	2°	-	1.5°	30° (0.250C)
Dassault Falcon 100	6.5	-	2°	-	1.5°	30° (0.250C)
Gates Learjet 55	6.72	0.391	-	-	-	13° (0.250C)

(Continued)

TABLE 9-6 Various Wing Layout Properties for Selected Aircraft (Based on Ref. [9])—cont'd

Aircraft	Aspect Ratio AR	Taper Ratio $\lambda$	Dihedral $\Gamma$	Washout $\phi_G$	Incidence (Root) $i_{root}$	Leading Edge Sweep $\Lambda_{LE}$
<b>EXPERIMENTAL AND HOMEBUILT</b>						
Colomban MC 15 Cri Cri	7.75	1	4°	1.5°	1°	0°
Corby Starlet	5.00	1	6°	3.5°	2.5°	0°
Rutan VariEze	9.20	-	-	-3°	-	-
Verilite Model 100 Sunbird	7.56	1	2°	2°	2°	0°
<b>SAILPLANES</b>						
Rolladen-Schneider LS4	21.4	-	4°	-	-	0°
Schempp-Hirth Nimbus-3D	35.9	-	3°	-	1.5°	-2°
Schleicher ASK 21	16.1	-	4°	-	-	-1.5° (0.250C)
Schweizer SGM 2-37	18.1	-	3.5°	1°	1°	0°

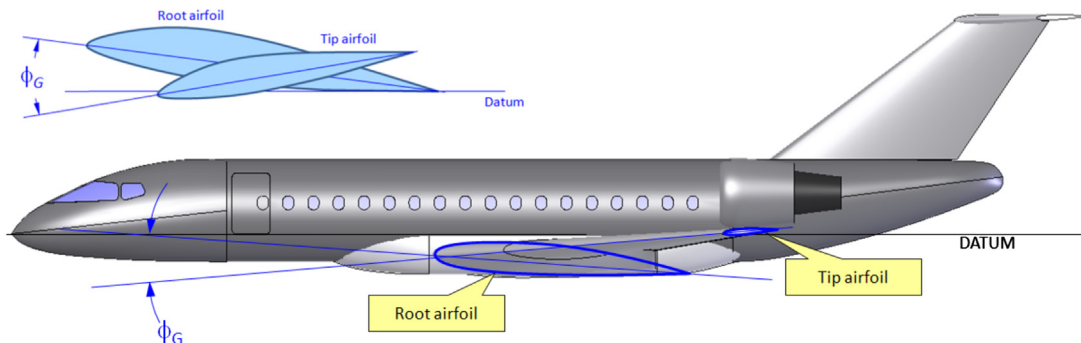


FIGURE 9-16 Definition of geometric washout.

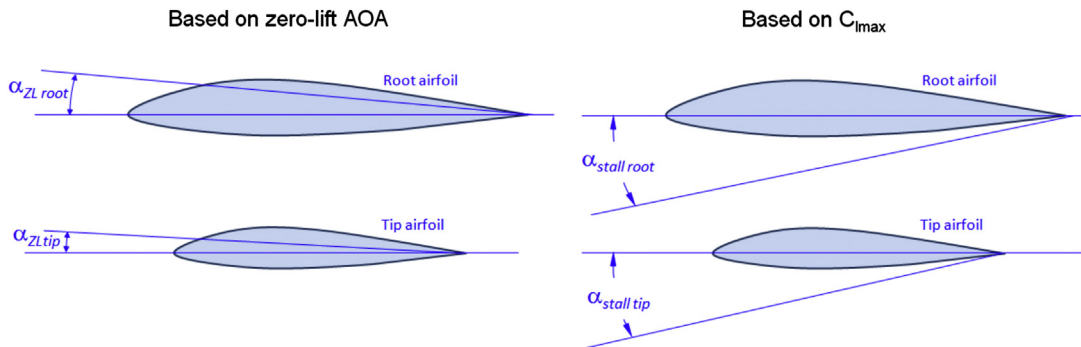


FIGURE 9-17 Definition of aerodynamic washout based on the stall AOA.

Twist based on zero lift AOA:

$$\phi_A = \alpha_{ZL_{root}} - \alpha_{ZL_{tip}} \quad (9-37)$$

Twist based on stall AOA:

$$\phi_A = \alpha_{stall_{root}} - \alpha_{stall_{tip}} \quad (9-38)$$

where

$\alpha_{ZL_{root}}$  = two-dimensional zero-lift AOA for the root airfoil

$\alpha_{ZL_{tip}}$  = two-dimensional zero-lift AOA for the tip airfoil

$\alpha_{stall_{root}}$  = two-dimensional stall AOA for the root airfoil

$\alpha_{stall_{tip}}$  = two-dimensional stall AOA for the tip airfoil

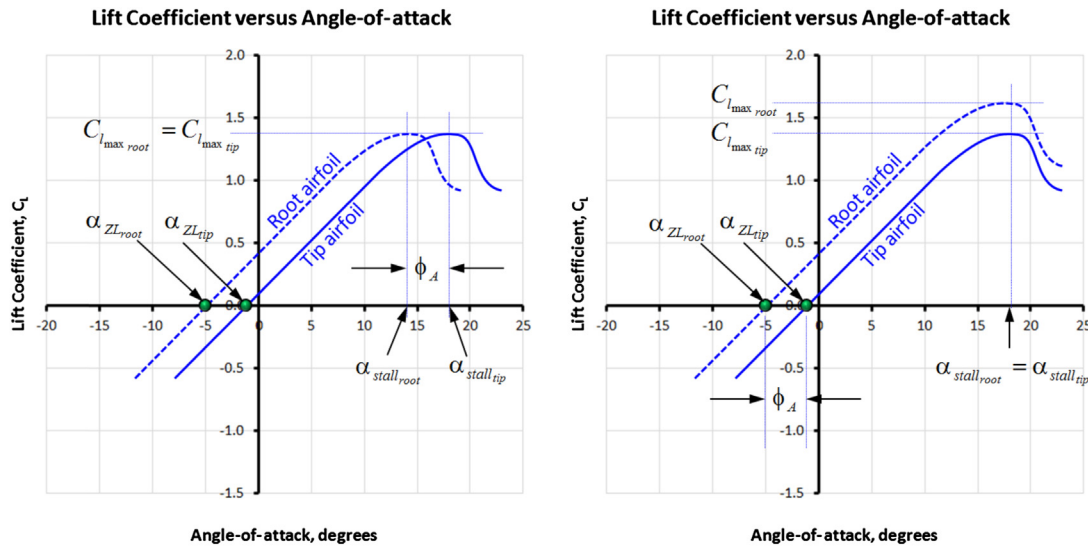


**FIGURE 9-18** Idealized effect of an aerodynamic washout. In the left graph, the root airfoil stalls at a lower  $AOA$  than the tip providing roll stability at stall. A problem for the zero-lift definition of the aerodynamic washout is shown to the right. The root airfoil has a higher  $C_{L_{max}}$  than the tip airfoil but stalls at the same  $AOA$ ; the effective washout is zero. This renders the definition of washout based on zero-lift angles misleading.

Note that there is an inherent problem with the definition based on Equation (9-37) and this is displayed in Figure 9-18. To begin with, the left graph of Figure 9-18 depicts the idea behind the aerodynamic washout: that the root airfoil stalls at an  $AOA$  less than the tip. It assumes that (1)  $\alpha_{ZL,tip} - \alpha_{ZL,root} = \alpha_{stall,root} - \alpha_{stall,tip}$ , which is not necessarily achieved in practice, and (2) requires  $C_{L_{max,tip}} = C_{L_{max,root}}$  (otherwise assumption (1) will not hold). This allows the aerodynamic washout can effectively be represented as the difference in the zero-lift  $AOAs$ .

One of the problems with this definition is shown in the right graph of Figure 9-18, which depicts the common case of the root airfoil being thicker than the tip airfoil. Consequently, its  $C_{L_{max}}$  may be larger than that of the tip airfoil and its stall  $AOA$  is greater. Furthermore, if the wing is tapered, the difference in Reynolds number between the two can make the  $C_{L_{max,tip}}$  and

$\alpha_{stall,tip}$  substantially smaller than that of the root. The figure effectively depicts a scenario in which the true washout is zero and possibly a washin, whereas relying on the zero-lift  $AOAs$  might indicate ample washout and therefore is misleading. Additional complexity must be considered in the magnitude of the section lift coefficients, which vary along the span. The above definition, thus, only gives a part of the whole picture; the remainder calls for analysis of the distribution of section lift coefficients along the span.

### A Combined Geometric and Aerodynamic Washout

If two different airfoils are selected for the root and tip, in addition to a geometric washout, the combined effect can be calculated from:

$$\phi_A = \alpha_{stall,root} - \alpha_{stall,tip} + \phi_G \quad (9-39)$$

### EXAMPLE 9-5

An airplane features two dissimilar airfoils at the root and tip whose  $\alpha_{stall,root} = 16.5^\circ$  and  $\alpha_{stall,tip} = 15.0^\circ$ . What is the combined washout for a geometric washout of  $0^\circ$  and  $3^\circ$ ?

#### Solution

Combined washout for  $\phi_G = 0^\circ$ :

$$\begin{aligned} \phi_C &= \alpha_{stall,root} - \alpha_{stall,tip} + \phi_G = 16.5^\circ - 15.0^\circ + 0^\circ \\ &= +1.5^\circ \text{ (washin)} \end{aligned}$$

Combined washout for  $\phi_G = 3^\circ$ :

$$\begin{aligned} \phi_C &= \alpha_{stall,root} - \alpha_{stall,tip} + \phi_G = 16.5^\circ - 15.0^\circ + (-3^\circ) \\ &= -2.5^\circ \end{aligned}$$

Recall that a negative angle means the root is at a greater  $AOA$  than that of the tip.

### Panknin and Culver Wing Twist Formulas

The wing twist of a flying wing is such a fundamental parameter that it should be determined early on in the design phase – effectively as soon as the design lift coefficient has been determined. The designer of tailless aircraft can determine the proper washout of the wing using one of two special formulas specifically devised to help with the layout of such configurations. They are called the Panknin and Culver twist formulas. They are presented here without derivation for completeness of the discussion in this article.

The *Panknin twist formula* is attributed to Dr. Walter Panknin, who in 1989 presented a method to the designers of radio-controlled (RC) aircraft intended to help them properly lay out the washout of flying wings so the elevons are in trail at cruise. The formulation has been applied with great success to many RC flying wing designs [2]. It determines the geometric twist  $\phi_G$  between the inboard and outboard airfoils of the wing (see Figure 9-19) using the following expression:

$$\phi_G = \frac{\left( K_1 C_{m_{root}} + K_2 C_{m_{tip}} \right) - C_{LC} \cdot K_{SM}}{1.4 \times 10^{-5} \times AR^{1.43} \times \Lambda_{C/4}} - (\alpha_{ZL_{root}} - \alpha_{ZL_{tip}}) \quad (9-40)$$

where

$AR$  = wing aspect ratio

$C_{m_{tip}}$  = pitching moment coefficient of the tip airfoil

$C_{m_{root}}$  = pitching moment coefficient of the root airfoil

$C_{LC}$  = lift coefficient at cruise (for which the aircraft is designed)

$K_{SM}$  = fraction design static margin (e.g. if  $SM = 10\%$  then  $K_{SM} = 0.1$ )

$$K_1 = \frac{3 + 2\lambda + \lambda^2}{4(1 + \lambda + \lambda^2)}$$

$$K_2 = 1 - K_1$$

$\alpha_{ZL_{root}}$  = zero-lift AOA for the root airfoil, in degrees

$\alpha_{ZL_{tip}}$  = zero-lift AOA for the tip airfoil, in degrees

$\Lambda_{C/4}$  = quarter-chord sweep angle, in degrees

The formula determines the geometric twist angle  $\phi_G$  based on the selected static margin, but allows the designer to select airfoils,  $AR$ , and quarter-chord sweep angle. It is applicable to both forward- and aft-swept wings. Note that one must exercise care in the application of units for the quarter-chord sweep. Its units must be in terms of degrees.

The *Culver twist formula* is attributed to Mr. Irv Culver, a former engineer at Lockheed Skunk Works. Like the Panknin formula, his formula is widely used by designers of small RC tailless aircraft. It is intended for flying wings of moderate sweep angles (typically  $\approx 20^\circ$ ) and design lift coefficients of 0.9–1.2, where the lower value indicates a high-speed glider and the higher is for high-performance sailplanes [8]. Note that the presentation here differs slightly from that of Ref. [8] in the simplification of terms.

$$\phi_G = \pi \cdot \Lambda_{C/2} \left( \frac{AR}{AR + 1} \right) \frac{C_{LC}}{C_{L_\alpha}} \quad (9-41)$$

where

$AR$  = wing aspect ratio

$C_{L_\alpha}$  = lift curve slope

$\Lambda_{C/2}$  = center-chord sweep angle, in degrees or radians

Once the washout is known its distribution along the span can be found using the following expression:

$$\phi(y) = \phi_G (1 - y)^{1+AR/2\pi} \quad (9-42)$$

### EXAMPLE 9-6

A flying wing is being designed for operation at a cruise  $C_L$  of 0.5 ( $C_{LC} = 0.5$ ) at a static margin of 10% ( $K_{SM} = 0.1$ ). It has been determined that its  $AR$  shall be 10, taper ratio ( $\lambda$ ) shall be 0.5, and quarter-chord sweep angle,  $\Gamma_{C/4}$ , is  $30^\circ$ . During the airfoil selection process, the designers compare the use of a NACA 4415 airfoil (a conventional highly cambered airfoil, whose  $C_m$  is  $-0.1$  and  $\alpha_{ZL} = -4^\circ$ ) and a NACA 0015 airfoil (whose  $C_m$  is 0.0 and  $\alpha_{ZL} = 0^\circ$ ). What is the required washout using each airfoil, in accordance with the Panknin formula?

### Solution

The solution is effectively “plug and chug” into Equation (9-40). First, the parameters  $K_1$  and  $K_2$  must be determined.

$$\begin{aligned} K_1 &= \frac{3 + 2\lambda + \lambda^2}{4(1 + \lambda + \lambda^2)} = \frac{3 + 2(0.5) + (0.5)^2}{4(1 + (0.5) + (0.5)^2)} \\ &= 0.6071 \Rightarrow K_2 = 1 - K_1 = 0.3929 \end{aligned}$$

Using these with Equation (9-40) for the NACA 4415 airfoil leads to:

**EXAMPLE 9-6 (cont'd)**

$$\begin{aligned}\phi_G &= \frac{(K_1 C_{m_{root}} + K_2 C_{m_{tip}}) - C_{L_{cruise}} \cdot K_{SM}}{1.4 \times 10^{-5} \times AR^{1.43} \times \Lambda_{C/4}} - (\alpha_{ZL_{root}} - \alpha_{ZL_{tip}}) \\ &= \frac{(0.6071 \times -0.1 + 0.3929 \times -0.1) - 0.5 \times 0.1}{1.4 \times 10^{-5} \times 10^{1.43} \times 30^\circ} \\ &\quad - (-4^\circ + 4^\circ) = -13.3^\circ\end{aligned}$$

Using these with Equation (9-40) for the NACA 0015 airfoil leads to:

$$\begin{aligned}\phi_G &= \frac{(K_1 C_{m_{root}} + K_2 C_{m_{tip}}) - C_{L_{cruise}} \cdot K_{SM}}{1.4 \times 10^{-5} \times AR^{1.43} \times \Lambda_{C/4}} - (\alpha_{ZL_{root}} - \alpha_{ZL_{tip}}) \\ &= \frac{(0 + 0) - 0.5 \times 0.1}{1.4 \times 10^{-5} \times 10^{1.43} \times 30^\circ} - (0^\circ + 0^\circ) = -4.42^\circ\end{aligned}$$

The analysis shows that using a conventional cambered airfoil like the NACA 4415 is a bad choice, as it would require a  $13.3^\circ$  washout. Using a symmetrical airfoil like the NACA 0015 would bring this down to  $4.42^\circ$ .

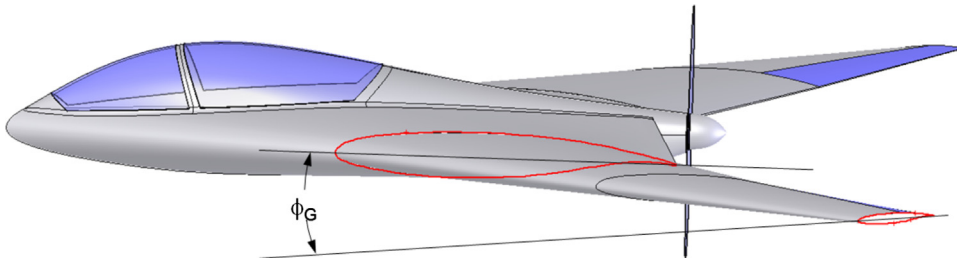


FIGURE 9-19 The Panknin and Culver formulas apply to the geometric washout of tailless aircraft.

### 9.3.6 Wing Angle-of-incidence, $i_W$

Once the general shape of the fuselage, wing, and horizontal tail has been selected, it is time to decide on the relative orientation of the three. Consider a commercial jet designed to cruise at a specified airspeed,  $V_C$ , and altitude (e.g.  $M = 0.8$  at 35,000 ft). Once the desired cruise altitude has been reached, we note the weight of the airplane at the beginning of its cruise segment as  $W_1$ . We also note its weight at the end of the cruise segment as  $W_2$ . It should be evident that if the airplane is operated using conventional fossil fuel, then  $W_1$  will be greater than  $W_2$ . This is particularly true for jet aircraft as large quantities of fuel are consumed en route. Consequently, the airplane will initially be cruising at a higher  $AOA$  than at the end of its mission. Keeping the change in  $AOA$  in mind it is prudent to determine the  $AOA$  at mid-cruise and use this as a representative  $AOA$  for the entire cruise segment. This  $AOA$  will be closer to both the initial and final  $AOAs$  than if either the initial or final  $AOA$  were selected.

Now consider Figure 9-20, which shows three possible orientations of a fuselage during the cruise. The top fuselage has its nose too low, the center too high, and the bottom one shows the correct orientation. Note that all three fuselage placements show a representative root airfoil mounted at the same cruise  $AOA$  (or  $\alpha_C$ ) – it is only the

fuselage that is mounted differently. Note that it is more convenient to refer the wing incidence to the root airfoil rather than the MGC airfoil, because this is usually directly referred to in the fuselage lofting.

The two top schematics in Figure 9-20 show fuselage and wing configurations that result in a higher total airplane drag than the bottom one. It is the responsibility of the designer to determine the optimum  $AOA$  for the fuselage and make sure this is the orientation of the fuselage at the selected cruise mission point. This  $AOA$  may be based on the minimum drag position of the fuselage, or its maximum lift-to-drag ratio, or its maximum lift contribution when combined with the wing. In other words, the optimum  $AOA$  of the fuselage should be determined as the one that maximizes the efficiency of the airplane as a whole. For instance, a minimum drag  $AOA$  for a typical commercial jetliner fuselage would be close to being parallel to the flight path during the design cruise condition and then the wing should be mounted at its required representative cruise  $AOA$  at that condition. The determination of the wing  $AOI$  can be considered a four-step process. The first step is to determine the fuselage minimum drag  $AOA$ , the second is to determine the required cruise  $AOA$ , the third is to add the two together, and the fourth is to determine the horizontal incidence angle that minimizes trim drag.

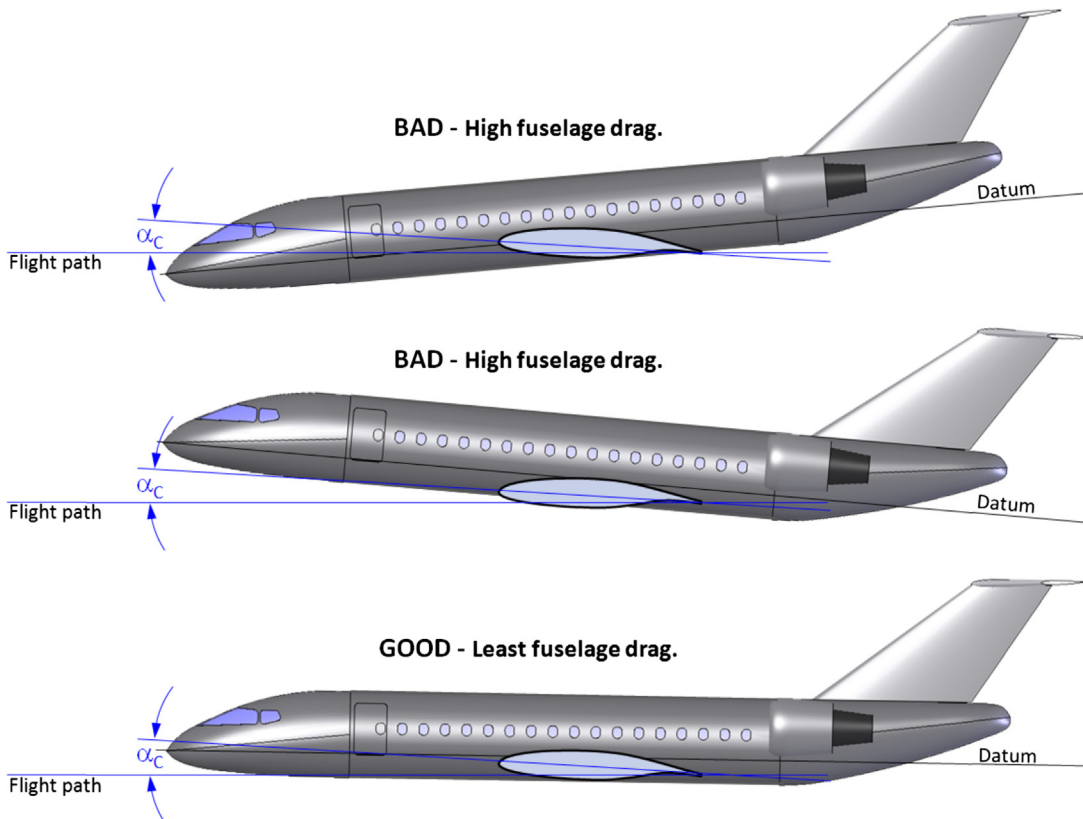


FIGURE 9-20 Determination of the fuselage minimum drag position. The two top configurations will generate greater drag at cruise than the bottom one, which places the fuselage in its minimum drag orientation at cruise. For a conventional pressurized aircraft the centerline of the fuselage will be close to parallel to the flight path during cruise.

### **Step 1: Determine the Optimum AOA for the Fuselage**

The first step will be highly dependent on the geometry of the aircraft, although when considering fuselages for conventional commercial aircraft it is good to assume it is parallel to the centerline of the tubular structure that forms the passenger cabin (see the datum in Figure 9-20). A wind tunnel testing or a CFD analysis should be used to determine the optimum orientation of the fuselage as its influence on the three-dimensional flow field may be quite complicated. The result from this step would be denoted by  $\alpha_{Fopt}$ , for AOA of optimum fuselage orientation, using the following stipulation:

- (1) If the optimum AOA results in the fuselage having a nose-down attitude, then let  $\alpha_{Fopt} > 0$ .
- (2) If the optimum AOA results in the fuselage having a nose-up attitude, then let  $\alpha_{Fopt} < 0$ .

### **Step 2: Determine the Representative AOA at Cruise**

The value of the midpoint cruise AOA,  $\alpha_C$ , can be determined from Equation (9-43) below:

$$\alpha_C = \left( \frac{1}{C_{L_\alpha}} \right) \frac{(W_1 + W_2)}{\rho V_C^2 S} + \alpha_{ZL} \quad (9-43)$$

where

$C_{L_\alpha}$  = lift curve slope

$S$  = reference wing area

$\alpha_{ZL}$  = zero lift angle-of-attack

$\rho$  = density at cruise altitude

### **Step 3: Determine the Recommended Wing Angle-of-incidence**

The angle-of-incidence (see Figure 9-21) at the root airfoil, denoted by  $i_W$ , can now be determined from:

$$i_W = \alpha_C + \alpha_{Fopt} - \Delta\phi_{MGC} \quad (9-44)$$

where

$i_W$  = recommended AOI

$\alpha_C$  = wing angle-of-attack at cruise midpoint

$\alpha_{Fopt}$  = fuselage minimum drag angle-of-attack

$\Delta\phi_{MGC}$  = correction to account for wing twist (see below)

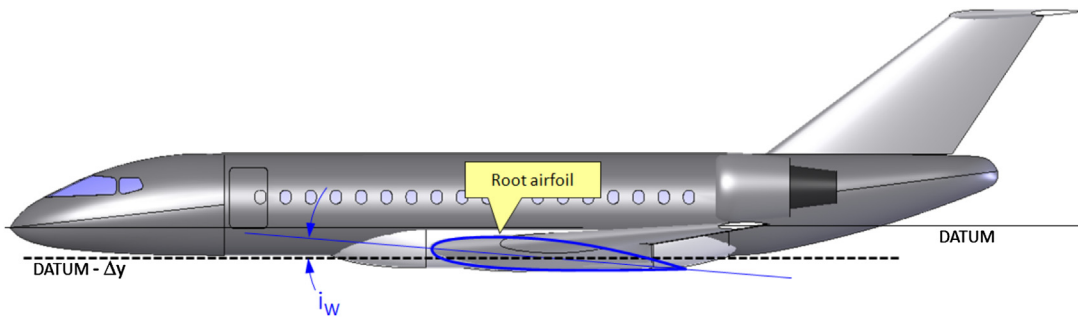


FIGURE 9-21 Definition of a wing incidence angle.

Note that since the first two terms of the above expression really return the AOI at the MGC rather than at the root, a correction must be introduced if the wing features a washout. This is denoted by the term  $\Delta\phi_{MGC}$ , which is the difference in angular incidences between the root and MGC airfoils. If the wing has a linear twist the value of  $\Delta\phi_{MGC}$  can be determined as follows by inserting the expression for the spanwise location of the MGC,  $y_{MGC}$ , of Equation (9-8) into Equation (9-36). Note that the minus sign in Equation (9-44) is required to ensure that a washout will be added to determine:

$$\Delta\phi_{MGC} = \left( \frac{1+2\lambda}{3+3\lambda} \right) \phi_G \quad (9-45)$$

#### **Step 4: Determine the Recommended HT Angle-of-incidence**

Once a recommended wing AOI has been determined, the incidence of the HT can be determined. Again using the representative cruise mission weight  $(W_1 + W_2)/2$  the horizontal tail should be mounted so the elevator deflection at this point will be neutral. This is called flying the horizontal in trail and simply means neutral deflection. This will result in a minimum trim drag.

#### **Derivation of Equation (9-43)**

Assuming the general lift properties of the wing are known, the lift coefficient can be written as follows combining either Equation (9-43) or (9-50):

$$C_L = C_{L0} + C_{L\alpha}\alpha = \frac{2W}{\rho V^2 S} \quad (i)$$

The weight of the airplane at the midpoint during the cruise is the average of the initial cruise weight,  $W_1$ , and the weight at the end of cruise,  $W_2$ :

$$C_L = C_{L0} + C_{L\alpha}\alpha_C = \frac{2\left(\frac{W_1+W_2}{2}\right)}{\rho V^2 S} = \frac{(W_1 + W_2)}{\rho V^2 S} \quad (ii)$$

Where  $\alpha_C$  is the midpoint cruise AOA. Solving for  $\alpha_C$  leads to:

$$C_{L\alpha}\alpha_C = \frac{(W_1 + W_2)}{\rho V^2 S} - C_{L0} \Leftrightarrow \alpha_C = \frac{(W_1 + W_2)}{\rho V^2 S C_{L\alpha}} - \frac{C_{L0}}{C_{L\alpha}}$$

The last term is simply the zero lift AOA,  $\alpha_{ZL}$ , which can be seen from:

$$C_{L0} + C_{L\alpha}\alpha = 0 \Rightarrow C_{L\alpha}\alpha = -C_{L0} \Rightarrow \alpha_{ZL} = -\frac{C_{L0}}{C_{L\alpha}}$$

Therefore, we can write:

$$\alpha_C = \frac{(W_1 + W_2)}{\rho V^2 S C_{L\alpha}} - \frac{C_{L0}}{C_{L\alpha}} = \left( \frac{1}{C_{L\alpha}} \right) \frac{(W_1 + W_2)}{\rho V^2 S} + \alpha_{ZL}$$

QED

#### **Derivation of Equation (9-45)**

Assuming the general lift properties of the wing are known, the lift coefficient can either be written as follows combining Equations (9-43) or (9-50):

$$\begin{aligned} \Delta\phi_{MGC} &= \phi(y_{MGC}) = \frac{2y_{MGC}}{b} \phi_G \\ &= \left( \frac{2}{b} \right) \left( \frac{b}{6} \right) \left( \frac{1+2\lambda}{1+\lambda} \right) \phi_G = \left( \frac{1}{3} \right) \left( \frac{1+2\lambda}{1+\lambda} \right) \phi_G \\ &= \left( \frac{1+2\lambda}{3+3\lambda} \right) \phi_G \end{aligned}$$

QED

### EXAMPLE 9-7

A reconnaissance aircraft is being designed and is expected to weigh 20,000 lb<sub>f</sub> at the start of its design mission cruise segment at a cruising speed  $V_C = 250$  KTAS at 25,000 ft, and 15,500 lb<sub>f</sub> at the end. Determine a suitable angle-of-incidence for its wing if the following parameters have been determined (ignore compressibility effects): where

$$C_{L\alpha} = \text{lift curve slope} = 4.2 \text{ per radian}$$

$$b = \text{reference wingspan} = 52.9 \text{ ft}$$

$$S = \text{reference wing area} = 350 \text{ ft}^2$$

$$\alpha_{ZL} = \text{zero lift angle-of-attack} = -2.5^\circ$$

$$\alpha_{Fopt} = \text{fuselage optimum angle-of-attack} = 1.2^\circ$$

$$\text{nose-up}$$

$$\lambda = \text{Wing taper ratio} = 0.5$$

$$\phi_G = \text{wing washout} = -3.0^\circ$$

#### Solution

**Step 1:** Establish the optimum AOA for the fuselage. Since the fuselage minimum drag position is  $1.2^\circ$  nose up, we set  $\alpha_{Fopt} = -1.2^\circ$ .

**Step 2:** Determine the representative AOA at the midpoint of the cruise segment (note that density at 25,000 ft is 0.001066 slugs/ft<sup>3</sup>).

$$\begin{aligned}\alpha_C &= \left(\frac{1}{C_{L\alpha}}\right) \frac{(W_1 + W_2)}{\rho V_C^2 S} + \alpha_{ZL} \\ &= \left(\frac{1}{4.2 \times \pi/180}\right) \frac{(20000 + 15500)}{(0.001066)(250 \times 1.688)^2(350)} \\ &\quad - 2.5^\circ = 4.789^\circ\end{aligned}$$

In other words, the MGC should be approximately at an AOA of  $4.8^\circ$  at the midpoint of the cruise. On a completely different note, at an initial wing loading of  $20,000 \text{ lb}_f / 350 \text{ ft}^2 = 57.1 \text{ lb}_f/\text{ft}^2$ , the designer may want to reconsider whether this airplane should have a greater wing area. Let us not digress.

**Step 3:** Determine the recommended AOI based on the minimum drag configuration of the fuselage at the cruise midpoint. First, calculate the correction angle since the wing has a  $3^\circ$  washout.

$$\begin{aligned}\Delta\phi_{MGC} &= \phi(y_{MGC}) = \left(\frac{1+2\lambda}{3+3\lambda}\right)\phi_G \\ &= \left(\frac{1+2(0.5)}{3+3(0.5)}\right)(-3^\circ) = -1.333^\circ\end{aligned}$$

Then, finish by calculating the recommended AOI for the wing root chord as follows:

$$\begin{aligned}i_W &= \alpha_C + \alpha_{Fopt} - \Delta\phi_{MGC} = 4.789^\circ - 1.2^\circ - (-1.333^\circ) \\ &= 4.922^\circ\end{aligned}$$

It can be seen that the AOA of the MGC is given by  $\alpha_C$  and is  $4.789^\circ$  and if the fuselage optimum AOA were  $0^\circ$ , rather than  $-1.2^\circ$ , the recommended AOI would be  $4.789^\circ - (-1.333^\circ) = 6.122^\circ$ . The resulting geometry is shown in Figure 9-22.

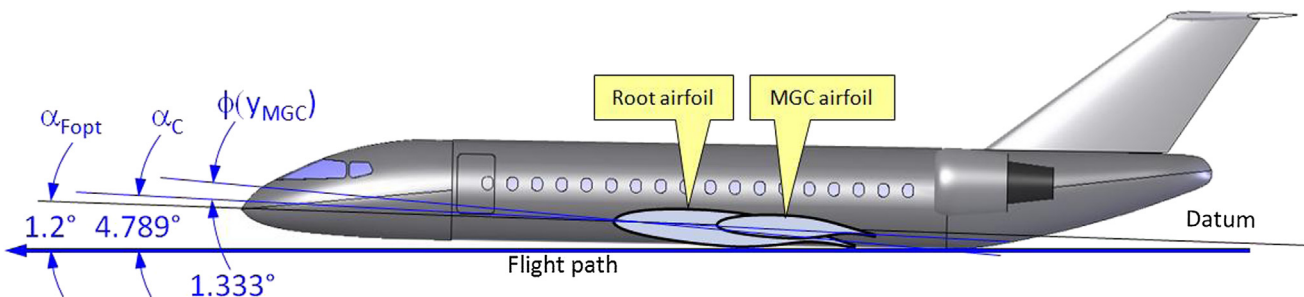


FIGURE 9-22 Wing incidence angle determined for the example aircraft.

#### Decalage Angle for a Monoplane

On a monoplane, a *decalage angle* is the difference between the incidence angles of the wing and horizontal tail: Figure 9-23. The angle is an important

indicator of the stability of the aircraft and generally requires substantial stability analyses to determine. Strictly speaking, the AOA of the HT,  $i_{HT}$ , is determined based on the wing AOA,  $i_W$ , and

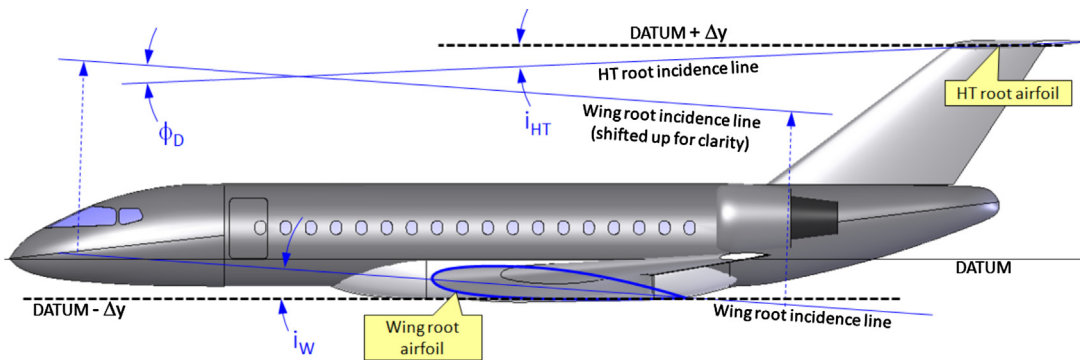


FIGURE 9-23 Definition of a decalage angle for a monoplane.

then the decalage angle can be calculated as shown below:

$$\phi_D = i_W - i_{HT} \quad (9-46)$$

### 9.3.7 Wing Layout Properties of Selected Aircraft

The purpose of Table 9-6 is to present the reader with typical values of some of the wing parameters presented above to help assessing appropriate values.

## 9.4 PLANFORM SELECTION

As stated in the introduction to this section, a glance at the history of aviation reveals a large number of planform shapes have been used. The success of some is glaring (e.g. constant-chord, tapered, swept back), while others have been a disappointment (e.g. triplanes, disc-shaped, circular, channel wings). This section evaluates the impact of varying the wing planform shape on the wing's capability to generate lift and to lose it at stall.

For convenience, the distribution of the section lift coefficients for the planform shapes will be compared to that of a rectangular constant-chord wing. This is done to help the reader realize the impact of selecting a particular geometry. All the planform shapes feature the same reference area ( $10 \text{ ft}^2$ ), the same airfoil (NACA 4416), and are exposed to airspeed of 100 KCAS at a  $10^\circ$  angle-of-attack. They should be thought of as a wing planform study for a generic airplane, so the physical geometry should be ignored and they should rather be evaluated in terms of parameters such as their aspect ratio (AR), taper ratio (TR), and leading edge sweep angles. Wing dihedral and washout is  $0^\circ$  for all examples. The AR and TR are varied to ensure all the examples have an equal area, while featuring values that are representative of typical airplanes. This

gives an excellent insight into the lifting capabilities of the planform. Examples of aircraft that use the said planform shapes are cited as well. The reader should be aware that the true maximum lift coefficient of each wing planform shape will ultimately depend on the airfoil selection and various viscous phenomena. Such effects are too complicated to deal with in general terms in this text and may have a profound impact on the actual stall characteristics.

### 9.4.1 The Optimum Lift Distribution

Generally, the objective during planform selection is to select geometry that (1) generates lift through an effective use of the available span, (2) does not generate excessive bending moment, (3) results in docile stall characteristics, and (4) offers acceptable roll responsiveness. Let's consider these in more detail.

Figure 9-24 shows the distribution of section lift coefficients,  $C_L$ , along the span of some arbitrary wing planform. The figure shows the frontal view of a cantilevered wing (the left wing is shown, looking toward the leading edge). The plane of symmetry (left) is where the wing root would be located and the right side is the left wingtip. The figure shows two kinds of distribution of  $C_L$ . The

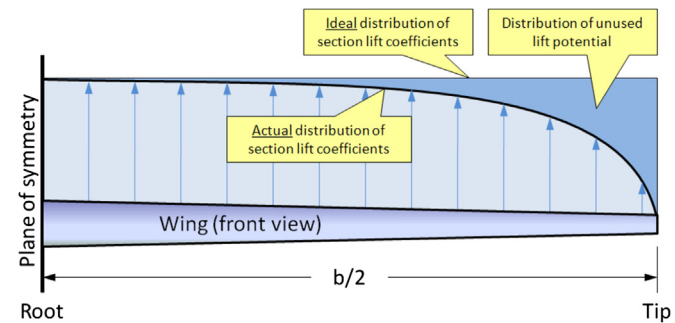
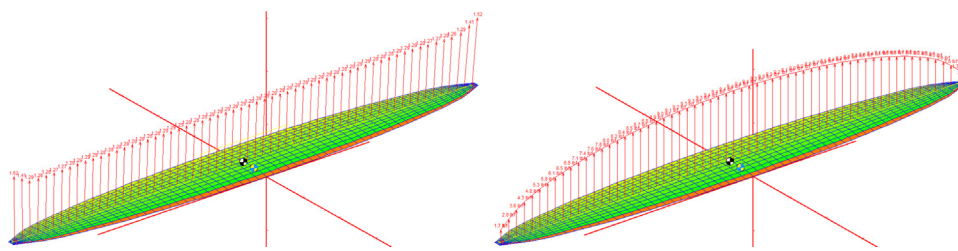


FIGURE 9-24 Ideal, actual, and wasted lift distributions.



**FIGURE 9-25** The difference between the distribution of section lift coefficients (left) and lift force (right). The distribution of section lift coefficients is indicative of stall tendency and induced drag coefficient. The lift force distribution is important for structural issues.

first can be considered an *ideal* spanwise distribution, which would be achieved if the laws of physics didn't require the lift to gradually go to zero at the wingtip. This distribution would result in each spanwise station contributing uniformly to the total lift coefficient. As a consequence, it would require the least amount of *AOA* at any given airspeed to maintain altitude. And as is shown in Chapter 15, the less the *AOA*, the less is the generation of lift-induced drag.

Figure 9-24 also shows the *actual* distribution of  $C_L$ . It represents the true section lift coefficients generated along the wing and it differs from the ideal distribution. Thus, the area between the ideal and actual distributions represents the distribution of *unused* lift potential. The smaller this area, the more efficient is the wing. The larger this area, the higher will be the stalling speed of the aircraft, because the missing lift must be made up for with dynamic pressure (i.e. airspeed) at stall. Similarly, the larger this area, the greater will be the induced drag at cruise, because the missing lift, again, must be made up by a larger *AOA* (which implies an increase in pressure and induced drag). In short, the design goal of the lifting surfaces should always be to minimize the wasted lift distribution.

Unfortunately, things are a bit more complicated than reflected by this. It turns out that wings designed to generate as uniform a distribution of  $C_L$ s as possible have a serious side effect: stall. Theoretically, if such a wing uses an identical airfoil (ignoring the viscous effects), every spanwise station stalls at the same instant. In real airplanes this causes the wing to roll to one side or the other, depending on factors like yaw angle, propeller rotation, deviations from the ideal loft, and others. A wing roll-off at stall can initiate a spin – a very dangerous scenario if the airplane is close to the ground, such as when maneuvering (banking) to establish final approach before landing. For this reason, some of the efficiency must be sacrificed for added safety in the handling the airplane, using techniques such as wing washout, dissimilar airfoils, discontinuous leading edges, and many others.

It turns out that there actually is a wing planform that, at least in theory, achieves the ideal lift distribution; the

elliptic planform (see Section 9.4.4, *Elliptic planforms*). The planform will generate section lift coefficients that are uniform along the entire span (see Figure 9-25). Unfortunately, as always, there is a catch – a very serious catch. The uniform distribution achieved by the elliptic planform is great for cruise, but awful near stall. As the elliptic planform reaches higher and higher *AOA*, the wing will stall fully – instantly, rather than progressing gradually from the inboard to the outboard wing, something that helps to maintain roll stability. This means that if there are manufacturing discrepancies – and there always are manufacturing discrepancies – the left or right wing may stall suddenly before the opposite wing. The consequence is a powerful wing roll to the left or right. This tendency can be remedied by a decisive wing washout; however, the resulting distribution of section lift coefficients will no longer be uniform. It is also possible to help stall progression with stall strips; however, whatever the remedy, the project will possibly be hampered by a troublesome stall improvement development during flight testing.

Another important observation can also be made from Figure 9-25. This is the difference between the distribution of section lift coefficients and that of lift force. While the distribution of section lift coefficients is a very important indicator of stall tendency and induced drag coefficient, the lift force distribution is imperative for structural reasons. The vertical shear force can be determined by integrating the distributed lift force along the span. Bending moments are obtained by integrating the shear along the span. With this in mind, the right graph of Figure 9-14 effectively shows how low taper ratio reduces the wing bending moments by moving the center of the lift inboard. For this reason tapered wings are essential to help reduce structural weight.

All the following images assume the leading edge faces up and the trailing edge down, and simple expressions of wing area and *AR* are provided for convenience. Always be mindful of the difference in Reynolds numbers for tapered wing planform shapes (root  $R_e$  is different from tip  $R_e$ ). This comparison is implemented

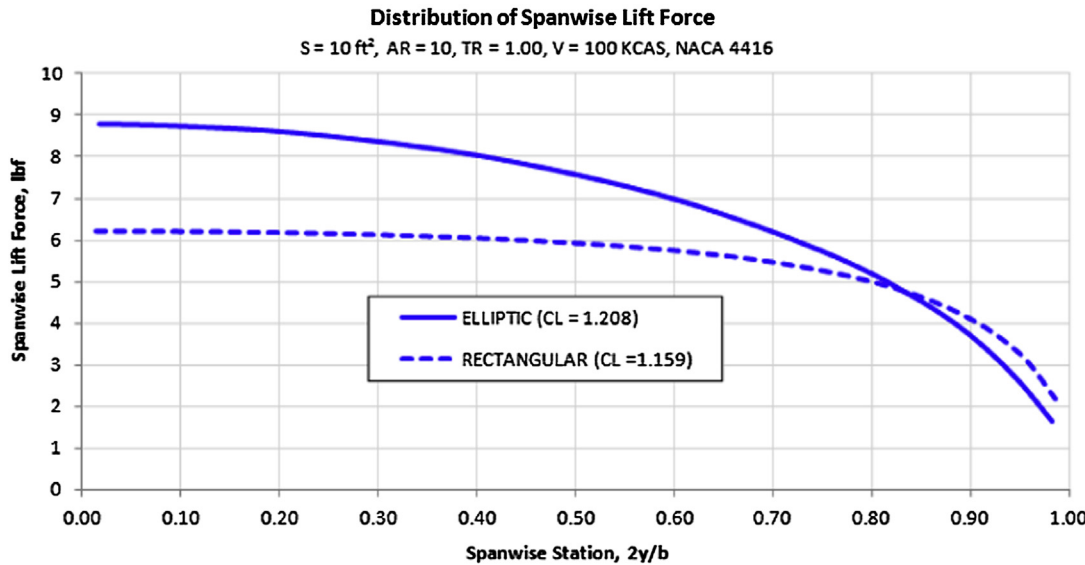


FIGURE 9-26 Comparison of spanwise force generated by a rectangular and elliptic planforms.

via the vortex-lattice method (VLM) using the commercially available code SURFACES [10]. All the models have 720 panels and are aligned along the camber line of the NACA 4416 airfoil.

#### 9.4.2 Methods to Present Spanwise Lift Distribution

The lift distribution is usually presented in three forms: force distribution, section lift distribution, and a distribution of the fraction of section lift coefficients to the total lift coefficient generated by the wing. All have their advantages and shortcomings. These are compared

in Figure 9-26, Figure 9-27, and Figure 9-28 using the rectangular and elliptic wing planform shapes of the previous section.

Figure 9-26 shows the distribution of lift as a force along the span. The area under the graph is the shear force along the span and, assuming a cantilevered wing, the progression of integration from tip inboard to root will provide the shear diagram. Then, integrating the shear diagram from tip to root will generate the moment diagram. Note that sometimes this graph is presented using the physical dimensions of the wingspan (e.g.  $b = 35$  ft or similar). In this case, the units for the  $y$ -axis of the graph are more correctly represented as

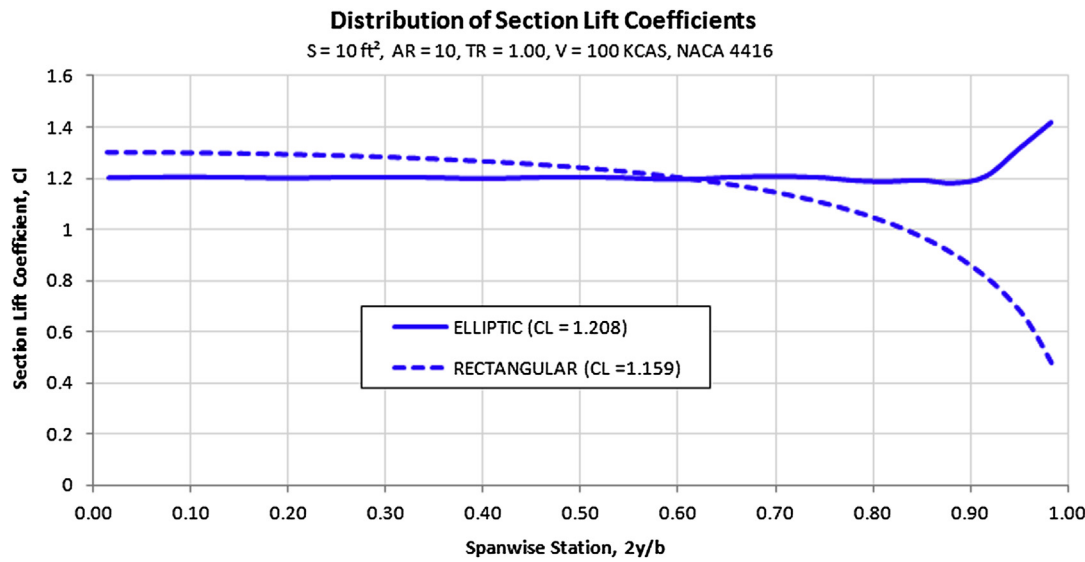


FIGURE 9-27 Comparison of section lift coefficient.

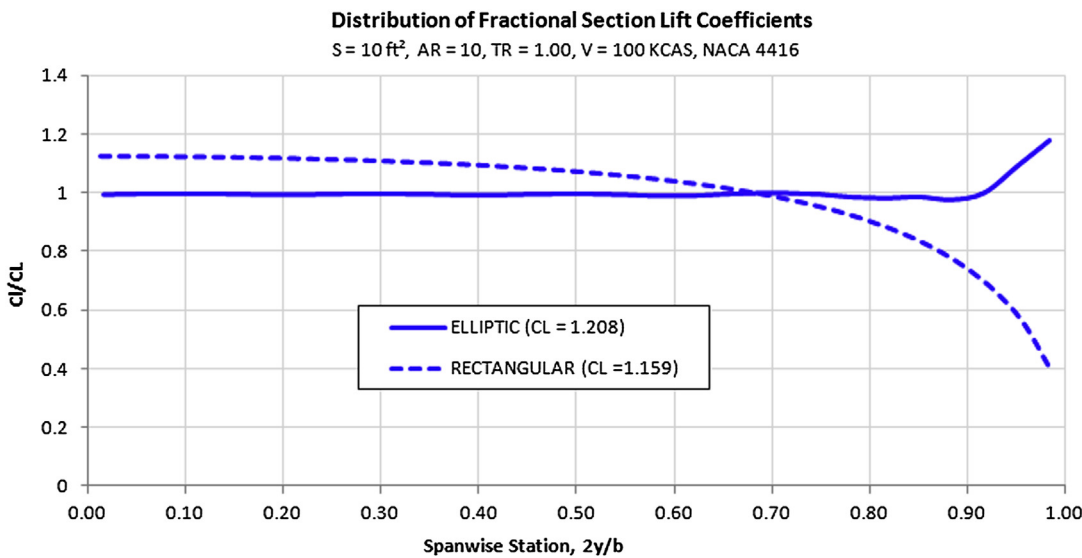


FIGURE 9-28 Comparison of fractional section lift coefficient.

$\text{lb}_f/\text{ft}$  (assuming the UK system is being used). Another important observation is the difference in the force generated by the elliptical wing planform when compared to the rectangular form.

Figure 9-27 shows the distribution of section lift coefficients along the span. The advantage of this presentation is that it can be used to evaluate the magnitude of geometric (or aerodynamic) twist required to help control stall progression or even bending moments. Since an airfoil will stall at a specific two-dimensional lift coefficient and this format presents the current two-dimensional lift coefficient (i.e. the section lift coefficient) this can be used to design good stall characteristics into the airplane (see Section 9.6.4, *Tailoring the stall progression*).

Figure 9-28 shows the distribution of the contribution of the section lift coefficient to the total lift generated by the geometry. It helps demonstrate regions that contribute a lot or little to the overall lift.

#### 9.4.3 Constant-chord (“Hershey-bar”) Planform

Nicknamed for its simple constant-width geometry, this planform is widely used for many different kinds of aircraft, small and large. Light planes that feature Hershey-bar wings include the Beech Model 77 Skipper, Piper PA-38 Tomahawk, Piper PA-28 Cherokee, and Piper J-3 Cub. Among larger aircraft are the de Havilland of Canada DHC-6 Twin Otter and the Shorts 360.

The distribution of spanwise section lift coefficients,  $C_l$ , for a Hershey-bar wing is shown in Figure 9-29. This is done for two  $AOAs$ ;  $0^\circ$  and  $10^\circ$ . For comparison purposes, the latter curve will be superimposed on all subsequent planform shapes so the reader can get a quick glimpse of how the lift distribution of other wing planform shapes differs from that of the constant-chord wing.

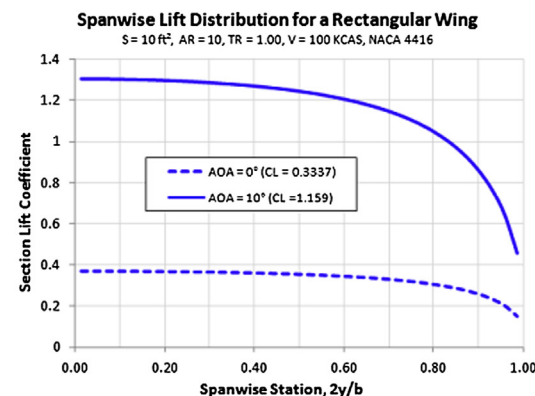
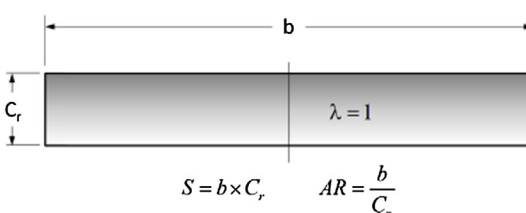


FIGURE 9-29 Basic geometry and lifting characteristics of the *constant-chord* wing planform.

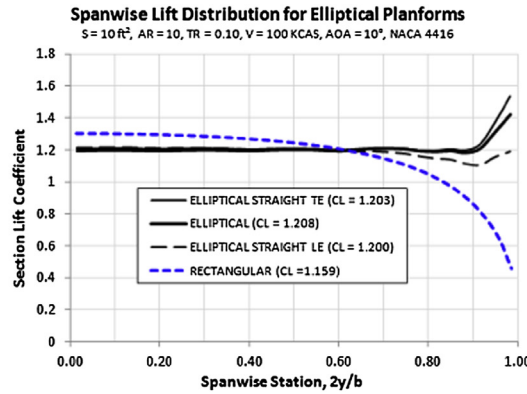
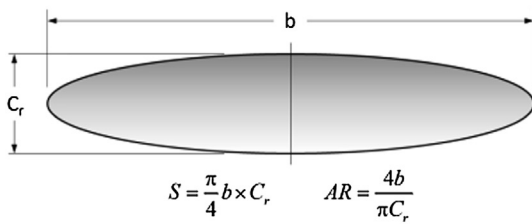


FIGURE 9-30 Basic geometry and lifting characteristics of the *elliptical* wing planform.

### Pros

The configuration has two primary advantages. The first is forgiving stall characteristics, attributed to the reduction in section lift coefficients toward the wingtip (see Figure 9-29). This promotes a very favorable stall progression (growth of flow separation) that begins at the root and moves outboard to the tip, rendering it the last part of the wing to stall. This effect is very desirable as it gives the configuration important roll stability at stall.

The other important advantage is the lower manufacturing costs because all ribs have the same basic geometry and the spar is a constant-thickness beam. This simplicity affects not only the wing ribs and spar, but also the control surfaces.

This configuration is ideal for trainer aircraft or airplanes for which manufacturing cost is imperative.

### Cons

Since the wingtip contributes less to the lift generation than the root (in terms of section lift coefficients), the planform is particularly inefficient. For this reason, the planform should never be used for efficient aircraft, such as sailplanes or long-range aircraft. This includes wings and stabilizing surfaces.

#### 9.4.4 Elliptic Planforms

The elliptical wing planform (see Figure 9-30) is most famous for its use in one of the most formidable fighters

of the Second World War, the British Supermarine Spitfire. Other aircraft that feature this configuration include: the American Republic P-47 Thunderbolt; and the German Heinkel He-70 He-112B, Mudry CAP-10, and CAP-20. Interestingly, the aerodynamic properties of the planform are widely publicized, even among some laypeople.

The planform shown in Figure 9-30 is a pure ellipse, which means that a straight line extending from tip-to-tip is located at the 50% chord. However, there is no requirement that an elliptic planform has to comply with that geometry. For instance, it would be structurally practical to design it so the quarter-chord was a straight line. This would simplify the design by allowing a straight main spar (albeit with a curved spar height) to be positioned at the quarter-chord.

Elliptical planforms with a straight leading edge or trailing edge (see Figure 9-31) are common on radio-controlled aircraft and sailplanes and are sometimes referred to as crescent-shaped wings. The graph of Figure 9-31 shows that, fundamentally, the distribution of section lift coefficients for the three planform shapes is the same, except at the tip. While all three planform shapes generate a similar total  $C_L$  at 10°, the one with the straight LE generates a lower section lift coefficient at the tip than the others, implying a less severe washout is required to improve stall characteristics. However, one must be careful in the interpretation of such linear curves because the sharp tip introduces important viscous effects at higher AOAs that render the linear

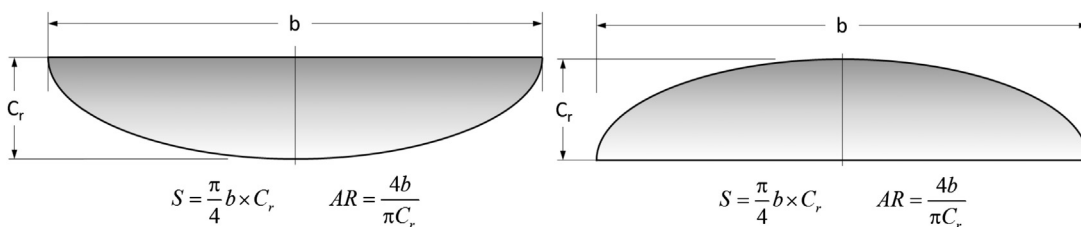


FIGURE 9-31 Basic geometry of *elliptical* planform with a *straight LE and TE*.

predictions invalid. These are discussed in Section 9.6.3, *Deviation from generic stall patterns*.

### Pros

Its primary advantage is the uniform distribution of section lift coefficients (see Figure 9-30). This distribution makes the planform very efficient when it comes to utilizing the entire span and results in the least amount of lift-induced drag of any planform.

### Cons

The planform's greatest drawback is its producibility, which is severely impaired by the complex compound surfaces. It is very difficult to manufacture using aluminum, as this would call for sheets to be stretched through hydroforming (or similar). However, it is much easier to produce using modern composites.

Another serious drawback is that the section lift coefficients are mostly uniform along the span, which causes the entire wing to stall at once (again assuming a constant airfoil and no washout). This can pose a serious problem for low-speed (or high AOA) operations and requires a decisive washout or airfoil selection to remedy.

### 9.4.5 Straight Tapered Planforms

A straight tapered wing planform is one for which the root chord is different from the tip chord, such that the smaller chord resides inside two lines that are perpendicular to the plane of symmetry and that are drawn at the LE and TE of the larger chord (see Figure 9-32).

Some authors define straight wings as those that have zero sweep on any spanwise line between 25% and 70% chord. The drawback with that definition is that it excludes common GA aircraft that feature a straight LE or TE.<sup>2</sup>

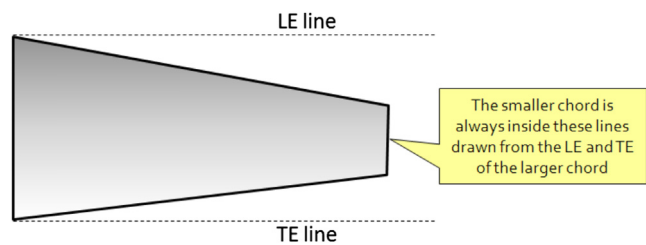
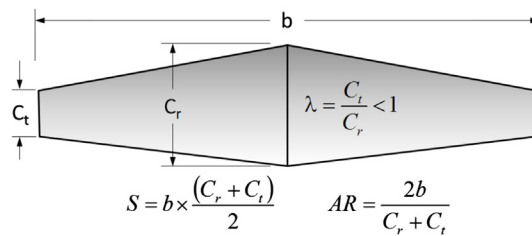


FIGURE 9-32 Definition of a straight tapered wing planform.

The list of airplane types that use this wing planform shape is very long. A generic tapered planform and its spanwise distribution of section lift coefficient is shown in Figure 9-33.

### Pros

The primary advantage of tapered wings is reduction in bending moments and lift-induced drag. Straight tapered wings offer improved efficiency over the Hershey-bar wing as the section lift coefficients are higher toward the tip. Consequently, the wingtips contribute more to the total lift coefficient. This, combined with the relative geometric simplicity of the linear taper, which is easier to manufacture than the elliptical planform, renders the planform ideal for most airplanes. The improved efficiency of the configuration usually warrants the increased production complications.

### Cons

The taper compromises the stall characteristics and requires a geometric or aerodynamic wing washout, or a combination of both, to be employed. An additional solution might be to select an airfoil for the tip that has a higher stall AOA than the root. It is common to locate root and tip airfoils such that their quarter-chords are on a line perpendicular to the plane of symmetry.

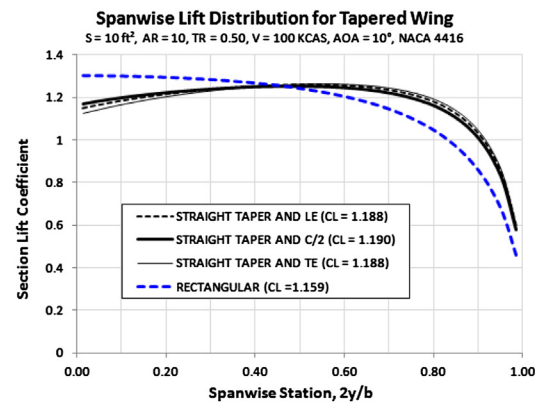


FIGURE 9-33 Basic geometry and lifting characteristics of *straight tapered* wing planforms.

<sup>2</sup>For example, it excludes a great many aircraft; a family of Zlin and Mooney aircraft, to name a few.

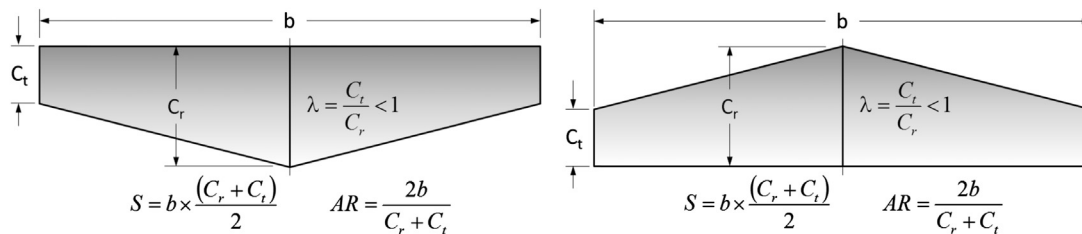


FIGURE 9-34 Basic geometry of the *straight-LE tapered* wing planform.

This allows a straight main spar to be placed at the quarter-chord of the wing, but this is an effective location as it results in good structural depth that provides the potential for reasonably large fuel tanks behind the spar. The configuration causes manufacturing complications due to the different geometry of each rib.

### **Straight Leading or Trailing Edges**

Other airplanes feature straight tapered wings whose leading or trailing edge is perpendicular to the plane of symmetry (see Figure 9-34). This means that a spanwise line going through the quarter-chord of the root and tip is swept forward or back.

#### **Pros**

Improved structural and aerodynamic efficiency over the constant-chord configuration. The straight LE planform may be advantageous if it is foreseen that the operational CG will be too far forward. The opposite holds for an operational CG that turns out to be too far aft.

#### **Cons**

It is a drawback that if the wing features a spar that is perpendicular to the plane of symmetry and extends from tip to tip, its caps will be curved. This can be eliminated by sweeping the spar forward, which makes the use of a single-piece spar more challenging.

The hinge line of control surfaces can have a significant forward sweep, which makes them less efficient aerodynamically and can complicate the design of the control system. Among a number of examples of aircraft that feature the straight LE are the Arado Ar-79, Cessna 177 Cardinal, Commonwealth Ca-12 Boomerang, and Fairey Barracuda, and a series of Mooney aircraft feature the planform shape for both the wing and stabilizing surfaces.

On the Mooney aircraft, the straight LE of the horizontal and vertical tails arguably renders them more efficient aerodynamically than the more popular aft-swept tails and, in theory, this allows the tail be a tad smaller, with less wetted area. This is an argument often heard among laypeople. However, an investigation reveals this is not true. Some of that efficiency is simply lost in lowered control authority of the less

effective control surfaces whose hinge lines are inevitably swept forward. Of course, the same argument can be made for aft-swept stabilizers – they also have hinge lines that are swept aft. The difference is that the aft sweep adds arm that makes up for the loss in aerodynamic efficiency. A VLM analysis of the Mooney M-20R revealed that its directional stability derivative,  $C_{n\beta}$ , is in the range of 0.054 per radian. Introducing a 45° aft sweep in the LE of the VT (no change in surface or wetted area and root chord precisely the same place) increased it to 0.060 per radian, directly contradicting any claims of greater effectiveness of the straight LE tail. This simply means that the reduction in  $C_{L\alpha}$  of the VT reduces less than the tail arm increases. The important point is that in the case of the Mooney, the tail is a signature feature for the brand. One can always recognize a Mooney tail and for the brand this is important. But more effective it is not.

Another version of the straight tapered wing is the straight trailing edge planform in Figure 9-34. Many of the same arguments for or against hold for this planform. It is featured on a number of aircraft, among others the Aermacchi MB-326 and MB-339, Bücker Bü-180 Student, Zlin Z-526, 726, and Z-26.

### **The Compound Tapered Planform**

The compound tapered wing planform consists of two tapered sections; the inboard section is an inverse taper and the outboard section has standard taper (see Figure 9-35). The lift distribution for this planform is also shown. It can be seen that section lift coefficients peak inboard, indicating this is where stall would initiate. This is significantly reduced midspan and then increases toward the tip. The analysis indicates the planform is not particularly efficient although the discontinuity at the leading edge may provide some viscous benefits. Among well-known aircraft featuring this planform is the Westland Lysander, a British single-engine observation aircraft with short take-off and landing (STOL) designed in the 1930s. The reason for this choice was pilot visibility – its STOL capability can be attributed to the high-lift system it was equipped with and not the planform itself.

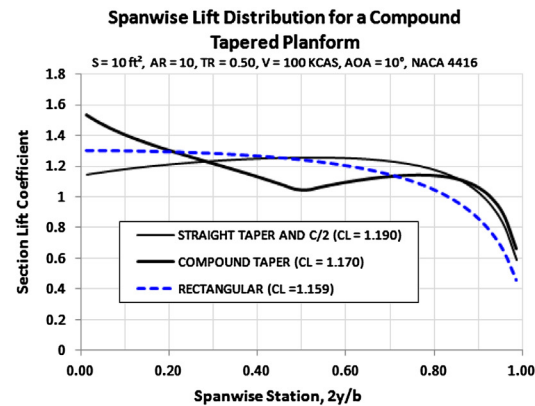
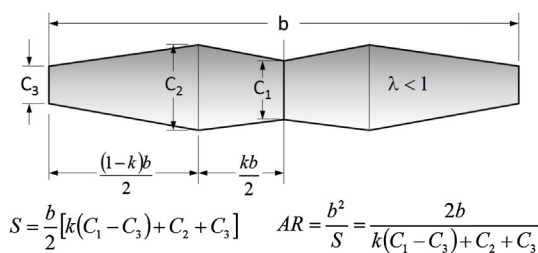


FIGURE 9-35 Basic geometry and lifting characteristics of the *compound tapered* wing planform.

#### 9.4.6 Swept Planforms

Like the tapered wing planform, the swept planform is one of the most common types of geometry found in aviation. Practically all commercial aircraft use swept wings, and even aircraft that operate at low subsonic speeds commonly use the planform shape for their stabilizing surfaces. For this reason, this geometry must be elaborated on in some detail.

##### **The Aft-swept Planform**

The invention of the planform is generally thought to date back to the 1930s. However, it was not possible without the work of scientists who preceded the era. Meier [11] takes this history back to Isaac Newton (1643–1727), Pierre-Simon, Marquis de Laplace (1749–1827), Ernst Mach (1838–1916), and many others, up to Adolf Busemann (1901–1986), who is generally credited with the invention of the swept-back wing. Busemann belonged to a group of very famous German scientists who were led by Ludwig Prandtl (1875–1953). The best known were Theodore von Kármán (1881–1963), Max M. Munk (1890–1986), and Jakob Ackeret (1898–1981) [12]. The result of Busemann's work was first published at the 5th Volta conference in Rome in 1935 [13]. The Volta conference was an annual conference of physics, mathematics, history, and philosophy, named to honor the great Italian physicist Alessandro Volta (1745–1827). In the USA, Robert T. Jones tested swept-back wings toward the end of 1944. It was the first such work in the USA. It was published in 1945 in NACA TR-863 [14]. In it, Jones cites Busemann's research from 1935 as one of his references.

##### **Pros**

One of the primary advantages of the configuration is that when used with high-speed aircraft, it delays the

formation of shockwaves to a higher Mach number (see Section 9.3.3, *Leading edge and quarter chord sweep Angles,  $\Lambda_{LE}$  and  $\Lambda_{C/4}$* ).

The aft-swept configuration is less susceptible to flutter than either the straight or the forward-swept configurations. This results from the tendency of a positive (vertical upward) lift force to reduce the *AOA* of the tip through aeroelastic effects.

The aft-swept (or forward-swept) configuration is also a possible solution when the CG is expected to end up too far aft or forward on a proposed configuration. The Messerschmitt Me-262 Schwalbe was the first jet aircraft to feature a swept-back wing. However, the modest sweep angle of 18.5° was insufficient to greatly impact divergence drag number and was a consequence of its Junkers Jumo jet engines being heavier than expected. For this reason its originally straight wings were swept aft to solve an issue with the location of its center of gravity [15].

##### **Cons**

Among drawbacks is the deterioration of airflow close to the tip of the planform with an increase in *AOA*. The reason for this deterioration is explained in Section 9.6.5, *Cause of spanwise flow for a swept-back wing planform*. Two important consequences of this phenomenon is a powerful nose pitch-up moment that develops as the *AOA* approaches stall and an accompanying deterioration in roll stability and aileron effectiveness.

Since the center of lift is positioned behind the wing root attachment there is an increase in wing torsion, often substantial, that increases the weight of the airframe.

The configuration is more susceptible to control reversal as a result of the tendency of the lift force to reduce the *AOA* of the tip through aeroelastic effects. The same effect moves the center of lift forward with *AOA* if the wing is flexible and regardless of flexibility

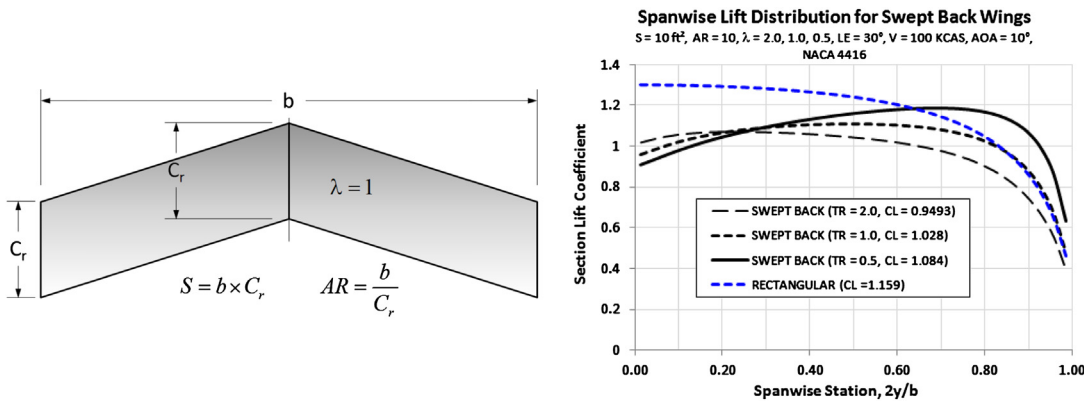


FIGURE 9-36 Basic geometry of the constant-chord swept-back wing planform.

when the wing stalls. It is the cause of the powerful and dangerous nose pitch-up moment at stall.

Aircraft with swept wings often experience issues with the wing fuel tanks. For instance, as the airplane rotates to take-off and begins to climb, fuel will flow toward the outboard and aft side of the tank. This may cause the CG to shift aft. This is solved using so-called *baffle check valves*, which are one-way flapper valves that allow fuel only to flow inboard [16]. Large transport aircraft, some carrying as much as 40% of their gross weight in fuel, can experience large changes in CG location as fuel is consumed. This often calls for a computer-controlled fuel management system that monitors and controls how fuel from the wing tanks is used.

In order to understand the advantages and disadvantages of the swept aft configuration, it is helpful to break it down depending on taper ratio,  $\lambda$ . This way it is possible to consider three classes;  $\lambda < 1$ ,  $\lambda = 1$ ,  $\lambda > 1$  (see Figure 9-36 and Figure 9-37). Most aircraft with aft-swept wings fall into the first category. In fact, there are so many different types of aircraft in this class that it would be unfair to name any particular one. Almost all high-speed military and passenger transport aircraft feature the configuration. These are particularly easy to locate.

The other two classes contain considerably fewer members. When it comes to the second class, for which  $\lambda = 1$ , there is a handful of examples. In current times, the Boeing B-2 Spirit is probably the best known.

However, there are others. Among those are the Dunne Monoplane and Biplane, designed in the 1910s by John W. Dunne (1875–1949). The English Electric Lightning, MiG-8 Outcka, MiG I-320, MiG-17, Sukhoi Su-15P, and Yakovlev Yak-25 (Flashlight) have a  $\lambda$  close to 1. And in the third category, the Republic XF-91 Thunderceptor is the only contender. Designed with the tip chord larger than the root chord, the idea was to reduce the section lift coefficients at the tip in order to improve low-speed handling.

### **The Forward-swept Planform**

One of the aerodynamic advantages of the forward-swept wing can be seen in Figure 9-38: the reduced section lift coefficients at the tip. The distribution ensures the inboard wing stalls first and gives the configuration great roll stability at stall (remember this also means while pulling high  $g$ s), making it almost impossible to tip stall. The reduced tip loading also means that the ailerons retain far more authority at high AOA than on an aft-swept configuration. This improves controllability during critical phases of the flight, such as during landing. The shape of the lift distribution places the center of lift closer to the plane of symmetry, reducing bending moments (although it does not prevent divergent torsional tendency). Additionally, spanwise flow is directed inboard rather than outboard, where the fuselage more or less acts like an endplate or a fence that prevents early separation.

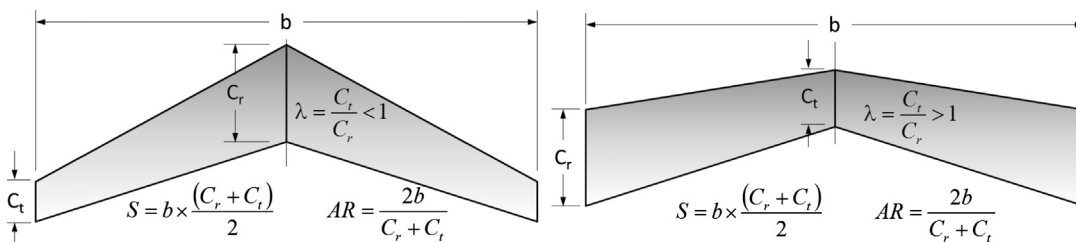


FIGURE 9-37 Basic geometry of the tapered and inverse tapered swept-back wing planform.

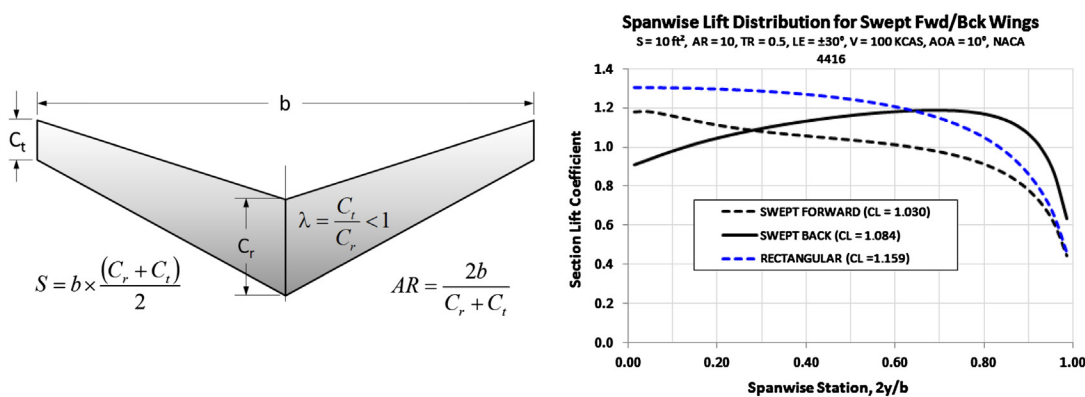


FIGURE 9-38 Basic geometry and basic lifting characteristics of the forward-swept wing, compared to the constant-chord and the tapered swept-back planform shapes.

The primary disadvantage of the geometry is divergent aeroelastic deformation. As the  $AOA$  of the wing is increased, the elastic torsional deformation twists the wing, increasing the  $AOA$  further. Forward-swept wings must be especially reinforced to keep the divergent deformation to a minimum, inevitably increasing their weight.

The first major development of a forward-swept wing configuration was the German Junker Ju-287. An interesting discussion of its development is given in Ref. [11]. The configuration has been used in a few other designs, including the Grumman X-29, the HFB-340 Hansajet, and the Sukhoi Su-47. A modest forward sweep is relatively common, for instance in sailplanes and a number of GA aircraft. However, it is almost always a solution to a CG problem and not for compressibility fixes.

### Variable Sweep Planform

The variable sweep planform (see schematic in Figure 9-39) dates back to the German Messerschmitt P.1101, whose incomplete prototype was discovered at

the end of WWII. It featured a swiveling wing design whose sweep angle was to be selected and set manually before each flight. Later, this innovative design led to fighter and bomber models, such as the General Dynamics F-111, Grumman F-14, Sukhoi Su-17, Panavia Tornado, and others. The configuration is not used in any GA aircraft, as it inevitably leads to a heavier airframe, control system complexity, and other complications. It is really a configuration suited for supersonic aircraft, where it solves problems at the high- and low-speed extremes of the flight envelope. It is included here for the sake of completion.

### 9.4.7 Cranked Planforms

The term "cranked" refers to a break in the leading or trailing edge of a wing that changes the leading (or trailing) edge sweep angle. It turns out that such planform shapes are surprisingly common – for instance a large number of Cessna single-engine aircraft feature cranked wings, as do other popular aircraft such as the Piper PA-28 Cherokee Archer or the Beechcraft Bonanza.

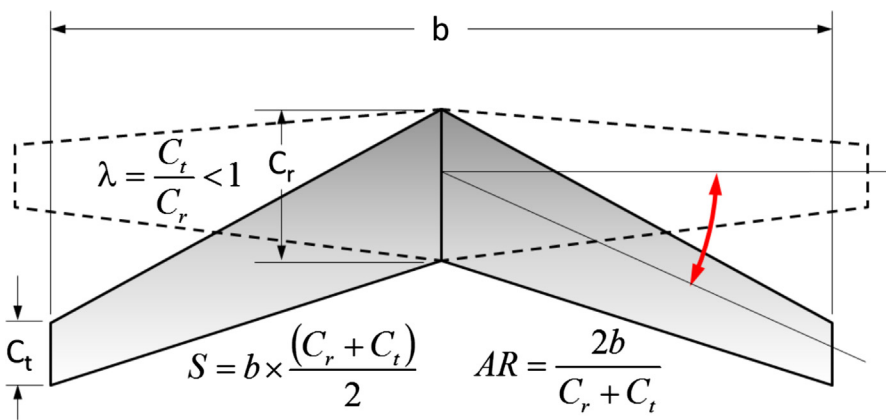
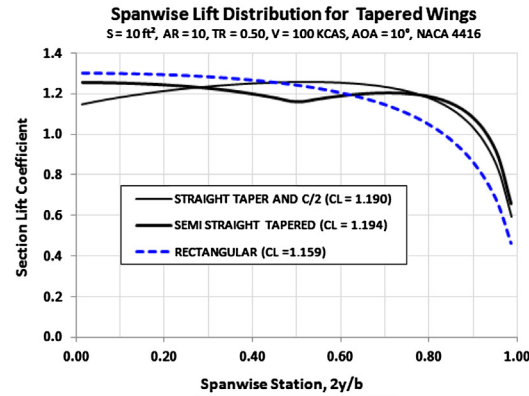
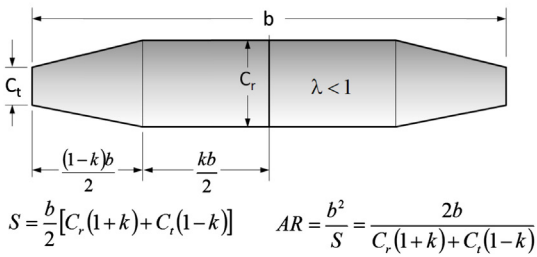


FIGURE 9-39 Basic geometry of the variable sweep wing planform.



**FIGURE 9-40** Basic geometry and lifting characteristics of the *semi-tapered* wing, compared to the constant-chord and the tapered swept-back planform.

Although included in a separate class, the double delta configuration is also technically a cranked planform. In fact, any aircraft that features a leading edge extension falls into this category. However, by convention, double deltas are considered a member of delta wings. Regardless, this class is inclusive and includes a number of wing planform shapes that otherwise might be considered unrelated.

### Semi-tapered Planform

The semi-tapered planform is one that has a constant-chord inboard section and a tapered outboard section (see Figure 9-40). The planform increases the section lift coefficients on the outboard wing and improves its efficiency over that of the Hershey-bar wing. A side benefit of this is improvement in aileron effectiveness. The drawback is the added complexity of construction, and reduction in the aileron effectiveness if its hingeline becomes highly swept.

The configuration is best known on a family of single-engine Cessna aircraft: the 150, 152, 172, 182, 206, and many others. It is also used on a number of Piper PA-28 Warrior and Cherokee Archer aircraft.

### Crescent Planform

The *crescent* wing planform (Figure 9-41) has seen very limited use. It is best known for its use on the British Handley-Page Victor, where the highly swept inboard section of the wing allowed the use of a thick airfoil without introducing early shock formation at high Mach numbers. The thick airfoil was needed to accommodate its four jet engines, which were buried in the wing root. The wing of the Victor varied in quarter-chord sweep and thickness, progressively from 22° and 4% *t/c* at the tip to 53° and 16% at the root. This allowed a constant  $M_{crit}$  to be maintained along the wing and resulted in more efficient reaction of bending moments. A consequence of this geometry was improved aileron control authority and reduced tendency for tip stall and subsequent nose pitch-up.

### Schuemann Planform

The Schuemann planform shape has already been thoroughly introduced in the Appendix C1.5.2, *The Schuemann wing*. It is featured on a number of sailplanes, for instance, the Stemme S-10 and the DG-1000. The wing style has also been introduced on commuter

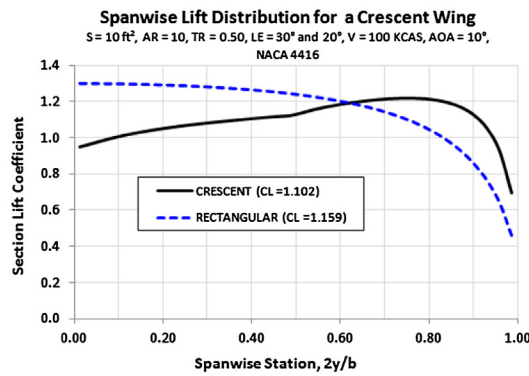
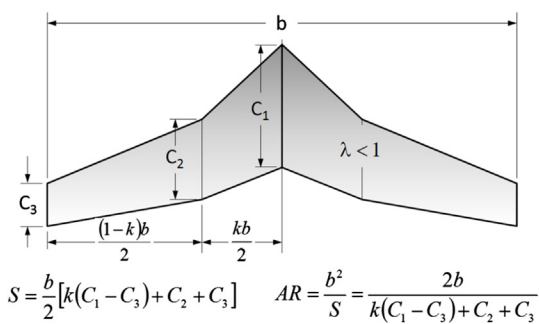


**FIGURE 9-41** Basic geometry of the *crescent* wing planform.

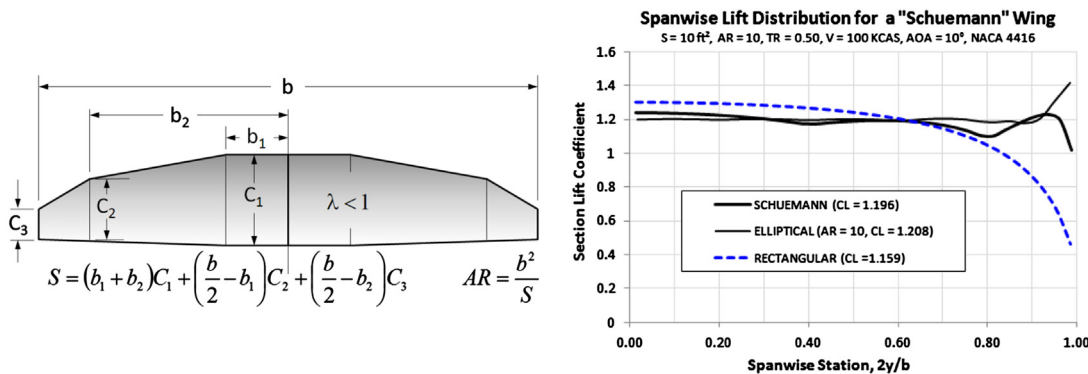


FIGURE 9-42 Basic geometry and lifting characteristics of the Schuemann wing planform.

aircraft such as the Dornier Do-228, Dornier 328, and Fairchild-Dornier 328JET.

Figure 9-42 shows the fundamental dimensions of the planform shape and the distribution of the section lift coefficients compared to those of a Hershey-bar and elliptical planform shapes. It can be seen that the distribution approximates that of the elliptical planform, leading to a reduction in lift-induced drag. This explains the wing's popularity for sailplanes. The figure also reveals that a potential problem with the wing is an early wing tip stall, not unlike the elliptical wing and is caused by the sharp outboard taper. This is of course complicated by viscous effects at the wingtip, as highly swept wingtips may position the tip vortex so it suppresses early tip stall tendency, not unlike delta wings. Sailplane wingtips at a high  $AOA$  will flex substantially due to aeroelastic effects. This effectively unloads the wingtip and loads up the center portion of the wing, which then stalls before the wingtip. For this reason, sailplanes usually have good

stall characteristics. A short and stiff wing, likelier to be used for a GA aircraft, will not flex nearly as much as the high  $AR$  wing and should thus be expected to feature decisive wing washout at the tip, unless the tip segment of the wing features a high enough sweep.

#### 9.4.8 Delta Planforms

##### The Delta Planform Shape<sup>3</sup>

A discussion of the pros and cons of delta wings (see schematic in Figure 9-43) is given in Appendix C1.5.5, *The delta wing*, and will not be elaborated on here, other than that they are planform shapes intended for high-subsonic or supersonic aircraft and not low-subsonic airplanes. Even though it is certainly possible to use delta wings for low-speed airplanes (as evident by the Dyke Delta) it is a choice that is hard to justify for reasons other than fun flying; with reduced storage space (thanks to a short wingspan), being another drawback.

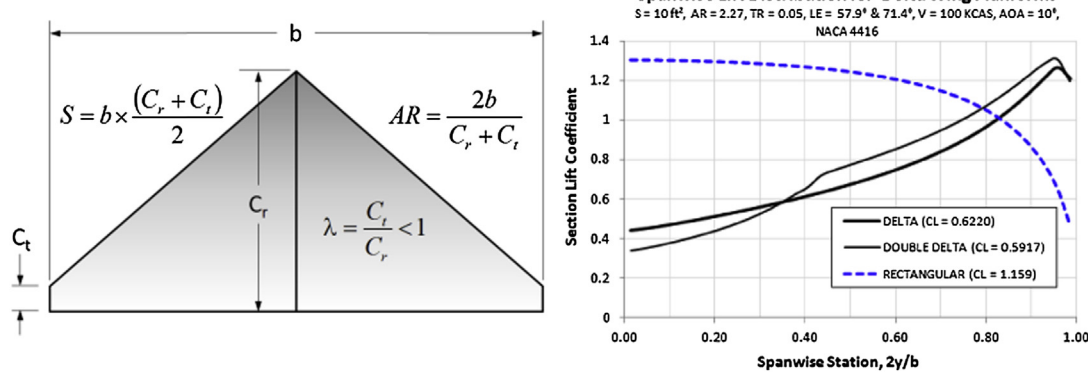


FIGURE 9-43 Basic geometry and lifting characteristics of the delta wing planform. Note that the results for the lift distribution are erroneous at the given  $AOA$ , as they do not reflect change in lift due to vortex lift.

<sup>3</sup>Note that the linear vortex-lattice method does not predict the viscous phenomenon of the leading edge vortex system experienced by delta wings that would already have begun to form at the  $AOA$  of  $10^\circ$ . The LE vortex would affect both the  $C_L$  and the lift distribution.

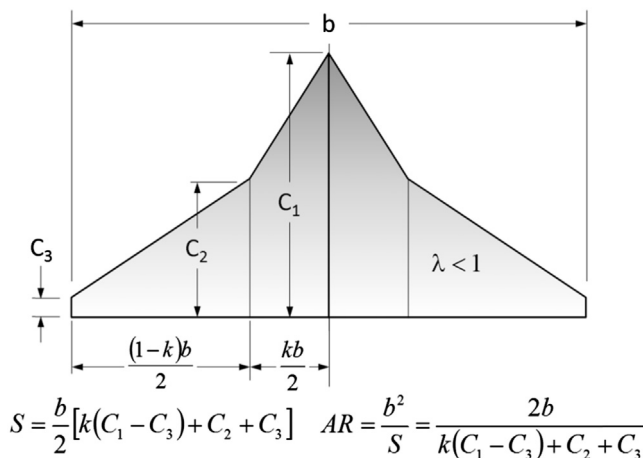


FIGURE 9-44 Basic geometry of the *double delta* wing planform.

Deltas stall at very high angles of attack and generate low  $C_{L\max}$  compared to straight un-swept wings; they will therefore require high approach speed and deck angles. As an example, the 2000 lb<sub>f</sub> Dyke JD-2 Delta reportedly stalls at about 61–65 KCAS [17]. This means that the 173 ft<sup>2</sup> wing area generates a  $C_{L\max}$  around 0.8–0.9. That is 50–65% less than conventional straight wings. They also have poor  $LD_{\max}$ , which is of concern for engine-out emergencies. The best-known aircraft that uses the configuration is the Dassault Mirage III and its various derivative aircraft (e.g. Mirage IV, 2000, Rafale).

#### The Double-delta Planform Shape

The double delta (see Figure 9-44) is also known as the *compound delta*. They have an advantage over conventional delta wings in that they produce a vortex pair, rather than a single vortex over each wing that mutually interfere with each other. The resulting system increases the lift of the double delta over that of the conventional delta, rendering supersonic fighter aircraft far

more maneuverable [18]. When it comes to subsonic aircraft, the configuration suffers from similar limitations to the single delta. The configuration has been used on military aircraft like the SAAB J-35 Draken and General Dynamics F-16E cranked arrow.

#### 9.4.9 Some Exotic Planform Shapes

##### *Disc- or Circular-shaped Planform*

In short, the disc-shaped planform (see Figure 9-45) is something no self-respecting aircraft designer should propose as a primary lifting surface. Perhaps inspired by the fad of UFO sightings in the 1950s, the well-respected but long-defunct Avro Canada Ltd, a company that at one time employed some 50,000 people, dared to develop the AVRO Canada VZ-9A, nicknamed the AVRO car. A secret military project, the Avrocar employed the Coandă effect to generate lift and thrust. The project was cancelled in 1961 when it became clear that insufficient thrust and stability issues would hamper its success.

Figure 9-45 shows a comparison of spanwise lift distribution between the disc planform and an elliptical and a Hershey-bar wing. In spite of the uniform distribution of section lift coefficients, the graph clearly shows how inefficient this planform shape is when compared to the Hershey-bar or elliptical wings; it barely ekes out one-third of the lift at the selected AOA (10°). From an efficiency standpoint, the disc-shaped wing is simply beyond objectionable. However, it is presented here as it is an ideal shape for a radar disc of the kind installed on a reconnaissance or early warning and control system (AWACS) military aircraft such as the Boeing E-3 Sentry (a modified Boeing 707) or Grumman E-2 Hawkeye. For such applications a shallow lift curve slope is essential for stability and control reasons.

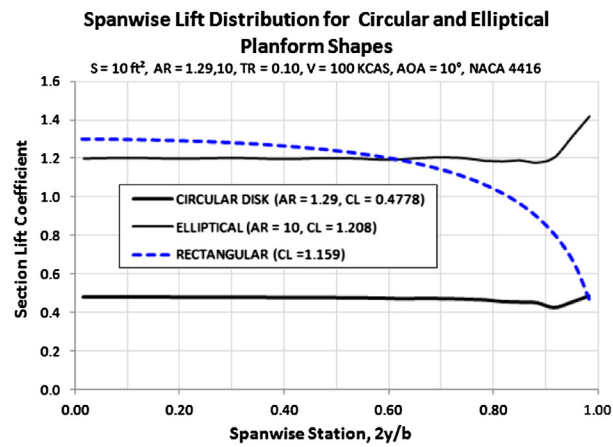
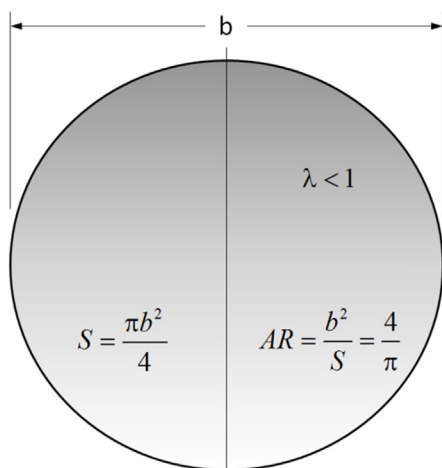


FIGURE 9-45 Basic geometry and lifting characteristics of the *disc* or *circular* wing planform.

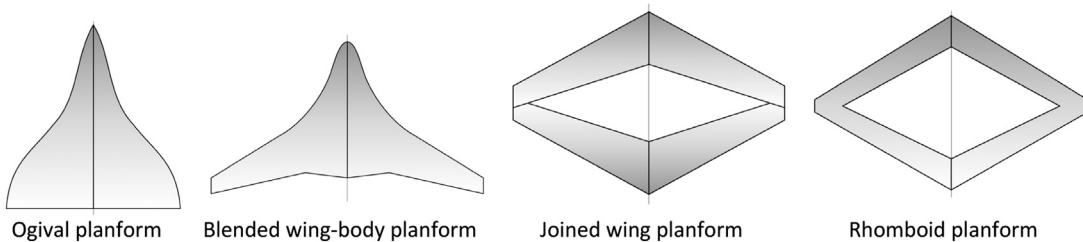


FIGURE 9-46 Selected unorthodox wing planform shapes.

### Other Configurations

Four other configurations are shown in Figure 9-46: an ogival, joined wing, blended wing-body, and a rhomboid planform. Lift distribution curves for these shapes will not be presented here, since these planform shapes are highly specialized or experimental.

## 9.5 LIFT AND MOMENT CHARACTERISTICS OF A 3D WING

As has already been thoroughly discussed, lift, drag, and pitching moment are almost always converted into a dimensionless coefficient form as this allows transferability (see Equation [8-8]). The lift, drag, and pitching moment coefficients are defined as shown below (note the capitalization of the forces and moments for the three-dimensional object):

$$\begin{aligned} L &= \frac{1}{2}\rho V^2 \cdot S \cdot C_L \\ D &= \frac{1}{2}\rho V^2 \cdot S \cdot C_D \\ M &= \frac{1}{2}\rho V^2 \cdot S \cdot c \cdot C_M \end{aligned} \quad (9-47)$$

where the variables have already been defined elsewhere (e.g. see Variables at the end of this chapter).

In this section, the three-dimensional lift and moment characteristics of the wing will be evaluated, whereas drag is treated in Chapter 15, *Aircraft drag analysis*. Here, a number of important characteristics will be discussed, including construction of the three-dimensional lift curve, estimation of span efficiency and the maximum three-dimensional lift coefficient, stall behavior, tailoring of stall characteristics, and others.

### 9.5.1 Properties of the Three-dimensional Lift Curve

Figure 9-47 shows a typical three-dimensional lift curve. Overall, the curve displays identical characteristics to that of the two-dimensional curve of Section 8.1.4, *Properties of typical airfoils*, except it represents the behavior of the entire aircraft (wings, fuselage, HT, etc.). The contribution of the individual components of the aircraft to the overall non-linear shape of the curve may make it very different from that of the selected airfoils. As before, the aircraft designer is most interested in the following characteristics:

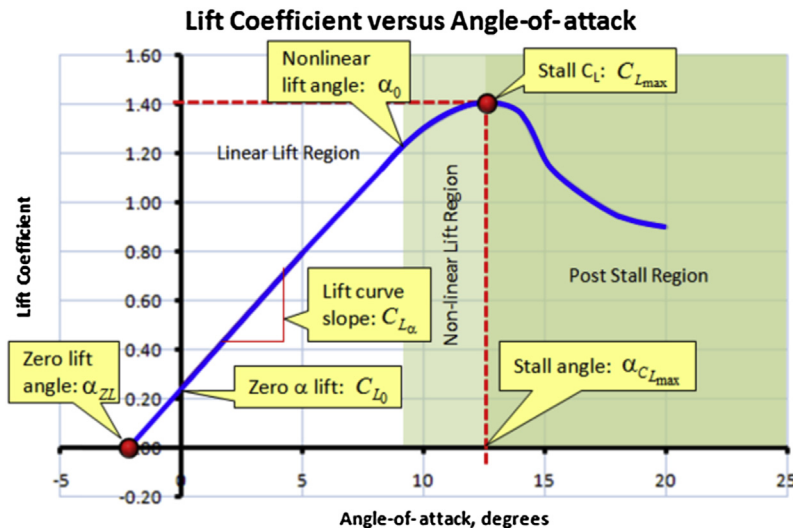


FIGURE 9-47 Important properties of the lift curve.

### Lift Curve Slope, $C_{L\alpha}$

The lift curve slope is a measure of how rapidly the wing generates lift with change in  $AOA$ . As stated in Section 8.1.4, the theoretical maximum is  $2\pi$ , although real airfoils deviate from it. The lift curve slope of a three-dimensional wing is *always less* than that of the airfoils it features (see Section 9.5.3, *Determination of lift curve slope,  $C_{L\alpha}$ , for a 3D lifting surface*). Once a certain  $AOA$  has been achieved the wing will display a pronounced reduction in the lift curve slope (see Figure 9-47). This point is called *stall* and, although not shown in the figure, occurs both at a positive and negative angle-of-attack. The lift at stall dictates how much wing area the aircraft must feature for a desired stalling speed.

### Maximum and Minimum Lift Coefficients, $C_{L\max}$ and $C_{L\min}$

The largest and smallest magnitudes of the lift coefficient are denoted by  $C_{L\max}$  and  $C_{L\min}$ , respectively. It indicates at what angle-of-attack the airplane will achieve its minimum airspeed (stalling speed), or what wing area is required for a desired stalling speed. As for the airfoil, the stall is defined as the flow conditions that follow the first lift curve peak, which is where the  $C_{L\max}$  (or  $C_{L\min}$ ) occur (see, for instance, Ref. [19]). Both values are required when generating aerodynamic loads for the structures group.

### $C_L$ at Zero AOA, $C_{L0}$

$C_{L0}$  is the value of the lift coefficient of the wing at zero  $AOA$ . It is of great importance in the scheme of things, because it affects the angle-of-incidence at which the wing must be mounted. Generally this value ranges from 0.0 (for symmetric airfoils) to 0.6 (for highly cambered airfoils). It is negative for under-cambered airfoils (e.g. airfoils used near the root of high subsonic jet aircraft).

### Angle-of-attack at Zero Lift, $\alpha_{ZL}$

This is the angle at which the wing generates no lift. For positively cambered airfoils this angle is always negative, unless some specific components (e.g. cambered fuselage) affect it greatly. For symmetrical airfoils it is always  $0^\circ$ .

### Linear Range

The linear range is analogous to that of the airfoil, except it applies to the entire aircraft. In this range, the following equation of a line can be used to describe how lift varies with  $AOA$ .

$$C_L = C_{L0} + C_{L\alpha} \alpha \quad (9-48)$$

### Angle-of-attack where Lift Curve Becomes Non-linear, $\alpha_{NL}$

Once a certain  $AOA$  is reached the wing begins to display a pronounced reduction in the lift curve slope. This always happens before the stall  $AOA$  is reached.

### Angle-of-attack for Maximum Lift Coefficient, $\alpha_{stall}$

Once a certain  $AOA$  is reached, a pronounced reduction in lift curve takes place; this is the stall.

### Design Lift Coefficient, $C_{Lc}$

The design lift coefficient is the  $C_L$  at which the aircraft is expected to operate during the mission for which it is designed. This is usually the lift coefficient during cruise. It is important to select an airfoil that has been designed to generate the least amount of drag at that lift coefficient (see Section 8.3.15, *Airfoil selection how-to*), as well as ensure flow separation areas are completely suppressed for minimum drag. In the case of a constant cruising speed (or loiter) mission, if the target airspeed is known, it is possible to estimate this design cruising speed using the weight of the airplane at the beginning and end of the mission using the following expression:

$$C_{Lc} = C_{L0} + \frac{(W_1 + W_2)}{\rho V_C^2 S} + C_{L\alpha} \alpha_{ZL} \quad (9-49)$$

where

$C_{L\alpha}$  = lift curve slope

$S$  = reference wing area

$\alpha_{ZL}$  = zero lift angle-of-attack

$\rho$  = density at cruise altitude

$W_1, W_2$  = aircraft weight at the beginning (1) and end (2) of the design mission

### Angle-of-attack for Design Lift Coefficient, $\alpha_C$

Ideally, the airplane should be flying at an  $AOA$  that generates the least amount of drag during the intended mission for which it is designed. For instance, this could be a cruise or long-range performance point. In the case of the design mission being a cruise or loiter mission, this  $AOA$  can be calculated from Equation (9-43).

### Derivation of Equation (9-49)

We start with Equation (9-43) for the design cruise  $AOA$ , repeated here for convenience:

$$\alpha_C = \left( \frac{1}{C_{L\alpha}} \right) \frac{(W_1 + W_2)}{\rho V_C^2 S} + \alpha_{0L}$$

Then we insert it into the Equation (9-51) and manipulate algebraically:

$$\begin{aligned} C_{Lc} &= C_{L0} + C_{L\alpha}\alpha_C \\ &= C_{L0} + C_{L\alpha} \left( \left( \frac{1}{C_{L\alpha}} \right) \frac{(W_1 + W_2)}{\rho V_C^2 S} + \alpha_{0L} \right) \\ &= C_{L0} + \frac{(W_1 + W_2)}{\rho V_C^2 S} + C_{L\alpha}\alpha_{0L} \end{aligned}$$

QED

### 9.5.2 The Lift Coefficient

The lift coefficient relates the *AOA* to the lift force. If the lift force is known at a specific airspeed the lift coefficient is obtained from Equation (9-47) and can be calculated from:

$$C_L = \frac{2L}{\rho V^2 S} \quad (9-50)$$

In the linear region of the lift curve, at low *AOA*, the lift coefficient can be written as a function of *AOA* as shown below:

$$C_L = C_{L_0} + C_{L_\alpha} \alpha \quad (9-51)$$

Equation (9-51) allows the *AOA* corresponding to a specific lift coefficient to be determined provided the lift curve slope known:

$$\alpha = \frac{C_L - C_{L_0}}{C_{L_\alpha}} \quad (9-52)$$

#### **The Relationship between Airspeed, Lift Coefficient, and Angle-of-attack**

Consider Figure 9-48, which shows an airplane being operated in horizontal flight at different airspeeds,

denoted by the ratio  $V/V_S$ , where  $V_S$  is its stalling speed. Starting with the upper left image, the aircraft is at a high airspeed (e.g. if  $V_S = 50$  KCAS, the figure shows it at  $V = 3 \times 50 = 150$  KCAS). This results in a very low lift coefficient,  $C_L$ , and an attitude that is slightly nose-down. As the aircraft slows down, it can only maintain altitude by exchanging less airspeed for a higher  $C_L$ , which calls for a higher  $\alpha$ . As it slows down further, a higher and higher nose-up attitude is required to generate a larger and larger  $C_L$ . Eventually, a maximum value of the  $C_L$  is achieved,  $C_{L\max}$ , after which the airplane can no longer maintain horizontal flight. This is followed by an immediate and forceful drop of the nose caused by the sudden loss of lift. The airplane begins a dive toward the ground, which increases its airspeed, making stall recovery possible. This is shown as the left bottom image, which shows the aircraft recovering and, while in a nose-down attitude, its higher airspeed has already lowered the  $\alpha$ .

#### **Wide-range Lift Curve**

A typical change in the lift coefficient with *AOA* ranging from  $0^\circ$  to  $90^\circ$  is shown in Figure 9-49. The graph is based on true wind tunnel test data, although the actual values have been normalized to the maximum lift coefficient. Two important observations can be made. The first is the linear range at low *AOA* (here shown ranging from *AOA* =  $0^\circ$  through  $10^\circ$ ). Note that the extent of this linear region depends on the geometry and operational airspeeds (via Reynolds numbers). The second observation is the relatively large value of the  $C_L$  at an *AOA* around  $45^\circ$ – $50^\circ$ , which, while large, is inefficient because of the high drag associated with it.

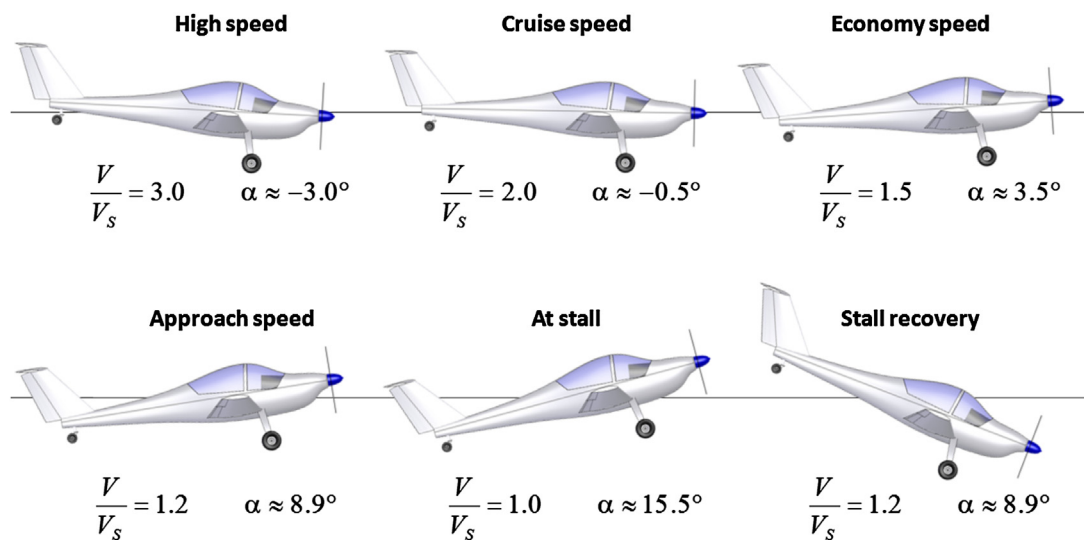


**FIGURE 9-48** A schematic showing the attitude of an aircraft at different airspeeds,  $V$ . Stalling speed is denoted by  $V_S$ . The *AOA* are typical values for light planes.

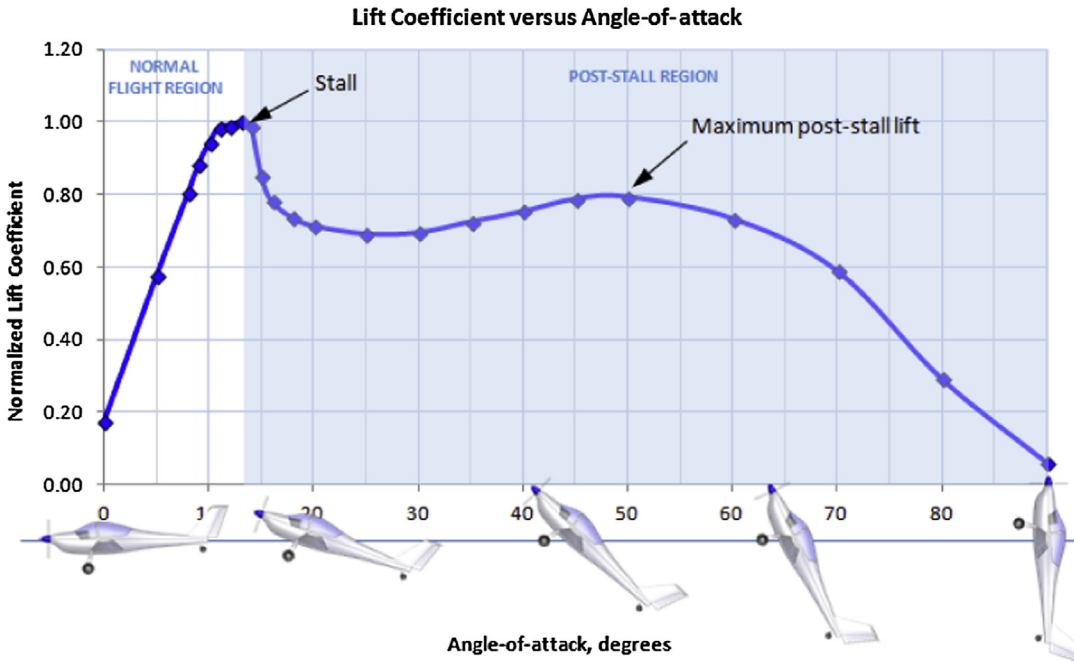


FIGURE 9-49 Example of change in lift coefficient with  $AOA$  ranging from  $0^\circ$  to  $90^\circ$  for a complete aircraft.

### 9.5.3 Determination of Lift Curve Slope, $C_{L\alpha}$ , for a 3D Lifting Surface

Consider the lift curve slope of an airfoil used for some specific lifting surface (which could be a wing, an HT, or a VT). For reasons that become clear in Section 9.7, *Numerical analysis of the wing*, the surface induces larger upwash in the flow field than the airfoil alone. Consequently, its effective  $AOA$  is less than that of the airfoil (because the induced  $AOA$  is larger). Therefore, the wing must operate at a larger  $AOA$  to generate the same lift coefficient as the airfoil. The lift curve slope for the wing is less steep than for the airfoil. This fact is used to derive the following expressions that allow the two-dimensional lift curve slope of an airfoil ( $C_{l\alpha}$ ) to be converted to three-dimensions for a wing ( $C_{L\alpha}$ ).

The transformation is usually derived using Prandtl's Lifting Line Theory (see Section 9.7.2, *Prandtl's lifting line method – special case: the elliptical wing*). The following expression is used with elliptical wings only:

Lift curve slope for an elliptical wing:

$$C_{L\alpha} = \frac{C_{l\alpha}}{1 + \frac{C_{l\alpha}}{\pi \cdot AR}} \quad (9-53)$$

A common (but not necessarily correct) assumption is that the lift curve slope of an airfoil is  $2\pi$ . This yields the following expression:

Elliptical wing with  $C_{l\alpha} = 2\pi$ :

$$C_{L\alpha} = 2\pi \frac{AR}{AR + 2} \quad (9-54)$$

NACA TN-817 [20] and TN-1175 [21] present methods to make Equation (9-54) suited for  $AR < 4$ , but these are generally unwieldy. The following expression is an attempt to extend Equation (9-53) to more arbitrary wing shapes and requires the correction factor,  $\tau$ , to be determined:

Lift curve slope for an arbitrary wing:

$$C_{L\alpha} = \frac{C_{l\alpha}}{1 + \frac{C_{l\alpha}}{\pi \cdot AR}(1 + \tau)} \quad (9-55)$$

The factor  $\tau$  is a function of the Fourier coefficients determined using the lifting line method and represents the following correction to the induced  $AOA$ , as shown in Dommash [22]. The actual value of  $\tau$  is calculated and provided by Glauert [23].

$$\alpha_i = \frac{C_L(1 + \tau)}{\pi \cdot AR}$$

By making some approximations and determining the downwash at the  $3/4$  chord station, rather than the  $1/4$  station, Helmbold [24] derived the expression shown below:

TABLE 9-7 Comparing  $C_{L\alpha}$  Calculated Using Three Selected Methods and the Vortex-lattice Method (VLM)

Wing Planform	AR	$\Lambda_{C/2}$	$C_{L\alpha}$ per Radian			
			Eq. (9-54)	Eq. (9-56)	Eq. (9-57)	VLM
Elliptical, straight C/2	10	0.00	5.24	5.15	4.90	5.02
Elliptical, straight LE	10	-6.60	5.24	5.15	4.87	4.99
Elliptical, straight TE	10	6.60	5.24	5.15	4.87	4.99
Schuemann	10	5.04	5.24	5.15	4.88	4.99
Semi-straight taper	10	0.00	5.24	5.15	4.90	4.98
Straight taper, straight C/2	10	0.00	5.24	5.15	4.90	4.96
Straight taper, straight LE	10	-3.81	5.24	5.15	4.89	4.95
Straight taper, straight TE	10	3.81	5.24	5.15	4.89	4.95
Compound taper	10	0.00	5.24	5.15	4.90	4.88
Rectangular	10	0.00	5.24	5.15	4.90	4.82
Crescent	10	22.48	5.24	5.15	4.59	4.60
Swept back, $TR = 0.5$ , LE sweep $30^\circ$	10	28.55	5.24	5.15	4.40	4.52
Swept forward, $TR = 2.0$ , LE sweep $30^\circ$	10	-32.78	5.24	5.15	4.24	4.32
Swept back, $TR = 1.0$ , LE sweep $30^\circ$	10	30.00	5.24	5.15	4.35	4.29
Swept back, $TR = 2.0$ , LE sweep $30^\circ$	10	27.05	5.24	5.15	4.45	3.98
Delta	2.27	38.59	3.34	2.84	2.51	2.44
Double delta	2.26	45.08	3.33	2.83	2.39	2.30
Disk	1.29	0.00	2.46	1.85	1.83	1.84

General lift curve slope:

$$C_{L\alpha} = \frac{2\pi \cdot AR}{2 + \sqrt{AR^2 + 4}} \quad (9-56)$$

Finally, the following expression, referred to as the Polhamus equation, is derived from NACA TR-3911 [25] and is based on a modification made to Helmbold's equation. It is also presented in USAF DATCOM [26]. The expression accounts for compressibility, deviation from the  $2\pi$  airfoil lift curve slope, and taper ratio. While  $TR$  does not explicitly appear in the equation, Reference [25] demonstrates that if the mid-chord sweep angle ( $\Lambda_{C/2}$ ) is used, the  $TR$  can be eliminated. The resulting expression is only valid for non-curved planform shapes and  $M \leq 0.8$ :

General lift curve slope:

$$C_{L\alpha} = \frac{2\pi \cdot AR}{2 + \sqrt{\left(\frac{AR \cdot \beta}{\kappa}\right)^2 \left(1 + \frac{\tan^2 \Lambda_{C/2}}{\beta^2}\right) + 4}} \quad (9-57)$$

where

$AR$  = wing aspect ratio

$\beta$  = Mach number parameter (Prandtl-Glauert) =  $(1 - M^2)^{0.5}$

$\kappa$  = ratio of two-dimensional lift curve slope to  $2\pi$

$\Lambda_{C/2}$  = sweepback of mid-chord

Of the above methods, Equation (9-57) compares well with experiment (and this author's experience). This can be assessed indirectly by comparing results using it to that of the vortex-lattice method (VLM), which, as has been shown before, compares well with experiment. Such a comparison is shown in Table 9-7. The general trend is that Equations (9-54) and (9-56) (intended for elliptical planform shapes) predict steeper lift curve slopes than Equation (9-57) and the VLM. Also, note the insensitivity of Equations (9-54) and (9-51) to other characteristics, such as sweep and general planform shape of the wing.

#### Derivation of Equation (9-53)

The graph in Figure 9-50 shows the lift curve for two ARs;  $AR = \infty$  (an airfoil) and an elliptical wing of an arbitrary  $AR$ . The lift coefficient for the airfoil can be written as follows:

$$C_L = \text{constant} + C_{l\alpha} \cdot \alpha$$

The wing induces upwash that reduces the  $\alpha$  by an amount denoted by  $\alpha_i$  (induced AOA). Therefore, the lift coefficient for the wing is given by:

$$C_L = \text{constant} + C_{l\alpha} \cdot (\alpha - \alpha_i)$$

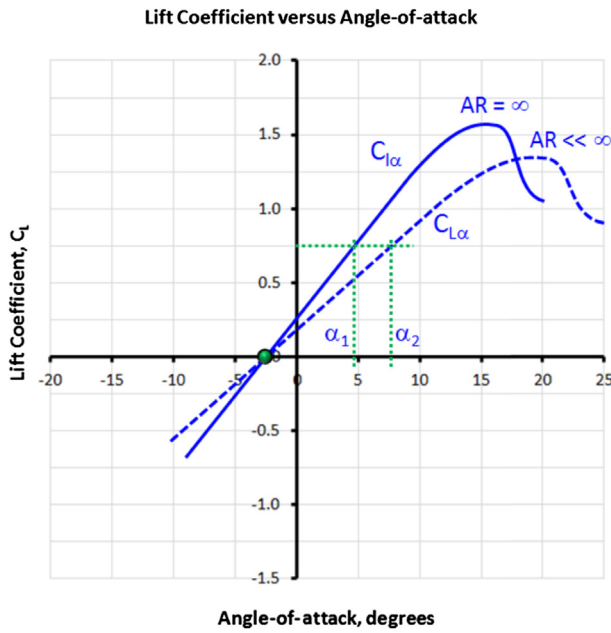


FIGURE 9-50 Lift curves for an airfoil and an elliptical wing.

The value of  $\alpha_i$  is given by Equation (9-87). Inserting this yields:

$$C_L = \text{constant} + C_{l\alpha} \cdot \left( \alpha - \frac{C_L}{\pi AR} \right)$$

The lift curve slope can now be found by differentiating with respect to  $\alpha$ :

$$\begin{aligned} \frac{dC_L}{d\alpha} &= C_{l\alpha} - C_{l\alpha} \cdot \frac{1}{\pi AR} \frac{dC_L}{d\alpha} \\ &= C_{l\alpha} - C_{l\alpha} \cdot \frac{1}{\pi AR} \frac{dC_L}{d\alpha} \Rightarrow \frac{dC_L}{d\alpha} = C_{l\alpha} \\ &= \frac{C_{l\alpha}}{\left( 1 + \frac{C_{l\alpha}}{\pi AR} \right)} \end{aligned}$$

QED

### Derivation of Equation (9-54)

We begin with Equation (9-53) and replace the airfoil lift-curve slope with  $2\pi$ :

$$C_{l\alpha} = \frac{C_{l\alpha}}{\left( 1 + \frac{C_{l\alpha}}{\pi AR} \right)} = \frac{2\pi}{\left( 1 + \frac{2\pi}{\pi AR} \right)}$$

Then manipulate algebraically:

$$\begin{aligned} C_{l\alpha} &= \frac{2\pi}{\left( 1 + \frac{2\pi}{\pi AR} \right)} = \frac{2\pi}{\left( \frac{\pi AR}{\pi AR} + \frac{2\pi}{\pi AR} \right)} = 2\pi \frac{\pi AR}{\pi AR + 2\pi} \\ &= 2\pi \frac{AR}{AR + 2} \end{aligned}$$

QED

### 9.5.4 The Lift Curve Slope of a Complete Aircraft

A complete aircraft typically consists of a wing, a stabilizing surface, such as a horizontal tail or a canard (or both), a fuselage, and, sometimes, engine nacelles and external stores. All of these components contribute to the total lift developed by the aircraft and, often, their contribution causes the lift curve slope of the aircraft to differ from that of the wing alone. It can be seen that, for instance, the HT produces lift that adds to the wing lift (assuming a fixed neutral elevator). If the combination is attributed to the reference wing area alone, it would “appear” the wing is generating greater lift than its actual contribution. This is important to keep in mind when considering gust loads for airframe loads and in some stability and control analyses. The following method can be used to estimate the total lift curve slope of a wing and HT, approximating that of the complete aircraft. Effectively, we want to write the total lift coefficient of the airplane,  $C_{L_{tot}}$ , as follows:

Lift coefficient:

$$C_{L_{tot}} = C_{L_{0,tot}} + C_{L_{\alpha,tot}} \alpha \quad (9-58)$$

where the zero AOA lift and lift curve slope are computed from:

Zero AOA lift:

$$C_{L_{0,tot}} = C_{L_0} + \frac{S_{HT}}{S} C_{L_{0,HT}} \quad (9-59)$$

Lift curve slope:

$$C_{L_{\alpha,tot}} = C_{L_{\alpha,W}} + \frac{S_{HT}}{S} C_{L_{\alpha,HT}} \left( 1 - \frac{\partial \epsilon}{\partial \alpha} \right) \quad (9-60)$$

where

$S$  = wing reference area

$S_{HT}$  = HT planform area

$C_{L_0}$  = zero AOA lift of the wing

$C_{L_{\alpha,W}}$  = wing lift curve slope

$C_{L_{0,HT}}$  = zero AOA lift of the HT (0 for symmetrical airfoils)

$C_{L_{\alpha,HT}}$  = HT lift curve slope

$\frac{\partial \epsilon}{\partial \alpha}$  = wing downwash angle  $\approx \frac{2C_{L_{\alpha,W}}}{\pi \cdot AR}$  for elliptical wings

### Derivation of Equations (9-59) and (9-60)

We can write the total lift of the wing and HT as follows:

$$qSC_{L_{tot}} = qSC_{L_W} + qS_{HT}C_{L_{HT}}$$

Divide through by  $qS$  to get the lift coefficient form:

$$C_{L_{tot}} = C_{L_{0tot}} + C_{L_{atot}} \alpha_W = C_{L_W} + \frac{S_{HT}}{S} C_{L_{HT}}$$

Expand in terms of component properties:

$$C_{L_{tot}} = (C_{L_0} + C_{L_{\alpha_W}} \alpha_W) + \frac{S_{HT}}{S} (C_{L_{0_{HT}}} + C_{L_{\alpha_{HT}}} \alpha_{HT})$$

Insert the  $AOA$  the HT is subjected to:

$$\begin{aligned} C_{L_{tot}} &= (C_{L_0} + C_{L_{\alpha_W}} \alpha_W) + \frac{S_{HT}}{S} \\ &\quad \times \left( C_{L_{0_{HT}}} + C_{L_{\alpha_{HT}}} \alpha_w \left( 1 - \frac{\partial \epsilon}{\partial \alpha} \right) \right) \end{aligned}$$

And finally, gather like terms to yield Equations (9-59) and (9-60):

$$\begin{aligned} C_{L_{tot}} &= \left( C_{L_0} + \frac{S_{HT}}{S} C_{L_{0_{HT}}} \right) \\ &\quad + \left[ C_{L_{\alpha_W}} + \frac{S_{HT}}{S} C_{L_{\alpha_{HT}}} \left( 1 - \frac{\partial \epsilon}{\partial \alpha} \right) \right] \alpha_w \end{aligned}$$

QED

### 9.5.5 Step-by-step: Transforming the Lift Curve from 2D to 3D

An important part of working with airfoils is the realization that the lift capabilities of a two-dimensional airfoil are superior to that of a three-dimensional wing. Figure 9-11 reveals how a two-dimensional lift curve changes once it is introduced to a wing of finite aspect ratio. Among noticeable effects is a reduction in the lift curve slope and lift at zero  $AOA$ . The maximum lift coefficient is reduced although the stall  $AOA$  increases. This section presents a method that allows the transformation of the two-dimensional lift curve into a three-dimensional one. The method assumes the same airfoil along the wing. If more than one airfoil is used, the properties of the airfoil at the MGC can be assumed.

**Step 1:** Compute a three-dimensional lift curve slope using Equation (9-57).

**Step 2:** Compute the zero-lift angle for the two-dimensional airfoil using the following expression,

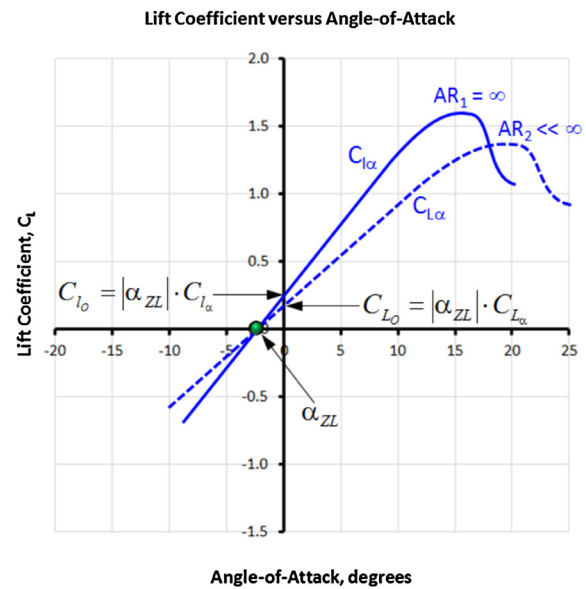


FIGURE 9-51 Determination of the lift coefficient at zero  $AOA$  for a three-dimensional lift curve.

which is obtained by inspection of the curves in Figure 9-51:

$$C_{lo} = -\alpha_{ZL} \cdot C_{l\alpha} \Leftrightarrow \alpha_{ZL} = -\frac{C_{lo}}{C_{l\alpha}}$$

**Step 3:** Compute lift at  $AOA = 0^\circ$  for the three-dimensional wing using:

Zero  $\alpha$  lift:

$$C_{L0} = |\alpha_{ZL}| \cdot C_{l\alpha} \quad (9-61)$$

**Step 4:** Compute pitching moment for three-dimensional wing, denoted by  $C_{m\alpha}$ . Note that since:

$$C_{m\alpha} = C_{l\alpha} \cdot \Delta x \Leftrightarrow \Delta x = C_{m\alpha} / C_{l\alpha}$$

It follows that:

$$C_{m\alpha} = C_{l\alpha} \cdot \Delta x = C_{l\alpha} \cdot \left( \frac{C_{m\alpha}}{C_{l\alpha}} \right) \quad (9-62)$$

A Hershey-bar wing ( $\lambda = 1$ ) with an aspect ratio of 20 is being evaluated for use in a low-speed vehicle ( $M \approx 0$ ). One of the airfoils being considered is a NACA 23012.

Convert the following two-dimensional data for the airfoil (which has been extracted from the *Theory of Wing Sections*, by Abbott and Doenhoff) for the three-dimensional:

### EXAMPLE 9-8

### EXAMPLE 9-8 (cont'd)

Lift curve slope:

$$C_{l\alpha} = 0.1051 \text{ per deg}$$

Lift at zero AOA:

$$C_{lo} = 0.1233$$

Slope of the pitching moment curve:

$$C_{m\alpha} = 0.00020 \cdot \alpha - 0.01198$$

The last expression is obtained from interpolation.

#### Solution

**Step 1:** Compute a 3D lift curve slope using Equation (9-57):

$$C_{L\alpha} = \frac{AR \cdot C_{l\alpha}}{2 + \sqrt{\frac{AR^2 \beta^2}{\kappa^2} \left(1 + \frac{\tan^2 \Lambda_{C/2}}{\beta^2}\right) + 4}}$$

where

$AR$  = wing aspect ratio = 20

$\beta$  = Mach number parameter (Prandtl-Glauert)  
 $= (1 - M^2)^{0.5} \approx 1$

$\kappa$  = ratio of 2D lift curve slope to  $2\pi$  = 0.1051 ×  $(180/\pi)/(2\pi) = 0.95840$

$\Lambda_{c/2}$  = sweepback of mid-chord = 0°

$$\begin{aligned} C_{L\alpha} &= \frac{2\pi \cdot 20}{2 + \sqrt{\frac{400}{0.95840^2} \left(1 + \frac{0}{1^2}\right) + 4}} = 5.472 \text{ per rad} \\ &= 0.09551 \text{ per deg} \end{aligned}$$

**Step 2:** Compute zero lift angle for the two-dimensional airfoil:

$$\alpha_0 = -\frac{C_{lo}}{C_{l\alpha}} = -\frac{0.1233}{0.1051} = -1.173^\circ$$

**Step 3:** Compute lift at zero angle for the 3D wing using:

$$C_{L0} = -\alpha_0 \cdot C_{L\alpha} = -(-1.173^\circ) \cdot 0.09551 = 0.1121$$

**Step 4:** Compute pitching moment for three-dimensional wing:

$$\begin{aligned} (C_{m\alpha})_{3D} &= C_{L\alpha} \cdot \left(\frac{C_{m\alpha}}{C_{l\alpha}}\right) = (0.09551) \cdot \left(\frac{-0.01198}{0.1051}\right) \\ &= -0.01089 \end{aligned}$$

#### 9.5.6 The Law of Effectiveness

Consider the estimation of the three-dimensional lift curve slope of a wing that has two distinct airfoils at the root and tip. As we have seen, the estimation of the wing's lift curve slope requires a representative two-dimensional lift curve slope of an airfoil, but which should be used? The *law of effectiveness* is a handy rule of thumb that helps solve this problem. This law contends that any representative two-dimensional aerodynamic property of a multi-airfoil wing can be approximated by the value at its area centroid, or the mean geometric chord (MGC). A mathematical representation is given by the following equation, obtained using a linear parametric equation:

The law of effectiveness:

$$P_{MGC} = P_{root} + \frac{2y_{MGC}}{b} (P_{tip} - P_{root}) \quad (9-63)$$

where  $P$  stands for *property*. The property can be the lift curve slope, maximum lift coefficient, drag coefficient, pitching moment, and similar. When applied to a wing

for which we intend to determine a representative lift curve slope, Equation (9-63) becomes:

$$(C_{l\alpha})_{MGC} = (C_{l\alpha})_{root} + \frac{2y_{MGC}}{b} [(C_{l\alpha})_{tip} - (C_{l\alpha})_{root}] \quad (9-64)$$

#### 9.5.7 Flexible Wings

The high-aspect-ratio wings of sailplanes tend to flex excessively during maneuvers and even in normal flight. Flex as large as 6 ft (2 m) is not unheard of in some cases. The same phenomenon occurs on many commercial aircraft (e.g. Boeing 747 and Airbus A380). Regardless of aircraft class, if excessive wing flex is anticipated, it is important to consider its effects on the lift capability of such aircraft.

Figure 9-52 shows the effect of wing flex on the distribution of section lift coefficients. In this example, a wing with a 50-ft wingspan is deflected so its tip is 5 ft higher than that of the unflexed wing. The figure shows that for a given AOA, the center of lift moves inboard, reducing the bending moment. However, less lift is also being

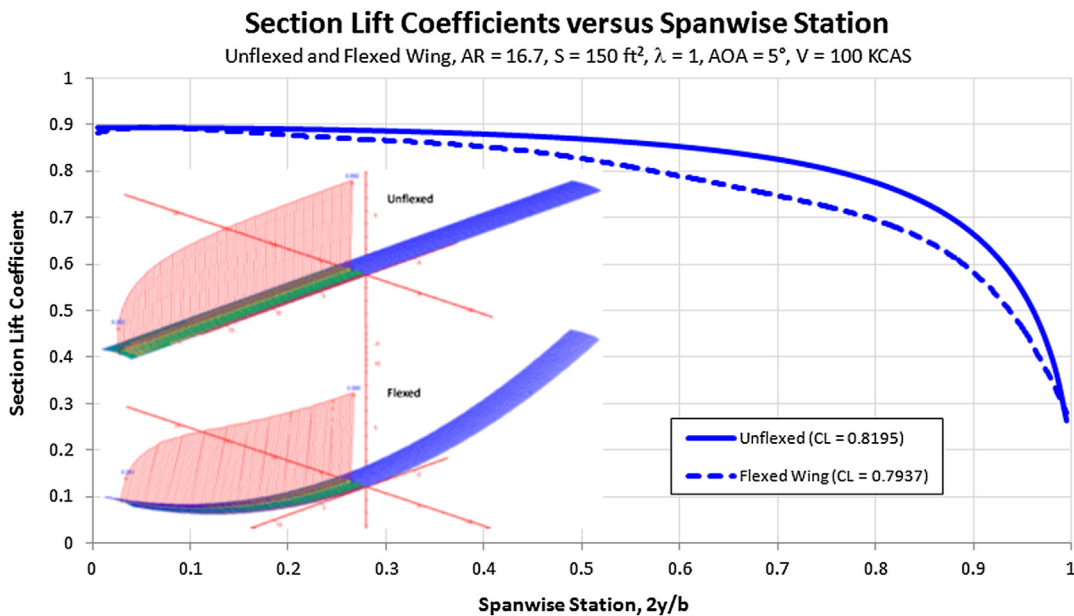


FIGURE 9-52 Lift distribution of the un-flexed and flexed wings compared.

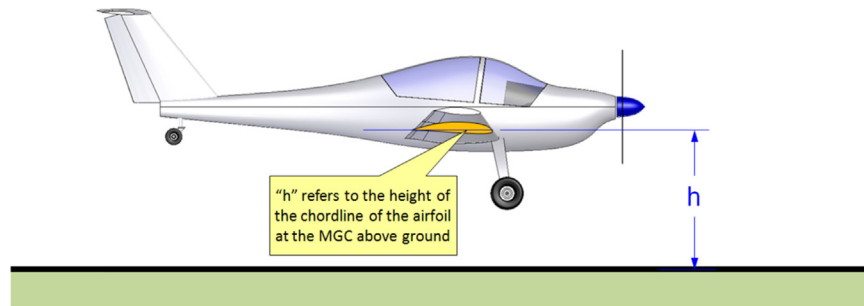


FIGURE 9-53 An airplane in ground effect.

produced (in this particular case, some 3% less), so the resulting aircraft will have to operate at a higher AOA. This will lead to a slightly higher operational lift-induced drag and will diminish the wing's long-range efficiency. Additionally, the lift curve slope reduces by about 3%. While this may sound detrimental, there are actually two sides to the topic; the other is discussed in Section 10.5.9, *The polyhedral wing(tip)*.

### 9.5.8 Ground Effect

Ground effect is the change in the aerodynamic forces as a consequence of the body being in close proximity to the ground. As the aircraft nears the ground, the ground will get in the way of the downwash, effectively preventing it from fully developing. This modifies the entire flow field around the aircraft and, thus, affects a number of its characteristics. Some formulation indicates the aerodynamic properties of

the airplane begin to change when it is as much as 2 wingspans from the ground. However, the changes are negligible at that height and it is more reasonable to include ground effect once the airplane is about 1 wingspan from the ground or less. Pilots begin to detect those effects at an even lower height, typically around half a wingspan.

The problem of ground effect was studied as early as 1912 by Albert Betz [27] (1885–1968). Using Prandtl's lifting line theory, Wieselberger [28] developed a formulation to estimate the reduction in the lift-induced drag near the ground. His work is translated in Ref. [29]. It does this by calculating a special *ground influence coefficient*, denoted by  $\Phi$ . The presentation here resembles that of Ref. [30], in which  $h$  stands for height of the wing above the ground and  $b$  is the wingspan. It differs only slightly from the presentation of Wieselberger, who used  $h/2$  for the height above the ground. Additionally, in order to correspond to the other two presentations

shown below, Wieselberger's coefficient (denoted by  $\sigma$ ) is subtracted from 1, yielding:

$\Phi$  per Wieselberger:

$$\Phi = 1 - \frac{1 - 1.32(h/b)}{1.05 + 7.4(h/b)} \quad (9-65)$$

This approximation appears in good agreement with experiment [29] for values of  $h/b$  between 0.033 and 0.25. Using the Biot-Savart law applied to a horseshoe vortex whose span is  $\pi b/4$ , McCormick [31] shows that the ground influence coefficient can be estimated from:

$\Phi$  per McCormick:

$$\Phi = \frac{(16 \cdot h/b)^2}{1 + (16 \cdot h/b)^2} \quad (9-66)$$

Assuming an elliptical lift distribution of a straight wing of  $AR \approx 5$  and using the lifting line theory, Asselin [32] estimates the following value of the ground influence coefficient:

$\Phi$  per Asselin:

$$\Phi = 1 - \frac{2}{\pi^2} \ln \left( 1 + \frac{\pi}{8 \cdot h/b} \right) \quad (9-67)$$

These approximations are compared in Figure 9-54. The ground influence coefficient is then used to adjust the following characteristics of the airplane:

Lift-induced drag:

$$(C_{Di})_{IGE} = \Phi \times (C_{Di})_{OGE} \quad (9-68)$$

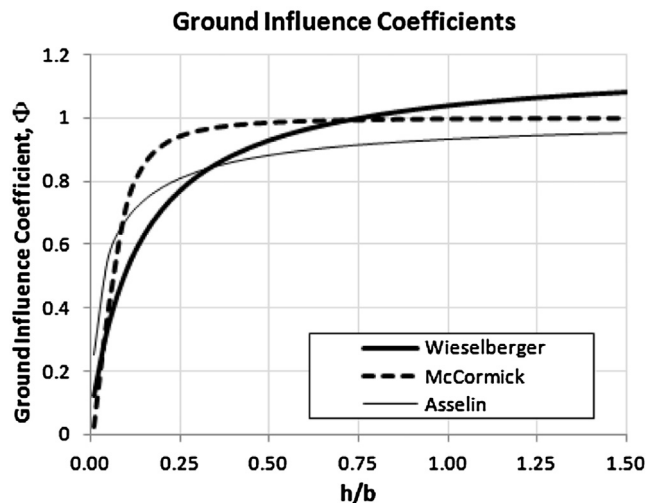
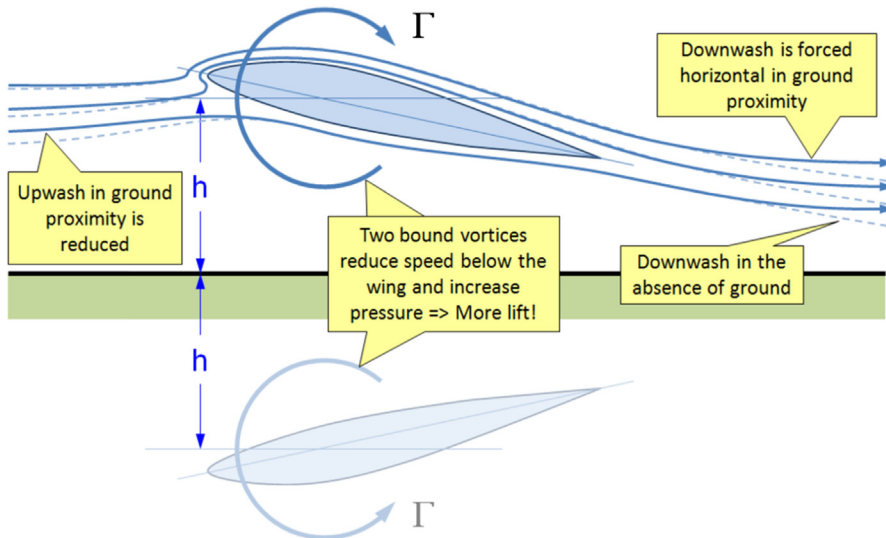


FIGURE 9-54 Comparing ground influence coefficients.

Maximum lift-to-drag ratio:

$$(LD_{\max})_{IGE} = \frac{(LD_{\max})_{OGE}}{\sqrt{\Phi}} \quad (9-69)$$

where IGE stands for *in ground effect* and OGE stands for *out of ground effect*.

Modeling the ground effect can be accomplished using vortex theories such as Prandtl's lifting line theory or Weissinger's vortex-lattice theory. By creating an inverted mirror image of the wing (or airfoil) with bound vortices of equal strength but rotating in opposite directions (see Figure 9-55) the resulting flow field will

FIGURE 9-55 Modeling the ground effect is done using a mirror image airfoil (or wing).

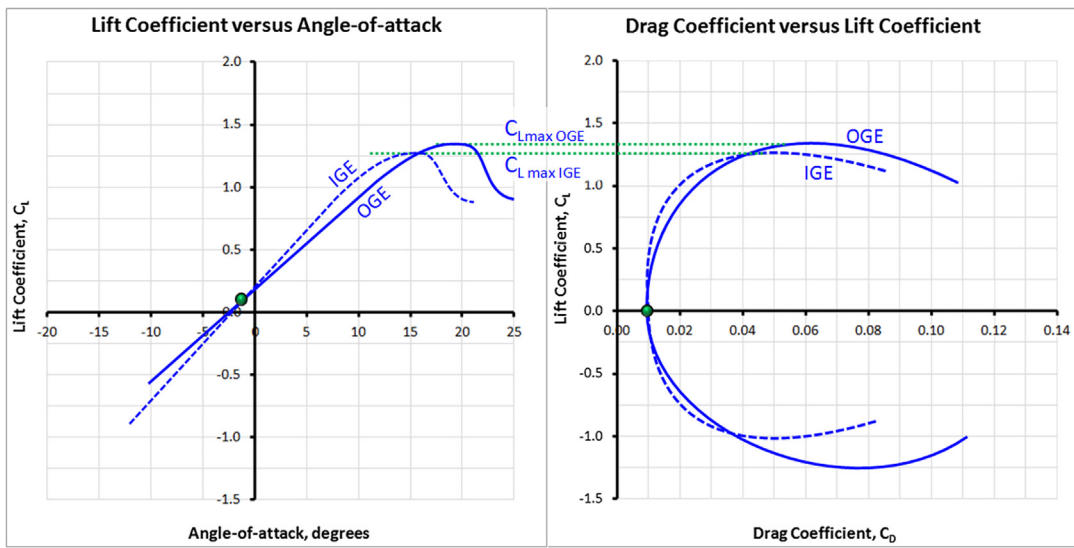


FIGURE 9-56 The impact of ground effect on the lift curve and drag polar.

feature a horizontal streamline along the ground plane. The streamlines above and below will be realigned when compared to the flow field in the absence of the ground as is shown in Figure 9-55. The impact on the lift curve, drag polar, and pitching moment curve is shown in Figure 9-56 and Figure 9-57. The following changes can be noted (these are in part based on Ref. 31). Note that IGE stands for in ground effect and OGE stands for out of ground effect.

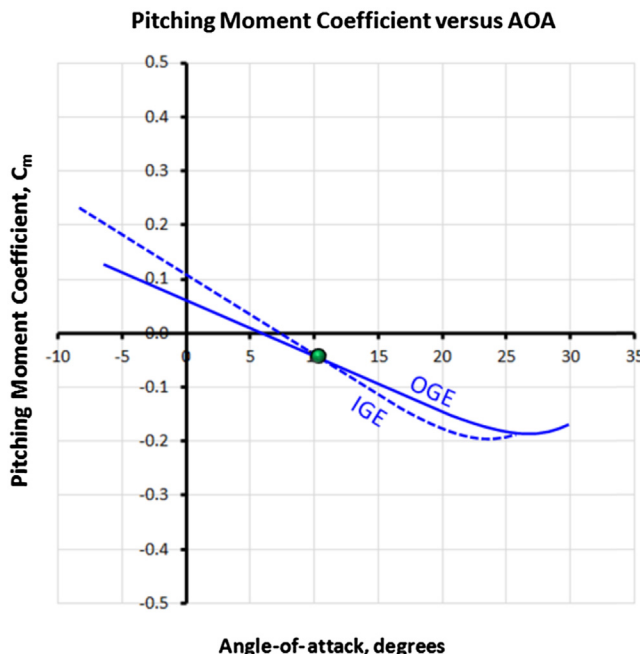


FIGURE 9-57 The impact of ground effect on the pitching moment.

- (1) Up- and downwash in the proximity of the ground is reduced compared to that in the far-field.
- (2) This reduction lowers the induced  $AOA$ , resulting in less aft tilting of the lift vector and, thus, less induced drag (see Section 15.3.4, *The lift-induced drag coefficient:  $C_{Dl}$* ). The minimum drag, however, is not reduced.
- (3) The reduced up- and downwash also reduces the lift. However, the two bound vortices (on either side of the ground plane) will cause a greater reduction in airspeed under the airfoil, increasing the pressure along the lower surface above that in the absence of the ground. This increase is greater than the reduction due to the diminished downwash, yielding an overall increase in lift at a given  $AOA$ .
- (4) The lift increase causes an increase in the lift curve slope. Based on Ref. [29] this tends to result in a small reduction in the zero- $AOA$  lift.
- (5) The steepening of the lift curve slope increases the pitching moment of the wing and shifts it downward.
- (6) The effective  $AR$  is increased because of the reduction in lift-induced drag. This, and the accompanying increase in lift at a given  $AOA$ , increases the  $L/D$  ratio, causing a “floating” tendency.
- (7) The trim  $AOA$  is reduced, which means that the airplane has a tendency to go to a lower  $AOA$ .
- (8) Elevator effectiveness of a conventional tail-aft configuration is reduced as the low-pressure region on the lower surface is counteracted by the

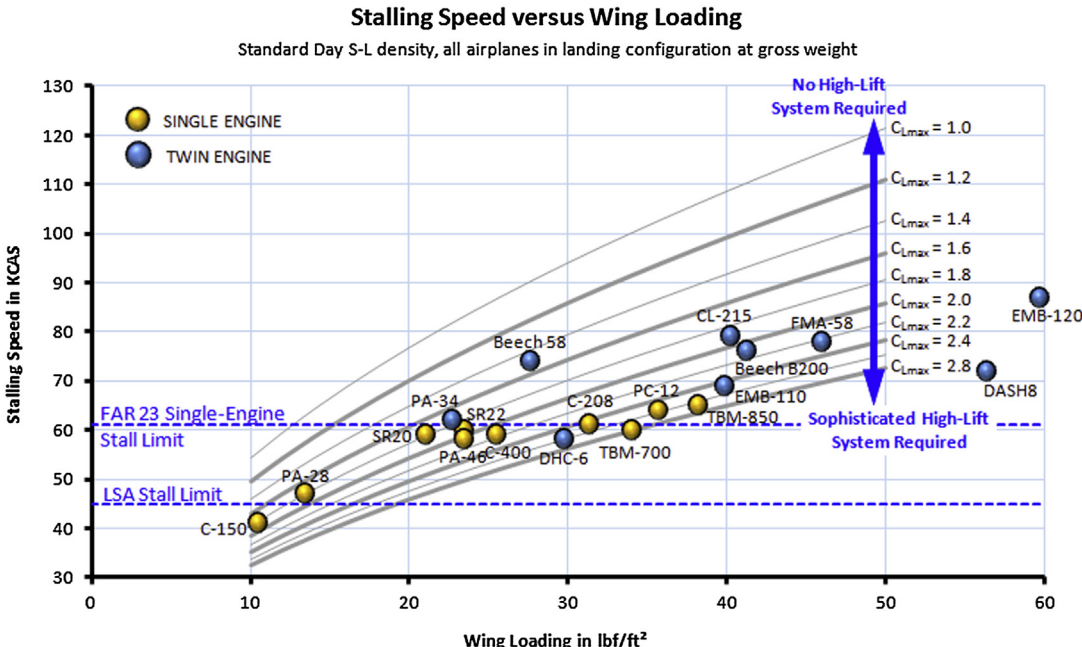


FIGURE 9-58 A carpet plot showing stalling speed as a function of wing loading and maximum lift coefficient.

formation of a high-pressure region similar to that of the wing. By the same token, the elevator effectiveness of a canard configuration will increase.

### 9.5.9 Impact of $C_{L\max}$ and Wing Loading on Stalling Speed

During the design stage the stalling speed and required wing area must be determined. Figure 9-58 highlights how wing loading ( $W/S$ ) and maximum lift coefficient ( $C_{L\max}$ ) affect the stalling speed (here shown in KCAS) by displaying it as a carpet plot. The figure shows the regulatory FAR 23 stall speed limit of 61 KCAS for single-engine aircraft and the 45 KCAS limit set forth in the Light Sport Aircraft (LSA) category. The graph has selected aircraft superimposed. Note that single-engine aircraft, such as the PC-12 and TBM-850, are turboprop aircraft that were granted exemption from the 61 KCAS rule on the grounds of envelope protection equipment they feature.

As an example of use, consider an airplane slated for FAR 23 certification characterized by a wing loading of some  $25 \text{ lb}_f/\text{ft}^2$ . It can be seen it must feature a high-lift system capable of at least  $C_{L\max} = 2.0$  in order to meet the 61 KCAS requirement.

Alternatively, consider another example in which the designer of an airplane slated for FAR 23 certification wants to feature a simple high-lift system capable of  $C_{L\max} = 1.8$ . Figure 9-58 reveals that as long as the wing loading is less than  $22 \text{ lb}_f/\text{ft}^2$  the FAR 23

single-engine stall speed limit (61 KCAS) will be complied with. The following expression is used to plot the curves in Figure 9-58, of which the right hand approximation is only valid at S-L. The constants ( $1/1.688 = 0.592$  and  $29/1.688 = 17.18$ ) convert the value in ft/s to knots.

$$V = 0.592 \sqrt{\frac{2W}{\rho SC_{L\max}}} \approx 17.18 \sqrt{\frac{(W/S)}{C_{L\max}}} \quad (9-70)$$

### 9.5.10 Step-by-step: Rapid $C_{L\max}$ Estimation [5]

The primary purpose of this method is to allow a fast estimation of a likely stalling speed. This method is very simple and, consequently, accuracy is suspect. It is presented here because it is acknowledged that, during the conceptual design stage, the designer needs a fast and simple method that has a "fair chance" of providing reasonably accurate results. It is acceptable only during the conceptual design phase and should be replaced with more accurate methods, once the design progresses.

**Step 1:** Calculate a representative  $C_{l_{\max}}$  (two-dimensional) for the airfoil at the MGC using the *law of effectiveness*:

$$C_{l_{\max}} = (C_{l_{\max}})_{root} + \frac{2y_{MGC}}{b} \left[ (C_{l_{\max}})_{tip} - (C_{l_{\max}})_{root} \right] \quad (9-71)$$

**Step 2:** Calculate the three-dimensional  $C_{L\max}$  from the following expression (this is the straight wing  $C_{L\max}$ ):

$$C_{L\max_0} = 0.9 \times C_{l\max} \quad (9-72)$$

**Step 3:** Correct for wing sweep angle. This reduces the maximum lift over that of a straight wing, highlighting yet another challenge for the operation of aircraft with swept wings. Generally, the reduction in the maximum lift can be estimated from the following expression:

$$C_{L\max} = C_{L\max_0} \times K_\Lambda \quad (9-73)$$

where

$C_{L\max_0}$  = max lift coefficient of the unswept wing  
 $K_\Lambda$  = Sweep correction factor (see Figure 9-59)

Raymer [5], Jenkinson [33], and others define  $K_\Lambda$  as follows, where it is based on the sweep of the quarter-chord:

$$K_\Lambda = \cos \Lambda_C / 4$$

Young [34], on the other hand, defines it in terms of the leading edge sweep. It matches historical data well:

$$K_\Lambda = \cos^3 \Lambda_{LE}$$

For instance, a wing sweep of  $35^\circ$  will reduce the  $C_{L\max}$  by about 15% per Figure 9-59. Note that these methods are also extended to evaluate the reduction in effectiveness of control surfaces with swept hinge-lines. In this case, replace  $\Lambda_C/4$  by the hingeline sweep angle.

### EXAMPLE 9-9

Compare the calculated maximum lift coefficient for the Cirrus SR22 using the Rapid  $C_{L\max}$  Method and compare to the “known” value of  $C_{L\max}$  of the airplane, which can be calculated using published information in the aircraft’s POH ( $S = 144.9 \text{ ft}^2$ ,  $W = 3400 \text{ lb}_f$ , and  $V_S = 70 \text{ KCAS}$  [ $M = 0.10$ ]) and the calculated values of Table 16-6. Assume the airfoil for the airplane is NACA 65-415 for both the root and tip.

#### Solution

Start by estimating the maximum three-dimensional lift coefficient to compare to, based on the POH information:

$$C_{L\max} = \frac{2W}{\rho V^2 S} = \frac{2 \cdot 3400}{0.002378 \cdot (70 \cdot 1.688)^2 \cdot 144.9} = 1.41$$

Next, let’s figure out the Reynolds number at stall, using the average chord for the airplane (in lieu of the MGC). The average chord can be found from Equation (9-17):

$$C_{avg} = \frac{S}{b} = \frac{144.9 \text{ ft}^2}{38.3 \text{ ft}} = 3.783 \text{ ft}$$

Therefore, using Equation (8-28) the Reynolds number equals:

$$R_e \approx 6400 VL = 6400 \times (70 \times 1.688) \times (3.783) \approx 2,860,000$$

We use this information to extract the maximum lift coefficient for the NACA 65-415 airfoil using the wind tunnel data in NACA R-824 [35]. Using the plot for

$R_e = 3.0$  million (which is closest to 2.86 million), displayed in Figure 9-60, the  $C_{l\max} = 1.45$  and this will be used at the root.

Since the airplane’s taper ratio is 0.5, the  $R_e$  at the root is two times that at the tip. By inspecting the graph in Figure 9-60 it is estimated that the tip  $C_{l\max}$  is approximately 1.35. Therefore, the 3D  $C_{L\max}$  for the SR22, assuming NACA 65-415 for root and tip, can be estimated as follows:

$$\begin{aligned} C_{l\max} &= (C_{l\max})_{root} + \frac{2y_{MGC}}{b} [(C_{l\max})_{tip} - (C_{l\max})_{root}] \\ &= 1.45 + \frac{2 \times 8.51}{38.3} [1.35 - 1.45] = 1.406 \end{aligned}$$

By observation, the quarter-chord sweep angle is  $0^\circ$ . Therefore, the three-dimensional maximum lift coefficient can be found to equal:

$$\begin{aligned} C_{L\max} &= 0.9 \times C_{l\max} \times \cos \Lambda_C / 4 \\ &= 0.9 \times 1.406 \times \cos 0^\circ = 1.265 \end{aligned}$$

The difference between the POH and estimated value using the POH is some 10% – in this case, underestimating the capability of the airplane. That level of accuracy could adversely affect the wing sizing of a brand-new aircraft and must be kept in mind, although it will give some idea of the maximum lift coefficient. However, the method does not account for the lift generated by the fuselage and HT at this high AOA.

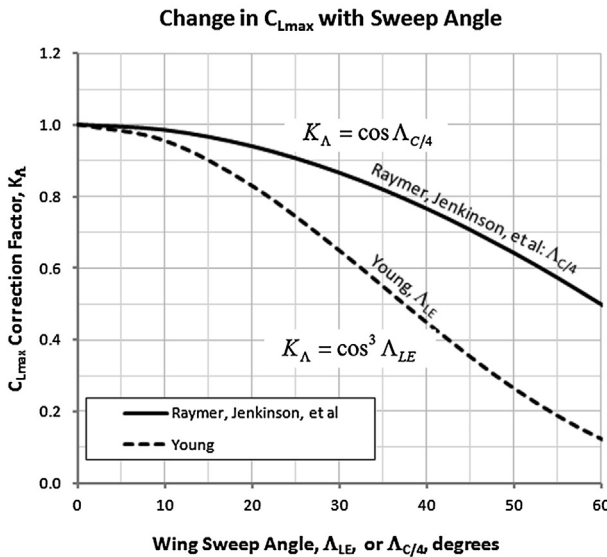
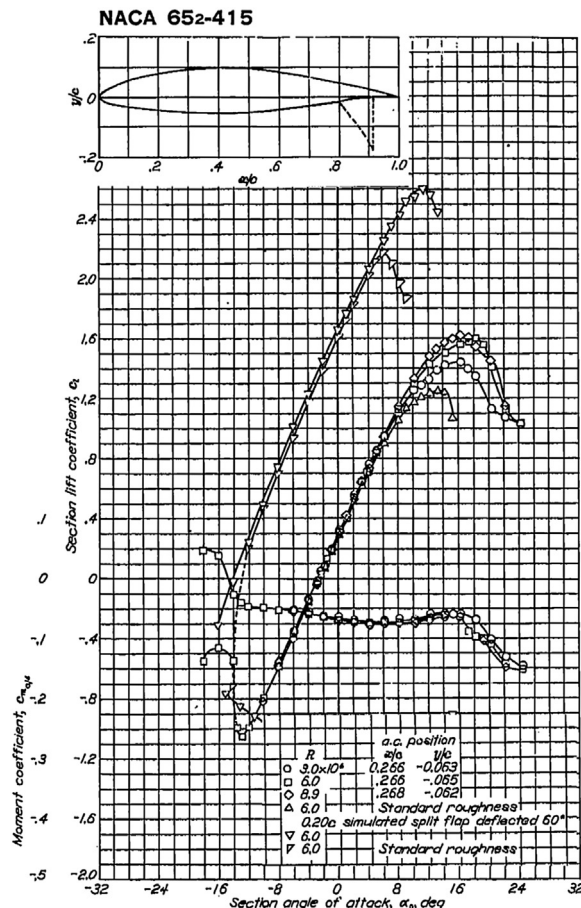
FIGURE 9-59 Sweep correction factor for  $C_{L_{max}}$ .

FIGURE 9-60 Lifting properties of the NACA 65-415 airfoils (from Ref. [34]).

### 9.5.11 Step-by-step: $C_{L_{max}}$ Estimation per USAF DATCOM Method 1

The wing's maximum lift coefficient can also be calculated using the following method from the USAF DATCOM (where it is referred to as Method 1). This method requires access to an accurate wingspan-wise loading analysis program, such as the vortex-lattice or doublet-lattice methods. The method is limited to moderately swept wing planforms, where LE vortex effects are not yet significant. Delta wings are excluded, unless the LE vortex can be estimated. Furthermore, the spanwise location where stall is first detected should be limited within a band extending from one local chord-length away from the wing root and tip. The DATCOM considers this method superior to Method 2 (see next section).

#### Step 1: Determine the Two-dimensional Maximum Lift Coefficient

Determine the 2D  $C_{l_{max}}$  along the span for the wing, based on the appropriate Mach number and Reynolds number. Experimental data should always be used if available.

#### Step 2: Plot the Distribution of Section Lift Coefficients

Plot the  $C_{l_{max}}$  along a normalized spanwise station ( $2y/b$ , ranging from 0 to 1), as shown by the dashed line in Figure 9-61.

#### Step 3: Determine the AOA at which Local $C_l$ Intersects $C_{l_{max}}$

Then plot the distribution of section lift coefficients for an AOA until the maximum of a local  $C_l$  intersects the airfoil's  $C_{l_{max}}$ . This is where the stall will first occur. An approximate value of where this occurs can be estimated from (Ref. [1], Article 4.1.3.4, Wing Maximum Lift) (note that  $\lambda$  = taper ratio):

$$\eta_{stall} = 1 - \lambda \quad (9-74)$$

#### Step 4: Compute $C_{L_{max}}$

Calculate the three-dimensional  $C_{L_{max}}$  by integrating along the span:

$$C_{L_{max}} = \frac{1}{S} \int_0^{1.0} b \cdot C_l(\eta) \cdot C(\eta) d\eta \quad (9-75)$$

where

$C_l(\eta)$  = section lift coefficient as a function of spanwise station

$C(\eta)$  = wing chord as a function of spanwise station

$\eta$  = spanwise station =  $2y/b$ ; ranges from 0 to 1 (for  $b/2$ )

### EXAMPLE 9-10

Predict the maximum lift coefficient for the Cirrus SR22 using the DATCOM method and compare to the “known” value of  $C_{L\max 3D}$  ( $= 1.41$ ), calculated in Example 9-9. Assume the airplane has an airfoil in the NACA 65<sub>2</sub>-415 class and account for the effect of Reynolds number on the  $C_{l\max}$  at the root and tip.

#### Solution

The results in Figure 9-61 were obtained using the vortex-lattice solver SURFACES, but similar data should be obtainable from other solvers as well. The model is based on measurements taken from Figure 16-15 and included the wing’s leading edge extensions (or cuffs), the fuselage, and horizontal tail. Note that the program calculates the total lift coefficient,  $C_L$  (see values in parentheses in the legend) and these represent values that would be returned by Equation (9-75) if the shape of the lift distribution were to be presented as a function of the spanwise station.

The stall limit (blue straight dashed line) indicates the  $C_{l\max} = 1.45$  at the root of the NACA 65<sub>2</sub>-415 airfoil and 1.35 at tip, determined in Example 9-9. This allows the stall AOA and the maximum lift coefficient to be estimated using the DATCOM method as follows:

$$C_{L\max} \approx 1.468 \quad \text{and} \quad \alpha_{stall} \approx 14^\circ$$

The difference between the POH ( $C_{L\max} = 1.41$ ) and the estimated value ( $C_{L\max} = 1.468$ ) is some 4.1% and, indeed, shows a very good agreement. This method generally agrees well with experiment and differs by approximately  $\pm 6\%$ .

Finally this; it is acknowledged that not all readers have access to codes like the one used in this example and this may present frustration to some. While the author empathizes with such emotions, ultimately, engineers working in industry have access to such codes and this example is intended for them. It is possible to use the method with the lifting line theory presented in Section 9.7, *Numerical analysis of the wing*.

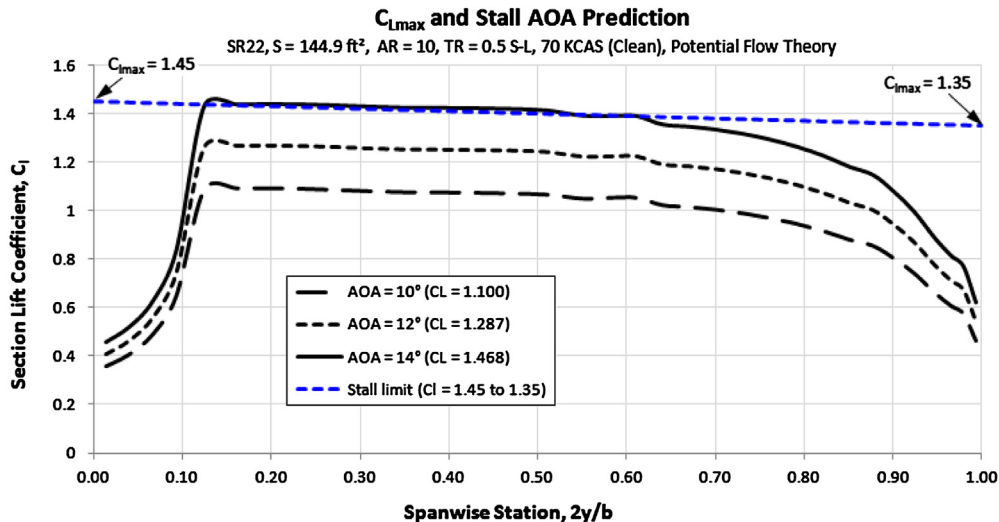


FIGURE 9-61 Lift distribution near stall as predicted by the vortex-lattice method. The waviness in places is due to the discontinuity in the segment of the wing, which features a leading edge extension.

#### 9.5.12 Step-by-step: $C_{L\max}$ Estimation per USAF DATCOM Method 2

The wing’s maximum lift coefficient can be calculated using the following method from the USAF DATCOM (where it is referred to as Method 2). While somewhat involved, the method allows the estimation of the

maximum lift and angle-of-attack for maximum lift at subsonic speeds. The method is empirically derived and is based on experimental data for predicting the subsonic maximum lift and the angle-of-attack for maximum lift of high aspect ratio, untwisted, constant section wings.

Generally, the maximum lift of high-aspect-ratio wings at subsonic speeds is directly related to the maximum lift of the wing section or airfoil. According to the DATCOM, the wing planform shape influences the maximum lift obtainable, although its effect is less important than that of the airfoil's section characteristics.

### **Step 1: Determine the Taper Ratio Correction Factor**

First determine if the wing in question complies with the DATCOM's "definition" of a high-aspect-ratio wing. Do this by determining the *taper ratio correction factor* (TRCF),  $C_1$ , from Figure 9-62. Alternatively, the TRCF can be approximated using the following empirical expression, based on the curve of Figure 9-62.

$$C_1 = \frac{1}{2} \sin \left\{ \pi(1 - \lambda)^{1.5 + 0.8 \sin^{0.4}(\pi(1 - \lambda)^2)} \right\} \quad (9-76)$$

### **Step 2: Determine if Wing Qualifies as "High AR"**

Then determine whether the wing complies with the DATCOM's "definition" of a high-aspect-ratio wing:

$$AR > \frac{4}{(C_1 + 1) \cos \Delta_{LE}} \quad (9-77)$$

If the airplane's  $AR$  is larger than the ratio of Equation (9-77) then the procedure is applicable to it.

### **Step 3: Determine the Leading Edge Parameter**

Determine the leading edge parameter (LEP), denoted by  $\Delta y$ , which is used several steps later. The parameter  $\Delta y$  is the difference between airfoil ordinate at 6% chord and ordinate at 0.15% chord and is represented in terms of %. Thus, a value of 0.03 would be written as 3.00. Since this method assumes a single airfoil wing, it is appropriate to approximate the leading

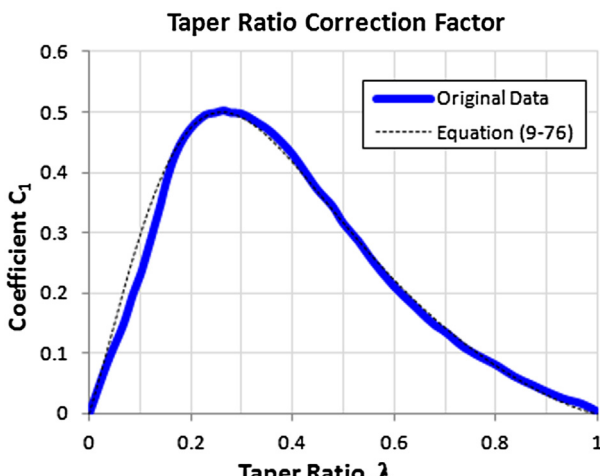


FIGURE 9-62 Taper ratio correction factor (Based on Ref. [1]).

edge parameter based on the geometry of the airfoil at the mean geometric chord. Figure 9-63 illustrates the process. Note that this is based on an airfoil ordinate table that has been normalized to a chord of unity ( $C = 1$ ).

The listing below contains expressions for the LEP,  $\Delta y$ , for selected types of airfoils, based on their thickness-to-chord ratios ( $t/c$ ). The explicit expressions in the list may make it easier to determine  $\Delta y$  without having to perform calculations based on the ordinate table. The list is based on Figure 2.2.1-8 of the USAF DATCOM [1].

NACA 4- and 5-digit Series airfoils:

$$\Delta y = 25(t/c) \quad (9-78)$$

NACA 63-Series:

$$\Delta y = 22.132(t/c) \quad (9-79)$$

NACA 64-Series:

$$\Delta y = 20.411(t/c) \quad (9-80)$$

NACA 65-Series:

$$\Delta y = 19.091(t/c) \quad (9-81)$$

NACA 66-Series:

$$\Delta y = 18.182(t/c) \quad (9-82)$$

Biconvex:

$$\Delta y = 11.667(t/c) \quad (9-83)$$

Double wedge:

$$\Delta y = 5.882(t/c) \quad (9-84)$$

### **Step 4: Determine the Max Lift Ratio**

Determine the ratio  $C_{Lmax}/C_{lmax}$  using Figure 9-64. The figure illustrates the variation of the ratio between the wing's maximum lift coefficient and the section maximum lift coefficient as a function of the leading edge sweep and the LEP  $\Delta y$ :

where

$C_{lmax}$  = section maximum lift coefficient  
 $C_{Lmax}$  = maximum three-dimensional lift coefficient

### **Step 5: Determine the Mach Number Correction Factor**

Determine the Mach number correction factor (MNCF),  $\Delta C_{Lmax}$ , from Figure 9-65, using the LEP, the wing's leading edge sweep ( $\Delta_{LE}$ ), and Mach number evaluated at the stalling speed. Note that the reference

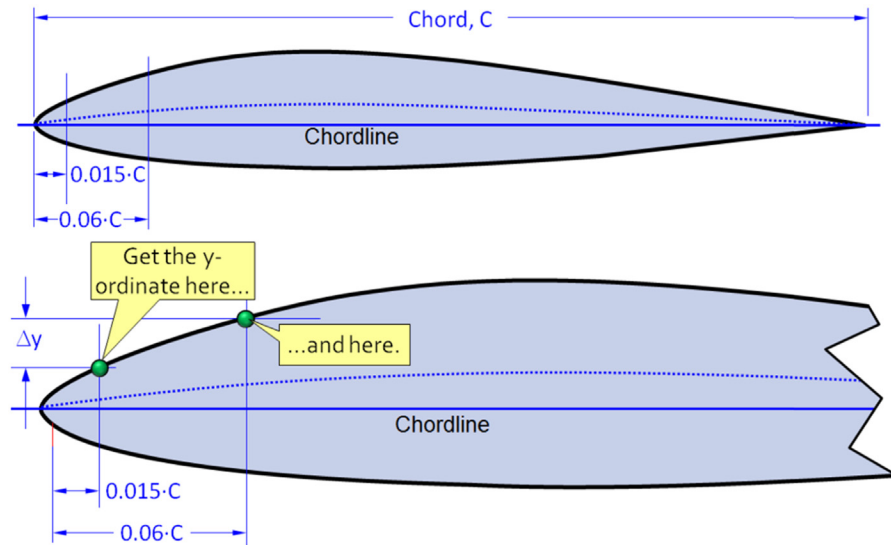
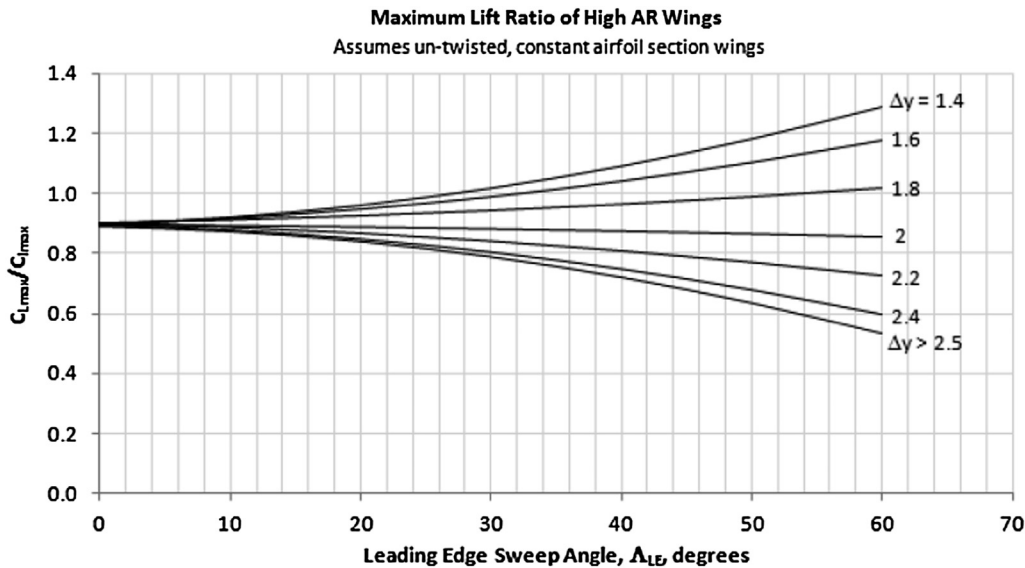


FIGURE 9-63 Determination of the LEP (Based on Ref. [1]).

FIGURE 9-64  $C_{L\max}/C_{l\max}$  ratio data plot (Based on Ref. [1]).

document also presents similar graphs for  $\Lambda_{LE} = 40^\circ$  and  $60^\circ$ , but such sweeps are rarely used on GA aircraft.

#### Step 6: Calculate the $C_{L\max}$

Calculate the wing's maximum lift coefficient  $C_{L\max}$  using the expression below:

$$C_{L\max} = \left( \frac{C_{L\max}}{C_{l\max}} \right) C_{l\max} + \Delta C_{L\max} \quad (9-85)$$

where

$C_{L\max}/C_{l\max}$  = ratio obtained from Figure 9-64

$C_{l\max}$  = section maximum lift coefficient

$\Delta C_{L\max}$  = Mach number correction factor obtained from Figure 9-65

#### Step 7: Determine Zero Lift Angle and Lift Curve Slope

Determine the wing's zero lift angle,  $\alpha_{ZL}$ , and lift curve slope,  $C_{L\alpha}$ . Both have to be in terms of degrees.

#### Step 8: Determine a Correction for the Stall Angle-of-attack

Determine the correction angle,  $\Delta\alpha_{stall}$ , for the nonlinear effects of vortex flow from Figure 9-66.

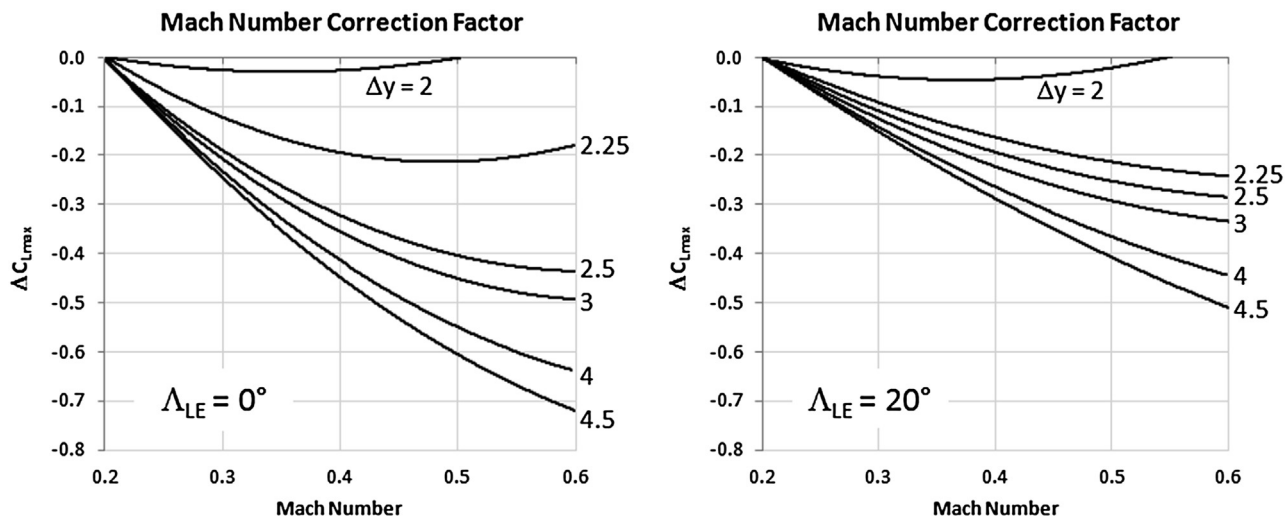


FIGURE 9-65 Determine  $\Delta C_{L\max}$  using the above graphs (Based on Ref. [1]).

### Step 9: Determine the Wing Stall Angle-of-attack

The angle-of-attack of the wing at stall can be calculated from the following equation:

$$\alpha_{stall} = \frac{C_{L\max}}{C_{L_\alpha}} + \alpha_{ZL} + \Delta\alpha_{stall} \quad (9-86)$$

where

$C_{L\alpha}$  = wing lift curve slope

$\alpha_{ZL}$  = wing zero lift angle

$\Delta\alpha_{stall}$  = correction factor from Figure 9-66

### EXAMPLE 9-11

Compare the calculated maximum lift coefficient for the Cirrus SR22 using the DATCOM method to the known value of  $C_{L\max}$  for the airplane, calculated as shown in Example 9-9.

#### Solution

All values in this solution were obtained by scaling the airplane in the 3-view (see Figure 16-15) based on the indicated wingspan. A reader trying to reproduce the solution may come up with slightly different dimensions.

Based on the 3-view, the leading edge sweep angle was found to equal:  $\Lambda_{LE} = 1.93^\circ$

The aspect ratio is found using the wingspan and area information in the 3-view:

$$AR = \frac{b^2}{S} = \frac{38.3^2}{144.9} = 10.12$$

Using Figure 16-15 the taper ratio is estimated to be 0.5. Additionally, the leading edge parameter  $\Delta y$  for the NACA 65-415 airfoil is approximately 2.86%, obtained using Equation (9-81).

The wing was checked to see if it complies with the DATCOM definition of a high AR wing. To do this, we calculate the taper ratio correction factor using Equation (9-76), which turns out to be  $C_1 = 0.3064$ .

Therefore, from Equation (9-77):

$$\frac{4}{(C_1 + 1)\cos\Lambda_{LE}} = \frac{4}{(0.3064 + 1)\cos(1.93^\circ)} = 3.064 < 9.32$$

This simply means that the method is applicable to the SR22. Next read Figure 9-64 to determine the ratio  $C_{L\max}/C_{l\max}$ . The resulting ratio is approximately:

$$C_{L\max}/C_{l\max} = 0.89$$

Note that a maximum section lift coefficient is estimated at  $C_{l\max} = 1.40$ , using Figure 9-60 (and as shown in Example 9-9). Next, let's estimate the Mach number correction factor (MNCF),  $\Delta C_{L\max}$ . We do this using Figure 9-65 with  $\Lambda_{LE} = 0$  (since the LE sweep is only  $1.93^\circ$ ),  $M = 0.10$  and  $\Delta y = 3.5$ :

$$\Delta C_{L\max} = 0$$

### EXAMPLE 9-11 (cont'd)

We can now estimate the three-dimensional maximum lift coefficient for the wing using Equation (9-85):

$$C_{L_{\max}} = \left( \frac{C_{L_{\max}}}{C_{l_{\max}}} \right) C_{l_{\max}} + \Delta C_{L_{\max}} = (0.89)1.40 + 0 = 1.246$$

The difference between the POH and estimated value using the POH is some 11.6%. Next, estimate the stall AOA. We do this by first estimating the lift curve slope for the SR22 using Equation (9-57), repeated for convenience.

$$C_{L_{\alpha}} = \frac{2\pi \cdot AR}{2 + \sqrt{\frac{AR^2 \beta^2}{\kappa^2} \left( 1 + \frac{\tan^2 \Lambda_{c/2}}{\beta^2} \right) + 4}}$$

where

$$AR = \text{wing aspect ratio} = 10.12$$

$$\beta = \text{Mach number parameter (Prandtl-Glauert)} = (1 - M^2)^{0.5} \approx 0.995. \text{ Call it } 1$$

$$\kappa = \text{ratio of 2D lift curve slope to } 2\pi = 0.107 \times (180/\pi)/(2\pi) = 0.9757$$

$\Lambda_{c/2}$  = sweepback of mid-chord is close  $0^\circ$

$$C_{L_{\alpha}} = \frac{2\pi \cdot 10.12}{2 + \sqrt{\frac{10.12^2}{0.9757^2}(1) + 4}} = 5.061 \text{ per rad}$$

$$= 0.08834 \text{ per deg}$$

From Table 8-5, the zero-lift angle for the 65-415 airfoil is  $\alpha_{ZL} = -2.6^\circ$ . Next, let's determine the nonlinear vortex flow-correction angle from Figure 9-66. Using the leading edge sweep angle  $\Lambda_{LE} = 1.93^\circ$  and the leading edge parameter  $\Delta y = 2.86\%$ , the correction angle is approximately  $\Delta\alpha_{stall} = 1.3^\circ$ . This allows us to calculate the stall angle-of-attack using Equation (9-16):

$$\alpha_{C_{L_{\max}}} = \frac{C_{L_{\max}}}{C_{L_{\alpha}}} + \alpha_{ZL} + \Delta\alpha_{stall} = \frac{1.291}{0.08834} - 2.6^\circ + 1.3^\circ$$

$$= 13.3^\circ$$

The actual stall angle for the SR22 is not published, so a comparison cannot take place. However, it is thought that this angle is probably  $1^\circ$  to  $3^\circ$  too low.

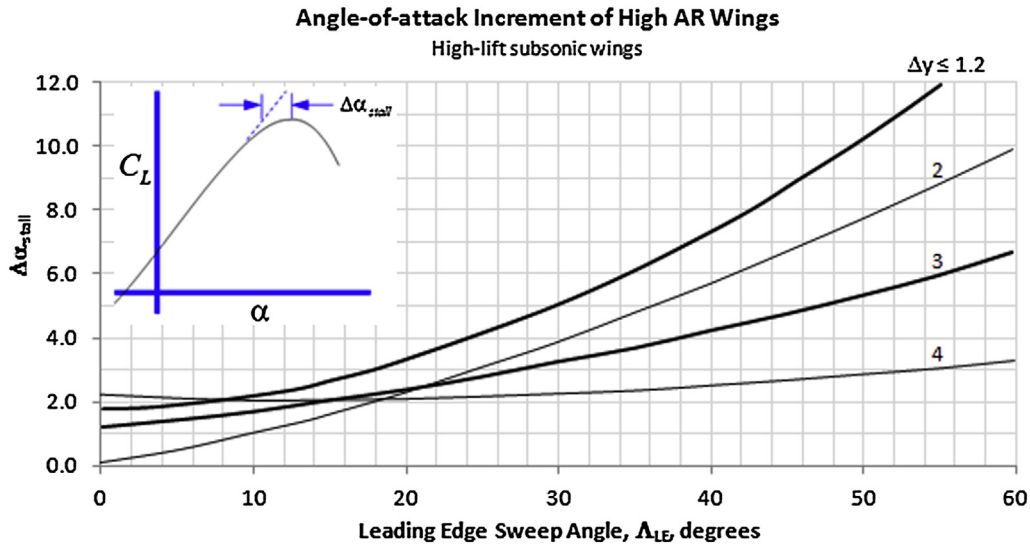


FIGURE 9-66 Determine  $\Delta\alpha_{stall}$  using the above graphs (Based on Ref. [1]).

#### 9.5.13 $C_{L_{\max}}$ for Selected Aircraft

Examples of the maximum lift coefficient for selected aircraft are shown in Table 9-8. The aspiring designer is encouraged to be realistic and careful when estimating

this value. It has a profound impact on the capability of the aircraft; an overestimation inevitably results in an undersized wing area, which could have a major impact on the stall and low speed characteristics of the

**TABLE 9-8** Maximum Lift Coefficients for Selected Aircraft

Name	Gross Weight	Wing Area	Stalling Speed, KCAS		Maximum Lift Coefficient		Source
	lb <sub>f</sub>	ft <sup>2</sup>	V <sub>0</sub> (flaps)	V <sub>1</sub> (clean)	C <sub>Lmax0</sub>	C <sub>Lmax1</sub>	
<b>SINGLE-ENGINE</b>							
Aerotec A-122A	1825	145	39	57	2.44	1.16	1
Bede BD-5A Micro	660	47	48	54	1.78	1.41	1
Cirrus SR20	3050	145	59	67	1.79	1.38	2
Cirrus SR22	3400	145	60	70	1.92	1.41	2
Cessna 162 Skycatcher	1320	120	40	44	2.03	1.68	1
Cessna 172 Skyhawk	2450	174	47	51	1.88	1.60	1
Cessna 182 Skylane	2950	174	50	56	2.00	1.60	2
Cessna 208B Grand Caravan	8750	279	61	78	2.48	1.52	2
Embraer EMB-201	3417	194	51	57	2.00	1.60	1
Let Z-37 Čmelák (Bumblebee)	3855	256	45	49	2.19	1.85	1
Neiva N621A	3306	185	57	64	1.65	1.31	1
Piper PA-46-350 Malibu	4340	175	58	69	2.18	1.56	1
Taylor J.T.1 Monoplane	610	76	33	40	2.18	1.48	1
Transavia PL-12 Airtruk	3800	256	52	55	1.62	1.45	1
<b>TWIN-ENGINE PROPELLER</b>							
Beechcraft Baron 55	5100	199	73	88	1.42	0.98	1
Beechcraft Duke B60	6775	213	76	86	1.63	1.27	3
Beechcraft Queenair B80	8800	294	71	85	1.75	1.22	1
Cessna 421 Golden Eagle	4501	215	74	83	1.13	0.90	6
Cessna 337 Skymaster	4630	201	61	70	1.83	1.39	1
Partenavia P.68	1960	200	56	64	0.92	0.71	1
Pilatus Britten-Norman BN-2B Islander	2993	325	40	50	1.70	1.09	1
Piper Seminole	3800	184	55	57	2.02	1.88	5
Rockwell Commander 112A	2650	152	54	61	1.77	1.38	4
Vulcanair P.68 Observer	4594	200	57	68	2.09	1.47	1
<b>COMMUTER TURBOPROPS</b>							
Beechcraft Kingair C90	9650	294	72	80	1.87	1.51	1
Beechcraft Kingair 100	10,600	298	76	92	1.82	1.24	1
CASA C-212 Aviocar	13,889	431	62	72	2.48	1.84	1
Frakes conversion Turbo-Mallard	14,000	444	66	76	2.14	1.61	1
Let L-140 Turbolet	11,905	354	64	83	2.43	1.44	1
Lockheed Model 35 Orion P-3	135,000	1300	112	133	2.44	1.73	1
Nomad N22	8000	324	47	65	3.30	1.73	1

**TABLE 9-8** Maximum Lift Coefficients for Selected Aircraft—cont'd

Name	Gross Weight	Wing Area	Stalling Speed, KCAS		Maximum Lift Coefficient		Source
	lb <sub>f</sub>	ft <sup>2</sup>	V <sub>0</sub> (flaps)	V <sub>1</sub> (clean)	C <sub>Lmax0</sub>	C <sub>Lmax1</sub>	
Piper PA-31P Pressurized Navajo	7800	229	72	80	1.94	1.57	1
Rockwell Commander 630A	10,250	266	77	82	1.92	1.69	1
Shorts SD3-30	22,000	453	74	92	2.62	1.69	1
<b>BUSINESS JETS</b>							
Beechjet 400A	16,100	241	82	87	2.93	2.60	1
Cessna Citation CJ1	10,700	240	77	82	2.22	1.96	1
Cessna Citation Mustang	8645	210	73	91	2.23	1.47	7
Dassault Falcon 900	45,500	527	85	106	3.53	2.27	1
Dassault-Breguet Mystère-Falcon 900	20,640	528	82	104	1.72	1.07	1
Dassault Falcon 2000X	41,000	527	84	98	3.26	2.39	1
Embraer Phenom 100	10,472	202	77	100	2.58	1.53	1
Gates Learjet 24D	13,500	232	99	126	1.75	1.08	1
Gulfstream Aerospace IV	71,700	950	108	120	1.91	1.55	1
Safire S-26	5130	143	69	92	2.23	1.26	1
<b>COMMERCIAL JETLINERS</b>							
A320-200	170,000	1320	121	179	2.60	1.19	1
A320-B4	360,000	2800	120	150	2.64	1.69	8
A330	520,000	3892	120	137	2.74	2.10	8
A340-200	610,000	3892	135	145	2.54	2.20	8
Boeing 727-200	172,000	1700	106	171	2.66	1.02	1
B737-400	150,000	1135	146	206	1.83	0.92	8
B757-200	255,000	1994	120	145	2.62	1.80	8
B777-200A	545,000	4005	170	150	2.43	1.55	8
Fokker 100	95,000	1006	109	160	2.35	1.09	1
Lockheed L-1011-1 Tristar	430,000	3456	125	166	2.35	1.33	1

**Sources:**

1. Jane's All the World's Aircraft
2. Type POH
3. [http://www.classg.com/aircraft\\_specs.i?cmd=compare&manid1=56&model1=60+Duke](http://www.classg.com/aircraft_specs.i?cmd=compare&manid1=56&model1=60+Duke)
4. [http://www.classg.com/aircraft\\_specs.i?cmd=compare&acids=568%2C520%2C172%2C922&replaceid=520&manid2=89&model2=phenom+100](http://www.classg.com/aircraft_specs.i?cmd=compare&acids=568%2C520%2C172%2C922&replaceid=520&manid2=89&model2=phenom+100)
5. [http://www.classg.com/aircraft\\_specs.i?cmd=compare&acids=568%2C520%2C172%2C922&replaceid=520&manid2=89&model2=phenom+100](http://www.classg.com/aircraft_specs.i?cmd=compare&acids=568%2C520%2C172%2C922&replaceid=520&manid2=89&model2=phenom+100)
6. [http://www.aeroresourcesinc.com/store\\_images/classifieds/119-1.pdf](http://www.aeroresourcesinc.com/store_images/classifieds/119-1.pdf)
7. <http://viewer.zmags.com/publication/f8e9ba38#f8e9ba38/1>
8. <http://webpages.charter.net/anw/ANW/performance.html>

TABLE 9-9 Examples of Oswald's Span Efficiencies for Selected Aircraft (Based on Ref. [39])

Single-engine Propeller						Twin-engine Propeller					
Manufacturer	Model	S, ft <sup>2</sup>	b, ft	AR	e	Manufacturer	Model	S, ft <sup>2</sup>	b, ft	Ag	e
Beechcraft	35	184	33.5	6.10	0.82	Beechcraft	AT-7	349	47.7	6.51	0.74
Boeing-Stearman	PT-18	298	32.2	6.94	0.75	Cessna	AT-8	295	41.9	5.96	0.61
Cessna	OE-2	174	36.0	7.45	0.7	Douglas	A-26B	540	70.0	9.07	0.79
Cessna	180	174	35.8	7.38	0.75	Curtiss	C-46A	1360	108.1	8.59	0.88
Cessna	150	160	33.3	6.94	0.77	Douglas	C-47B	987	95.5	9.24	0.89
Cessna	172	174	36.1	7.48	0.77	North American	B-25D	610	67.6	7.49	0.78
Cessna	182	174	36.0	7.45	0.84	Martin	B-26F	658	71.0	7.66	0.76
Cessna	185	174	35.8	7.38	0.86	Cessna	310	175	35.0	7.00	0.73
Cessna	177	174	35.5	7.24	0.57	Gulfstream	G-I	610.3	76.5	9.59	0.78
Douglas	O-46A	332	45.8	6.30	0.8	SAAB	SF340	450	70.3	10.99	0.8
Stinson	L-5	155	34.0	7.46	1.02						

new design. Always compare your maximum lift coefficient to that of similar aircraft to ensure unrealistic overestimation is avoided.

#### 9.5.14 Estimation of Oswald's Span Efficiency

The *Oswald span efficiency* is a vital parameter required to predict the lift-induced drag of an airplane. It is named after W. Bailey Oswald, who first defined it in a NACA report published in 1933 [36]. Interestingly, Oswald called it the *airplane efficiency factor*. It is not always easy to estimate, but here several methods will be demonstrated. Note that examples of the Oswald efficiency for selected single- and twin-engine aircraft are shown in Table 9-9.

##### Basic Definition

The span efficiency can be defined as the resultant of the lift and side force, divided by the product of  $\pi$ , AR, and the lift-induced drag coefficient, as shown below. The expression assumes that  $C_{Di}$  is already known, for instance through flight or wind tunnel testing.

Definition of the span efficiency:

$$e = \frac{C_L^2 + C_Y^2}{\pi \cdot AR \cdot C_{Di}} \quad (9-87)$$

where

$C_L$  = lift coefficient

$C_Y$  = side force coefficient

$C_{Di}$  = induced drag coefficient

AR = reference aspect ratio

If the wing has winglets the aspect ratio should be corrected by modifying the AR using the following expression [32]:

$$AR_{corr} = AR \left( 1 + \frac{1.9h}{b} \right) \quad (9-88)$$

where

$AR$  = original "clean wing" AR

$AR_{corr}$  = boosted AR

$b$  = wingspan

$h$  = height of winglets

##### Method 1: Empirical Estimation for Straight Wings

Raymer [5] presents the following statistical expression to estimate the Oswald efficiency of straight wings. Note that it omits dependency on taper ratio, but is still handy for conceptual design work. The expression is limited to lower AR only:

$$e = 1.78(1 - 0.045AR^{0.68}) - 0.64 \quad (9-89)$$

##### Method 2: Empirical Estimation for Swept Wings

Raymer [5] also presents the following statistical expression to estimate the Oswald efficiency of swept wings. It has limitations similar to Equation (9-89):

$$e = 4.61(1 - 0.045AR^{0.68})(\cos \Lambda_{LE})^{0.15} - 3.1 \quad (9-90)$$

Brandt et al. [4] present the following expression to estimate the factor:

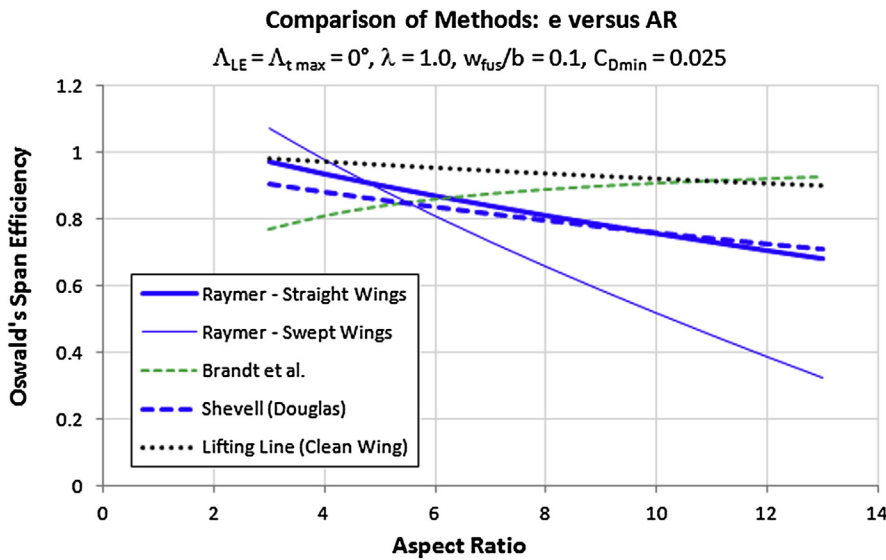


**FIGURE 9-67** A comparison of four methods for estimating the Oswald span efficiency factor.

$$e = \frac{2}{2 - AR + \sqrt{4 + AR^2(1 + \tan^2 \Lambda_{t\max})}} \quad (9-91)$$

where

$\Lambda_{LE}$  = leading edge sweep angle

$\Lambda_{t\max}$  = sweep angle of the maximum wing thickness line

### Method 3: Douglas Method

Shevell [37] presents the following expression to calculate the Oswald efficiency, which is in part based on unpublished studies by the Douglas aircraft company. Its presentation has been modified slightly to better fit the discussion here. Other than that, it returns exactly the same values.

$$e = \frac{1}{\pi \cdot AR \cdot r \cdot C_{Dmin} + 1 / ((1 + 0.03t - 2t^2)u)} \quad (9-92)$$

where

$t$  = fuselage width to wingspan ratio =  $w_{fus}/b$

$w_{fus}$  = maximum width of the fuselage and  $b$  is the wingspan

$u$  = correction factor for non-elliptical wing planform, typically 0.98 to 1.00.

$r$  = parasitic correction factor and  $r = 0.38 - \Lambda_{LE}/3000 + \Lambda_{LE}^2/15000$  and  $\Lambda_{LE}$  is in degrees

### Method 4: Lifting Line Theory

The *lifting line theory* is presented in Section 9.7, *Numerical analysis of the wing* and Section 15.3.4, *The*

*lift-induced drag coefficient:  $C_{Di}$ .* The Oswald span efficiency can be calculated using the method shown in Section 9.7.5, *Computer code: Prandtl's lifting line method.*

Note that Methods 1 through 4 are compared in Figure 9-67 with a straight Hershey-bar wing. The results for the lifting line theory are theoretical results for a clean wing. Also note that Methods 1 and 2 do not reflect dependency on the taper ratio,  $\lambda$ .

### Method 5: USAF DATCOM Method for Swept Wings – Step-by-step

The USAF DATCOM [1, p. 2.2.1-8] is based on a paper by Frost and Rutherford [38] published in 1963. The paper suggests that the Oswald efficiency depends on the factor  $R$ , which is the ratio between the actual drag force of a wing and that of an elliptical wing. The idea assumes that both utilize a symmetrical airfoil. Using statistical analysis of a large number of NACA reports, the authors devised a method to estimate the span efficiency for a larger range of  $AR$ . Per Ref. [37] the method compared to test data that included following planform and flight conditions:

Aspect ratio:

$$2 \leq AR \leq 10.7$$

Taper ratio:

$$0 \leq \lambda \leq 0.713$$

Leading edge sweep angle:

$$19.1^\circ \leq \Lambda_{LE} \leq 63.4^\circ$$

Leading edge suction parameter:

$$2 \leq R_{LER} \leq 10$$

Mach number:

$$0.13 \leq M \leq 0.81$$

This does not mean it is not applicable to other planform shapes. The method is used to estimate a special factor, called the *leading edge suction parameter*,  $R$ , which is used with the following expression to estimate the span efficiency:

$$e = \frac{1.1(C_{L\alpha}/AR)}{R(C_{L\alpha}/AR) + (1-R)\pi} \quad (9-93)$$

where  $R$  = leading edge suction parameter (must be read from Figure 4.7 in the reference document).

This method requires several parameters to be determined, which are then used to extract the LE suction parameter,  $R$ , for use with Equation (9-93).

### Step 1: Calculate the Lift Curve Slope

Lift curve slope can be calculated from Equation (9-57) (where the variables are explained):

$$C_{L\alpha} = \frac{\partial C_L}{\partial \alpha} = \frac{2\pi \cdot AR}{2 + \sqrt{\left(\frac{AR \cdot \beta}{\kappa}\right)^2 \left(1 + \frac{\tan^2 \Lambda_{C/2}}{\beta^2}\right) + 4}}$$

### Step 2: Calculate the Leading Edge Suction Parameter

Leading edge suction parameter:

$$R_{LER} = \frac{\rho V l_{LER}}{\mu}$$

where

$l_{LER}$  = leading edge radius (from airfoil data)

$V$  = airspeed

$\mu$  = air viscosity, in  $\text{lb}_f \cdot \text{s}/\text{ft}^2$

$\rho$  = air density, slugs/ $\text{ft}^3$

### Step 3: Calculate Special Parameter 1

Special parameter 1:

$$P_1 = \frac{AR \cdot \lambda}{\cos \Lambda_{LE}}$$

where

$\lambda$  = taper ratio

$\Lambda_{LE}$  = sweep of the LE

### Step 4: Calculate Special Parameter 2

Special parameter 2:

$$P_2 = R_{LER} \times \cot \Lambda_{LE} \sqrt{1 - M^2 \cos^2 \Lambda_{LE}}$$

where

$M$  = Mach number

### Step 5: Read or Calculate the Leading Edge Suction Parameter

If  $P_2 \leq 1.3 \times 10^5$  determine  $R$  from Figure 9-68 or calculate from the following expression:

$$R = \left( -4.728 + 2.185 \cdot \log_{10}(P_2) - 0.2131 \cdot \log_{10}(P_2)^2 \right) + 0.095 \cdot \sin\left(\frac{\pi P_1}{20}\right)$$

If  $P_2 > 1.3 \times 10^5$  determine  $R$  from Figure 9-68 or calculate from the following expression:

$$R = 0.86 + 0.1119 \cdot \left(\frac{P_1}{10}\right)^{\frac{1}{1.8+P_1}}$$

Neither equation is based on theoretical analysis, but rather derived using a curve fit methodology that results in acceptable fit to the graphs.

## EXAMPLE 9-12

Determine the Oswald's span efficiency for the Learjet 45XR, whose  $AR = 7.33$  and  $TR = 0.391$ . Compare methods 2 and 4. Assume the airfoil has a section lift curve slope of  $2\pi$ , a LE sweep of  $17^\circ$ , mid-chord sweep of  $10.5^\circ$ , and a LE radius of 0.1 ft. Assume the maximum thickness is at the mid-chord as well. Assume an airspeed of  $M = 0.3$  at S-L on a standard day ( $V = 335 \text{ ft/s}$ ) and ignore the fact the airplane has winglets.

### Solution

#### Method 2

Using Equation (9-90):

$$\begin{aligned} e &= 4.61(1 - 0.045AR^{0.68})(\cos \Lambda_{LE})^{0.15} - 3.1 \\ &= 4.61(1 - 0.045(7.33)^{0.68})(\cos(17^\circ))^{0.15} - 3.1 \\ &= 0.6807 \end{aligned}$$

### EXAMPLE 9-12 (cont'd)

Using Equation (9-91):

$$\begin{aligned} e &= \frac{2}{2 - AR + \sqrt{4 + AR^2(1 + \tan^2 \Lambda_{f\max})}} \\ &= \frac{2}{2 - 7.33 + \sqrt{4 + 7.33^2(1 + \tan^2(10.5^\circ))}} = 0.8374 \end{aligned}$$

#### Method 4

**Step 1:** Mach number parameter:

$$\beta = \sqrt{1 - M^2} = \sqrt{1 - 0.3^2} = 0.9539$$

$$\begin{aligned} C_{L_a} &= \frac{2\pi \cdot AR}{2 + \sqrt{\left(\frac{AR \cdot \beta}{\kappa}\right)^2 \left(1 + \frac{\tan^2 \Lambda_{C/2}}{\beta^2}\right) + 4}} \\ &= \frac{2\pi \cdot 7.33}{2 + \sqrt{\left(\frac{7.33 \times 0.9539}{1}\right)^2 \left(1 + \frac{\tan^2 10.5^\circ}{0.9539^2}\right) + 4}} \\ &= 4.90 \end{aligned}$$

**Step 2:**

$$R_{I_{LER}} = \frac{\rho V I_{LER}}{\mu} = \frac{(0.002378)(335)(0.1)}{3.745 \times 10^{-7}} = 212718$$

**Step 3:**

$$P_1 = \frac{AR \cdot \lambda}{\cos \Lambda_{LE}} = \frac{7.33 \times 0.391}{\cos 17^\circ} = 2.997$$

#### Step 4:

$$\begin{aligned} P_2 &= R_{I_{LER}} \times \cot \Lambda_{LE} \sqrt{1 - M^2 \cos^2 \Lambda_{LE}} \\ &= 212718 \times \cot(17^\circ) \sqrt{1 - 0.3^2 \cos^2(17^\circ)} = 6.67 \times 10^5 \end{aligned}$$

**Step 5:** Since  $P_2 > 1.3 \times 10^5$ ,  $R$  can be determined as follows:

$$\begin{aligned} R &= 0.86 + 0.1119 \cdot \left(\frac{P_1}{10}\right)^{\frac{1}{1.8+P_1}} \\ &= 0.86 + 0.1119 \cdot \left(\frac{2.997}{10}\right)^{\frac{1}{1.8+2.997}} = 0.947 \end{aligned}$$

#### Step 6:

$$\begin{aligned} e &= \frac{1.1(C_{L_a}/AR)}{R(C_{L_a}/AR) + (1 - R)\pi} \\ &= \frac{1.1(4.90/7.33)}{0.947(4.90/7.33) + (1 - 0.947)\pi} = 0.919 \end{aligned}$$

Clearly, there is a range of values to consider, begging the question: which one should we pick? Unless there is confidence in a particular method, this author would take the average of the three (0.812) until a better number is determined.

## 9.6 WING STALL CHARACTERISTICS

All normal airplanes need to exceed a certain minimum airspeed before they can become airborne and maintain level flight. The minimum airspeed required for level flight is the stalling speed. What transpires at this speed arguably inflicts one of the most important design challenges for the wing design, or for that matter, the entire airplane. This section is dedicated to the stall and intended to provide important information about this well-known phenomenon.

It is helpful to visualize the stall maneuver in terms of altitude as well as airspeed. A pilot-controlled stall maneuver is depicted in Figure 9-69. It begins with engine power being cut and a subsequent deceleration. For compliance with 14 CFR Part 23.201, *Wings level stall*,

this deceleration should be as close to 1 KCAS per second as possible.

As the airplane slows down, a larger and larger  $\alpha$  is required to maintain altitude and the *approach to stall* phase culminates in the stall itself, as the airplane reaches  $\alpha_{STALL}$  or  $\alpha_{CLmax}$  and breaks the stall by the sudden drop of the nose. The drop leads to a dive, which, in turn, results in altitude being lost, as shown in the figure. This altitude loss depends on the size of the aircraft and can be as small as 25–50 ft for a small and light homebuilt or ultralight aircraft; 200–400 ft for a two- to four-seat single-engine GA aircraft; to 2000 ft or more for a large commercial jetliner aircraft. The *stall recovery* phase ends with power being added and a subsequent climb to altitude.

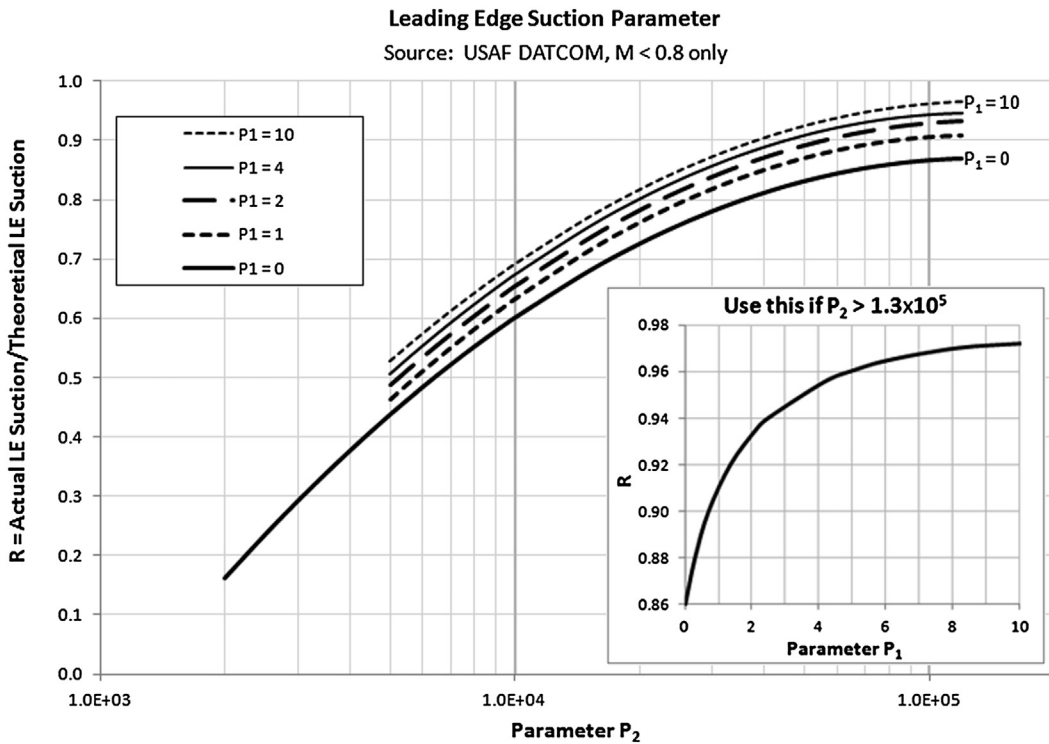


FIGURE 9-68 Leading edge suction parameter (Based on Ref. [4]).

### 9.6.1 Growth of Flow Separation on an Aircraft

Flow separation can be a serious issue for aircraft and one that the designer must be fully aware of in order to minimize it. Consider the series of images in Figure 9-70, which shows an airplane seen from the same perspective at different airspeeds. Note that the airspeed ratios and  $AOA$  are approximate and correspond to the design in the figure only, although they would be applicable to many aircraft types. If the aircraft is well designed there should not be any flow

separation regions at the cruising speed. This ensures it will be as efficient as possible at cruise because the flow separation is a source of increased pressure drag. Once slowing down from cruising speed the  $AOA$  begins to rise and it is inevitable that separation regions begin to form and increase as well.

As soon as the airplane has decelerated to approximately its economy cruising speed (or best rate-of-climb airspeed), a separation region has already begun to form in two places: mid-span and at the wing/fuselage juncture. This is highly undesirable,

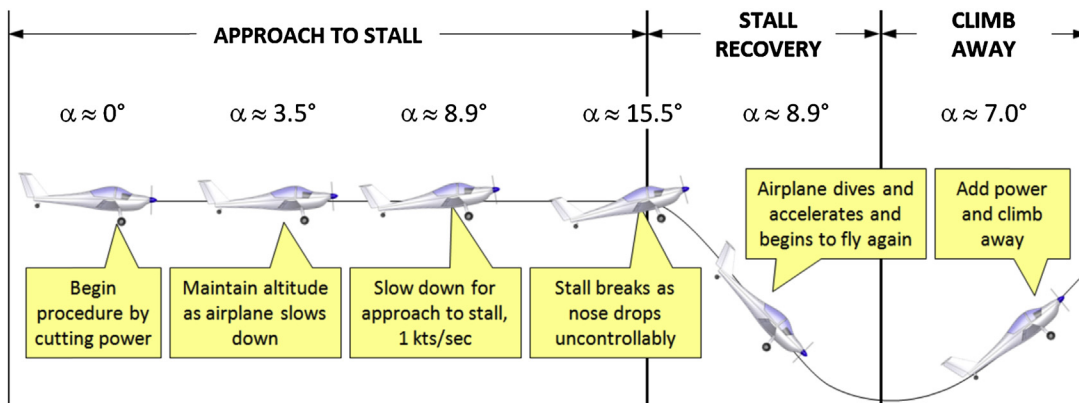


FIGURE 9-69 A schematic showing an approach to stall, stall recovery and subsequent climb away.

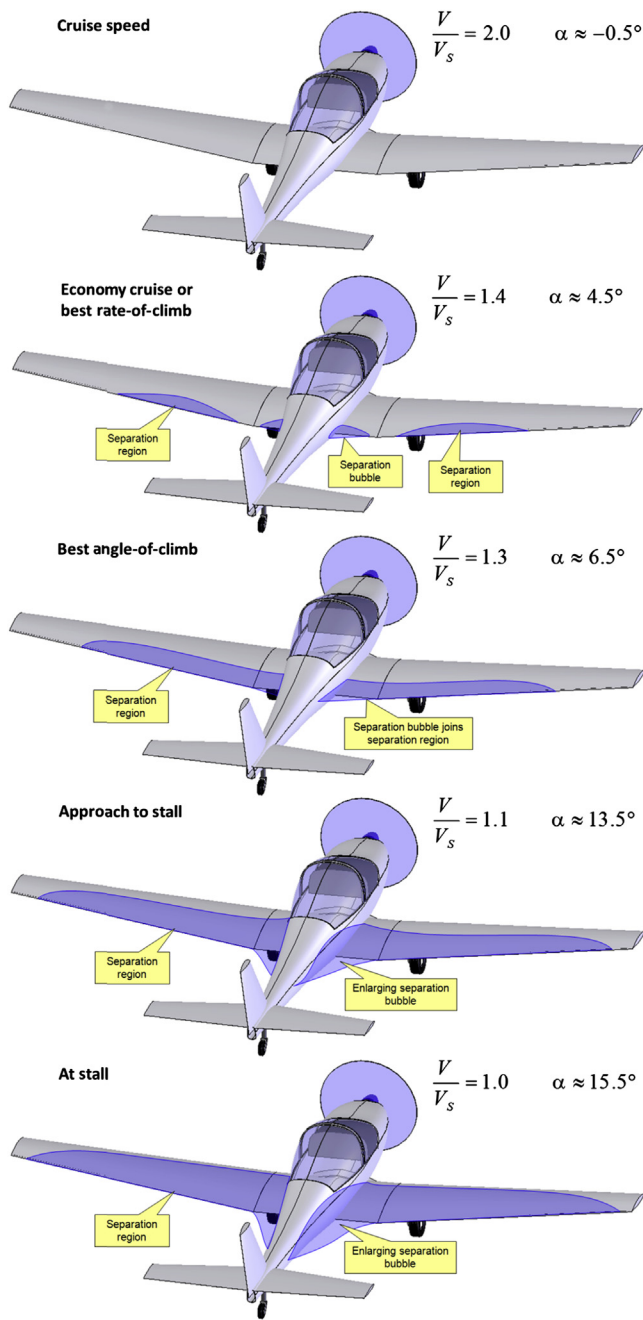


FIGURE 9-70 Growth of flow separation region on an aircraft as seen from a fixed point from the aircraft.

but unavoidable. The separation on the wing depends solely on its geometry. For instance, the aircraft shown in Figure 9-70 has a tapered wing planform whose section lift coefficients are highest around the mid span (see Section 9.4.5, *Straight tapered planforms*), although an attempt has been made here to suppress them at the tip with a geometric wing washout. This causes the flow to begin to separate mid-span rather than elsewhere on the wing. Of course, we seek a progression of the separation that begins at the root and moves

toward the tip, but achieving this would require a large wing washout that would be detrimental to the wing's efficiency, which, by the way, is the reason why a tapered planform was chosen in the first place.

With respect to the flow separation at the wing/fuselage juncture, we must distinguish between separation caused by the high *AOA* on the wing, and that caused by poor geometry between the two. The former is unavoidable with an increase in *AOA*, whereas the latter forms prematurely at relatively low *AOA*, sometimes even before any separation is visible on the wing itself. It is the responsibility of the aerodynamicist to suppress this formation as long as possible and this can be achieved by a careful tailoring of the wing root fairing. The shape of this separation is best described as one having a distinct volume that extends as far as a chord length or more into the flow field behind the juncture. For this reason it is appropriately called a *separation bubble*. The airplane in Figure 9-70 does not have a wing root fairing in this area, but the formation of the separation bubble should encourage the aspiring aircraft designer to design a fairing to suppress it. The pressure inside it is less than in the surrounding area and, therefore, it increases the drag of the aircraft. Additionally, it reduces the airplane's lift curve slope, requiring it to fly at a higher *AOA* than otherwise, with the associated increase in induced drag. A manifestation of such a slope increase is shown in Figure 8-56.

Separation bubbles form easily because of the large rise in airspeed in the channel formed by the wing and the fuselage juncture. To visualize why, one must keep in mind that as a volume of air approaches the airplane, the pressure within it changes from the static or atmospheric pressure it had. As the volume approaches and passes the vehicle, it undergoes a rapid rise and reduction in pressure and a subsequent rise back to atmospheric pressure. The pressure change is associated with the change in the speed of the molecules within the volume, but this deceleration or acceleration is ultimately caused by the geometry over which the volume flows. When the pressure drops, as it does when the airspeed increases, we call the rate at which this takes place a *favorable pressure gradient*. When the pressure rises, as happens when the speed of the molecules slows down, we call it an *adverse pressure gradient*.

These concepts are fundamental to understanding the nature of flow separation. For instance, the volume of air flowing over the upper surfaces of the wing accelerates to a maximum airspeed on the highest part of the airfoil (and depends on the *AOA*). There is also a similar acceleration in airspeed along the fuselage side. At the juncture of the wing and fuselage the effects of the two combine, to make the resulting airspeed greater than elsewhere along the wing (or fuselage). This higher airspeed results in a lower pressure in that region than

elsewhere. Clearly, this pressure must rise back to the atmospheric pressure aft of the wing, however, because it was lower to begin with it must do so more rapidly. This results in a large adverse pressure gradient, which generates a flow deceleration problem that nature solves by separating the flow from the surface. Depending on the geometry of the airplane, this separation can easily begin to form at moderate  $AOA$ s, even during a high-speed climb.

Further deceleration of the aircraft to, say, its best angle-of-climb airspeed, causes the two separation regions to join into a single one that extends from the fuselage to a specific span station. The separation bubble at the wing/fuselage juncture continues to grow into the flow field and this is represented as the volume aft of the wing root trailing edge. As the aircraft approaches stall, a larger and larger area of the wing is covered with flow separation. The direction of the progression of the separation should be away from the fuselage toward the wingtips. Eventually, at stall, the wing is mostly separated, but if well-designed the wingtip should still be un-stalled for roll stability.

General progression of stall on selected wing planform shapes is illustrated in the next section.

### 9.6.2 General Stall Progression on Selected Wing Planform Shapes

### 9.6.3 Deviation from Generic Stall Patterns

While Figures 9-71 and 9-72 provide a fundamental understanding of the impact planform has on stall progression, this is further complicated by the selection of airfoils and wing washout that may be employed for those planform shapes. As an example of this consider Figure 9-73, which shows the stall progression over three separate straight tapered planform shapes [40–42]. The figure shows that once different airfoils,  $AR$ ,  $\lambda$ , and even surface roughness are accounted for the impact of the stall progression will be modified. This introduces asymmetry in the stall progression, as well as regions of initial flow separation, and intermittent and complete stalling. It indicates that each wing style must be evaluated based on its own specific geometry.

Another example is depicted in Figure 9-74, which compares the progression of the separation region on untwisted elliptical and crescent-shaped wing planform shapes, based on a paper written by van Dam, Vijgent, and Holmes [43], showing how the stall progression can be highly affected by vortical flow forming along a highly swept outboard leading edge. In the paper, the authors indicate that the separation-induced vortex flow over the highly swept tips of the crescent wing

improved its stall characteristics when compared to the unmodified elliptical wing (whose stall characteristics were shown to be abrupt and unsteady). This viscous phenomenon delayed full stall of the experimental wing to a higher stall  $AOA$  ( $14.5^\circ$  versus  $13.0^\circ$  for the elliptical wing) and yielded a higher  $C_{L\max}$  (1.06 versus 0.98, respectively). At lower  $AOA$ , the lift characteristics were found to be practically identical, something important to keep in mind for cruise operations. The complex surface flow depicted in Figure 9-80 shows that at  $14^\circ$  the outboard portion of the elliptical wing is fully separated, while it is mostly attached on the crescent wing. The crescent-shaped wing planform is reminiscent of that of numerous species of birds.

### 9.6.4 Tailoring the Stall Progression

Good stall characteristics are simply a question of safety. An airplane that constantly rolls left or right at stall is at an increased risk of entering spin. If the airplane stalls close to the ground, perhaps as a consequence of the pilot banking hard to turn on final approach, there simply is no time (or altitude) to recover, no matter how good spin recovery characteristics the airplane has or how proficient the pilot. The consequence is usually a fatal crash.

There is no good reason to develop an airplane without good stall characteristics, especially considering these can be tailored into the airplane from its inception. It is not being claimed that this is easy, although nowadays it is easier using CFD solvers. CFD methods such as vortex-lattice, doublet-lattice, and other panel codes can be used to determine the distribution of section lift coefficients along the span of the aircraft, even though such solvers ignore viscosity. Navier-Stokes solvers can be of even greater use, as long as the selected turbulence model does not mislead the user in the extent and shape of the flow separation (for instance, see Section 23.3.16, *Reliance upon analysis technology*). Then, armed with an understanding of how the stall progresses along the wing, the designer can select a combination of airfoil types and wing washout to control the stall progression along span of the wing.

#### Design Guidelines

The target stall pattern should always begin at the root and progress toward the tip as the  $AOA$  is increased. This ensures the wingtips will be the last part of the wing to stall, providing vital roll stability and control throughout the maneuver. If inviscid design methodology is used to tailor the stall progression, the goal should be to ensure the section lift coefficient ( $C_l$ ) at the 70% span station is no higher than the maximum lift coefficient ( $C_{l\max}$ ) of the airfoil at that station. Furthermore, from 70% to 100%,  $C_l$  should gradually

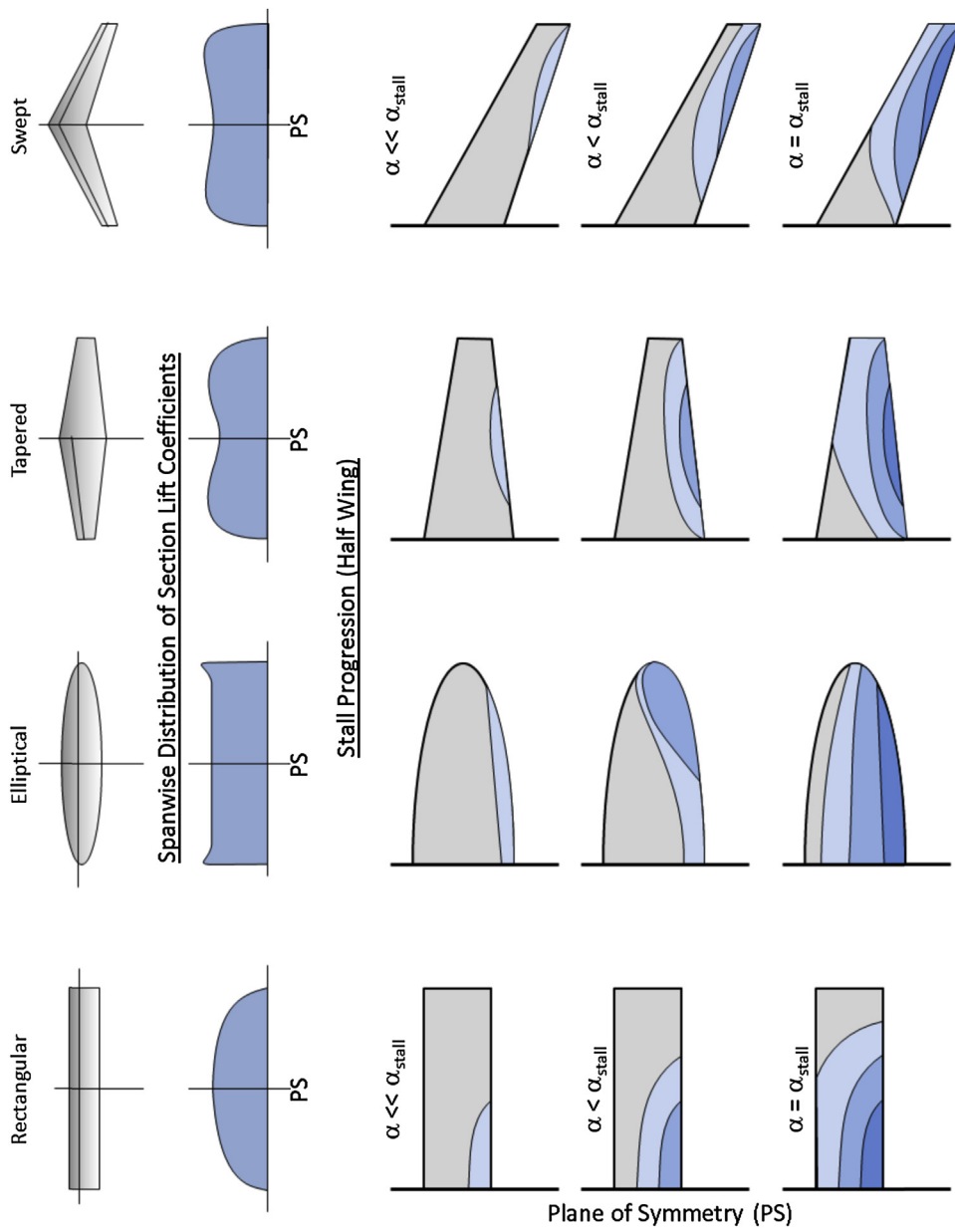


FIGURE 9-71 Stall progression on selected wing planforms.

fall to zero. Some authors (e.g. Torenbeek [44]) recommend ( $C_{l\max} = 0.1$ ), but this may be hard to achieve in practice without excessive washout. At any rate, the idea is to promote roll stability at stall and washout is a powerful tool to provide this function. If a viscous analysis method is used (e.g. Navier-Stokes solvers), then a more pinpointed tailoring can be accomplished, but only if the flow separation prediction is deemed trustworthy. For something as serious as stall tailoring, flow visualization of the separated region obtained from wind tunnel testing should always be used to validate the CFD model.

Figure 9-75 shows an example of typical linear analysis for a tapered wing ( $\lambda = 0.5$ ) that features the same airfoil (NACA 65<sub>2</sub>-415) throughout the wing. Since the Reynolds number at the tip is only one-half of the root value, the  $C_{l\max}$  is less at the tip and this should be taken into account for airplanes that feature tapered planform shapes. The baseline wing design (solid curve) has no washout, whereas the other three have a 2°, 4°, and 6° washout, respectively. The graph shows the distribution of  $C_l$  for these four models at AOA of 16°. The thick dashed line shows the distribution of the  $C_{l\max}$  from root to tip.

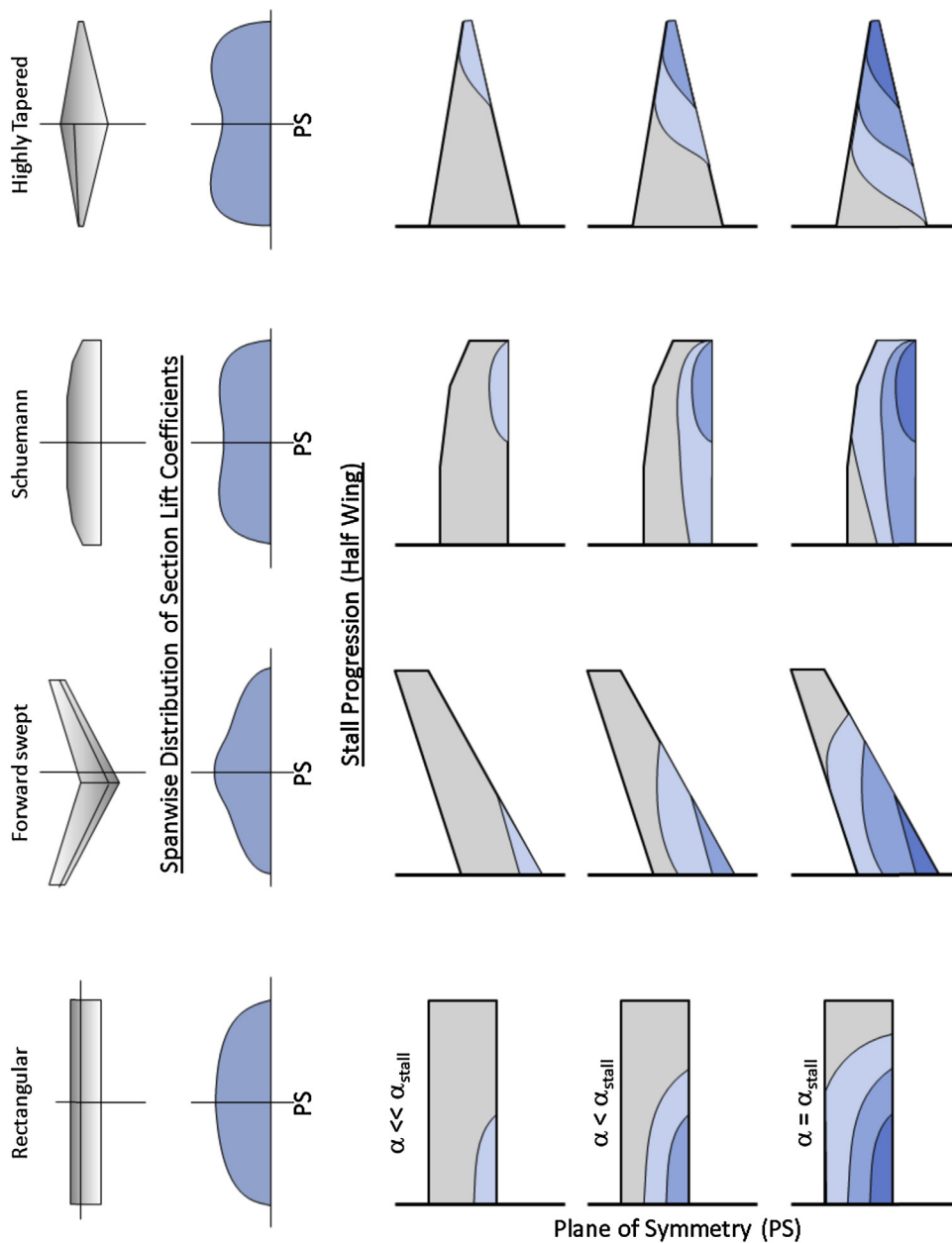


FIGURE 9-72 Stall progression on selected wing planforms.

The graphs in Figure 9-75 show that the  $C_L$  for the baseline wing exceeds the  $C_{L\max}$  between Spanwise Station 0 to about 0.87. This means the wing should be expected to be fully stalled to that point, something that would result in poor stall characteristics, as barely 10% of the span (at the tip) is un-stalled. The proposals for a 2°, 4°, and 6° washout all lead to improvements, especially the last one (6°), which brings the stall to Spanwise Station 0.65. However, as can be seen in Table 9-6, washout higher than 4° is rare. Excessive washout can lead to an increase in the lift-induced drag as the wing must be operated at a higher AOA to generate the

same airplane lift coefficient ( $C_L$ ). A better solution would be to feature less washout, say somewhere between 2° and 4°, and feature a tip airfoil that has a higher  $C_{L\max}$  than the root (an aerodynamic washout). Of course it is assumed such an airfoil would offer gentle stall characteristics (not those of the NACA 23012 airfoil presented in Section 8.2.10, *Famous airfoils*).

#### **Tailoring Stall Characteristics of Wings with Multiple Airfoils**

A possible stall tailoring remedy is proposed in the graph of Figure 9-75. It consists of increasing the  $C_{L\max}$

$M = 0.23, R_e = 6.9 \times 10^6$   
 $AR = 6, \lambda = 0.5, \text{washout} = 4^\circ$   
Smooth surface  
Source: NACA-TN-1299

$M = 0.17, R_e = 5.3 \times 10^6$   
 $AR = 6, \lambda = 0.5, \text{washout} = 1.5^\circ$   
Rough surface  
Source: NACA-TN-2753

$M = 0.07-0.17, R_e = 4.61 \times 10^6$   
 $AR = 10.05, \lambda = 0.4, \text{washout} = 3^\circ$   
Smooth surface  
Source: NACA-TN-1677

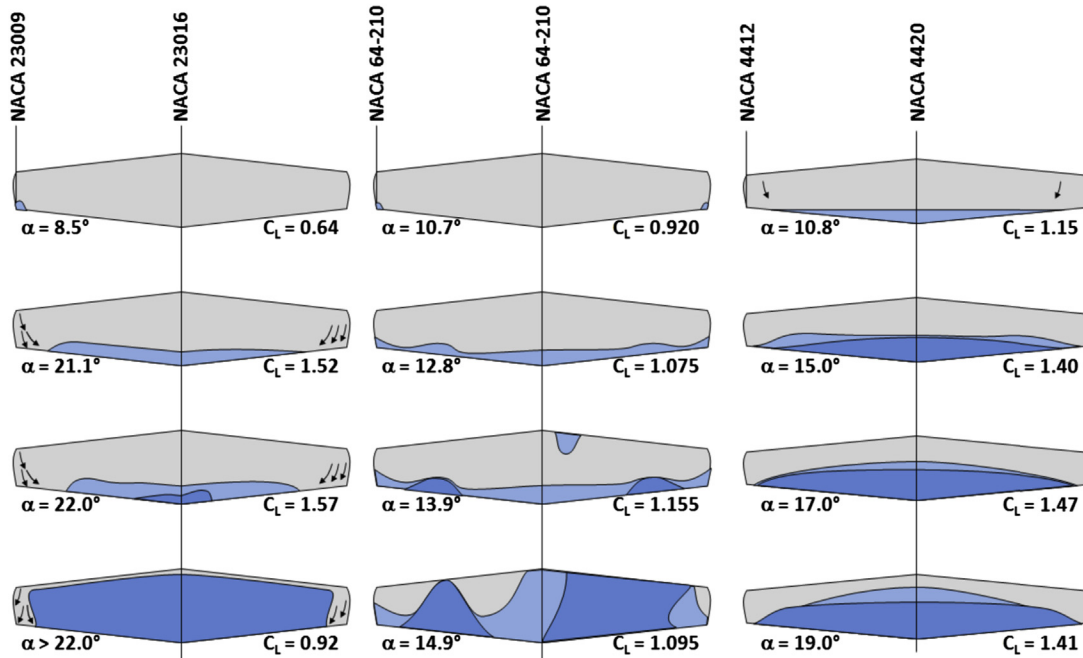


FIGURE 9-73 Stall progression on straight tapered wing planforms differing in  $AR$ ,  $\lambda$ , washout, and surface roughness (Based on Refs [39–41]).

$R_e = 6.9 \times 10^6, AR = 7, S = 6.42 \text{ ft}^2$ , Airfoil: NACA 0012

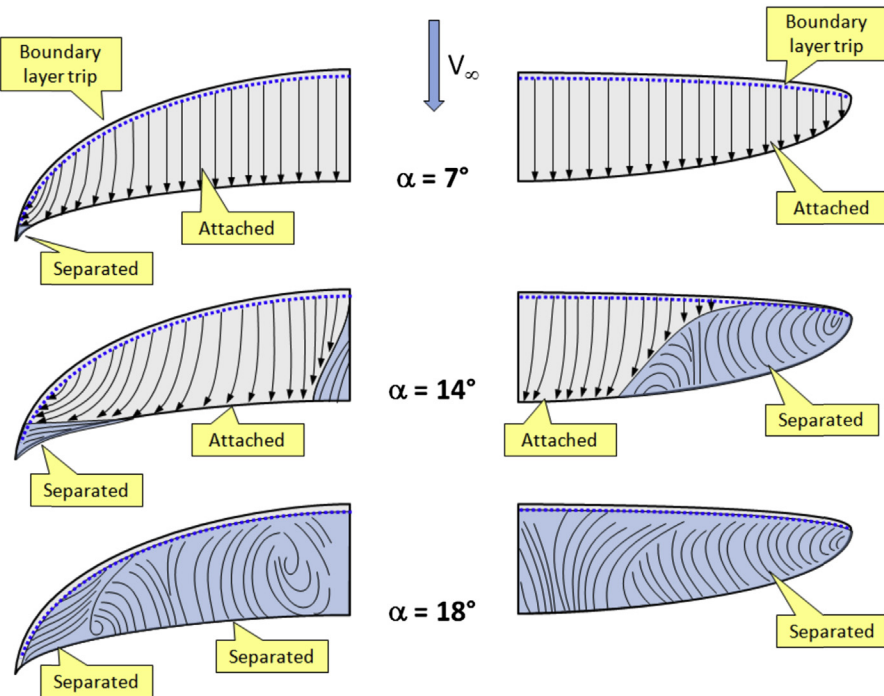


FIGURE 9-74 Stall progression on a crescent-shaped and an elliptical wing planform of comparable geometry shows the complex flow inside a separation region (Based on Ref. [42]).

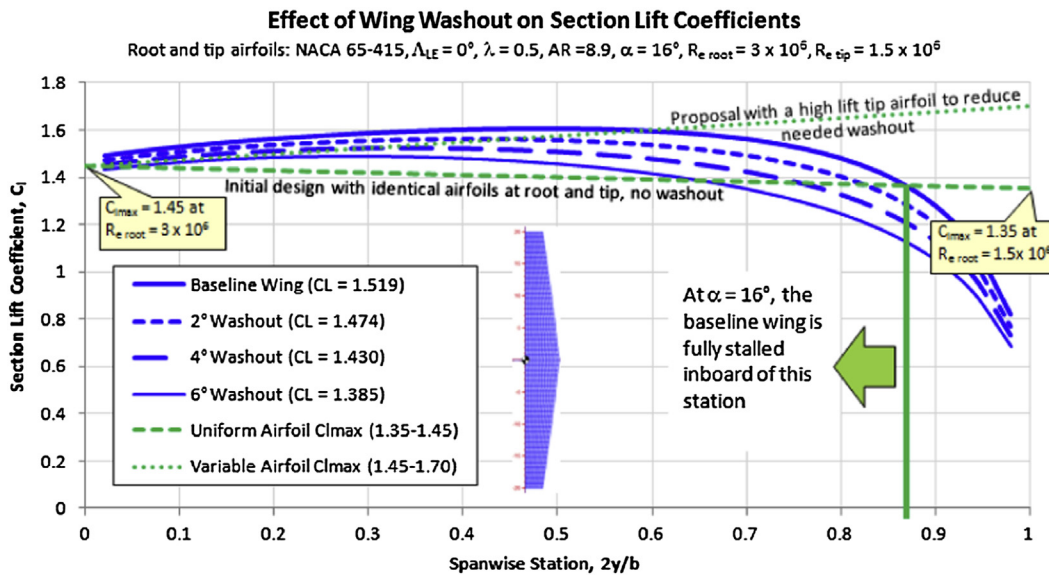


FIGURE 9-75 The effect of washout on probable stall progression. The baseline wing is more tip-loaded than the ones with washout and this will cause it to stall closer to the wingtip, which may cause roll-off problems. Washout is a powerful means to control stall progression and can be enhanced by selecting a high-lift airfoil at the tip.

of the tip airfoil from 1.57 to about 1.7, by defining a new tip airfoil. Of course, this may pose some challenges; such an airfoil might possess some undesirable characteristics too. However, assuming this is achievable; it may be possible to manufacture the wing without a geometric washout. This can be an advantage for some composite wing designs, as it allows uni-directional plies in the spar to be laid up in a more manufacturing-friendly fashion than a twisted spar. In practice, however, tailoring the wing for good stall progression is solved using a combination of both geometric and aerodynamic washouts.

#### Other Issues Associated with Wings with Multiple Airfoils

Multi-airfoil wings are the norm for high-performance aircraft, but are also common in smaller and simpler GA aircraft. High-performance aircraft require wings that allow the airplane to operate at low airspeeds while avoiding compressibility effects associated with high-speed flight. It takes sophistication in manufacturing to produce such wings. This is particularly challenging in the production of wings made from alloys, as the difference in geometry inevitably requires the wing skin to be stretched to conform to the resulting compound surface. This will become clearer in a moment.

A hypothetical multi-airfoil wing is shown in Figure 9-76, Figure 9-77, and Figure 9-78, with the layout presented in Figure 9-76. It should be stressed there is no rhyme or reason why the particular airfoils have been selected other than to demonstrate

aerodynamic, structural, and manufacturing complexities that may arise in such a wing design. The wing is defined using three airfoils: at the plane of symmetry (the “root”); at the intersection of the flap and aileron; and at the tip. Structurally, the intersection of the flap and aileron is a good location to anchor a new airfoil as a rib is required there to mount the hard-points for the control surfaces.

Figure 9-76 also shows that the airfoil selection will affect the extent of the laminar boundary layer on the wing’s upper surface (assuming this is achievable). This change must be accounted for in the drag estimation for the wing. Achieving a laminar boundary layer is difficult, as has already been discussed in Chapter 8, *The anatomy of the airfoil*. Attempting this on the above wing will require careful and more expensive manufacturing tooling.

Figure 9-77 shows the distribution of section lift coefficients along both wing halves at  $\alpha = 16.5^\circ$  and is based on potential flow analysis. It also shows how the maximum lift varies along the span because of the three airfoils and that the progression of stall begins just outside the 50% span station. Also plotted is the distribution of  $C_l$  for the same wing with a  $3^\circ$  washout, showing improvements, although the wing is still highly tip-loaded. The reader is also reminded that the linear method used does not correctly predict flow separation due to chord- and spanwise flow (recall this is a swept wing design). Therefore, although the linear method is helpful in understanding the airflow around the wing, ultimately the graph represents an ideal flow scenario that is not present in the real flow.

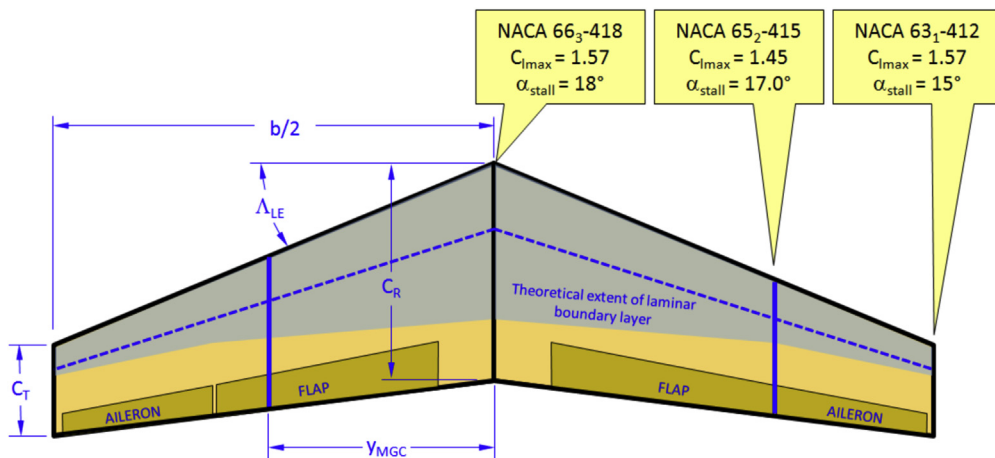


FIGURE 9-76 An example wing layout, showing the theoretical extent of laminar boundary layer and variation in its maximum lift capability.

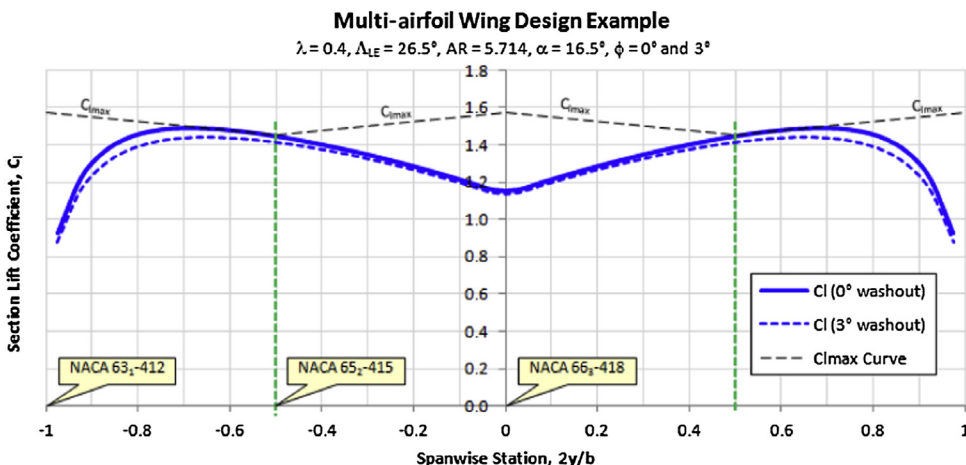


FIGURE 9-77 An example of a potential flow lift analysis of the multi-airfoil wing layout that features 0° and 3° washout.

Figure 9-78 shows some structural and manufacturing issues that present themselves in wings with multiple airfoils. The geometry that results often comes as a surprise to novice engineers designing the structure of such wings. Since the three airfoils used have dissimilar geometry, the spar extending from root to tip will be subject to a geometric non-linearity; the skin will form a compound surface. In the figure, the wing is cut along a proposed spar-plane. The view along the cut shows two situations are present: first, there is a discontinuity in the spar OML at the mid-span station. Second, mathematically, the spar cap must also feature a slightly curved surface, extending from root to mid-span and then to the tip. If it is required that the skin must adhere perfectly to the compound surface and it will be made from aluminum, the sheet metal for the spar and skin will have to be pressed to shape using hydraulic presses. This will greatly increase the cost of production. In real aircraft, especially less expensive ones,

the discontinuity is usually solved by sheets terminating along the discontinuity. The curvature may have to be solved by straightening the spar cap and accepting that the wing will not be what the aerodynamics group really wants or by inserting shims between the spar and the skin. This may also make it more challenging to achieve a laminar boundary layer, as the resulting shape may no longer present the intended theoretical shape.

### 9.6.5 Cause of Spanwise Flow for a Swept-back Wing Planform

Swept-back wings can experience a significant and uncontrollable pitch-up moment at high angles-of-attack. The reason for this is twofold:

- (1) The aft-swept planform induces local upwash near the tip which increases the local section lift coefficients. This means that the tip airfoils reach

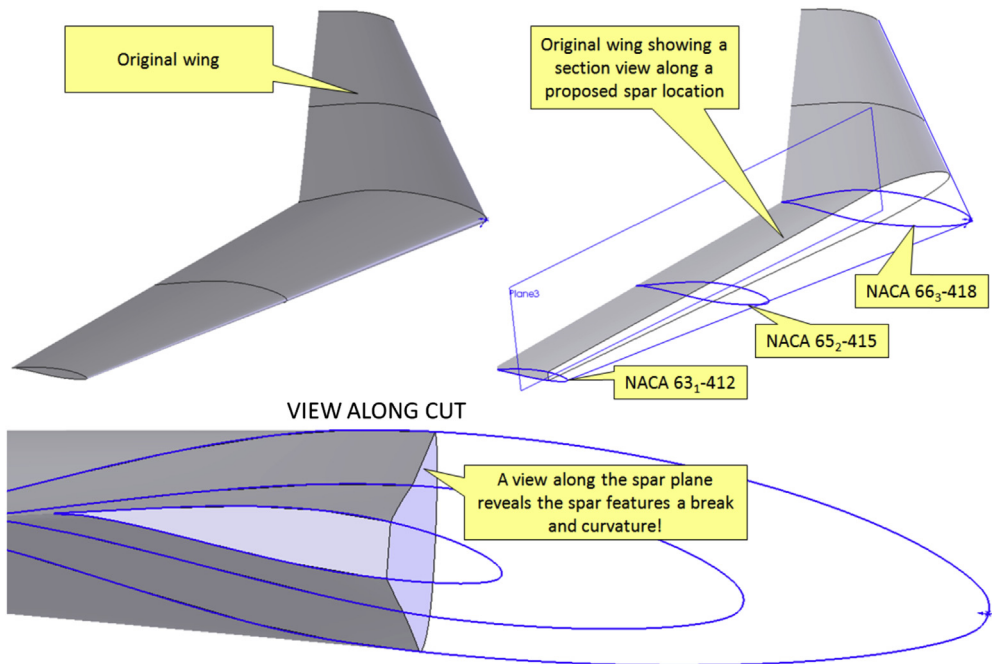


FIGURE 9-78 An example of geometric complexities arising from the multi-airfoil wing layout.

their stall section lift coefficients sooner than the inboard airfoils.

- (2) Air begins to flow in a spanwise direction near the tip, but this leads to an early flow separation.

The first cause is somewhat hard to explain in layman's terms, but we will try. Imagine the wing is cut into a finite number of small sections along the span of the wing. The sections extend from the root to the tip such that the inboard section is always upstream of the adjacent outboard section. For this reason, the inboard section will begin to disturb the flowfield before the section outboard of it. A part of this disturbance is an upwash ahead of that section which extends spanwise into the flowfield. Then, when the outboard section begins to disturb the flowfield ahead of it, there is already an upwash component in it, induced by the section inboard of it. This section will then impart its own influence on the flowfield, which manifests itself as a slightly greater upwash for the section outboard of it, and so on. The upwash implies a greater local AOA. A greater local AOA implies a higher section lift coefficient.

The cause of the spanwise flow, on the other hand, and which is the topic of this section, can be explained as follows. Consider the swept-back wing of Figure 9-79, which shows an aircraft with a swept-back wing at some AOA. Two sample chordwise pressure distributions are drawn on the right wing. Also, the locus of the peak spanwise pressure distribution along the wing is shown as the dotted curve drawn at the pressure peaks. It can be seen that the pressure peak on the outboard wing is higher than inboard. Now, consider a line perpendicular

to the centerline of the fuselage at some arbitrary chord station. It cuts through the chordwise pressure distributions as indicated by the vertical arrows. The inboard arrow is shorter than the outboard one, indicating higher pressure than on the outboard one (remember these distributions represent low and not high pressures). For this reason the higher pressure on the inboard station forces air to flow from the inboard to the outboard station, giving the flow field an overall outboard spanwise speed component. This is shown as the streamlines on the left wing.

### 9.6.6 Pitch-up Stall Boundary for a Swept-back Wing Planform

As stated in the previous section, swept-back wings suffer from significant pitch-up moment near and at stall. The effect depends on the quarter-chord sweep angle,  $\Lambda_{C/4}$ , and aspect ratio, AR. The effect is investigated in NACA TR-1339 [45] and NACA TN-1093 [46]. Figure 9-80 is reproduced from those references and summarizes the effect. It shows that the higher the AR, the less is the  $\Lambda_{C/4}$  at which the pitch-up is experienced. This is very important in the development of long-range high-subsonic aircraft as a high AR favors long-range but high  $\Lambda_{C/4}$  favors high airspeed. These properties are therefore mutually detrimental. As contemporary airliners demonstrate, the development of the modern airfoil has remedied this limitation with its greater critical Mach number (at which shocks begin to form). This has allowed aircraft with lower  $\Lambda_{C/4}$  ( $\approx 20^\circ$ – $27^\circ$ )

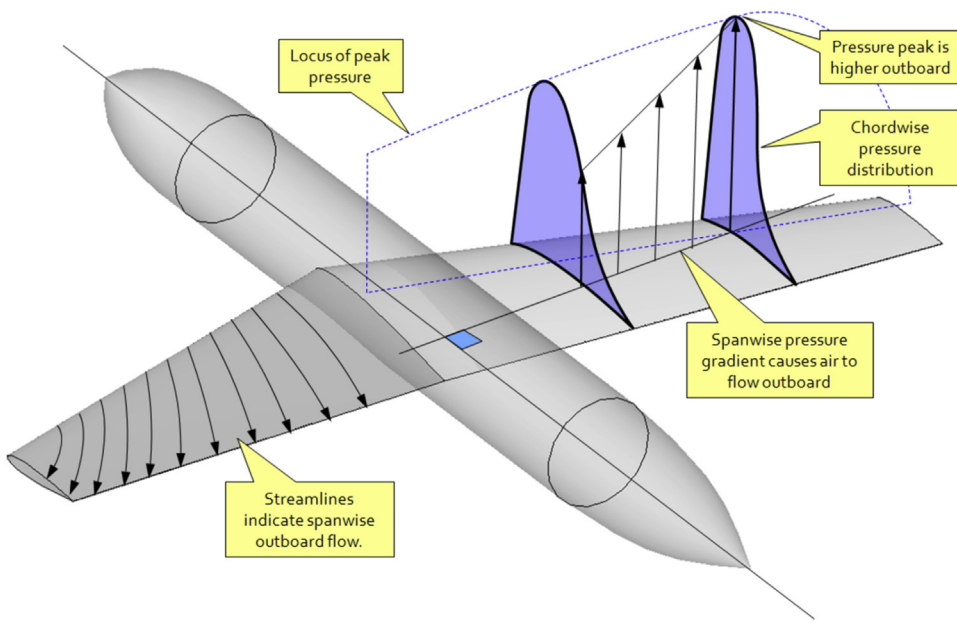


FIGURE 9-79 The spanwise pressure gradient on an aft-swept wing results in an outboard spanwise flow. The opposite holds true for a forward swept wing (Based on Ref. [17]).

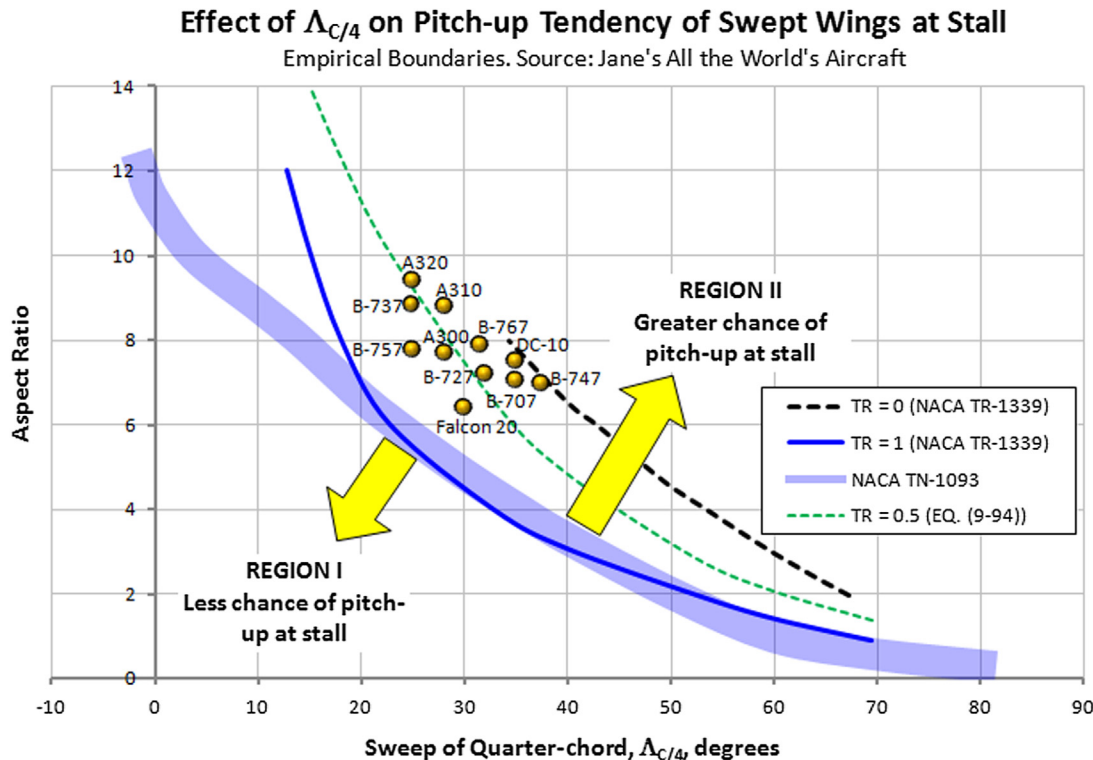


FIGURE 9-80 Empirical pitch-up boundary for a swept-back wing. Reproduced based on Refs [44] and [45].

to utilize higher AR and, thus, operate more efficiently at the usual cruising speeds of such aircraft ( $M \approx 0.78\text{--}0.82$ ).

An empirical equation based on the data in Ref. [44] can now be developed. It relates the taper ratio,  $\lambda$ , and,

sweep angle of the quarter chord in degrees,  $\Lambda_{C/4}$ , to calculate an AR limit for swept-back wings. For a given  $\Lambda_{C/4}$  the selected AR should be less than this limit:

$$AR_{\text{lim}} \leq 17.714(2 - \lambda)e^{-0.04267\Lambda_{C/4}} \quad (9-94)$$

Alternatively, given a target  $AR$ , the  $\Lambda_{C/4}$  in degrees should not exceed the value below:

$$\Lambda_{C/4\text{lim}} \leq 23.436[\ln(17.714(2 - \lambda)) - \ln(AR)] \quad (9-95)$$

As shown in Figure 9-81, the combination of  $AR$ ,  $\lambda$ , and  $\Lambda_{C/4}$  can lead to desirable or undesirable results in terms of nose pitch-down or pitch-up characteristics at stall. Aircraft that feature aft-swept wings should always be wind tunnel tested for stability at stall, but the awareness of the data used to produce Figure 9-80 can go a long way in preventing serious stall problems from presenting themselves.

Finally, NACA RM-L8D29 [47] presents various results that are helpful to the designers of swept-back wings. It investigated the effect of a number of high-lift devices and fences on the stall characteristics on stall characteristics (see Figure 9-82). It concluded that the half-span, leading-edge slats eliminated the tip stall and prevented the nose-up pitching moment. The flaps complicated the stall characteristics and formed a loop in the pitching moment curve (in the figure), although it was suggested it could be brought under control using an appropriately stabilizing surface.

### Derivation of Equations (9-94) and (9-95)

The derivation is based on the data obtained using Ref. [44], which presents two curves that are functions of the quarter-chord sweep angle,  $\Lambda_{C/4}$ ; one represents a taper ratio  $\lambda = 0$  and the other  $\lambda = 1$ . The idea is to derive an empirical expression that is a function of  $\lambda$  and  $\Lambda_{C/4}$  that closely fits both

expressions. This can be done with some numerical analysis. A least-squares exponential fit to the two curves yields the two following expressions:

For  $\lambda = 0$ :

$$AR = 35.885 \cdot e^{-0.04206\Lambda_{C/4}}$$

For  $\lambda = 1$ :

$$AR = 18.171 \cdot e^{-0.04329\Lambda_{C/4}}$$

Since the values of the two exponents are relatively close to each other it can be deduced that the value of  $\lambda$  has minimal impact on it and primarily affects the constant. For this reason the average of the two ( $-0.04267$ ) can justifiably be used for the empirical expression. Assuming a function of the form:

$$AR = f(\lambda) \cdot e^{-0.04267\Lambda_{C/4}} \quad (i)$$

The function  $f(\lambda)$  can then be approximated by noting that the constant changes from 35.885 when  $\lambda = 0$  to 18.171 when  $\lambda = 1$ . It is convenient to employ a parametric representation for this variation, in particular considering that  $\lambda$  can be used unmodified as the parameter. Thus, Equation (i) can be rewritten as follows:

$$\begin{aligned} AR &= (35.885(1 - \lambda) + 18.171\lambda)e^{-0.04267\Lambda_{C/4}} \\ &= (35.885 - 35.885\lambda + 18.171\lambda)e^{-0.04267\Lambda_{C/4}} \\ &= 17.714(2 - \lambda)e^{-0.04267\Lambda_{C/4}} \end{aligned} \quad (ii)$$

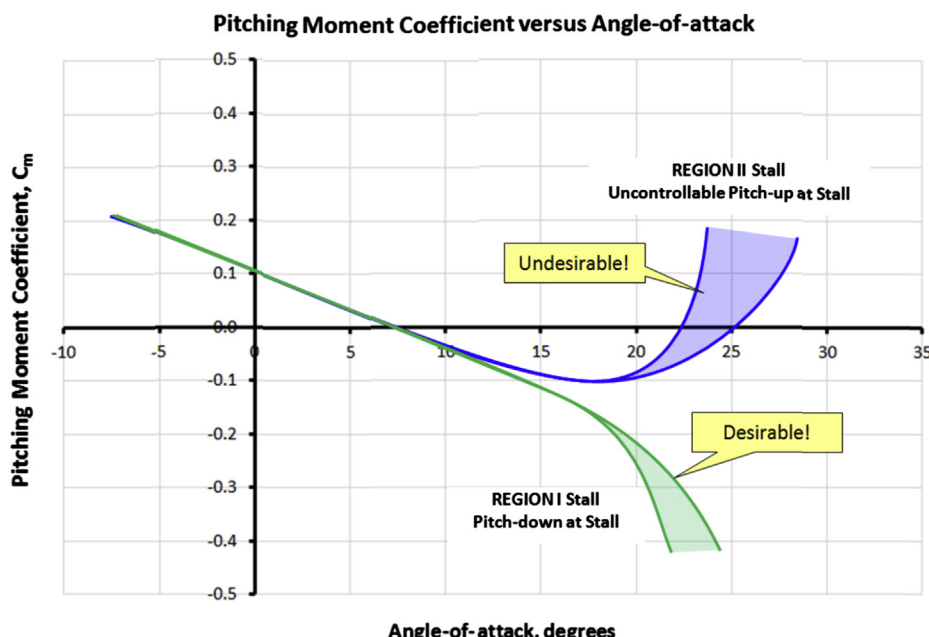
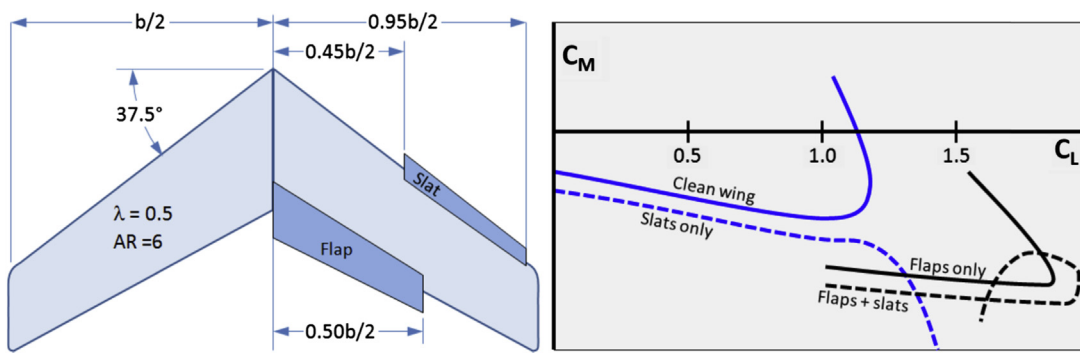


FIGURE 9-81 The combination of  $AR$ ,  $TR$ , and quarter-chord sweep can lead to desirable or undesirable pitch characteristics at stall.



**FIGURE 9-82** The effect of various combinations of a double-slotted flaps and slats on the pitching moment of a  $37^\circ$  swept wing. The loop is attributed to the section characteristics of the double-slotted flap (Based on Ref. [46]).

And this is Equation (9-94). Equation (9-95) is simply obtained by solving for  $\Lambda_{C/4}$ .

$$\begin{aligned} AR &= 17.714(2 - \lambda)e^{-0.04267\Lambda_{C/4}} \\ \Rightarrow \ln(AR) &= \ln(17.714(2 - \lambda)) - 0.04267\Lambda_{C/4} \\ \Rightarrow \Lambda_{C/4} &= 23.436[\ln(17.714(2 - \lambda)) - \ln(AR)] \end{aligned}$$

QED

### 9.6.7 Influence of Manufacturing Tolerances on Stall Characteristics

Inherent roll instability at stall is one of the most common handling deficiencies affecting aircraft. In fact,

most aircraft ever built have displayed the condition to some extent, requiring the introduction of “fixes” to remedy it. The manifestation of this condition occurs at stall as the aircraft does not drop the nose with wings level, but rather rolls uncontrollably to the left or right side (see Figure 9-83). Its root causes are complicated and one should not assume there is a single cause, but rather a combination of factors.

It may sound strange, but all aircraft are inherently asymmetric, even though this is usually impossible to discern with the naked eye. Nevertheless, every single serial number differs slightly from the previous or the following one in its deviation from the intended outside mold line (OML). Not even the left wing of any given airplane is a perfect mathematical mirror image of the

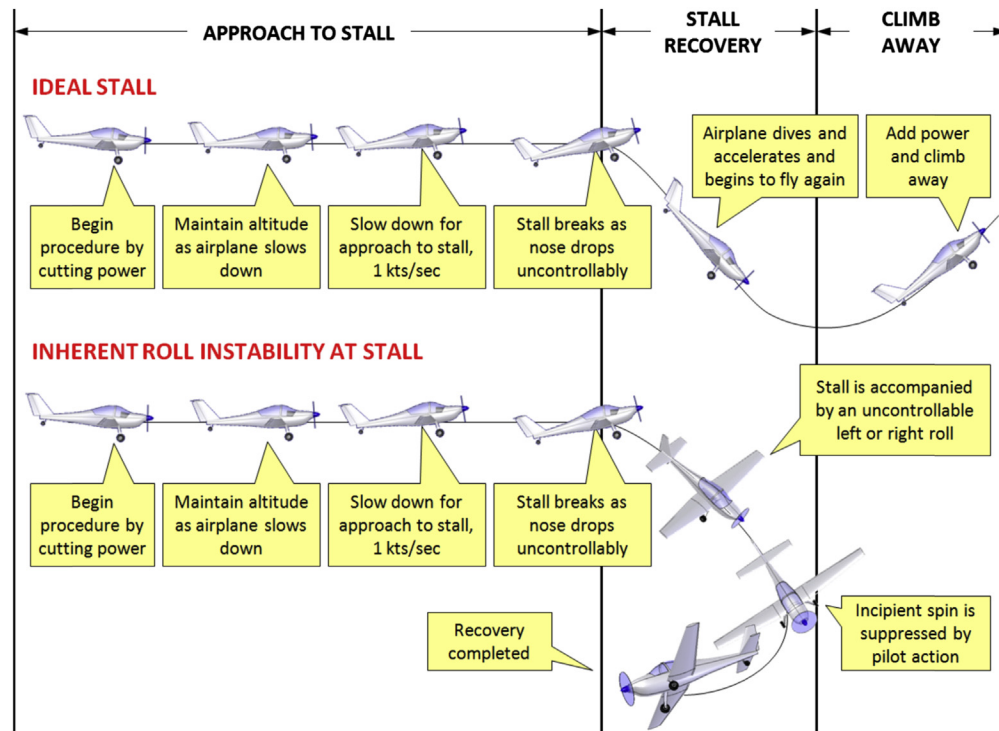


**FIGURE 9-83** Comparing an “ideal stall” (top) to one with an inherent roll instability (bottom).

right one, although it is completely invisible to the casual observer. There are always subtle differences in washout, thickness, waviness, and their corresponding locations on each wing, all of which may combine to promote roll instability at stall.

A typical deviation from the OML in the aviation industry amounts to  $\pm 0.125$  inches, although most wings must usually meet tolerances ranging from  $\pm 0.050$  to  $\pm 0.100$  inches over the lifting surfaces. Manufacturers of GA aircraft that feature NLF lifting surfaces often take it one step further and maintain even tighter tolerances; sometimes as tight as  $\pm 0.005$  inches along the leading edge. While maintaining tolerances is imperative in the manufacture of aircraft, overly tight tolerances are of detrimental value. They call for expensive and robust inspection procedures and additional manpower to demonstrate such wings meet the set specifications. Very tight tolerances should always be justified with research.

One of the main concerns manufacturers have with NLF wings is their sensitivity to deviations from the OML, as this may promote early transition of a laminar boundary layer into a turbulent one, which, in turn, increases drag. This often requires expensive repairs to be made to wings that arguably are just fine. The author of this book once investigated the some 300 production aircraft with NLF wings to determine whether there was a correlation between the magnitude of such small manufacturing deviations and stall characteristics reported by the production flight test pilots. No correlation could be found. Tight tolerances had subjected the production to costly inspection procedures without measurable benefits.

While this is not intended to reject the application of tight tolerances in the manufacturing of NLF wings, there clearly is a point of diminishing returns. It turns out that near stall AOA, the flow is altogether separated anyway and, therefore, insensitive to minor deviation from the OML. The source of roll instability should be looked for elsewhere, such as in deviation in thickness, twist, dihedral, and objects that are asymmetrically exposed to the airflow.

It would seem from the above discussion that if too tight tolerances are a problem, then perhaps loose tolerances may be desirable. However, this is not the case. Loose tolerances allow an airplane to be excessively asymmetric, not just in surface qualities, but in large deviation from the OML of the surface that almost certainly would cause an inherent roll instability. It is best to design sensitivity to small deviations out of the OML by providing assertive aerodynamic roll stability at high AOA. This can be done by increasing the camber of the wingtip airfoil (by specifically selecting a high-lift airfoil), or by reducing its AOA using washout, or by providing a leading-edge extension (see Section

23.4.11, *Stall handling – wing droop (cuffs, leading-edge droop)*, or by introducing slats.

## 9.7 NUMERICAL ANALYSIS OF THE WING

The advent of the digital computer has clearly revolutionized science and engineering. As far as aircraft design is concerned, the technology allows far more complicated and realistic analyses to be performed than previously possible. In its most sophisticated form, the use of computer technology allows the full Navier-Stokes equations (NSE) to be solved for extremely complex situations. This ranges from airflow resembling that experienced by an insect to that of a tumbling meteorite entering Earth's atmosphere at hypersonic speeds. At the present time, however, the application of this method is both time-consuming and expensive as it requires a detailed digital model of the geometry to be prepared and flow solution obtained using a cluster of interconnected computers. Meshing the model is often more art than science and requires an experienced individual to complete. Improperly designed mesh simply yields erroneous results. This is further compounded by the amount of time required to solve the problem. It can easily take a couple hours to a couple of days to accomplish, depending on the complexity of the body and the computational prowess of the individual (or company) involved. For this reason, conceptual design using NSE solvers is very impractical and should not even be considered. Currently, NSE is really a *post-conceptual* design tool; it should be used *after* the concept has been designed and not to design it.

There are a number of practical numerical methods available to the designer that, in comparison, are lightning fast and, for attached flow, are equally as accurate as the solution obtained using the NSE. Among those are the *lifting line method* and panel methods such as the vortex-lattice or doublet-lattice. While programmatically considerably older than the modern Navier-Stokes solver, they remain far more practical during the conceptual design phase and are simple enough to implement using a desktop computer. Due to space limitations, only the most basic of these methods will be demonstrated; *Prandtl's lifting line method*. For other methods, the reader is directed toward excellent texts such as those by Katz and Plotkin [48]; Pope [49]; Bertin and Smith [50]; and Moran [51].

### 9.7.1 Prandtl's Lifting Line Theory

Developed by Ludwig Prandtl (1875–1953) and his colleagues at the University of Göttingen between

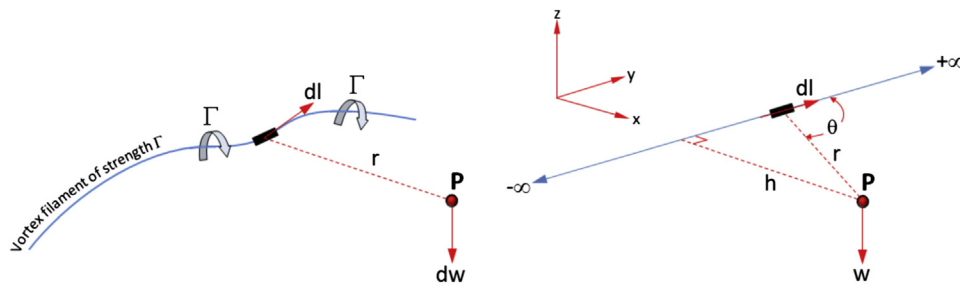


FIGURE 9-84 A curved vortex filament (left) and an infinite, straight vortex filament (right).

1911–1918, the lifting line theory can be used to determine the aerodynamic characteristics of straight three-dimensional wings. The method does not treat wings with dihedral or sweep, but can account for wing twist and varying airfoils and chords along the span of the wing. It is reliable for wings whose  $AR$  is no smaller than about 4. The method mathematically replaces the wing with a number of constant-strength vortices, here denoted with the Greek letter  $\Gamma$ . The problem, effectively, revolves around determining their strength; however, once this has been accomplished, it is possible to estimate a number of characteristics, such as lift and drag, downwash, and distribution of lift along the wing. It is thus useful not only for aerodynamic properties, but also for structures and stability and control. A derivation of the method will now be presented, but first the following mathematical constructs must be introduced.

### The Vortex Filament and the Biot-Savart Law

A vortex filament is an imaginary spatial curve that induces a rotary flow in the space through which it passes (see Figure 9-84). The best analogy is to think of it as the center of a tornado with the associated circulatory flow around its core. The ability of the filament to induce circulation around it depends on its strength, denoted by  $\Gamma$ . Consider an infinitely small vector segment  $dl$  along the filament and some arbitrary point  $P$  in space. The small segment will induce a velocity  $dw$  at the point  $P$ , whose magnitude can be determined using the Biot-Savart<sup>4</sup> law:

Biot-Savart law:

$$dw = \frac{\Gamma}{4\pi} \frac{dl \times r}{|r|^3} \quad (9-96)$$

The Biot-Savart law is named after the French mathematician and physicist Jean-Baptiste Biot (1774–1862) and Félix Savart (1791–1841), a fellow Frenchman who trained for a career in medicine, although his mind was absorbed by natural philosophy.

The derivation of the law is beyond the scope of this book, but interested readers can refer to almost any textbook on electrical engineering. The law was actually derived to relate a magnetic field induced by an electric current in a wire, but it can also be used to estimate the circulation of flow around a wing. This is because the Biot-Savart law is one of numerous solutions of *Laplace's equation*, which is the governing equation for irrotational, incompressible fluid flow. It is shown below for convenience:

Laplace's equation

$$\nabla^2 \phi = \frac{\partial^2 \phi}{\partial x^2} + \frac{\partial^2 \phi}{\partial y^2} + \frac{\partial^2 \phi}{\partial z^2} = 0 \quad (9-97)$$

where  $\phi$  is the *velocity potential*. Note that the direction of the velocity is imperative. In accordance with a right-handed coordinate system, assume the thumb of the right hand to point in a direction indicated by the filament  $dl$  in Figure 9-84. Then the other four fingers curl around the filament as if holding a rope. The direction of the velocity is always in the direction the four fingers make. This is an important concept to keep in mind for what follows.

In the development of the lifting-line theory, we will be applying the Biot-Savart law to a number of straight (versus curved) vortex filaments that are infinitely long. Such a straight segment is shown in Figure 9-84. It stretches from  $-\infty$  to  $+\infty$ . Knowing the contribution of the tiny segment  $dl$ , the total velocity induced at the point  $P$  can be determined by integrating the contribution along the entire filament, i.e.:

$$w = \int_{-\infty}^{+\infty} \frac{\Gamma}{4\pi} \frac{dl \times r}{|r|^3} \quad (9-98)$$

In order to constrain the discussion here to the bare essentials, the solution of the integral is omitted and only the final result presented. The interested reader

<sup>4</sup>Pronounced bee-yo-suh-var.

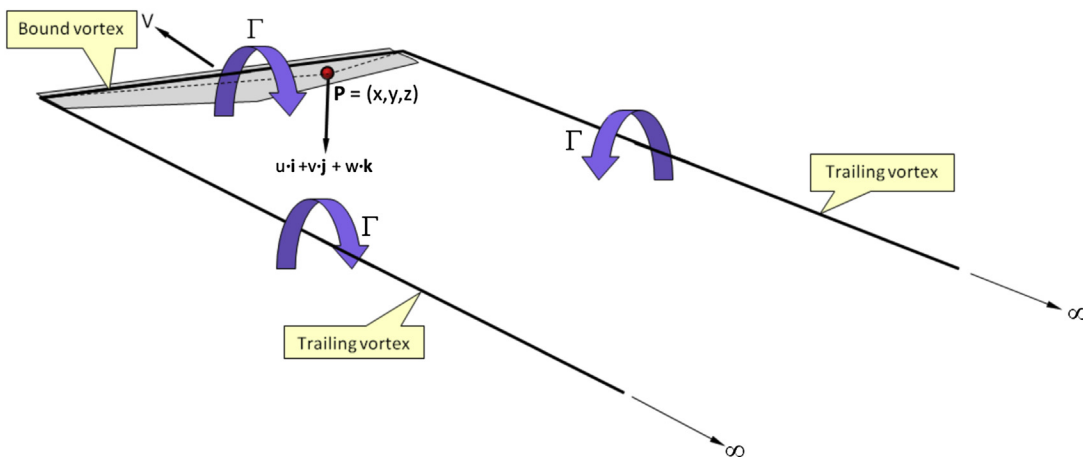


FIGURE 9-85 The flow field around a wing approximated by three connected constant-strength straight vortex filaments. On the wing plane,  $u = v = 0$ .

can, for instance, refer to Anderson [52] for the evaluation. The solution involves relating the parameters  $h$ ,  $r$ , and  $\theta$  in Figure 9-84, and inserting into the integral prior to its evaluation. Thus, the fluid speed at the point  $P$ , induced by the straight vortex filament of strength  $\Gamma$ , is given by:

Velocity induced a point  $P$ :

$$w = \frac{\Gamma}{2\pi h} \quad (9-99)$$

### Helmholz's Vortex Theorems

In 1858, the German scientist Hermann von Helmholtz (1821–1894) made the next step by using the vortex filament to analyze inviscid, incompressible fluid flow. In doing so he established what has become known as *Helmholz's vortex theorems*. These state that:

- (1) The strength of the vortex filament is constant along its entire length; and
- (2) A vortex filament cannot end in a fluid, but must either extend to infinity or form a closed path.

These theorems are used to evaluate a special kind of vortex called a horseshoe vortex. The horseshoe vortex has important properties that will be discussed shortly and that allow it to be used to represent the lift of a finite wing.

### Lifting Line Formulation

Now that we have established that a straight vortex induces a circulation around the vortex filament, it is possible to extend the idea to a three-dimensional wing. An observation of real finite wings reveals two important facts:

- (1) The wing induces circulation that extends from tip to tip; and

- (2) Each wingtip sheds a vortex that extends far into the flow field behind the wing.

This fact can be approximated using three separate vortex filaments as shown in Figure 9-85. First, a *trailing vortex* extends from infinity to the left wingtip. Then, a *bound vortex* extends from the left wingtip to the right wingtip. And finally, a third *trailing vortex* extends from the right wingtip back to infinity. This system of vortices not only satisfies Helmholtz's vortex theorems, it also induces a flow field that resembles that of real three-dimensional wings. Additionally, the three vortices, which are of a constant strength  $\Gamma$ , all have the same sign, as can be observed using the right-handed rule (the thumb of the right hand should point forward for the first vortex, to the right for the second one, and backward for the third one).

While promising, there is a problem with this system in that it leads to a spanwise lift distribution that is constant. However, this implies that the lift at the wingtips is non-zero, but this is physically impossible. In fact, a single vortex like this will cause the downwash at the wingtip to go to infinity. The solution to this dilemma is to add more horseshoe vortices to the system, each of lesser span than the next, and with its own constant circulation (see Figure 9-86). The inboard vortices usually have greater strength than the outboard ones, but the interaction of all of them causes the resulting downwash to resemble that shown by experiment. This way, the strength of each individual vortex will be constant, but their total interaction along the span will result in a variable spanwise load distribution.

The lifting line method is based on the assumption that the vortex strength along the span is known. Consider that, at some spanwise wing station  $y$ , the vortex strength is given by the value  $\Gamma(y)$ . This means that if we move a distance  $\Delta y$  to another spanwise station, the

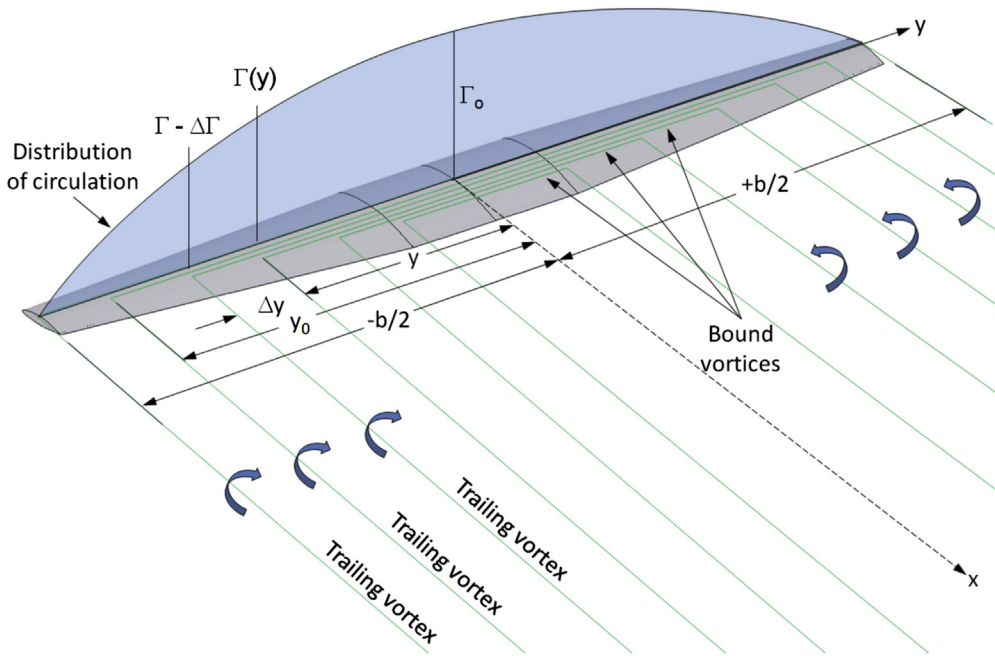


FIGURE 9-86 A wing simulated with a system of vortices.

change in the strength of the vortex,  $\Delta\Gamma$ , can be found from:

$$\Delta\Gamma = \frac{d\Gamma}{dy} \Delta y \quad (9-100)$$

Now consider the spanwise station at  $y_0$  and the vortex at  $y$ , shown in Figure 9-86. It is possible to determine the downwash (i.e. the vertical speed) induced at  $y_0$  by the vortex at  $y$  (see depiction in Figure 9-87).

Let's denote the contribution to the total downwash at  $y_0$  by  $\delta w_{y_0}$ . Since the trailing vortex extends from infinity to  $x = 0$  where it stops (because that is where we have planted our vortex system, so it does not extend to  $-\infty$  also), the influence will be half of that shown by Equation (9-99), or:

$$\delta w_{y_0} = \frac{1}{2} \left[ + \frac{d\Gamma}{dy} dy \frac{1}{2\pi(y - y_0)} \right] \quad (9-101)$$

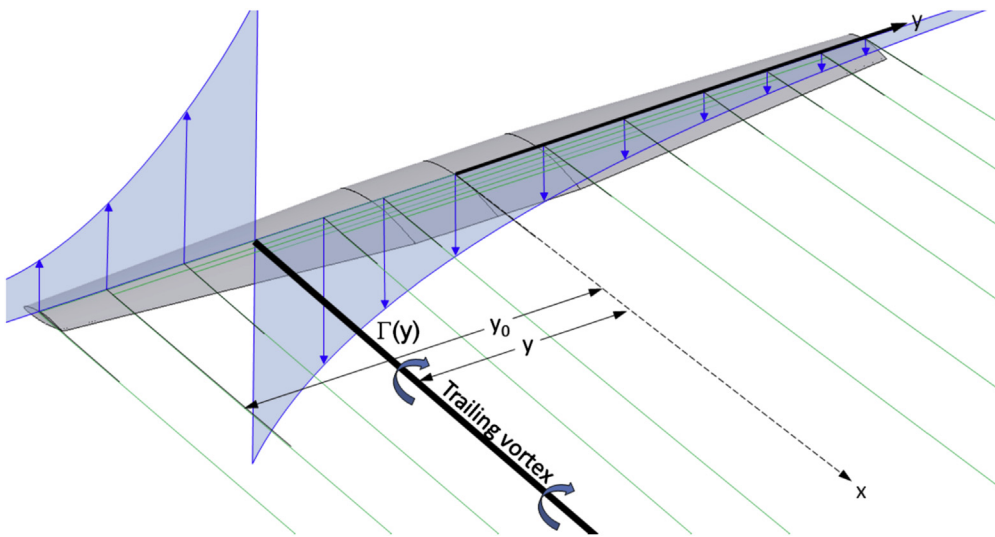


FIGURE 9-87 A depiction of how the single trailing vortex at  $y$  influences the vertical flow at the other stations. The other trailing vortices affect the one at  $y$  in a similar fashion.

Note that as depicted in Figure 9-86 and Figure 9-87, the vortex at  $y$  will induce an upward pointing contribution at  $y_0$ . This is emphasized by the + sign in the equation. In order to calculate the total downwash at  $y_0$  due to all the vortices distributed along the span, Equation (9-101) is integrated from the left wingtip ( $y = -b/2$ ) to the right one ( $y = +b/2$ ):

$$w_{y_0} = +\frac{1}{4\pi} \int_{-b/2}^{b/2} \frac{d\Gamma/dy}{(y - y_0)} dy \quad (9-102)$$

As can be seen, the downwash will ultimately depend on the strength of the circulation along the span. The contributions of other vortices in the system eventually yield a downward-pointed velocity at  $y_0$ . With the downwash at  $y_0$  known, the downwash angle  $\alpha_{i,y_0}$  at  $y_0$  can now be calculated as follows:

$$\alpha_{i,y_0} = \tan^{-1} \left( -\frac{w_{y_0}}{V} \right) \approx -\frac{w_{y_0}}{V} \quad (9-103)$$

where  $V$  denotes the far-field airspeed. As stated in Section 15.3.4, *The lift-induced drag coefficient:  $C_{Di}$* , the downwash behind the wing and corresponding upwash in front of it effectively “tilt” the undisturbed air through an *induced AOA*, denoted by  $\alpha_i$ , reducing the

geometric angle-of-attack,  $\alpha$ , at the quarter-chord by a magnitude, to what is called the *effective AOA*,  $\alpha_e$  (see Figure 9-88):

Effective AOA:

$$\alpha_e = \alpha - \alpha_i \quad (9-104)$$

Note that if the wing features washout,  $\alpha_i$  and thus  $\alpha_e$  become a function of the spanwise station. Similarly, cambered airfoils are treated by subtracting the angle of zero lift from the geometric AOA. The presence of the induced AOA tilts the lift force back by the angle  $\varepsilon$  (see Figure 15-20) and must therefore be resolved into two force components: one normal to the flight path (lift) and the other parallel to the flight path (lift-induced drag). The Kutta-Joukowski theorem (see Section 8.1.8, *The generation of lift*) makes it possible to calculate these two forces per unit span using the following expressions:

Lift per unit span:

$$l(y) = \rho V \cdot \Gamma(y) \quad (9-105)$$

Lift-induced drag per unit span:

$$d_i(y) = -\rho w(y) \cdot \Gamma(y) \quad (9-106)$$

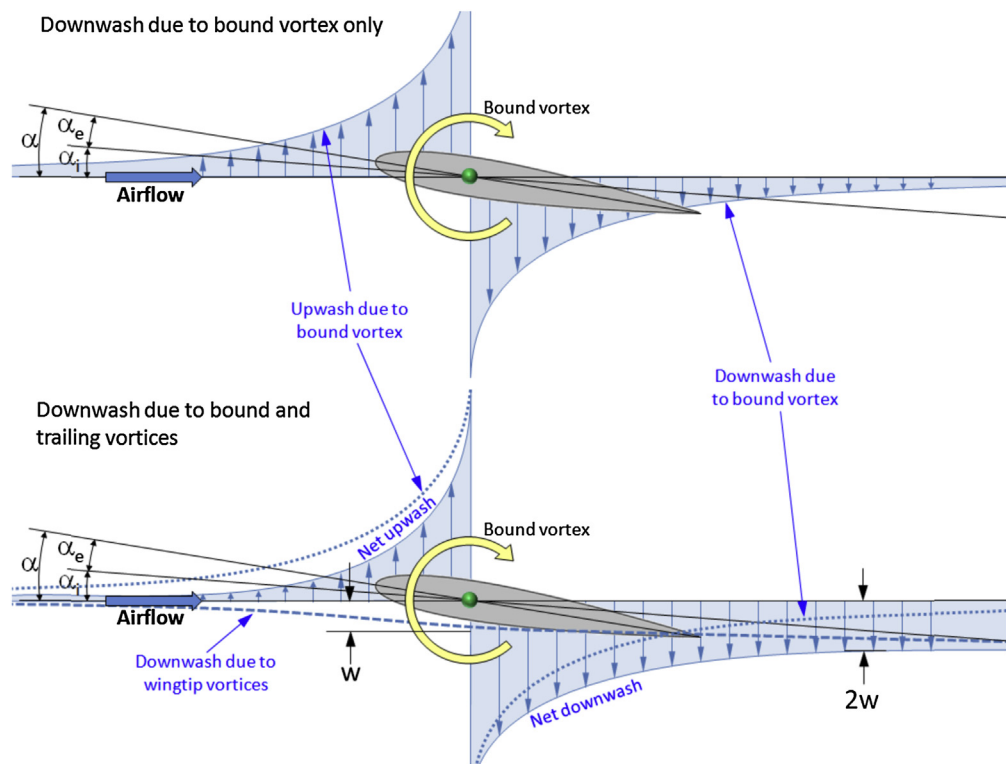


FIGURE 9-88 A side view of the bound vortex along the wing and the resulting up- and downwash.

The minus sign is necessary to ensure the negative value of the downwash produces a positive drag force. The total lift and lift-induced drag forces can now be determined as shown below:

$$\text{Lift: } L = \rho V \int_{-b/2}^{b/2} \Gamma(y) dy \quad (9-107)$$

$$\text{Drag: } D_i = -\rho \int_{-b/2}^{b/2} w(y) \Gamma(y) dy \quad (9-108)$$

Consequently, the lift and lift-induced drag coefficient are given by:

Lift coefficient:

$$C_L = \frac{2L}{\rho V^2 S} = \frac{2}{VS} \int_{-b/2}^{b/2} \Gamma(y) dy \quad (9-109)$$

Lift-induced drag coefficient:

$$C_{Di} = \frac{2D_i}{\rho V^2 S} = -\frac{2}{VS} \int_{-b/2}^{b/2} w(y) \Gamma(y) dy \quad (9-110)$$

If there is a representative zero-lift AOA for the wing, the lift curve slope can be calculated from:

Lift curve slope:

$$C_{L_\alpha} = \frac{C_L}{\alpha - \alpha_{ZL}} \quad (9-111)$$

The subsequent articles present several applications of this method.

### 9.7.2 Prandtl's Lifting Line Method – Special Case: The Elliptical Wing

As discussed in Section 9.4.4, *Elliptic planforms*, from a standpoint of efficiency the elliptical wing planform is very practical in aircraft design and is therefore of great interest to the aircraft designer. In this article, the lifting line method is applied to an elliptical planform and several useful closed-form solutions of selected aerodynamic characteristics are derived. These characteristics are helpful even if they are only used for comparison reasons. The solution assumes that the distribution of circulation is known and is given by:

Elliptical lift distribution:

$$\Gamma(y) = \Gamma_0 \sqrt{1 - \left(\frac{2y}{b}\right)^2} \quad (9-112)$$

Using this distribution, the following aerodynamic characteristics for the elliptical planform can be derived (see derivation section that follows):

Vortex strength (constant):

$$\Gamma_0 = \frac{2C_L S}{\pi b} V \quad (9-113)$$

Downwash (constant):

$$w = -\frac{\Gamma_0}{2b} \quad (9-114)$$

Induced AOA:

$$\alpha_i \approx \frac{\Gamma_0}{2bV} = \frac{C_L}{\pi AR} \quad (9-115)$$

Lift force:

$$L = \rho V \cdot \Gamma_0 \frac{\pi b}{4} \quad (9-116)$$

Lift-induced drag force:

$$D_i = \rho \Gamma_0^2 \frac{\pi}{8} \quad (9-117)$$

Lift coefficient:

$$C_L = \frac{\pi b \Gamma_0}{2VS} \quad (9-118)$$

Lift-induced drag coefficient:

$$C_{Di} = \frac{C_L^2}{\pi AR} \quad (9-119)$$

### Derivation of Equations (9-113) through (9-119)

First evaluate the derivative  $d\Gamma/dy$ . This can be done using the chain rule of differentiation:

$$\begin{aligned} \frac{d\Gamma}{dy} &= \Gamma_0 \frac{d}{dy} \left( 1 - \left( \frac{2y}{b} \right)^2 y^2 \right)^{\frac{1}{2}} \\ &= \Gamma_0 \frac{1}{2} \left( 1 - \left( \frac{2y}{b} \right)^2 y^2 \right)^{-\frac{1}{2}} \left( -\frac{8}{b^2} y \right) \\ &= -\frac{4\Gamma_0}{b^2} \frac{y}{\sqrt{1 - (2y/b)^2}} \end{aligned}$$

This can be used with Equation (9-102) to calculate the total downwash at any spanwise station, say  $y_0$  (for the sake of consistency):

$$\begin{aligned} w_{y_0} &= \frac{1}{4\pi} \int_{-b/2}^{b/2} \frac{d\Gamma/dy}{(y - y_0)} dy = \frac{1}{4\pi} \int_{-b/2}^{b/2} \frac{-\frac{4\Gamma_0}{b^2} \frac{y}{\sqrt{1-(2y/b)^2}}}{(y - y_0)} dy \\ &= -\frac{\Gamma_0}{\pi b^2} \int_{-b/2}^{b/2} \frac{y}{\sqrt{1-(2y/b)^2}(y - y_0)} dy \end{aligned}$$

It is helpful to evaluate the integral by transforming spanwise stations into an angular form as follows:

$$y = (b/2)\cos\phi \Rightarrow dy = -(b/2)\sin\phi d\phi \quad (9-120)$$

Using this transformation, we find the lower limit ( $-b/2$ ) becomes 0 and the upper one ( $+b/2$ ) becomes  $\pi$ . If we define  $y_0 = (b/2)\cos\phi_0$  the above integral can be rewritten as follows:

$$\begin{aligned} w_{y_0} &= -\frac{\Gamma_0}{\pi b^2} \\ &\times \int_{\pi}^0 \frac{(b/2)\cos\phi}{\sqrt{(b/2)^2 - (b/2)^2\cos^2\phi} \times ((b/2)\cos\phi - (b/2)\cos\phi_0)} \\ &\times (-b/2)\sin\phi d\phi \end{aligned}$$

Simplifying further yields:

$$\begin{aligned} w_{y_0} &= \frac{\Gamma_0}{2\pi b} \int_{\pi}^0 \frac{\cos\phi \sin\phi d\phi}{\sqrt{1-\cos^2\phi} \times (\cos\phi - \cos\phi_0)} \\ &= \frac{\Gamma_0}{2\pi b} \int_{\pi}^0 \frac{\cos\phi \sin\phi d\phi}{\sin\phi \times (\cos\phi - \cos\phi_0)} \end{aligned}$$

Finally, this leads to:

$$w_{y_0} = -\frac{\Gamma_0}{2\pi b} \int_0^\pi \frac{\cos\phi}{\cos\phi - \cos\phi_0} d\phi \quad (i)$$

The evaluation of this integral is beyond the scope of this text, but a solution is provided in Karamcheti [53]. An alternative solution method based on the original expression omitting the transformation is presented by Bertin and Smith [50]. In either case, the resulting expression reduces to:

$$w_{y_0} = -\frac{\Gamma_0}{2b} \quad (ii)$$

This is Equation (9-114). Note that the distribution of downwash is constant along the span. The downwash angle can thus be obtained from Equation (9-103):

$$\alpha_{iy_0} \approx -\frac{w_{y_0}}{V} = \frac{\Gamma_0}{2bV} \quad (iii)$$

This is Equation (9-115). Note that this angle is constant along the span as well. Inserting Equation (9-112) into (9-107) yields the total lift generated by the wing:

$$\begin{aligned} L &= \rho V \int_{-b/2}^{b/2} \Gamma(y) dy \\ &= \rho V_\infty \int_{-b/2}^{b/2} \Gamma_0 \sqrt{1 - \left(\frac{2y}{b}\right)^2} dy \end{aligned} \quad (iv)$$

Using the above angular transformations, Equation (iv) can be rewritten and simplified as follows:

Lift:

$$\begin{aligned} L &= \rho V \cdot \Gamma_0 \int_0^\pi \sqrt{1 - \cos^2\phi} (b/2) \sin\phi d\phi \\ &= \rho V_\infty \Gamma_0 \frac{\pi b}{4} \end{aligned} \quad (v)$$

This is Equation (9-116). The lift coefficient can now be determined from:

$$C_L = \frac{2L}{\rho V_\infty^2 S} = \frac{\pi b \Gamma_0}{2VS} \quad (vi)$$

This is Equation (9-118). Alternatively, the vortex strength  $\Gamma_0$  is readily obtained from Equation (vi) as follows:

$$\Gamma_0 = \frac{2SC_L}{\pi b} V \quad (vii)$$

This is Equation (9-113). Similarly, the lift-induced drag can be computed from Equation (9-108):

$$\begin{aligned} D_i &= -\rho \int_{-b/2}^{b/2} w(y) \Gamma(y) dy \\ &= -\rho \int_{-b/2}^{b/2} w(y) \Gamma_0 \sqrt{1 - \left(\frac{2y}{b}\right)^2} dy \end{aligned} \quad (viii)$$

Inserting Equation (9-114) and using the spanwise angular transformation of Equation (9-120), we get Equation (9-117):

$$\begin{aligned} D_i &= -\rho \int_{-b/2}^{b/2} \frac{-\Gamma_0}{2b} \Gamma_0 \sqrt{1 - \left(\frac{2y}{b}\right)^2} dy \\ &= \frac{\rho \Gamma_0^2}{2b} \int_0^\pi \sqrt{1 - \cos^2 \phi} (b/2) \sin \phi d\phi = \rho \Gamma_0^2 \frac{\pi}{8} \end{aligned} \quad (\text{ix})$$

The lift-induced drag coefficient can now be determined as follows, using Equation (vii):

$$\begin{aligned} C_{Di} &= \frac{2D_i}{\rho V^2 S} = \frac{2(\rho \Gamma_0^2 \frac{\pi}{8})}{\rho V^2 S} = \frac{\pi}{4V^2 S} \Gamma_0^2 \\ &= \frac{\pi}{4V^2 S} \left( \frac{2SC_L}{\pi b} V \right)^2 = \frac{SC_L^2}{\pi b^2} = \frac{C_L^2}{\pi AR} \end{aligned} \quad (\text{x})$$

This is Equation (9-119).

QED

where

$\alpha_{ZL}$  = zero lift angle for the airfoil at station  $\phi$   
 $\phi_i$  = angles (in radians) that correspond to the spanwise angular stations obtained from  
 $y_i = (b/2)\cos\phi_i$  (i.e. Equation [9-120]), in radians  
 $\mu = C \cdot C_{l_a}/4b$ , dimensionless; the airfoil's lift curve slope,  $C_{l_a}$ , may be a function of  $\phi$   
 $b$  = wingspan, in ft or m  
 $C$  = chord at station  $\phi_i$ , in ft or m

Solving the system leads to a number of interesting results, some of which are presented below.

Lift force:

$$L = \frac{1}{2} \rho V \cdot S \cdot (\pi \cdot AR \cdot A_1) = \frac{1}{2} \rho V \cdot b^2 \cdot \pi \cdot A_1 \quad (9-124)$$

Lift-induced drag:

$$D_i = \frac{\rho V^2}{2} b^2 \pi \sum n A_n^2 \quad (9-125)$$

$$\text{Lift coefficient: } C_L = \pi \cdot AR \cdot A_1 \quad (9-126)$$

The lift curve slope can thus be calculated from:

Lift curve slope:

$$C_{L_a} = \frac{C_L}{\alpha - \alpha_{ZL}} = \frac{\pi \cdot AR \cdot A_1}{\alpha - \alpha_{ZL}} \quad (9-127)$$

And lift-induced drag coefficient:

$$C_{Di} = \frac{C_L^2}{\pi \cdot AR} (1 + \delta) = \frac{C_L^2}{\pi \cdot AR \cdot e} \quad (9-128)$$

where  $\delta = \sum_{n=2}^N n \left( \frac{A_n}{A_1} \right)^2$  and  $e = \frac{1}{1+\delta}$ .

As stated above, if the spanwise distribution of lift is symmetrical, all the even indexed constants ( $A_2, A_4, \dots$ ) of the summation are set to zero. This can be written as follows:

$$\delta = \sum_{n=2}^N n \left( \frac{A_n}{A_1} \right)^2 = 3 \left( \frac{A_3}{A_1} \right)^2 + 5 \left( \frac{A_5}{A_1} \right)^2 + 7 \left( \frac{A_7}{A_1} \right)^2 + \dots \quad (9-129)$$

See Figure 15-22 for a graph plotting  $\delta$  as a function of taper ratio and aspect ratio for straight tapered wings.

$$\begin{bmatrix} \sin\phi_1(\mu + \sin\phi_1) & \sin 2\phi_1(2\mu + \sin\phi_1) & \cdots & \sin N\phi_1(N\mu + \sin\phi_1) \\ \sin\phi_2(\mu + \sin\phi_2) & \sin 2\phi_2(2\mu + \sin\phi_2) & \cdots & \sin N\phi_2(N\mu + \sin\phi_2) \\ \vdots & \vdots & \ddots & \vdots \\ \sin\phi_N(\mu + \sin\phi_N) & \sin 2\phi_N(2\mu + \sin\phi_N) & \cdots & \sin N\phi_N(N\mu + \sin\phi_N) \end{bmatrix} \begin{Bmatrix} A_1 \\ A_2 \\ \vdots \\ A_N \end{Bmatrix} = \begin{Bmatrix} \mu(\alpha - \alpha_{ZL_1}) \sin\phi_1 \\ \mu(\alpha - \alpha_{ZL_2}) \sin\phi_2 \\ \vdots \\ \mu(\alpha - \alpha_{ZL_N}) \sin\phi_N \end{Bmatrix} \quad (9-123)$$

### Change in Induced Angle-of-attack

The induced AOA on an arbitrary planform differs from that of an elliptical planform of an equal AR according to the following expression:

$$\alpha_{wing} - \alpha_{airfoil} = \frac{C_L}{\pi AR} (1 + \tau) \quad (9-130)$$

where  $\tau$  is given by:

$$(1 + \tau) = \frac{\alpha_{wing}}{A_1} - \frac{\pi AR}{C_{l_a}} \quad (9-131)$$

### Derivation of Equations (9-124) through (9-128)

In order to determine the coefficients  $A_1, A_2, A_3, \dots, A_N$ , the circulation for the  $N$  vortices must be determined. The procedure begins by relating the section lift coefficient at any angular station  $\phi$  as follows:

$$C_l(\phi) = \frac{\text{lift per unit span}}{\frac{1}{2}\rho V^2 C} = \frac{\rho V \cdot \Gamma(\phi)}{\frac{1}{2}\rho V^2 C(\phi)} = \frac{2\Gamma(\phi)}{VC(\phi)} \quad (\text{i})$$

where  $C(\phi)$  is the chord at a specific angular station  $\phi$ . However, if the lift curve slope,  $C_{l_a} = dC_l/d\alpha$ , of the airfoil at the angular station  $\phi$  is known, the section lift coefficient can also be determined from:

$$C_l = \left( \frac{dC_l}{d\alpha} \right) (\alpha_e - \alpha_{ZL}) = C_{l_a} (\alpha - \alpha_i - \alpha_{ZL}) \quad (\text{ii})$$

where  $\alpha_{ZL}$  is the zero-lift AOA of the airfoil at the angular station  $\phi$ . Note that  $\alpha, \alpha_{ZL}$ , and  $\alpha_i$  are all functions of the angular station  $\phi$ . By equating Equations (i) and (ii) we get:

$$\begin{aligned} \frac{2\Gamma(\phi)}{VC(\phi)} &= C_{l_a} (\alpha - \alpha_i - \alpha_{ZL}) \\ \Rightarrow \frac{2\Gamma(\phi)}{C_{l_a} C(\phi)} &= V(\alpha - \alpha_{ZL}) - V\alpha_i \end{aligned} \quad (\text{iii})$$

The term  $V\alpha_i$  is given by Equation (9-102):

$$V\alpha_i = -w = -\frac{1}{4\pi} \int_{-b/2}^{+b/2} \frac{d\Gamma/dy}{y - y_0} dy \quad (\text{iv})$$

where the minus sign indicates a downward flow of air. Using the definition of  $\Gamma(\phi)$  given by Equation (9-121) this can be rewritten as follows:

$$-w(\phi) = -V \frac{\sum n A_n \sin n\phi}{\sin \phi} \quad (\text{v})$$

Therefore, Equation (iii) can be rewritten as follows:

$$\frac{2\Gamma(\phi)}{C(\phi) \cdot C_{l_a}} = V(\alpha - \alpha_{ZL}) - V \frac{\sum n A_n \sin n\phi}{\sin \phi} \quad (\text{vi})$$

Expanding by inserting  $\Gamma(\phi)$  per Equation (9-121) yields:

$$\frac{4b}{C \cdot C_{l_a}} \sum A_n \sin n\phi = (\alpha - \alpha_{ZL}) - \frac{\sum n A_n \sin n\phi}{\sin \phi} \quad (\text{vii})$$

Let  $\mu = C \cdot C_{l_a} / 4b$  and insert into Equation (vii). This leads to:

$$\begin{aligned} \sin \phi \sum A_n \sin n\phi &= \mu(\alpha(\phi) - \alpha_{ZL}(\phi)) \sin \phi - \mu \sum n A_n \sin n\phi \\ &\Rightarrow \sin \phi \sum A_n \sin n\phi + \mu \sum n A_n \sin n\phi \\ &= \mu(\alpha(\phi) - \alpha_{ZL}(\phi)) \sin \phi \end{aligned}$$

Simplify terms in the summation sign to yields a governing equation that is called the *monoplane equation*.

$$\sum_{n=1}^N A_n \sin n\phi (\mu n + \sin \phi) = \mu(\alpha - \alpha_{ZL}) \sin \phi \quad (9-122)$$

This equation yields a set of equations that must be solved simultaneously to obtain the constants  $A_1, A_2, A_3, \dots, A_N$ . The angle  $\phi$  refers to a spanwise angle transformation of Equation (9-120). If the problem deals with symmetrical load distribution, all even terms ( $n = 2, 4, \dots$ ) are omitted from the solution.

Next consider the lift coefficient generated by the wing, given by:

$$C_L = \frac{2L}{\rho V^2 S} = \frac{2}{VS} \int_{-b/2}^{b/2} \Gamma(y) dy \quad (\text{viii})$$

Again using the definition of  $\Gamma(\phi)$  given by Equation (9-121), Equation (viii) becomes:

$$\begin{aligned} C_L &= \frac{2}{VS} \int_{-b/2}^{b/2} \Gamma(y) dy \\ &= \frac{2}{VS} \int_0^\pi \left[ 2bV \sum_{n=1}^N A_n \sin n\phi \right] \left( \left( \frac{b}{2} \right) \sin \phi d\phi \right) \\ &= \frac{2b^2}{S} \int_0^\pi \left[ \sum_{n=1}^N A_n \sin n\phi \right] \sin \phi d\phi \end{aligned}$$

The integral can be solved noting that:

$$\int_0^\pi \sin n\phi \sin \phi d\phi = \begin{cases} \pi/2 & \text{if } n = 1 \\ 0 & \text{if } n \neq 1 \end{cases}$$

This allows Equation (ix) to be rewritten as follows:

$$\begin{aligned} C_L &= \frac{2b^2}{S} \int_0^\pi \left[ \sum_{n=1}^N A_n \sin n\phi \right] \sin \phi d\phi = \frac{2b^2 \pi}{S} A_1 \\ &= \frac{\pi b^2 A_1}{S} = \pi \cdot AR \cdot A_1 \end{aligned} \quad (\text{ix})$$

This is Equation (9-126). Then consider the lift-induced drag coefficient generated by the wing. Equation (9-108) defines the lift-induced drag,  $D_i$ . Inserting Equation (v) for  $w(y)$  and Equation (9-121) for  $\Gamma(\phi)$  we get:

$$\begin{aligned} D_i &= -\rho \int_{-b/2}^{b/2} w(y) \Gamma(y) dy \\ &= -\rho \int_{-b/2}^{b/2} \left[ -V \frac{\sum nA_n \sin n\phi}{\sin \phi} \right] \\ &\quad \times \left[ 2bV \sum A_n \sin n\phi \right] \left( \left( \frac{b}{2} \right) \sin \phi d\phi \right) \\ &= \frac{\rho V 2bbV}{2} \int_0^\pi \left[ \frac{\sum nA_n \sin n\phi}{\sin \phi} \right] \\ &\quad \times \left[ \sum A_n \sin n\phi \right] (\sin \phi d\phi) \end{aligned}$$

This reduces to:

$$D_i = \rho V^2 b^2 \int_0^\pi \sum nA_n \sin n\phi \sum A_n \sin n\phi d\phi$$

Where the evaluation of the integral yields:

$$\int_0^\pi \sum nA_n \sin n\phi \sum A_n \sin n\phi d\phi = \frac{\pi}{2} \sum nA_n^2$$

Therefore, the lift-induced drag is given by:

$$D_i = \frac{\rho V^2}{2} b^2 \pi \sum nA_n^2 \quad (\text{x})$$

Using Equation (9-110) it is now possible to determine the lift-induced drag coefficient:

$$\begin{aligned} C_{Di} &= \frac{2D_i}{\rho V^2 S} = \frac{2 \left[ \frac{\rho V^2}{2} b^2 \pi \sum nA_n^2 \right]}{\rho V^2 S} = \frac{b^2 \pi}{S} \sum nA_n^2 \\ &= \pi \cdot AR \cdot \sum nA_n^2 \end{aligned} \quad (\text{xi})$$

Since  $C_L = \pi \cdot AR \cdot A_1 \Leftrightarrow A_1 = \frac{C_L}{\pi \cdot AR}$  it is possible to rewrite this as follows:

$$\begin{aligned} C_{Di} &= \pi \cdot AR \cdot \sum nA_n^2 = \pi \cdot AR \cdot \left( A_1^2 + \sum_{n=2}^N nA_n^2 \right) \\ &= \frac{C_L^2}{\pi \cdot AR} \left( 1 + \sum_{n=2}^N n \left( \frac{A_n}{A_1} \right)^2 \right) \end{aligned} \quad (\text{xii})$$

This is a classic form of this equation, typically written in the following form, using the term  $\delta$  to denote the lift-induced drag factor.

$$C_{Di} = \frac{C_L^2}{\pi \cdot AR} (1 + \delta) \quad (\text{xiii})$$

It is evident that the minimum  $C_{Di}$  is obtained when  $\delta = 0$ , but this represents an elliptic lift distribution.

QED

### Derivation of Equation (9-130)

Consider a two-dimensional airfoil and three-dimensional wing whose cross-sectional geometry is that of the said airfoil. The airfoil is akin to a three-dimensional wing of infinite wingspan. Consider these at specific  $AOA$  such that they both generate an equal lift coefficient,  $C_L$ . This allows the aerodynamic  $AOA$ <sup>5</sup> for each “wing” to be determined as follows:

Airfoil:

$$\alpha_{airfoil} = C_L / C_{l_\alpha}$$

Wing:

$$\alpha_{wing} = C_L / C_{L_\alpha}$$

Subtracting one from the other leads to:

$$\alpha_{wing} - \alpha_{airfoil} = \frac{C_L}{C_{L_\alpha}} - \frac{C_L}{C_{l_\alpha}} = C_L \left( \frac{1}{C_{L_\alpha}} - \frac{1}{C_{l_\alpha}} \right)$$

This represents the difference in  $AOA$  between the two geometries. Next, insert  $A_1 = C_L / \pi AR$  into the expression for the three-dimensional wing,

<sup>5</sup>The aerodynamic  $AOA$  is measured with respect to zero lift; in other words:  $\alpha - \alpha_{ZL}$ .

i.e.  $C_{L_\alpha} = C_L/\alpha_{wing}$ . This yields the following relationship between  $C_{L_\alpha}$  and  $A_1$ :

$$\begin{aligned} A_1 &= C_L/\pi AR \Rightarrow C_L = A_1\pi AR \Rightarrow C_{L_\alpha} = C_L/\alpha_{wing} \\ &= A_1\pi AR/\alpha_{wing} \end{aligned}$$

Replacing the corresponding term in the above equation for the difference in AOA leads to:

$$\begin{aligned} \alpha_{wing} - \alpha_{airfoil} &= C_L \left( \frac{1}{C_{L_\alpha}} - \frac{1}{C_{l_\alpha}} \right) \\ &= C_L \left( 1 \left/ \left( \frac{C_L}{\alpha_{wing}} \right) \right. - \frac{1}{C_{l_\alpha}} \right) \\ &= \frac{C_L}{\pi AR} \left( \frac{\alpha_{wing}}{A_1} - \frac{\pi AR}{C_{l_\alpha}} \right) \end{aligned}$$

QED

### EXAMPLE 9-13

Estimate the aerodynamic characteristics of the SR22 wing planform (ignoring the presence of the fuselage) using the lifting line method. Determine this using four terms in the monoplane equation, assuming symmetrical lift distribution. Assume the aircraft is flying at an AOA of  $5^\circ$  ( $0.08727$  radians) and that the wing uses the NACA 65-415 airfoil (see Figure 9-60). Assume the airfoil's zero-lift AOA,  $\alpha_{ZL}$ , is approximately  $-2.7^\circ$  ( $-0.04712$  radians) and its lift curve slope,  $C_{l_\alpha}$ , is  $2\pi$ . Note that the dimensions in Figure 9-89 are calculated based on the geometry shown and are not the "official" numbers (e.g. official  $S = 144.9$  ft $^2$  and  $AR = 10$ ). Determine the airspeed that the airplane must fly at S-L if it weighs 3400 lb $_f$ .

#### Solution

Begin by creating the relationship between the physical and angular span stations (see Figure 9-90). Note that the physical stations are given by  $y_i = (b/2)\cos\phi_i$  (Equation [9-120]). For this reason, the cosine of  $\phi$  is in effect a parameter that varies between 1 and 0 that can be used

with a parametric representation for the chord. Thus, the chord at any spanwise station can be calculated from the following parametric equation:

$$C_i = C_t \cos\phi_i + C_r(1 - \cos\phi_i)$$

where  $C_t = 5.18$  ft and  $C_r = 2.59$  ft.

Next tabulate the following values:

Column ① and ②: contain the spanwise angular stations from Figure 9-90 both in degrees and radians.

Column ③: contains the cosine of the angular station.

Column ④: contains the wing chord at the angular station. Calculated using  $C_i = C_t \cos\phi_i + C_r(1 - \cos\phi_i)$ .

Using the root and tip chords,  $C_t = 5.18$  ft and  $C_r = 2.59$  ft, respectively, this expression becomes:

$$C_i = 2.59 \cos\phi_i + 5.18(1 - \cos\phi_i)$$

Columns ⑤ through ⑩: contain the various sines of the angular stations. These are needed to properly setup the matrix as required by the monoplane equation.

① Angular Station	② Deg	③ Rad	④ $\cos \phi$	⑤      ⑥      ⑦      ⑧      ⑨					
				④ $C(\phi)$	⑤	⑥	⑦	⑧	⑨
ID	Deg	Rad	$\cos \phi$	ft	$\sin \phi$	$\sin 3\phi$	$\sin 5\phi$	$\sin 7\phi$	$\mu$
1	22.5	0.3927	0.9239	2.79	0.3827	0.9239	0.9239	0.3827	0.1143
2	45.0	0.7854	0.7071	3.35	0.7071	0.7071	-0.7071	-0.7071	0.1373
3	67.5	1.1781	0.3827	4.19	0.9239	-0.3827	-0.3827	0.9239	0.1718
4	90.0	1.5708	0.0000	5.18	1.0000	-1.0000	1.0000	-1.0000	0.2124

### EXAMPLE 9-13 (cont'd)

Column ⑨: is calculated as follows, using values from the first row ( $ID = 1$ ):

$$\mu_1 = C_1 \cdot C_{l_\alpha} / 4b = (2.79) \cdot (2\pi) / 4(38.3) = 0.1143$$

Next prepare the aerodynamic influence matrix per Equation (9-123). Note that since the lift distribution is symmetrical, we are only concerned with the constants  $A_1$ ,  $A_3$ ,  $A_5$ , and  $A_7$ . This leads to the following setup.

$$\begin{bmatrix} 0.1902 & 0.6704 & 0.8816 & 0.4527 \\ 0.5971 & 0.7913 & -0.9856 & -1.1798 \\ 1.0123 & -0.5508 & -0.6823 & 1.9646 \\ 1.2124 & -1.6373 & 2.0622 & -2.4871 \end{bmatrix} \begin{Bmatrix} A_1 \\ A_3 \\ A_5 \\ A_7 \end{Bmatrix} = \begin{Bmatrix} 0.005879 \\ 0.001305 \\ 0.002133 \\ 0.028551 \end{Bmatrix}$$

For instance, the first row in the above matrix is calculated as follows, using the monoplane equation:

$$\begin{aligned} A_{11} &= \sin \phi_1 (\mu + \sin \phi_1) \\ &= (0.3827)(0.1143 + 0.3827) = 0.1902 \end{aligned}$$

$$\begin{aligned} A_{12} &= \sin 3\phi_1 (3\mu + \sin \phi_1) \\ &= (0.9239)(3 \times 0.1143 + 0.3827) = 0.6704 \end{aligned}$$

$$\begin{aligned} A_{13} &= \sin 5\phi_1 (5\mu + \sin \phi_1) \\ &= (0.9239)(5 \times 0.1143 + 0.3827) = 0.8816 \end{aligned}$$

$$\begin{aligned} A_{14} &= \sin 7\phi_1 (7\mu + \sin \phi_1) \\ &= (0.3827)(7 \times 0.1143 + 0.3827) = 0.4527 \end{aligned}$$

$$\begin{aligned} B_1 &= \mu(\alpha - \alpha_{ZL}) \sin \phi_1 \\ &= (0.1143)(0.08727 - (-0.04712))(0.3827) = 0.005879 \end{aligned}$$

Solving the equations requires the square matrix to be inverted and then multiplied to the column matrix on the right-hand side, yielding the following values for the constants:

$$\begin{Bmatrix} A_1 \\ A_3 \\ A_5 \\ A_7 \end{Bmatrix} = \begin{Bmatrix} 2.251 \times 10^{-2} \\ 8.674 \times 10^{-4} \\ 1.195 \times 10^{-3} \\ -8.441 \times 10^{-5} \end{Bmatrix}$$

This allows the following aerodynamic parameters to be calculated. First, the lift coefficient can be calculated from Equation (9-126):

$$C_L = \pi \cdot AR \cdot A_1 = \pi \cdot (9.858) \cdot 2.251 \times 10^{-2} = 0.6971$$

The lift-induced drag coefficient can be found by first determining the factor  $\delta$ :

$$\begin{aligned} \delta &= \sum_{n=2}^N n \left( \frac{A_n}{A_1} \right)^2 = 3 \left( \frac{A_3}{A_1} \right)^2 + 5 \left( \frac{A_5}{A_1} \right)^2 + 7 \left( \frac{A_7}{A_1} \right)^2 \\ &= 0.01865 \end{aligned}$$

This yields the following drag coefficient per Equation (9-128):

$$C_{Di} = \frac{C_L^2}{\pi \cdot AR} (1 + \delta) = \frac{(0.6971)^2}{\pi \cdot (9.858)} (1 + 0.01865) = 0.01599$$

Oswald's span efficiency is thus:

$$e = \frac{1}{1+\delta} = \frac{1}{1+0.01865} = 0.9817$$

Note that this value is for the wing without the detrimental effects of the fuselage. The lifting line method will always return efficiency that is too high for this reason. Finally, the wing's lift curve slope can be determined as follows:

$$\begin{aligned} C_{L_\alpha} &= \frac{C_L}{(\alpha - \alpha_{ZL})} = \frac{0.6971}{(0.08727 + 0.04712)} \\ &= 5.187 \text{ per radian} \end{aligned}$$

Finally, the airspeed the airplane must fly at in order to generate 3400 lb<sub>f</sub> of lift at 5° AOA can be determined as follows:

$$\begin{aligned} V &= \sqrt{\frac{2W}{\rho S C_L}} = \sqrt{\frac{2(3400)}{(0.002378)(148.8)(0.6971)}} = 166 \text{ ft/s} \\ &= 98.4 \text{ KCAS} \end{aligned}$$

#### 9.7.4 Accounting for a Fuselage in Prandtl's Lifting Line Method

The lifting line method is seriously limited in that it applies directly to a "clean" wing; that is, the presence of a fuselage is not included. Consequently, the prediction will tend to return inflated span efficiencies, which

can be detrimental to performance analysis. One way of correcting for this shortcoming is to consider only the exposed part of the wing. This is shown in Figure 9-91, which shows three wing planform shapes of equal spans, reference areas, and (therefore)  $AR$ . The top one is a "clean" elliptical wing, to which all other wings

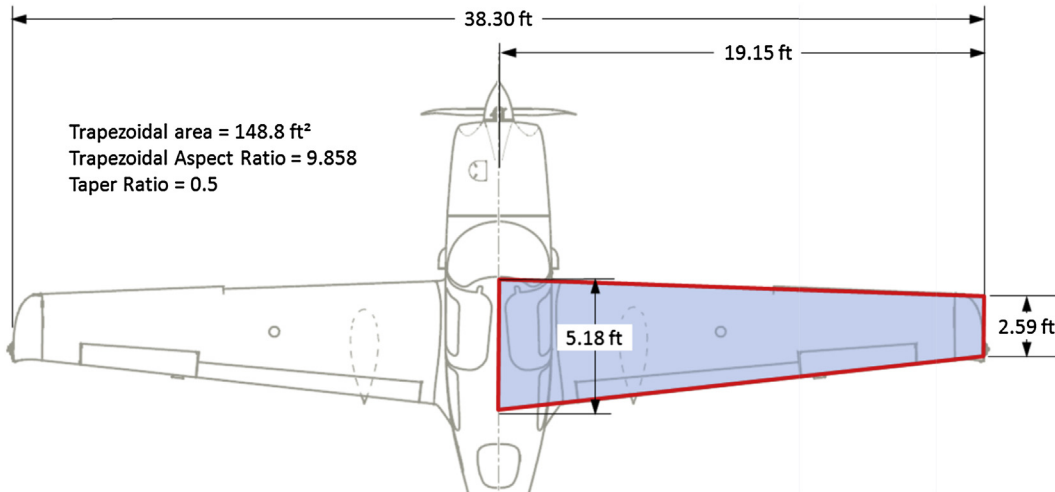


FIGURE 9-89 A top view of the SR-22 showing dimensions used for this example.

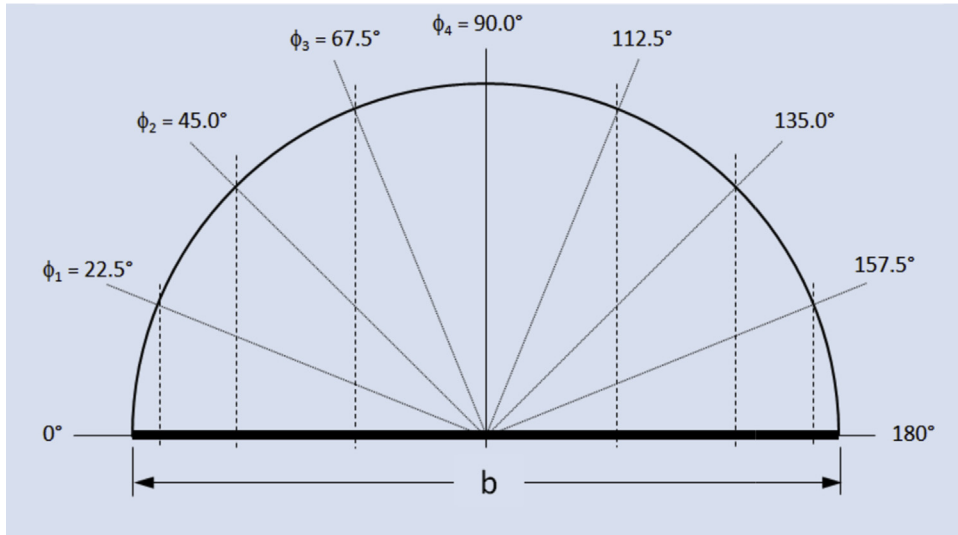


FIGURE 9-90 Relationship between physical and angular stations along the wingspan.

are compared when using the lifting line method. The wing in the center is a “clean” trapezoidal wing, whereas the bottom one is the same wing, except with a fuselage present. A schematic of the corresponding distribution of section lift coefficients is shown in the right portion of the figure.

It is evident from the preceding analysis that it compares the top (elliptical) and center wing (trapezoidal), whereas it would be more appropriate to compare the top and the bottom one. The fact that the fuselage so reduces the lift generated by the wing means that the airplane will have to fly at a higher *AOA* to make up for it. This is largely why the wing with the fuselage

generates higher lift-induced drag than the clean wing and, when compared to the clean elliptical wing, reduces the Oswald span efficiency. The following method allows this to be taken into account when using the lifting line method, but first the following assumptions are introduced.

- (1) Assume that the lift is entirely generated by the exposed wing panels and not by the region over the fuselage. This means that the section lift coefficients over the fuselage region are assumed to be zero.
- (2) Assume that the fuselage acts as a wall. This allows the lifting line method to be applied to the exposed part of

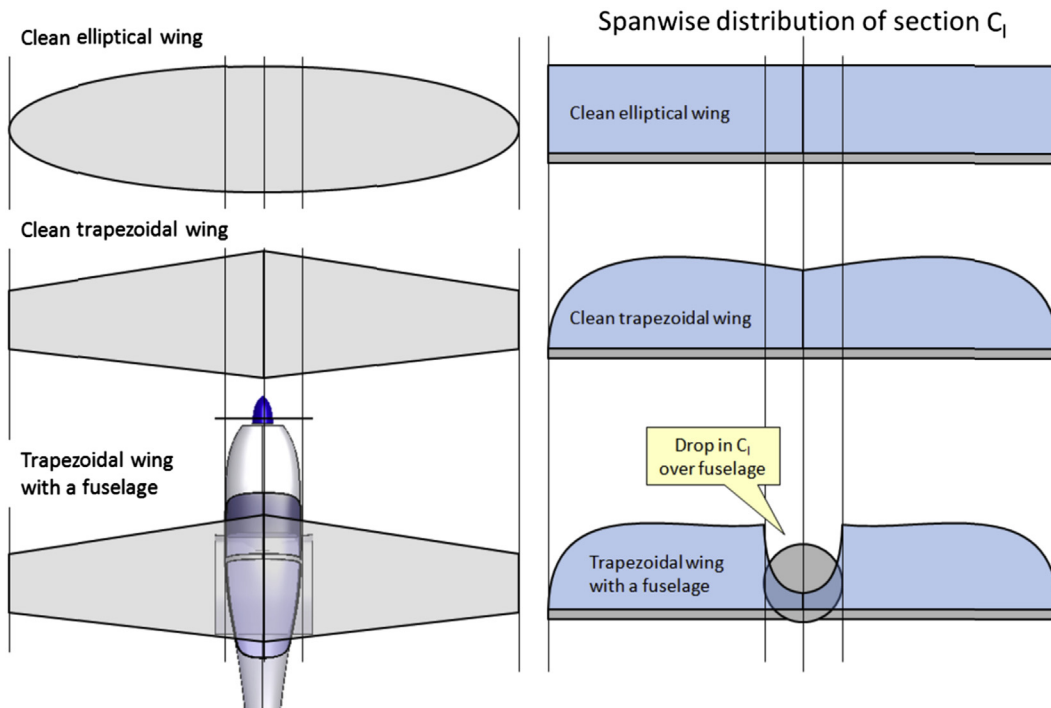


FIGURE 9-91 A schematic showing how the presence of a fuselage reduces the magnitude of the section lift coefficient over the fuselage.

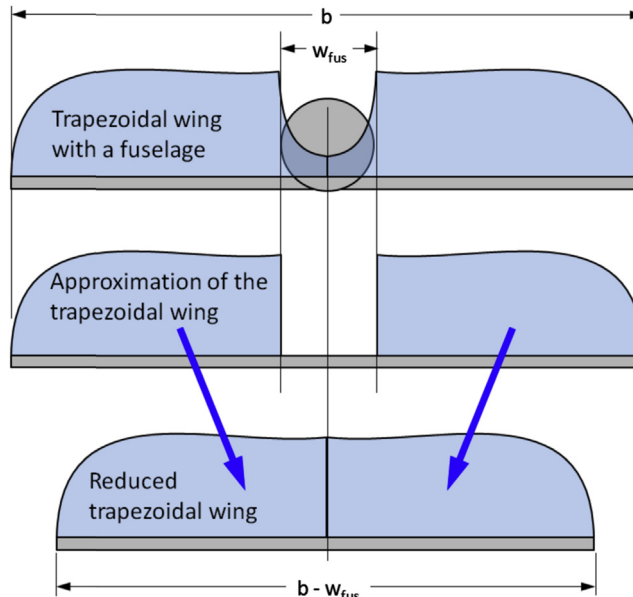


FIGURE 9-92 A schematic showing how the presence of a fuselage can be accounted for using the lifting line method.

the wing by simply reducing the wing geometry as shown in Figure 9-92. For instance, the wingspan,  $b$ , will be reduced by the width of the fuselage,  $w_{fus}$ . Reduced wingspan,  $b_R$ :

$$b_R = b - w_{fus} \quad (9-132)$$

Let the planform area corresponding to the wing inside the fuselage be given by  $C_r \times w_{fus}$ . Therefore, the reduced wing area  $S_R$  is given by:

Reduced wing area,  $S_R$ :

$$S_R = S - C_r w_{fus} \quad (9-133)$$

Reduced aspect ratio,  $AR_R$ :

$$AR_R = \frac{b_R^2}{S_R} \quad (9-134)$$

Furthermore, reducing the wingspan will modify the taper ratio because the root chord changes. The reduced taper ratio can be estimated using a parametric representation for the chord:

$$C_{rR} = C_r(1-t) + tC_t = \left(1 - \frac{w_{fus}}{b}\right)C_r + \left(\frac{w_{fus}}{b}\right)C_t$$

This can be used to determine the reduced taper ratio,  $\lambda_R$ :

$$\begin{aligned} \lambda_R &= \frac{C_t}{C_{rR}} = \frac{bC_t}{C_r(b-w_{fus}) + w_{fus}C_t} \\ &= \frac{bC_t}{C_r(1-w_{fus}) + w_{fus}C_t} \end{aligned} \quad (9-135)$$

So, rather than analyzing the complete wing, its wing span and area should be reduced using the above expressions. Therefore, the wing will now require a higher AOA in order to generate the  $C_L$  required for a given flight condition.

### EXAMPLE 9-14

Estimate the aerodynamic characteristics of the SR22 wing planform (including the presence of the fuselage) using the corrected lifting line method just discussed. Use all the information from Example 9-9 and assume a fuselage width of 50 inches (4.167 ft). Determine the  $C_L$  required for the airplane to generate 3400 lb<sub>f</sub> at 98.4 KCAS and use this to estimate the aerodynamic characteristics. Then, compare it to that of Example 9-9 (the AOA and  $C_L$  of Example 9-13 are  $5^\circ$  and 0.6971, respectively).

#### Solution

The procedure is identical to that of Example 9-13, so only results will be cited. First, compute the reduced wing parameters:

Reduced wingspan,  $b_R$ :

$$b_R = b - w_{fus} = 38.30 - 4.167 = 34.13 \text{ ft}$$

Reduced wing area,  $S_R$ :

$$\begin{aligned} S_R &= S - C_r w_{fus} = 148.8 - 5.18 \times 4.167 \\ &= 127.2 \text{ ft}^2 \end{aligned}$$

Reduced aspect ratio,  $AR_R$ :

$$AR_R = \frac{b_R^2}{S_R} = \frac{34.13^2}{127.2} = 9.16$$

Reduced taper ratio,  $\lambda_R$ :

$$\lambda_R = \frac{bC_t}{C_r(b-w_{fus}) + w_{fus}C_t} = 0.5288$$

Then, estimate the  $C_L$  required by the smaller wing:

$$C_L = \frac{2W}{\rho V^2 S} = \frac{2(3400)}{(0.002378)(98.5 \times 1.688)^2 (127.2)} = 0.8132$$

Proceeding with the analysis method presented before, the results presented in Table 9-10 were obtained. It can be seen that while the “clean” wing requires  $5^\circ$  to lift 3400 lb<sub>f</sub> at 98.4 KCAS, the reduced wing (more realistic) requires  $6.43^\circ$  (see Table 9-10 below, where ‘original’ refers to the clean wing and ‘reduced’ refers to the wing with the fuselage). Consequently, its induced drag coefficient is 47% greater than the “clean” wing.

#### 9.7.5 Computer code: Prandtl’s Lifting Line Method

The following code implements the lifting line method for an arbitrary wing using the above formulation. It is written using Visual Basic for Applications (VBA) and can be used as is in Microsoft Excel. It allows as many vortices as system resources allow to be used for the analysis, represented by the

variable  $N$  (see the commented variable definitions in the code). A value of  $N$  larger than 50 is impractical;  $N$  in the ballpark of 10–14 is adequate in most instances.

In order to use the code and assuming Microsoft Excel 2007 is being used, the reader must select the *Developer* tab and then click on the *Visual Basic* icon to open a window containing the programming

TABLE 9-10 Comparing Results for the Original and Reduced Wing

		Elliptical	Original	Reduced	%Change
Taper ratio	$\lambda =$	N/A	0.5000	0.5288	5.8
Aspect ratio	$AR =$	9.86	9.86	9.16	-7.1
Wing area	$S =$	148.8	148.8	127.2	-14.5
Angle-of-attack	$\alpha =$	5.00	5.00	6.43	28.6
Lift coefficient	$C_L =$	0.6971	0.6971	0.8148	16.9
Induced drag factor	$\delta =$	0.0000	0.01865	0.01894	1.6
Lift induced drag coefficient	$C_{Dl} =$	0.01569	0.01599	0.02351	47.0
Oswald's efficiency	$e =$	1.0000	0.9817	0.9814	0.0

environment. This window will feature a title like *Microsoft Visual Basic*, followed by the filename, visible in the upper-left corner. In the project pane, typically docked at the left-hand side of this window, right-click to reveal a pop-up menu. One of the commands is the *Insert* command and it has a submenu indicated by a dark triangle. Hover with the mouse cursor over this triangle until the submenu appears. Select the

*Module* command. This will open a VBA editor inside the main window. The program below must be entered there. The function is then called from the spreadsheet itself as shown in Figure 9-93. It can be seen that simple cell references are used to pass arguments to the routine. Here 50 vortices are being used, and the Mode is 2, which means that the term  $\delta$  is returned.

```

Function LiftingLine(AR As Single, TR As Single, S As Single, Cla As Single, AOA As Single, AOA_ZL As Single, N As Integer, Mode As Byte) As Single
    'This function implements Prandtl's Lifting Line theory
    '
    'Variables: AR = Aspect Ratio
    '           TR = Taper Ratio
    '           S = Wing area (ft2)
    '           Cla = Average airfoil lift curve slope (per rad)
    '           AOA = Angle of attack (rad)
    '           AOA_ZL = Average zero-lift AOA of airfoils (rad)
    '           N = Number of vortices
    '
    'Mode:   =0 Return CL
    '       =1 Return CDi
    '       =2 Return del
    '       =3 Return e
    '
    'Initialize
    Dim i As Integer, j As Integer, m As Single
    Dim Pi As Single, Sum As Single
    Dim dPhi As Single, sinPhi As Single, t As Single, C_of_Phi As Single
    Dim Cr As Single, Ct As Single, b As Single
    Dim CL As Single, CDi As Single, CLalpha As Single, del As Single
    '
    'Dimension arrays
    ReDim Phi(N) As Single
    ReDim mu(N) As Single

```

```

ReDim A(N, 1) As Double
ReDim MatB(N, N) As Double
ReDim MatC(N, 1) As Double
'Presets
Pi = 3.14159265
b = Sqr(S * AR) 'Wing span
Cr = 2 * S / (b + b * TR) 'Root chord
Ct = TR * Cr 'Tip chord
'Create stations
dPhi = 0.5 * Pi / CSng(N) 'in Radians
For i = 1 To N
  'Calculate station angle
  Phi(i) = Phi(i - 1) + dPhi

  'Calculate mu
  t = Cos(Phi(i)) 'Parameter t
  C_of_Phi = (1 - t) * Cr + t * Ct 'Chord determined using parametric formulation
  mu(i) = 0.25 * C_of_Phi * Cla / b
  Next i
'Prepare aerodynamic influence coefficients
For i = 1 To N
  'Calculate the sine of the angle Phi(i) so it won't have to be calculated over and over
  sinPhi = Sin(Phi(i))
  'Calculate the vortex influence matrix
  For j = 1 To N
    m = 2 * j - 1
    MatB(i, j) = Sin(m * Phi(i)) * (m * mu(i) + sinPhi)
  Next j
  'Calculate the boundary conditions
  MatC(i, 1) = mu(i) * (AOA - AOA_ZL) * sinPhi
  Next i
'Invert matrix
i = MAT_GaussP(MatB(), MatC(), A())
'Calculate lift coefficient
CL = A(1, 1) * Pi * AR
CLalpha = CL / (AOA - AOA_ZL)
'Calculate lift induced drag coefficient
Sum = 0
For i = 2 To N
  m = 2 * i - 1
  Sum = Sum + m * A(i, 1) ^ 2
Next i
del = Sum / (A(1, 1) ^ 2)
e = 1 / (1 + del)
CDi = CL ^ 2 * (1 + del) / (Pi * AR)
'Return
If Mode = 0 Then LiftingLine = CL
If Mode = 1 Then LiftingLine = CDi
If Mode = 2 Then LiftingLine = del
If Mode = 3 Then LiftingLine = e
If Mode = 4 Then LiftingLine = CLalpha
End Function

```

$\lambda$	AR					
	4	6	8	10	12	14
0.000	=LiftingLine(\$\$76,\$R77,\$B\$78,\$C\$10,\$D\$11,\$F\$16,50,2)					
0.025	0.065281	0.094001	0.1168008	0.135233	0.15044	0.163215
0.050	0.048375	0.071701	0.0907342	0.106382	0.119439	0.130495
0.075	0.036884	0.055819	0.0716159	0.084796	0.09591	0.105397
0.100	0.028594	0.044003	0.0571099	0.068196	0.077639	0.085766
0.125	0.022418	0.035006	0.0459075	0.055252	0.063296	0.070277
0.150	0.017731	0.028068	0.0371802	0.045099	0.051992	0.058032
0.200	0.011383	0.018526	0.0250679	0.030929	0.036164	0.040852
0.250	0.007684	0.012912	0.0179135	0.022556	0.026827	0.030751
0.300	0.005684	0.009896	0.0141123	0.018168	0.02201	0.025628
0.350	0.004839	0.008689	0.0126825	0.016632	0.020457	0.024124
0.400	0.004818	0.008789	0.0129866	0.017198	0.021323	0.025317
0.450	0.005404	0.009864	0.0145909	0.019347	0.024019	0.028555
0.500	0.00645	0.011681	0.0171895	0.022711	0.028121	0.033366
0.600	0.009535	0.016921	0.0245386	0.032065	0.039365	0.046386
0.700	0.013535	0.023628	0.0338427	0.043794	0.053344	0.062452
0.800	0.018141	0.031289	0.0443947	0.057018	0.069022	0.08039
0.900	0.023164	0.03958	0.0557491	0.071178	0.085743	0.099453
1.000	0.028477	0.04829	0.0676113	0.085907	0.103072	0.119149

FIGURE 9-93 An example of how calls can be made to the *Lifting Line* function from within Microsoft Excel.

## EXERCISES

- (1) Determine all the variables of the wing in Figure 9-94, if its planform area,  $S$ , is 200 ft<sup>2</sup>,  $AR = 7.5$ , and  $\lambda = 0.5$ . Approximate its internal volume if it features a constant 15% thick airfoil, whose maximum thickness is at 50% chord. If 30% of this volume is to be used for the fuel

tanks, how much fuel can the wing hold and how much will it weigh assuming Jet-A fuel (1 US gal = 231.02 in<sup>3</sup>)?

Answer:  $b = 38.73$  ft,  $C_r = 6.885$  ft,  $MGC = 5.355$  ft,  $Y_{MGC} = 8.607$  ft,  $X_{MGC} = 4.969$  ft,  $\Lambda_{C/4} = 28.05^\circ$ ,  $\Lambda_{C/2} = 26.03^\circ$ , wing volume is approximately 100 ft<sup>3</sup>; it can hold 225 US gallons, which weigh 1510 lb<sub>f</sub>.

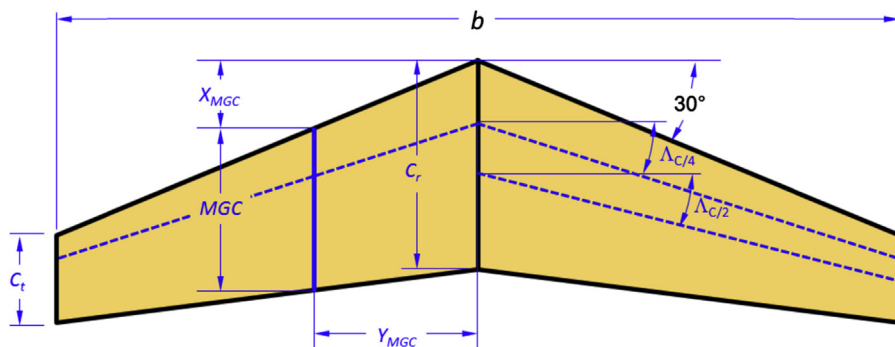


FIGURE 9-94 Wing used in Exercise (1).

## VARIABLES

Symbol	Description	Units (UK and SI)	Symbol	Description	Units (UK and SI)
$AOA$	Angle-of-attack	Degrees or radians	$c_r$	Root chord length	ft or m
$AR$	Aspect ratio		$C_{rR}$	Reduced root chord length	ft or m
$AR_{corr}$	Boosted aspect ratio		$c_t$	Tip chord length	ft or m
$AR_e$	Effective aspect ratio ( $AR \cdot e$ )		$c_t$	Thrust specific fuel consumption	1/s
$AR_{lim}$	Aspect ratio limit		$C_Y$	Side force coefficient	
$AR_R$	Reduced aspect ratio		$D$	Drag	lb <sub>f</sub> or N
$b$	Wingspan	ft or m	$d_i(y)$	Lift-induced drag per unit span	lb <sub>f</sub> /ft or N/m
$b_R$	Reduced wingspan	ft or m	$dl$	Infinitesimally small vector length	ft or m
$c$	Chord length	ft or m	$dw$	Velocity induced at arbitrary point P by dl	ft/s or m/s
$c_{avg}$	Average chord length	ft or m	$e$	Oswald's span efficiency	
$c_{bhp}$	Specific fuel consumption of a piston engine	(lb <sub>f</sub> /hr)/BHP or g/J	$E$	Endurance	s
$C_d$	Two-dimensional drag coefficient		$h$	Component of distance to point P perpendicular to velocity	ft or m
$C_D$	Three-dimensional drag coefficient		$h$	Height of winglets	ft or m
$C_{Di}$	Lift-induced drag coefficient		$i_{HT}$	Horizontal tail angle-of-incidence	Degrees or radians
$C_{DM}$	Compressibility drag coefficient		$i_{root}$	Wing root airfoil angle-of-incidence	Degrees or radians
$C_{Dmin}$	Minimum drag coefficient		$i_W$	Wing angle-of-incidence	Degrees or radians
$C_l$	Two-dimensional lift coefficient		$K_{SM}$	Fraction design static margin	
$C_L$	Three-dimensional lift coefficient		$L$	Lift	lb <sub>f</sub> or N
$C_{L0}$	Zero AOA lift coefficient		$LD_{max}$	Maximum lift-to-drag ratio	
$C_{LC}$	Average cruise lift coefficient		$l_{LER}$	Leading edge radius	ft
$C_{Lmax}$	Maximum 3D lift coefficient		$M$	Mach number	
$C_{Lmin}$	Minimum coefficient of lift		$M$	Pitching moment	lb <sub>f</sub> ·ft or N·m
$C_{lp}$	Roll damping coefficient		$MAC$	Mean aerodynamic chord	ft or m
$C_{l\alpha}$	Two-dimensional lift curve slope	Per degree or per radian	$M_{crit}$	Critical Mach number	
$C_{L\alpha}$	Three-dimensional lift curve slope	Per degree or per radian	$MGC$	Mean geometric chord	ft or m
$C_m$	Two-dimensional pitching moment coefficient		$P_1$	Special parameter 1	
$C_M$	Pitching moment coefficient		$P_2$	Special parameter 2	
$C_{mROOT}$	Pitching moment coefficient of the root airfoil		$r$	Distance to arbitrary point P	
$C_{mTIP}$	Pitching moment coefficient of the tip airfoil		$R$	Leading edge suction parameter	
$C_{m\alpha}$	Two-dimensional pitching moment curve slope	Per degree or per radian	$R$	Range	ft
$C_{M\alpha}$	Three-dimensional pitching moment curve slope	Per degree or per radian	$R_e$	Reynolds number	
			$S$	Planform area	ft <sup>2</sup> or m <sup>2</sup>
			$S_R$	Reduced wing area	
			$t$	Airfoil thickness	ft or m
			$TR$	Taper ratio	

(Continued)

Symbol	Description	Units (UK and SI)	Symbol	Description	Units (UK and SI)
$u$	$x$ -component of total velocity vector	ft/s or m/s		Sweep of the maximum wing thickness line	
$v$	$y$ -component of total velocity vector	ft/s or m/s	$\alpha$	Angle-of-attack	Degrees or radians
$V$	Velocity	ft/s or m/s	$\alpha_0$	Nonlinear lift angle-of-attack	Degrees or radians
$V_C$	Average cruising speed	ft/s	$\alpha_C$	Cruise angle-of-attack	Degrees or radians
$V_n$	Normal component of velocity	ft/s or m/s	$\alpha_{stall}$	Stall AOA	Degrees or radians
$V_p$	Parallel component of velocity	ft/s or m/s	$\alpha_{stall\ root}$	Two-dimensional stall AOA for the root airfoil	Degrees or radians
$V_s$	Stall velocity	ft/s or m/s	$\alpha_{stall\ tip}$	Two-dimensional stall AOA for the tip airfoil	Degrees or radians
$w$	Total velocity induced at arbitrary point P	ft/s or m/s	$\alpha_e$	Effective AOA	Degrees or radians
$w$	$z$ -component of total velocity vector	ft/s or m/s	$\alpha_{F\ opt}$	Optimum AOA for the fuselage	Degrees or radians
$W_1$	Aircraft weight at the beginning of the design mission	lb <sub>f</sub> or N	$\alpha_i$	Induced AOA	Degrees or radians
$W_2$	Aircraft weight at the end of the design mission	lb <sub>f</sub> or N	$\alpha_{stall}$	Stall angle-of-attack	Degrees or radians
$W_{avg}$	Average weight during cruise	lb <sub>f</sub>	$\alpha_{ZL}$	Zero lift angle-of-attack	Degrees or radians
$W_{fin}$	Final weight at cruise	lb <sub>f</sub>	$\alpha_{ZLroot}$	Two-dimensional zero-lift AOA for the root airfoil	Degrees or radians
$w_{fus}$	Fuselage width	ft or m	$\alpha_{ZLtip}$	Two-dimensional zero-lift AOA for the tip airfoil	Degrees or radians
$W_{ini}$	Initial weight at cruise	lb <sub>f</sub>	$\beta$	Prandtl-Glauert Mach number parameter	
$w_{y0}$	Downwash velocity induced by vortices	ft/s or m/s	$\delta$	Lift-induced drag factor	
$X_{MGC}$	$x$ -distance to the leading edge of the MGC	ft or m	$\phi$	Velocity potential	
$y$	Spanwise station	ft or m	$\phi$	Washin/washout angle	Degrees or radians
$Y_{MGC}$	$y$ -distance from the root chord to the MGC	ft or m	$\phi_A$	Aerodynamic washout	Degrees or radians
$\Delta C_{Lmax}$	Mach number correction factor		$\phi_D$	Decalage angle	Degrees or radians
$\Delta y$	Leading edge parameter		$\phi_G$	Geometric washout	Degrees or radians
$\Delta \alpha_{CLmax}$	Correction angle for stall AOA	Degrees or radians	$\eta$	Spanwise station (for b/2)	
$\Delta \phi_{MGC}$	Correction to account for wing twist	Degrees or radians	$\eta_P$	Propeller efficiency	
$\Gamma$	Dihedral/anhedral angle	Degrees or radians	$\kappa$	Ratio of 2D lift curve slope to $2\pi$	
$\Gamma$	Vortex filament strength		$\lambda$	Taper ratio	
$\Lambda_{c/2}$	Sweep of the mid-chord line	Degrees or radians	$\lambda_R$	Reduced taper ratio	
$\Lambda_{c/4}$	Sweep of the quarter-chord line	Degrees or radians	$\mu$	Air viscosity	lb <sub>f</sub> ·s/ft <sup>2</sup>
$\Lambda_{c/4\ lim}$	Limit sweep of the quarter-chord line	Degrees or radians	$\rho$	Density of air at altitude	slugs/ft <sup>3</sup> or kg/m <sup>3</sup>
$\Lambda_{LE}$	Sweep of the leading edge	Degrees or radians	$\tau$	Lift curve slope correction factor	
$\Lambda_{t\ max}$		Degrees or radians			

## References

- [1] Hoak DE. USAF Stability and Control DATCOM. Flight Control Division, Air Force Flight Dynamics Laboratory; 1978.
- [2] Kuhlman Bill, Bunny. On the Wing... R/C Soaring Digest October 2003.
- [3] Thomas Fred. Fundamentals of Sailplane Design. College Park Press; 1999.

- [4] Brandt Steven A, Stiles Randall J, Bertin John J, Whitford Ray. Introduction to Aeronautics: A Design Perspective. AIAA Education Series; 1997.
- [5] Raymer DP. Aircraft Design: A Conceptual Approach. AIAA Education Series; 1996.
- [6] Loftin, Laurence Jr K. Quest for Performance; The Evolution of Modern Aircraft. NASA SP-468 1985:93.
- [7] NACA R-823. Experimental Verification of a Simplified Vee-Tail Theory and Analysis for Available Data on Complete Model with Vee Tails. Purser, Paul E., and John P. Campell; 1944.
- [8] AIAA-1977-607-721. The AV-8B Wing: Aerodynamic Concept and Design. Lacey, I.R., and K. Miller, AIAA; 1977.
- [9] Taylor, John W. R. Jane's All the World's Aircraft. Jane's Yearbooks, various years.
- [10] <http://www.flightlevelengineering.com>.
- [11] Meier Hans-Ulrich. German Development of the Swept Wing 1935-1945. AIAA; 2006.
- [12] Jones Robert T. Adolf Busemann, 1901-1986, vol. 3. Memorial Tributes. National Academy of Engineering; 1989.
- [13] Busemann, Adolf. Aerodynamischer Auftrieb bei Überschallgeschwindigkeit. Luftfahrtforschung, Bd. 12, Nr. 6, Oct.
- [14] NACA TR-863. Wing Plan Forms for High-Speed Flight. Jones, Robert T; 1945.
- [15] Boyne Walter J. Messerschmitt Me 262: Arrow to the Future. Schiffer Publishing, Ltd; 1992.
- [16] Langton Roy, et al. Aircraft Fuel Systems. John Wiley and Sons, Ltd; 2009.
- [17] Sargent, Barnes Sparky. A Dyke Delta Reborn. EAA Sport Aviation Magazine; December, 2008.
- [18] Whitford Ray. Design for Air Combat. Jane's; 1987.
- [19] NACA-TN-2502. Examples of Three Representative Types of Airfoil-Section Stall at Low Speed. McCullough, George B., Gault, Donald E; 1951. p. 1.
- [20] NACA TN-817. Correction of the Lifting Line Theory for the Effect of the Chord. Jones, Robert T; 1941.
- [21] NACA TN-1175. Lifting-Surface-Theory Aspect-Ratio Corrections to the Lift and Hinge-Moment Parameters for Full-Span Elevators on Horizontal Tail Surfaces. Swanson, Robert S., and Stewart M. Crandall; 1947.
- [22] Dommash Daniel O, Sherby Sydney S, Connolly Thomas F. Airplane Aerodynamics. 4th ed. Pittman; 1967. pp. 154–160.
- [23] Glauert Hermann. The Elements of Aerofoil and Airscrew Theory. Cambridge University Press; 1926.
- [24] Helmbold, H. B. Der unverwundene Ellipsenflügel als tragende Fläche. Jahrbuch 1942 der Deutschen Luftfahrtforschung, R. Oldenbourg (Munich), pp. I 111–I 113.
- [25] NACA TR-3911. A Method for Predicting Lift Increments due to Flap Deflection at Low Angles of Attack in Incompressible Flow. Lowry, John G., and Edward C. Polhamus; 1957.
- [26] Hoak DE. USAF Stability and Control DATCOM. Flight Control Division, Air Force Flight Dynamics Laboratory; 1978. pp. 4.1.3.2–49.
- [27] Betz Albert. Lift and Drag of a Wing Near a Horizontal Surface. Zeitschrift für Flugtechnik und Motorluftschiffahrt 1912:212.
- [28] Wieselberger C. Wing Resistance Near the Ground. Zeitschrift für Flugtechnik und Motorluftschiffahrt 1921;(No. 10).
- [29] NACA TM-77. Wing Resistance Near the Ground. Wieselberger, C; 1922.
- [30] NASA TN-D-970. Effect of Ground Proximity on the Aerodynamic Characteristics of Aspect-Ratio-1 Airfoils With and Without End Plates. Carter, Arthur W; 1961.
- [31] McCormick Barnes W. Aerodynamics, Aeronautics, and Flight Mechanics. John Wiley & Sons; 1979. p. 420.
- [32] Asselin Mario. An Introduction to Aircraft Performance. AIAA Education Series; 1997.
- [33] Jenkinson Lloyd R, Simpkin Paul, Rhodes Darren. Civil Jet Aircraft Design. AIAA Education Series; 1999.
- [34] Young AD. The Aerodynamic Characteristics of Flaps. R.&M. No. 2622, British A. R. C; 1947.
- [35] NACA R-824. Summary of Airfoil Data. Abbott, Ira H., Albert E. von Doenhoff and Louis S. Stivers Jr; 1945.
- [36] NACA TR-408. General Formulas and Charts for the Calculation of Airplane Performance. Oswald, Bailey W; 1933.
- [37] Shevell Richard S. Fundamentals of Flight. Prentice Hall; 1983. 181–183.
- [38] Frost Richard C, Rutherford Robbie. Subsonic Wing Span Efficiency. AIAA Journal April 1963;vol. 1(No. 4).
- [39] Roskam Jan. Airplane Design, Part VI. DARcorporation; 2000.
- [40] NACA TN-1299. Effects of Mach Number and Reynolds Number on the Maximum Lift Coefficient of a Wing of NACA 230-Series Airfoil Sections. Furlong, G. Chester, and James E. Fitzpatrick; 1947.
- [41] NACA TN-2753. Effects of Mach Number Variation between 0.07 and 0.34 and Reynolds Number Variation between 0.97x106 and 8.10x106 on the Maximum Lift Coefficient of a Wing of NACA 64-210 Airfoil Sections. Fitzpatrick, James E., and William C. Schneider; 1952.
- [42] NACA TN-1677. Experimental and Calculated Characteristics of Several High-Aspect-Ratio Tapered Wings Incorporating NACA 44-series, 230-series, and Low-Drag 64- Series Airfoil Sections. Bollech, Thomas V; 1948.
- [43] van Dam CP, Vijgent PMHW, Holmes BJ. Aerodynamic Characteristics of Crescent and Elliptic Wings at High Angles of Attack. Journal Aircraft April 1991;vol. 28(No. 4).
- [44] Torenbeek Egbert. Synthesis of Subsonic Aircraft Design. Delft University Press; 1986.
- [45] NACA TR-1339. A Summary and Analysis of the Low-Speed Longitudinal Characteristics of Swept Wings at High Reynolds Numbers. Furlong GC, and McHugh JG; 1957.
- [46] NACA TN-1093. Effect of Sweepback and Aspect Ratio on Longitudinal Stability Characteristics of Wings at Low Speeds. Shortal JA, and Maggin B; 1946.
- [47] NACA RM-L8D29. Wind-Tunnel Investigation of High-Lift and Stall-Control Devices on a 37 degree Sweptback Wing of Aspect Ratio 6 at High Reynolds Numbers. Koven, William, and Robert R. Graham; 1948.
- [48] Katz Joseph, Plotkin Allen. Low-Speed Aerodynamics. Cambridge University Press; 2001.
- [49] Pope Alan. Basic Wing and Airfoil Theory 2009. Dover.
- [50] Bertin John J, Smith Michael L. Aerodynamics for Engineers. Prentice-Hall; 1979. p. 171.
- [51] Moran Jack. An Introduction to Theoretical and Computational Aerodynamics. John Wiley and Sons; 1984.
- [52] Anderson, John Jr D. Fundamentals of Aerodynamics. 4th ed. McGraw-Hill; 2007.
- [53] Karamcheti Krishnamurty. Principles of Ideal-Fluid Aerodynamics. John Wiley & Sons; 1966. Appendix E, p. 624.